The chemist who turns pills to gold *p. 622*

Impressions from a festival of environmental films *p. 628*

Confining electrons in a graphene corral *p. 672*

Science

$10
8 MAY 2015
sciencemag.org

AAAS

Mapping our differences

A catalog of variation in human gene expression *pp. 618, 640, & 648*

CONTENTS

8 MAY 2015 • VOLUME 348 • ISSUE 6235

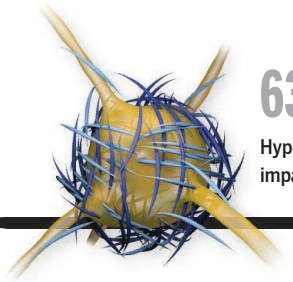

636
Hyperactive astrocytes impair brain development

NEWS

IN BRIEF

IN DEPTH

FEATURES

INSIGHTS

BOOKS *ET AL.*

PERSPECTIVES

PHOTO (BOTTOM): ANTOINE DOYEN

Published by AAAS

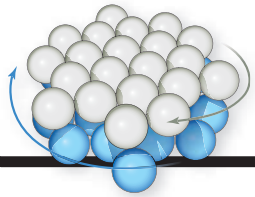

632 & 679
Getting a tighter grasp on friction

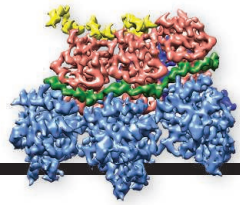

704
A high-resolution view of measles virus capsid protein

ON THE COVER

A representation of how variation in the human genome affects gene expression among individuals and tissues. Colors and shapes show variations between people and within individuals. The Genotype-Tissue Expression (GTEx) Consortium examined postmortem tissue to document how genetic variants confer differences in gene expression across the human body. See pages 618, 640, 648, 660, and 666. *Illustration: Thomas Danthony*

SCIENCE (ISSN 0036-8075) is published weekly on Friday, except the last week in December, by the American Association for the Advancement of Science, 1200 New York Avenue, NW, Washington, DC 20005. Periodicals mail postage (publication No. 484460) paid at Washington, DC, and additional mailing offices. Domestic individual membership and subscription (51 issues): $153 ($74 allocated to subscription). Domestic institutional subscription (51 issues): $1282; Foreign postage extra: Mexico, Caribbean (surface mail) $55; other countries (air assist delivery) $85. First class, airmail, student, and emeritus rates on request. Canadian rates with GST available upon request, GST #1254 88122. Publications Mail Agreement Number 1069624. **Printed in the U.S.A.**
Change of address: Allow 4 weeks, giving old and new addresses and 8-digit account number. **Postmaster:** Send change of address to AAAS, P.O. Box 96178, Washington, DC 20090–6178. **Single-copy sales:** $10.00 current issue, $15.00 back issue prepaid includes surface postage; bulk rates on request. *Science* is indexed in the *Reader's Guide to Periodical Literature* and in several specialized indexes.

Published by AAAS

Science
AAAS
1200 New York Avenue, NW, Washington, DC 20005
Bateman House, 82-88 Hills Road, Cambridge, UK CB2 1LQ

SUBSCRIPTION SERVICES For change of address, missing issues, new orders and renewals, and payment questions: 866-434-AAAS (2227) or 202-326-6417, FAX 202-842-1065. Mailing addresses: AAAS, P.O. Box 96178, Washington, DC 20090-6178 or AAAS Member Services, 1200 New York Avenue, NW, Washington, DC 20005

INSTITUTIONAL SITE LICENSES 202-326-6755 **REPRINTS:** Author Inquiries 800-635-7181 **COMMERCIAL INQUIRIES** 803-359-4578 **PERMISSIONS** 202-326-6765, permissions@aaas.org **AAAS Member Services** 202-326-6417 or http://membercentral.aaas.org/discounts

Science serves as a forum for discussion of important issues related to the advancement of science by publishing material on which a consensus has been reached as well as including the presentation of minority of conflicting points of view. Accordingly, all articles published in *Science*—including editorials, news and comment, and books reviews—are signed and reflect the individual views of the authors and not official points of view adopted by AAAS or the institutions with which the authors are affiliated.

INFORMATION FOR AUTHORS See pages 678 and 679 of the 6 February 2015 issue or access www.sciencemag.org/about/authors

Published by AAAS

EDITORIAL

Give women an even chance

Marcia McNutt
Editor-in-Chief
Science *Journals*

An important part of the mentoring role of academic advisors is writing letters of recommendation for worthy students who are applying for research grants, fellowships, and entrance to elite programs. Such letters often have more impact than grades or test scores at the graduate level, where factors such as initiative, hard work, creativity, independence, problem-solving ability, and teamwork are prized skills. Well-crafted, honest letters help in determining whether a candidate is a good fit. For that reason, I was surprised recently when asked to review 60 proposals from graduate students for small research grants. More than 10% of the applicants had a least one supporting letter containing inappropriate material for the decision at hand. All of the students so affected, unfortunately, were women, and those writing the problematic letters were nearly equally men and women. By describing how these instances appear from the standpoint of a selection committee member, my hope is that the professionalism in recommendation letters will improve.

"...'nice' never got me a research grant or professional position."

As examples of the sort of problems, one letter described how the candidate was so good to her elderly mother, yet still enjoyed life, spending time in nature with her husband and her animal friends. Another letter reflected amazement that the candidate managed to balance so efficiently being a student, a scientist, and a mother. Such comments do indeed make impressions on a committee that must select only 1 in 10 for an award from a highly competitive pool. They cannot help but put a candidate at a disadvantage when compared to others who are praised for their self-initiated research projects, interesting uses of coursework to address new scientific problems, or careful background preparation for the research project proposed.

Beyond comments that were simply out of place for the decision at hand, I noted an overall bias in the language used to describe the male candidates versus some of the female candidates. In some letters, women were described as "friendly," "kind," "pleasant," "humble," and frequently, "nice." While I am sure they were all of that, those were not necessarily the most relevant characteristics I was looking for in the next generation of scientists to advance the frontiers of discovery. Very different words were used to describe the male candidates (and many of the females as well): "brilliant," "creative," "hard-working," "insightful," and "showing leadership."

Studies have documented bias in referees' unblinded reviews of manuscripts for publication, but this was the first time that I noted such a bias in the language used to assess a student's suitability for a research grant—a bias that could carry over to future funding decisions. I suspect that such bias creeps in unintentionally in most cases, but I also understand that gender stereotypes persist and that they have a basis in reality. Women still bear the majority of caregiver burdens for children and elderly parents. But that information does not belong in letters of recommendation. I like to think that I am a nice person. But "nice" never got me a research grant or professional position.

Now is the time to promote women as well as other underrepresented groups in science. The future strength of the global scientific enterprise depends on boosting the influx of diverse and talented researchers into science and engineering fields. Subtle bias, even unintended, in advancing this cohort can be more damaging than outright bias, because it is more difficult to detect and correct. I urge all who write these important letters of recommendation to take a last look before hitting "send" to be sure that what you have written is free of bias.

– Marcia McNutt

10.1126/science.aac4767

NEWS

> "[T]he application of reason, more than any other means, has proven to offer hope for human survival on Earth."
>
> **U.S. Representative Mike Honda (D–CA)**, introducing a resolution to declare a National Day of Reason as a secular alternative to the National Day of Prayer.

IN BRIEF

Whale mouths sport bungee-cord nerves

Feeding humpback whales can open wide thanks to expandable nerves (*right*).

When a humpback whale gets hungry, it pumps its tail and fluke to lunge through the briny, prey-laden water with its jaw dangling nearly perpendicular to its body. To accommodate that mouthful, the family of baleen whales called rorquals (Balaenopteridae)—which includes blue, fin, and humpback whales—has evolved unique features such as highly flexible jaw joints, a deformable tongue that inverts into a sac to hold the seawater, and grooved, expandable blubber on their undersides. Now, scientists have identified another necessary adaptation: Nerves in the whales' tongue and mouth can extend to more than double their original length. Stretching vertebrate nerves normally leads to pain, paralysis, or even the detachment of nerve roots from the spinal cord. But researchers report this week in *Current Biology* that rorquals' nerves consist of a core of folded bundles of nerve fibers surrounded by a thick wall of folded collagen and elastin—the same protein that keeps skin elastic. The nerves unfold until the collagen stiffens, preventing overelongation, and the elastin snaps the nerves to their previous shape.

AROUND THE WORLD

House bill recommends NIH boost

WASHINGTON, D.C. | The U.S. House of Representatives last week released a bipartisan draft bill that aims to jump-start biomedical innovation with new policies at the National Institutes of Health (NIH) and the Food and Drug Administration. The 21st Century Cures Act, spearheaded by Energy and Commerce Committee Chair Fred Upton (R–MI) and a senior democrat, Diana DeGette (D–CO), delighted research advocates with a suggested NIH budget increase of $10 billion over 5 years. An earlier draft released by Upton in January failed to win DeGette's support and disappointed NIH advocates (*Science*, 6 February, p. 594). The new version cuts incentives for drug developers and creates an NIH innovation fund to support "young emerging scientists," precision medicine, and a third unspecified category. http://scim.ag/Cures2

Giant telescope picks U.K. HQ

JODRELL BANK, U.K. | The countries building the Square Kilometre Array (SKA), a vast radio telescope to be constructed in South Africa and Australia, have turned down the chance of headquartering it in the historic Castello Carrarese in Padua, Italy, in favor of a new purpose-built HQ at SKA's current interim home near Manchester, U.K. Castello Carrarese, until recently used as a prison, made early running in the race to host the HQ. "Both [nations] offered substantial financial support," says SKA Director General Philip Diamond. But the 11 member countries opted for the United Kingdom, which will chip in £200 million to the project, including the HQ bid and its contribution to phase I of construction from 2018 to 2023. http://scim.ag/SKAhome

Americas declared rubella-free

WASHINGTON, D.C. | North and South America have become the first region in the world to eliminate rubella, the Pan American Health Organization (PAHO) announced on 29 April. Rubella symptoms

A protester in Baltimore throws a gas canister back at police during riots on 28 April.

Three Q's

Riots convulsed Baltimore, Maryland's streets last week following the funeral of a 25-year-old African-American man who died in police custody. **Dan Braha**, a social scientist at the New England Complex Systems Institute in Cambridge, Massachusetts, has been collecting Twitter data related to the riot as part of a larger study of social media and civil unrest.

Q: How does Baltimore's rioting compare to that in Ferguson, London, and elsewhere?
A: In terms of the communications and patterns of spread, they are remarkably similar. Even if the causes are different, there seems to be a universal pattern to civil unrest.

Q: What can you learn about the Baltimore riots from social media?
A: It's interesting to see the pattern of spread, much like forest fires, spreading in clusters and locally. The riots, in my view, could easily spread across other cities in the United States where racial tensions are high and are close to a tipping point.

Q: How do you spot this tipping point?
A: There are three basic data from tweets: location, time, and intensity. First, you create a network of communication, where the nodes are people or groups. Then, you correlate the communication patterns with characteristics such as gender [and] political attitudes. ... It is the intensity of the communication—how many messages over time—that predicts what is to come. Full interview at **http://scim.ag/_riots.**

are usually mild, but if contracted in early pregnancy, the virus can lead to miscarriage or birth defects known as congenital rubella syndrome (CRS). The last endemic cases of rubella in the Americas were reported in Argentina in 2009, and the last case of CRS was reported in Brazil the same year. The 15-year-long elimination campaign vaccinated an estimated 250 million adolescents and adults in 32 countries and territories in the Americas, said PAHO Director Carissa Etienne.

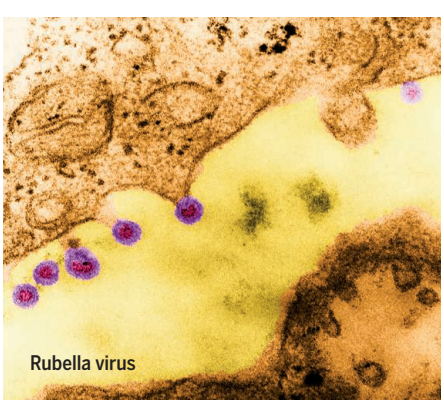

Rubella virus

Researcher drops primate work

TÜBINGEN, GERMANY | A researcher targeted by animal rights activists is giving up his work on primates. Nikos Logothetis, a director at the Max Planck Institute for Biological Cybernetics, says that he will conclude his experiments on macaques "as quickly as possible" and focus future work on rodents. In a 28 April letter, he cited the failure of the Max Planck Society (MPS) and other scientific organizations to press criminal charges against aggressive activists as a factor in his decision. Logothetis's research was the subject of a German television program in September that included footage filmed by an undercover activist. MPS says it was advised not to bring charges against the activist.
http://scim.ag/Logothetis

California climate goals

SACRAMENTO | California has raised the bar for global climate change action. The state, halfway to its goal of cutting greenhouse gas emissions to 1990 levels by 2020, now aims to drive carbon pollution 40% below that mark by 2030. Governor Jerry Brown signed an executive order on 29 April matching the European Union's ambitious pledge for international climate change negotiations, to be finalized in Paris this December. California, unlike Europe, has created jobs while slashing carbon. The move by the world's eighth largest economy will inspire nations to aim high on climate action, Brown's supporters say. Critics maintain California business will suffer if the state is too far ahead of the pack. Indeed, because California generates less than 2% of global greenhouse gas emissions, Brown's move helps the planet only if others follow.
http://scim.ag/climateCA

PHOTOS: (TOP TO BOTTOM) © ERIC THAYER/REUTERS/CORBIS; MARY MARTIN/SCIENCE SOURCE

Protesters, here flying Hawaiian flags, have halted construction of one of the world's largest optical telescopes.

PHOTO: MALIE DEMELLO

ASTRONOMY

Telescope clash deeply rooted in Hawaii's past

Opponents say Thirty Meter Telescope violates sovereignty and sacred ground

By **Ilima Loomis** *and* **Adrian Cho**

A month after protests halted work on the Thirty Meter Telescope (TMT) on Hawaii's Big Island, the impasse over what would be one of the world's largest optical telescopes has deepened. Last week, as protesters continue to occupy the construction site on Mauna Kea, a 4205-meter dormant volcano, a state panel representing Native Hawaiians pulled its support for the project.

The 30 April decision by the quasi-governmental Office of Hawaiian Affairs (OHA) underscores a deeper challenge for the TMT. Besides offending cultural and religious sensitivities by occupying a site on a sacred mountain, the project—led by an international consortium based in Pasadena, California—has gotten snagged on the thorny issue of Hawaiian sovereignty. "It comes down to the fact that there is an occupation of Hawaii by the United States," says Anne Keala Kelly, an independent filmmaker in Honolulu, who is making a documentary about the protests.

Managers of the $1.4 billion project still have the permits, issued 6 March by the state's Department of Land and Natural Resources, to start construction. But they have held off since 31 protesters were arrested on 2 April. The TMT team worked for years to address Native Hawaiians' concerns, says Sandra Dawson, TMT's manager for Hawaii community affairs, so researchers were taken aback by the flare-up, especially on social media. "Some of the people we're seeing now are people we've never seen before," she says.

TMT collaborators say they have strived to be respectful of Mauna Kea, which many Native Hawaiians consider the "piko," or navel, that connects the island to Wakea, the Sky Father. Planners chose a site 193 meters below the sacred summit that has no known archaeological remains, researchers say. Opponents of the TMT say that is not much help, given that 13 telescopes already dot Mauna Kea. "It's like an industrial park up there," Kelly says. "This is cultural strip mining."

More important, opponents say, the TMT is emblematic of the greater dispossession of Native Hawaiians, which dates back to 1893, when the United States claimed the islands. "You can say, 'Well, it's a cultural issue,' but it's more than that," Kelly says.

Such sentiments struck a chord with the trustees of OHA, whose mission is to protect and perpetuate Hawaiian culture. "Self-determination is right at our fingertips," said OHA Trustee Dan Ahuna before last week's vote. "We have the opportunity to send a strong message that it is no longer business as usual for Hawaiians."

OHA's vote withdraws its 2009 endorsement of the TMT. In a meeting in Honolulu, the board voted 6 to 0 to rescind support, with one trustee abstaining and two absent. Still, many Hawaiian groups felt the vote didn't go far enough and that the board should have expressed clear opposition to the project. A vote rejecting that stronger stance was met with shouts of "aole!" or "no!" from a standing-room-only crowd.

"We're disappointed that OHA cannot come out in full support of their people, their constituents, their lahui [nation]," says Andre Perez, an organizer with Movement for Aloha No ka ⊠Āina, one of the groups that sent protesters to Mauna Kea. However, OHA Trustee Peter Apo said during the meeting that maintaining a more neutral position would allow OHA to retain a voice in the project's future.

The TMT dispute has divided Native Hawaiians, who constitute about 10% of the state's population. The TMT has pledged to invest $3 million per year in the local community, says Paul Coleman, an astronomer at the University of Hawaii, Manoa. It will

pay $1 million to the quasigovernmental Office of Mauna Kea Management and OHA to lease the site (existing telescopes pay $1) and supply another $1 million each to support science, technology, engineering, and mathematics (STEM) education and to train Hawaii residents to work on the TMT and the other telescopes on Mauna Kea. "This is a fantastic opportunity to give our kids a chance for the jobs that come along with the telescopes," says Coleman, a Native Hawaiian. The STEM money has already begun to flow, he notes.

At the OHA meeting, Mailani Neal, an 18-year-old high school student from the Big Island, testified that it was her dream to study physics and become an astronomer. "The stars brought our Hawaiian ancestors to Hawaii, and now we have the opportunity to bring the people of Hawaii to the stars," she said, fighting back tears. "The Thirty Meter Telescope has provided a beacon for me and motivated me in all that I do."

But $3 million per year is meager compensation for the expropriation Hawaiians have endured, says Williamson Chang, a law professor at the University of Hawaii, Manoa, who opposes the TMT. The real issues are sovereignty and social justice, Chang says, noting that Native Hawaiians often end up on the bottom of the economic heap in their own land. "Even if you go to the university, you end up working in a restaurant," he says. "You work two or three jobs and you can't afford to raise a family."

Hawaii's governor, David Ige, has called for dialogue among the various parties. In the meantime, TMT officials have set no date for starting construction and have no plans to push for the removal of the protesters, says Michael Bolte, an astronomer at the University of California, Santa Cruz, and associate director of the project. For now, he says, they're encouraging Native Hawaiians who support the project to speak up. "They're our strongest allies."

As for the protesters, Kahookahi Kanuha, a leading organizer, says they are expanding their focus beyond the TMT to the state's management of the whole mountain, pushing to ensure compliance with environmental requirements and completion of a required cultural impact assessment. Protest groups will also oppose a planned 65-year extension on the University of Hawaii's lease of the summit area, which is set to expire in 2033—just 11 years into TMT's planned decades-long lifetime. Stopping the extension "would put the TMT in a very tough position," Kanuha says, "and they would be forced to look for a new location." ■

Ilima Loomis is a freelance journalist in Maui, Hawaii.

EVOLUTION

Deep-ocean microbe is closest living relative of complex cells

Genomic study of "Loki" supports a revisionist view of the origin of eukaryotes

By **Mitch Leslie**

It's one of the most significant, and most vexing, splits in life's history. About 2 billion years ago, the prokaryotes, relatively simple single-celled organisms that include bacteria and archaea, gave rise to the more elaborate eukaryotes, the lineage that ultimately spawned multicellular life forms such as fungi, plants, and animals like us. Now, researchers combing through muck from the bottom of the North Atlantic Ocean have identified an archaeon that is the closest living relative of eukaryotes so far discovered.

The microbe, informally dubbed Loki and described this week in *Nature*, has set off a buzz among evolutionary biologists. "It tells us something very important about the origin of eukaryotes," says Eugene Koonin of the National Center for Biotechnology Information in Bethesda, Maryland. "The ancestor of eukaryotes was a highly complex organism related to other archaea." The deep-sea microbe "looks like a potential transitional form" that preserves one of the evolutionary steps between archaea and eukaryotes, adds evolutionary cell biologist Mark Field of the University of Dundee in the United Kingdom.

Unlike prokaryotes, eukaryotes sport organelles such as power-generating mitochondria and—in plants and some protists—light-capturing chloroplasts. Moreover, they stow DNA inside a nucleus that's enclosed by a membrane, and their cells feature other internal structures built of membranes, such as the Golgi apparatus, lysosomes, and the endoplasmic reticulum.

Mitochondria and chloroplasts, researchers agree, are descended from formerly free-living prokaryotes that took up residence in other ancient cells. But the identity of the organism that captured and tamed those microbes remains unclear. Molecular evidence suggests that archaea are the closest relatives of eukaryotes. Researchers have disagreed, however, about whether eukaryotes branched off from a simpler prokaryote before archaea emerged—the traditional three-domain view of life—or evolved later, directly from archaea (see diagram).

Loki, known only from its gene fragments, supports the second hypothesis. As part of a project to uncover novel types of archaea, evolutionary biologist Thijs Ettema of Uppsala University in Sweden and colleagues analyzed 10 grams of sediment brought up from the ocean bottom midway between Greenland and Norway. They found that it contained distinctive gene sequences that indicated the presence of unidentified microorganisms. Although the researchers could separate out only a few nanograms of shattered DNA, they were able to use a technique called metagenomics to piece together these fragments and produce partial genomes for three new types of archaea.

The researchers weren't able to isolate any living or dead microbes from the muck, but they could infer the characteristics of the one with the most complete genome. (Because the sediment sample came from near the undersea volcanic vents known as Loki's Castle, the researchers dubbed this organism Lokiarchaeum, or Loki for short.) Its genome reveals several telling

All in the family

A newly discovered deep-sea microbe named Loki suggests eukaryotes evolved from archaea (right) rather than representing a separate branch of life (left).

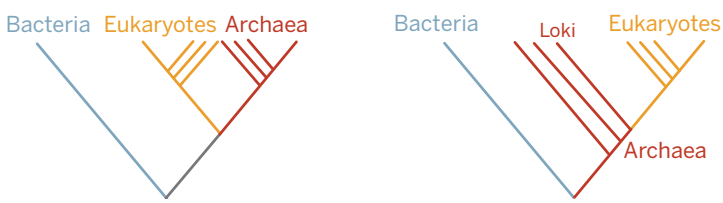

similarities with eukaryotes, the researchers say. For example, actin proteins help form the cytoskeleton that braces eukaryotic cells and enables them to move. Loki carries actinlike genes that are more similar to the eukaryotic versions than are the varieties found in other archaea.

In eukaryotic cells, enzymes known as small GTPases perform a slew of functions, from shaping the cytoskeleton to orchestrating the transportation of material in tiny membrane containers called vesicles. Genes for a handful of these enzymes have turned up in bacteria and in other archaea, but "we found 60 to 70 of those guys in Loki," Ettema says. Unlike other prokaryotes, Loki also harbors several genes for parts of the ESCRT protein complex that in eukaryotes bends and snips membranes, abilities important for cell division and for forming vesicles that ferry molecular junk for disposal.

"This is the most eukaryotelike prokaryote we've ever seen," says evolutionary biologist James McInerney of the National University of Ireland, Maynooth. An evolutionary tree based on the genomes of all three new archaea suggests that they are the closest known relatives of eukaryotes. To McInerney, the result "is another stake through the heart of the three-domain tree."

Loki's molecular features suggest that eukaryotes' ancestor could have had an actin cytoskeleton and might have been able to gobble up cells or other types of food.

> ***"It tells us something very important about the origin of eukaryotes."***
>
> **Eugene Koonin**, National Center for Biotechnology Information

It might also have had the beginnings of internal structure, with a transport system involving vesicles. However, it likely lacked some signature features of eukaryotes, including a nucleus and mitochondria.

Not everyone is persuaded that Loki bridges the gap between eukaryotes and prokaryotes. The claim is based on too few genes, says evolutionary biologist William Martin of Heinrich Heine University Düsseldorf in Germany. "Six proteins, does that bridge the gap? Not in my book," he says.

If researchers could pinpoint some of Loki's cells, they might be able to strengthen the case by confirming that it really has the features hinted at by its genes. The hunt is on, Ettema says. "We are currently looking very hard to get these cells out of sediments." ■

BIOMEDICAL RESEARCH

Japan's 'NIH' starts with modest funding but high ambitions

Key priority is filling nation's sparse drug pipeline

By **Dennis Normile**

Japan's biomedical community has long envied the funding and political clout of the U.S. National Institutes of Health (NIH). Now, after 2 years of planning, the country has its own version in the Japan Agency for Medical Research and Development (AMED).

Officially launched last month, AMED has a wide-ranging mandate to smooth the flow of basic discoveries to the clinic and the market. But unlike NIH, AMED does not have its own campus or facilities. The fledgling agency's budget—roughly $1.2 billion this year—is also a fraction of NIH's $30 billion in 2015, and three different ministries have a say in how much of that money is spent. Makoto Suematsu, AMED's first president, says he aims to increase the portion of the budget under his direct control and improve cooperation between the ministries. "The moment of truth will come in the next 1 or 2 years," he says.

AMED's "moment of truth," Suematsu says, will come in the next 1 or 2 years.

In spring 2013, Prime Minister Shinzo Abe made biomedical reform a central plank of his economic growth strategy. He noted that despite success in cutting-edge research, Japan was not competitive in world markets for drugs and medical devices. Driving that point home, a 2013 paper in the journal *Joho Kanri* reported that in 2012, Japanese pharmaceutical companies had 780 small molecule drug candidates in the clinical pipeline while U.S. competitors had 4110.

Abe and others suspected that bureaucracy was at least partly to blame for a feeble drug pipeline. Separate ministries oversee each of the three activities critical to developing new treatments: basic research, health care delivery, and commercialization. As a result of this balkanization, for example, in the mid-2000s the education ministry (in charge of basic research) purchased high-throughput genome sequencers under a scheme to promote personalized medicine. But regulations precluded the machines from being used for cancer research at hospitals, which are overseen by the health ministry. Similar barriers block collaborations in regenerative medicine, robotics, and other work. Suematsu, a medical doctor and biochemist, says that one of his primary objectives is "to tackle these barriers one by one."

When first announced, Abe's "Japan NIH" plan got a rocky reception from academics. Worried that an emphasis on applications would come at the expense of basic research, the heads of 52 scientific societies in June 2013 signed an "Emergency Declaration" expressing "strong concerns about the distribution of resources and the process of training researchers." Those concerns have largely evaporated, as the largest source of grants to academics (about $2.5 billion in 2014) remains independent of AMED.

AMED is charged with advancing work in fields ranging from infectious diseases to cancer and brain science to rare maladies and regenerative medicine. The agency will start to stake out its own territory later this year, Suematsu says, when it begins its own grantmaking. It will start small, with just $170 million in funding up for grabs.

Grants won't be enough to fill the treatments pipeline, however. In the United States, small and venture businesses play a key role in shepherding new pharmaceuticals though preclinical work and trials. But Japan is weak in mechanisms to license academic discoveries and lacks "systems which support small and medium enterprises and [startup] ventures," says Yoshiyuki Osabe, an intellectual property specialist at the Japan Patent Office in Tokyo.

"AMED can't do it alone," agrees Ryuichi Morishita, a gene-therapy scientist at Osaka University. Other initiatives in the works, he says, will address gaps that must be filled to make Japan's medical industry an engine of economic growth. ■

PHOTO: D. NORMILE

PALEONTOLOGY

When modern birds took flight

Feathered fossils from China show that modern birds could fly and wade earlier than expected

By **Michael Balter**

Put yourself on the planet 130 million years ago. Most of the animals, from horned dinosaurs to swimming plesiosaurs, would be deeply alien, not to say terrifying. But rising from the wetlands and winging across the sky were birds startlingly like today's. That's the message from two bird skeletons—spectacularly preserved with feathers and all—reported this week.

The 130-million-year-old fossils of wading birds, found in northeast China by a team led by paleontologists Min Wang and Zhonghe Zhou of the Institute of Vertebrate Paleontology and Paleoanthropology in Beijing, push back the lineage that led to today's birds by at least 5 million years and make it almost certain that its origin was much older still. The fossils' specialized anatomy suggests that key factors in birds' long-term success, such as expert flying ability and rapid growth rates, arose surprisingly early in avian evolution.

"New bird fossils seem to come out every week now, and they are revolutionizing our understanding of bird evolution. But of all the new specimens, this is one of the most important found over the last decade," says paleontologist Stephen Brusatte of the University of Edinburgh in the United Kingdom. Not only does the bird look nearly modern, but it was also apparently a water dweller, showing that "ancient birds became specialized in their respective habits" very early, says paleontologist Luis Chiappe of the Natural History Museum of Los Angeles County in California.

Birds were born about 150 million years ago, when a group of small meat-eating dinosaurs spread their feathered wings and took to the skies. They soon split into two distinct groups: the lineage that led to modern birds, called the ornithuromorphs, and the so-called opposite birds, or enantiornithines, whose shoulder ball-and-socket joints connected in an inverse way from those of living birds. Relatively poor fliers, the opposite birds also typically had teeth and clawed wings. They thrived for millions of years, but vanished along with their dinosaur relatives in the mass extinction at the end of the Cretaceous.

Meanwhile, the lineage of modern birds evolved "huge chest muscles and wings comprised of many different types of feathers layered over each other"—features essential to high-powered flight, Brusatte explains. Their bone structure also suggests that they grew much faster than the opposite birds. But researchers did not know when those features emerged. They had found some excellent specimens of the earliest birds, such as Germany's famed 150-million-year-old *Archaeopteryx*, as well as stunning later fossils from northeastern China (*Science*, 15 March 2013, p. 1261). But a yawning gap remained between *Archaeopteryx* and other fossils, most of which were opposite birds, Chiappe says.

The new fossils help fill the gap in time and also in anatomy. Writing in *Nature Communications*, the Beijing team describes two skeletons of a species they call *Archaeornithura meemannae*. (*Archaeornithura* means "ancient ornithuromorph," and *meemannae* is in honor of Chinese paleontologist Meemann Chang.) Each exquisitely preserved specimen has the telltale traits of a modern bird: fan-shaped tail feathers, highly fused bones at the ends of the wings, and the U-shaped wishbone familiar to anyone who has carved a roast chicken. The fossils even have a small projection on the front edge of their wings—known to boost maneuverability during flight—that is remarkably similar to that of today's birds.

Furthermore, *Archaeornithura* had long legs and feet apparently adapted to wading in water, similar to those of today's plovers, suggesting that modern birds arose in aquatic habitats. Finding such a modern bird, already specialized for wading, suggests that millions of years of aquatic evolution took place even before *A. meemannae* came on the scene, Zhou explains. He suggests that while the opposite birds found safety in the trees, life in more open, aquatic spaces may have given the ornithuromorphs "more choices of high protein food" and favored their evolution into swift fliers so they could avoid the danger of predators. All this evolution must have happened after *Archaeopteryx* but before 130 million years ago.

PHOTO: WANG *ET AL.*, *NATURE COMMUNICATIONS*

This 130-million-year-old bird, the oldest known member of the line that led to modern birds, had feathers suited for skillful flight.

The fossils reveal the origins of the features that, tens of millions of years later, may have allowed modern birds to survive the Cretaceous extinction when other birds did not, Zhou and Wang say. No one is sure just what conditions prevailed in the postasteroid apocalypse, but Wang speculates that the fast growth rates of modern birds, which let them reach adulthood faster and spend less time dependent on their parents, may have given them an advantage. Skilled flight may also have been a boon.

But this idea is "too simplistic," counters Sankar Chatterjee, a paleontologist at Texas Tech University in Lubbock, because many ornithuromorphs vanished during the extinction, too. Nevertheless, Brusatte argues, "from the ashes of that extinction, a few groups of more sophisticated birds, with better flight abilities and perhaps faster growth rates, were able to survive." Those key traits, the new fossils show, arose near the dawn of bird evolution. ■

GENOMICS

New database links regulatory DNA to its target genes

Recent big genomics projects aid disease studies

By **Elizabeth Pennisi**

Scientists have known for years that the genome is much more than a set of codes for proteins. It is also a giant switchboard, riddled with sequences that control gene activity. This extra layer of complexity has hampered searches for the genetic basis of diseases and for drugs that would target just the DNA at fault. In the past few months, however, several major research consortia have delivered what amount to user's manuals for the genome, mapping the locations of thousands of those switches, the specific genes they control, and where in the body they are turned on or off.

On pages 648, 660, and 666, the latest and arguably boldest of these big biology efforts reports preliminary results. By analyzing genetic material gleaned from more than 100 people who had died just hours before, the Genotype-Tissue Expression (GTEx) project catches gene regulation in action, identifying the genes switched on or off by subtle changes in DNA within 2 million bases of any gene. By evaluating multiple tissues from each body, it also charts the reach of those regulatory sequences across cell types—some affect a gene in all tissues; others are influential in a few tissues or just one.

Three efforts reported earlier took other approaches to mapping the genome's many switches. Two, called BLUEPRINT and the NIH Roadmap Epigenomics Project, chased down the locations of DNA and its associated proteins that are the target of chemical modifications called epigenetic marks, which determine whether a gene can be activated. A third, the latest iteration of a 20-year effort called FANTOM (Functional ANnoTation Of the Mammalian genome), provides an extensive catalog of the beginnings of genes and of their control sequences. Thanks to these four efforts, "we are on the cusp of learning a lot more about genome function," says Jonathan Pritchard, a geneticist at Stanford University in Palo Alto, California.

Not everyone is persuaded that these massive data-gathering efforts offer much practical help to biologists. "I am not a fan of big science," says Dan Graur, an evolutionary geneticist at the University of Houston in Texas. Simon Xi, a computational biologist in Cambridge, Massachusetts, who is using the GTEx data in his work on drug development, believes the databases are vital, however, but says they could be more user-friendly: "The challenge for us is how to integrate all those data."

The new work aims to address an ongoing source of frustration among disease researchers. A decade ago, geneticists set out to link specific DNA sequences to common diseases. In so-called genome-wide association studies (GWAS), massive consortia pooled tens of thousands of patients and came up with thousands of subtle genetic changes, called single nucleotide polymorphisms (SNPs), which appeared to increase the risk of inflammatory bowel disease, schizophrenia, autism, and a whole host of other common disorders. Puzzlingly, many of these changes occurred outside genes (*Science*, 27 May 2011, p. 1031). The mutations presumably affected gene expression. But how? The impasse "suggested we needed to get moving on understanding regulatory variation," recalls Nancy Cox, a quantitative human geneticist at Vanderbilt University in Nashville.

> ***"We are on the cusp of learning a lot more about genome function."***
> **Jonathan Pritchard**, Stanford University

FANTOM5, a $100 million effort led by the RIKEN institute in Japan, has provided part of the answer by mapping two kinds of regulatory sequences in the genome: "promoters" that help kick off transcription and are located at the start of a gene, and "enhancers," regulatory DNA that can be far from the genes they act on. The project developed technology to capture RNA right as it starts to form off the DNA, which pinpoints promoters. It catalogs enhancers as well, because these pieces of regulatory DNA are also transcribed into RNA. Led by RIKEN's Yoshihide Hayashizaki, FANTOM5 surveyed RNA in every major human organ, hundreds of cancer cell lines, more than 200 purified primary cell types, and in cells at various stages of differentiation.

Earlier this year, the team described 201,000 human promoters and 65,000 human enhancers, showing that genes often contained several promoters that were activated differentially in various tissues (*Science*, 27 February, p. 1010). The effort is "absolutely unprecedented," says Bing Ren, a molecular geneticist at the San Diego, California, branch of the Ludwig Institute for Cancer Research. "This is really a significant resource."

The $300 million NIH Roadmap Epigenomics project took a different approach to identifying enhancers. It mapped the epigenetic changes that associate with enhancers. For each cell type studied, assays of chemical marks called methylation and other changes in the DNA-protein matrix called chromatin helped pinpoint enhancers. Based on their sequences, investigators were also able to identify the proteins that help those enhancers turn on genes. The study, reported on 19 February in *Nature*, included 127 reference epigenomes—all the epigenetic marks on a genome—for various embryonic and adult tissues and cell types, including immune, brain, heart, muscle, gut, fat, and skin cells.

The European Union's €30 million BLUEPRINT project took an even deeper look into epigenomes, focusing on white and red blood cells. It determined the epigenomes of the primary blood stem cells and of those cells at various stages in their differentiation into mature white or red cells. Among other goals, BLUEPRINT is looking for differences between these cellular epigenomes in healthy individuals and people with leukemia, whose blood cells proliferate uncontrollably. "BLUEPRINT is going to show, together with Roadmap, the rules of regulation of gene expression," says BLUEPRINT's Willem Ouwehand, an experimental hematologist at the University of Cambridge in the United Kingdom.

Once a GWAS identifies a SNP, data from Roadmap, BLUEPRINT, or FANTOM can provide further evidence that it might influence health by showing whether the variation falls in a regulatory region. GTEx goes a step further: It pins down how genetic variation, particularly in noncoding DNA, affects a gene's activity across different parts of the body. To measure that gene activity, the project pulls out the transcribed RNA of tissues in multiple individuals. The researchers can then correlate changes in levels of specific RNA transcripts—an indicator that specific genes are active—with SNPs or other DNA sequence variations. "It will help the researchers narrow down the discoveries they have made in GWAS studies," says Simona Volpi, a pharmacologist at the National Human

Gene regulation cataloged

Studies linking DNA to disease find that 80% of the genetic risk factors lie outside of genes themselves. Multiple large-scale efforts are helping geneticists home in on what DNA really matters in determining when, where, and how much a gene is active.

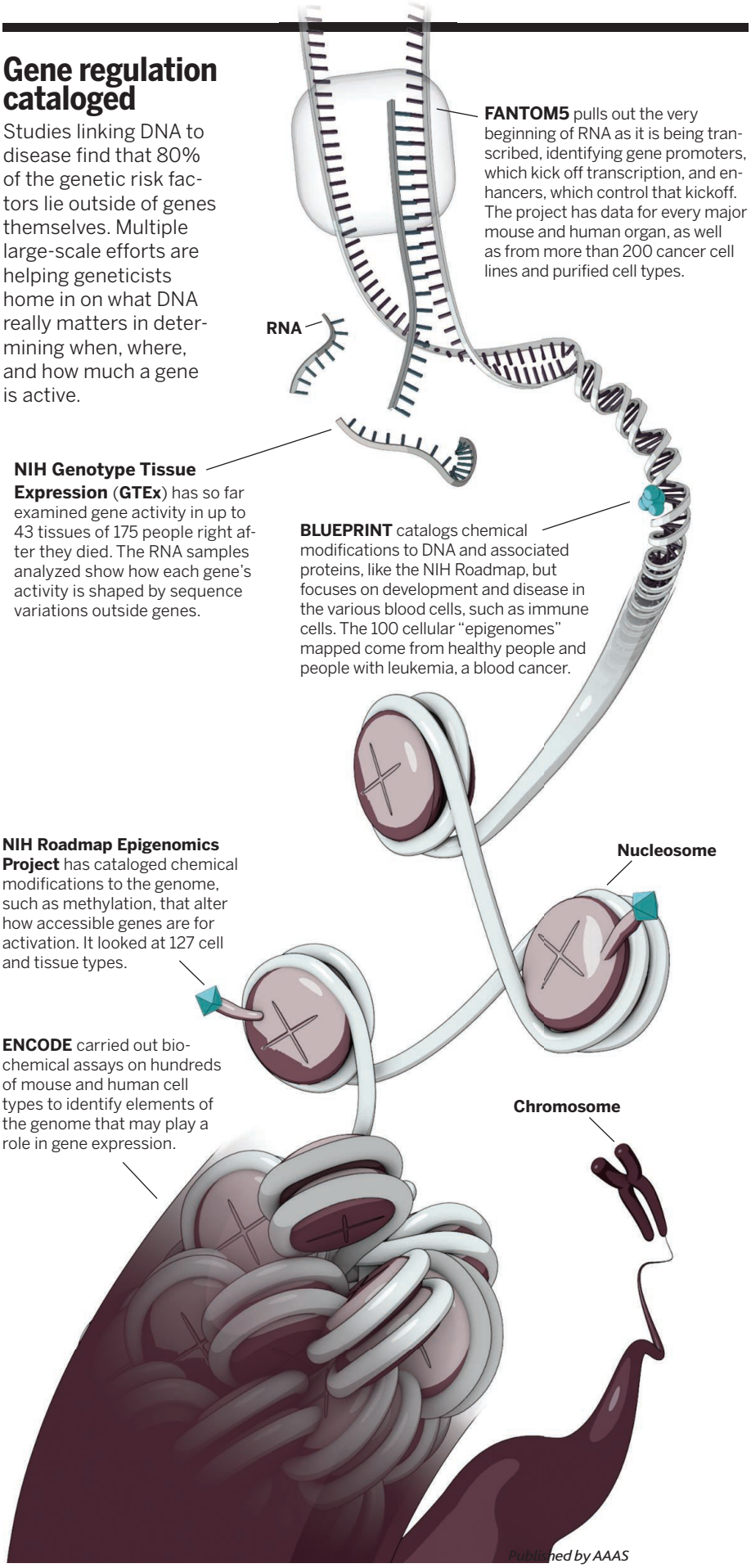

ILLUSTRATION: V. ALTOUNIAN/*SCIENCE*

Genome Research Institute based in Rockville, Maryland, who helps coordinate GTEx.

Because the researchers needed multiple tissue samples from internal organs—too many to collect from living people—they turned to recently deceased people whose kin donated their bodies for research. The ultimate goal of the $100 million NIH-funded project is to collect and analyze about 25,000 tissues from 900 individuals; the data published so far include RNA from up to 43 tissue sites from 175 people. With those samples, "GTEx has the power to compare tissues within individuals and across individuals," Volpi adds. "This is something that nobody has been able to do before at this scale."

Xi, who is tracking down drug targets for depression, schizophrenia, and Alzheimer's and Parkinson's diseases, is already turning to GTEx data to follow up on SNPs previously implicated in those brain disorders. "Having GTEx data helps connect the dots," he says. The data also enable him to check whether DNA sequences implicated by GWAS are only active in the brain. That could make them especially promising drug targets, reducing the risk of broad side effects.

Graur, who made a name for himself with his withering criticisms of a predecessor genomics project called ENCODE, distrusts the GTEx results because the project relied on postmortem samples. RNA degrades quickly, he notes. "If you want to do [gene] expression, you have to have live organisms," he says. GTEx counters that it has validated that samples taken within 6 hours of death faithfully reflect natural gene activity.

Still, GTEx and the other genomic projects have shortcomings. They don't comprehensively cover all tissues, disappointing some eager for such data on their favorite cell type. Diabetes researcher Mark McCarthy of the University of Oxford in the United Kingdom, for example, is doing his own mini Roadmap and GTEx projects on pancreatic islet cells, which were omitted from the large-scale efforts. And tapping these genomic databases can also be challenging. "I see people going to the sites and struggling," says Chris Tyler-Smith, an evolutionary geneticist at the Wellcome Trust Sanger Institute in Hinxton, U.K.

Nonetheless, Tyler-Smith welcomes GTEx and the other genomic projects, saying they represent "getting together in large groups to do things that one could hardly do in one's lab." And for people like McCarthy, there is newfound hope of unraveling the complex genomic networks that underlie diabetes and other diseases. "I'm more optimistic than 4 to 5 years ago when it really wasn't clear how we were going to deal with these regulatory signals," he says. "We now have quite a few a clues." ■

FOOD SECURITY

Italy's olives under siege

Blight alarms officials across Europe

By **Erik Stokstad**

All across the heel of Italy's boot, centuries-old olive trees are falling victim to a devastating pathogen. "It's beyond belief," says Brion Duffy, a plant bacteriologist at the Zurich University of Applied Sciences in Switzerland, who has visited the Salento peninsula and seen hectare upon hectare of desiccated, dying trees. "This is the center of olive production in Italy, Europe, and the world, and it's like a bomb went off."

In spite of control efforts, the disease is spreading north, threatening olive groves throughout Italy and beyond and ringing alarms across Europe. In January, the European Food Safety Authority (EFSA) warned of yield losses and rising costs from control measures. Italy declared its first national emergency for a plant disease and appointed a special commissioner with new powers. And last month, France closed its border to all susceptible plant varieties from Salento, sparking accusations of a trade war. "It's a quite major issue for Europe," says Jean-Claude Grégoire, an entomologist with the Université libre de Bruxelles.

The culprit is *Xylella fastidiosa*, a bacterium widespread in the Americas that has been on Europe's quarantine list since 1981. One strain appears to cause mild symptoms in olive groves in California but does not kill trees. Other subspecies have wreaked havoc in South American citrus groves and North American vineyards. The microbe kills plants by multiplying inside vascular tissue, thereby slowly clogging their water transport system. Many kinds of sap-sucking insects transmit it, even from healthy-looking plants—or from hundreds of mildly susceptible host species—making it extremely hard to contain.

X. fastidiosa's assault on Italy was uncovered by Donato Boscia, a plant virologist with the Italian National Research Council's Institute for Sustainable Plant Protection in Bari. He first observed unusual symptoms in his father-in-law's olive grove in the summer of 2013. Desiccated leaves clung to branches for several months, instead of falling off. Other farmers had noticed the problem, too. That October, Boscia and his colleagues confirmed the culprit was *X. fastidiosa* and also found it in almond trees and oleander growing near infected groves in the province of Lecce (see map). The European and Mediterranean Plant Protection Organization was quickly alerted. Within weeks, Italy banned the movement of olive saplings and other susceptible plant material from Lecce.

But the disease spread. By December 2013, some 8000 hectares were in trouble. Often entire orchards fell sick, with the largest and oldest trees hit hardest. "People are observing the decline of trees that were cultivated by their parents and grandparents," Boscia says. Two months later, the European Union banned transport of most plants from the affected region, which has hurt commercial nurseries, and required member nations to start testing for *X. fastidiosa*.

Boscia and colleagues raced to figure out what was going on. Genetic markers match those of a strain isolated from ornamental coffee plants and oleander exported from Costa Rica to Europe. Infected plants may have arrived in Italy while they were asymptomatic. In any event, European inspections and testing have been too lax, says Giovanni Martelli, a plant virologist with the University of Bari Aldo Moro.

In Italy, the primary vector is the spittlebug *Philaenus spumarius*, Boscia and colleagues reported in August 2014 in the *Journal of Economic Entomology*. These insects are common across Europe and abundant in olive groves. In summer, adults fly up from the grass into the trees, feeding on sap and repeatedly infecting each tree. Last August, tests revealed that up to 80% of the insects in afflicted orchards were carrying the bacterium. "It's terrifying," Martelli says. "It's an army of insects loaded with bullets."

By October 2014, *X. fastidiosa* had spread to an estimated 23,000 hectares. This past February, the agriculture ministry tripled its funding, to €7.6 million, for combating the blight. (The regional government has allocated another €5.9 million.) To prevent *X. fastidiosa* from spreading north, authorities designated a 3-kilometer-wide eradication strip and buffer zone spanning the peninsula; workers are clearing it of sick trees and host plants like oleander and will spray insecticides to kill adult spittlebugs. Elsewhere, farmers have plowed thousands of hectares of orchards to kill juvenile spittlebugs.

Some environmental groups doubt that *X. fastidiosa* is the cause of the declines. They suspect endemic fungi or leopard moths, which have plagued olives in the past. (Last month, EFSA issued a report dismissing this theory.) The groups have rallied protesters to block efforts to cull sick olive trees. In February, a special commissioner was empowered to enforce tree removal, and police have been called in to keep protesters away from chainsaw-wielding forestry workers.

Yet the disease continues to advance. Last month, infected trees were discovered about 30 kilometers north of the containment zone. Quick action might eliminate this new hotspot, Martelli says. And more measures are in the works. An E.U. advisory committee last week recommended that the European Commission ban imports of ornamental coffee plants from Costa Rica and Honduras. It also specified that countries should squelch new outbreaks by removing infected plants and all host plants within 100 meters.

At ground zero, the epidemic has taken a grim toll, says Blanca Landa, a plant pathologist with the Spanish National Research Council's Institute for Sustainable Agriculture in Córdoba who visited Lecce in November. "I saw a farmer crying in his field," she says. "He told me, 'I'm taking care of my olives better than my own children.' " Now, his orchard is dying. "I came back feeling completely demolished," Landa says. ■

Bringing a pathogen to heel

Italy hopes that an anti-*Xylella* cordon will save olive trees north of Lecce province.

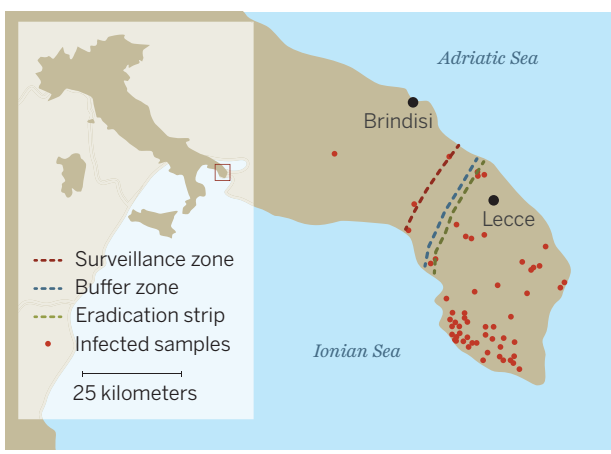

ILLUSTRATION: M. ATAROD/*SCIENCE*

FEATURES

KING OF THE PILLS

Raymond Schinazi's handful of lifesaving drugs has earned him riches, esteem, and a dose of enmity

By **Jon Cohen**

On the deck of a sportfishing boat on a sparkling Saturday morning in Mexico's Gulf of California, Raymond Schinazi is singing.

Sky of blue
Sea of green
In my yellow submarine

The fish aren't biting, but this 65-year-old organic chemist from Emory University in Atlanta is delighted to watch the humpback whales spout, soak up the Baja sun, and be out of cell tower range. "There is lots of sea, and there are lots of fish," he says after a few hours pass without landing a big one. "You have to be an optimist."

The name of the boat is *No Big Deal*.

Few scientists who work in academia have benefited more from big deals than Schinazi. He specializes in the synthesis of so-called nucleoside and nucleotide drugs that interfere with viral replication—an idea once widely dismissed. Two years ago, Schinazi pocketed $440 million on a deal involving sofosbuvir, a yellow submarine–shaped pill that has revolutionized hepatitis C (HCV) treatment and had blockbuster sales for Gilead Sciences of Foster City, California. In 2005, an anti-HIV drug he helped develop, FTC, netted $540 million for Emory—which gave $71 million to Schinazi. Emory and Schinazi have made millions more in royalty fees for a sister drug, 3TC, which treats both HIV and hepatitis B. And Schinazi, who also runs a lab at Atlanta's VA Medical Center, had a hand in two other drugs on the market. He holds more than 90 patents and recently helped form a company that he contends will make still more effective drugs against hepatitis B and C. But on his way up, Schinazi has rocked a few boats.

A bear-sized man who speaks bluntly, negotiates fiercely, and favors splashy, multicolored shirts, Schinazi is a polarizing force. Friends and colleagues call him a genius, a superstar, a hero. James Curran, who heads the Rollins School of Public Health at Emory, offers quieter praise. "He's a very, very solid academic researcher who is out-of-the-world entrepreneurial."

Others wince at what they see as his abrasive style and charge that he receives more profit and scientific credit than he deserves. His former business partner Jean-Pierre Sommadossi, who heads Atea Pharmaceuticals in Cambridge, Massachusetts, says Schinazi "wasn't involved with anything" in the actual development of the HCV drug sofosbuvir, other than starting the company that invented it. The two no longer speak. Medicinal chemist David Chu of the University of Georgia, Athens, who published more than 100 papers with Schinazi, cut ties, too. Protracted lawsuits have challenged Schinazi's patents and financial decisions. He

PHOTO: MICHAEL A. SCHWARZ

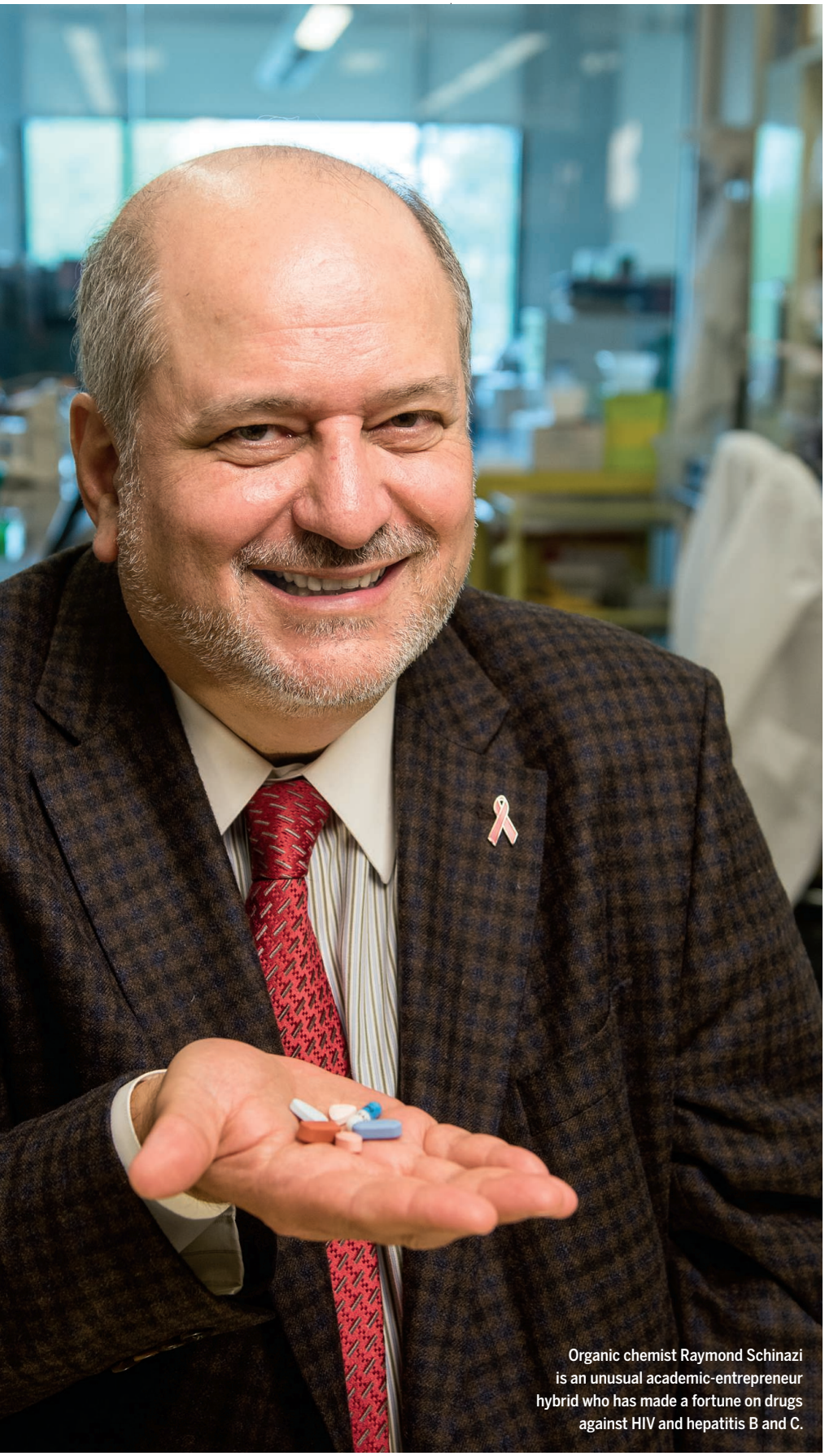

Organic chemist Raymond Schinazi is an unusual academic-entrepreneur hybrid who has made a fortune on drugs against HIV and hepatitis B and C.

also suffered collateral damage when Gilead debuted sofosbuvir at $1000 per pill, which one news article pilloried as a "poster child for pharmaceutical greed."

Schinazi, who lives mostly in Atlanta, makes no apologies for his wealth, which allows him to enjoy a plush ocean-view condo in Baja's San Jose del Cabo (I stayed in a spare bedroom because of its remote location and our tight schedule), a third home in Miami, and the occasional flight on a private jet service. "I save lives," he tells me as we wait for a fish to strike. "If I make money along the way, what's wrong with that?" Schinazi sees a common motivation driving his critics. "When you're very successful," he says, "people are very jealous."

THE FRIDAY EVENING BEFORE the fishing expedition, I join Schinazi on the 30-minute drive from his secluded condo into the rowdy party town of Cabo San Lucas. But we do not stop at the Cabo Wabo Cantina, the Jungle Bar, or the Husband Day Care Center. We attend synagogue.

The service takes place in the apartment of a Chabad rabbi who wears a traditional black hat and a 17th century black frock coat. We sit with 20 or so men, expats from all over the world, dressed in T-shirts, flip-flops, shorts, and fedoras. Save for the ark holding a Torah and the room divider separating men from women in Orthodox Jewish tradition, we could be at a poker game. When we come to a passage about the Jews' flight from Egypt, Schinazi leans over and says, "I lived it. A real exodus."

Schinazi was born in 1950 in Alexandria, Egypt, where his father had an import/export business, a glue factory, and made sheep casing for sausages. Raymond attended a private British school. "When he was around 9, 10 years old I asked him what he wanted to do," says childhood friend Yves Salama. "He said, 'I'm going to be a scientist and I'm going to cure cancer.' I was quite impressed he knew there was such a thing as cancer."

Salama says he and Schinazi "were free-range children" who had great fun shooting clay pots with their BB guns and making tinfoil bombs with gunpowder from shotgun shells. But Schinazi's idyllic childhood ended abruptly in 1962 when the family returned from vacation to find their home sealed, bank accounts frozen, and cars gone. It was part of President Gamal Abdel Nasser's socialist agenda and his push to oust Jews. "Everything was taken from us," says Schinazi, whose family moved into a hotel.

By 1964, the Schinazis were broke and took a ship to Naples, Italy, where they lived in a refugee camp for a time. An elite boarding school in England for Jewish children eventually accepted Raymond. From there he

went to England's University of Bath, where he completed an undergraduate degree and a Ph.D. in chemistry. He lived on 100 English pounds a month, working as a parking attendant to help pay his way, and didn't have real money in his pocket until he won 3000 pounds in the Spanish lottery.

While at Bath, Schinazi met his mother's brother, pediatrician André Nahmias, who left Egypt before his nephew was born and had become a well-known herpesvirus researcher at Emory. Nahmias helped Schinazi secure a postdoc at Yale with William Prusoff, a chemist dubbed "the father of antiviral chemotherapy." Prusoff synthesized the first antiviral used in clinical practice, a drug called idoxuridine that treats herpes infection of the eye. It is a synthetic nucleoside.

Nucleosides are chemical precursors to the nucleotides that make up DNA and RNA. When viruses copy themselves, they string together nucleotides. Chemical modifications can create defective analogs of these building blocks. Viruses incorporate them into a growing chain of nucleotides but usually cannot add new links, gumming up production of genetic material and aborting viral replication.

Nucleotide analogs typically make lousy drugs: The molecules are highly charged and have difficulty entering cells. Not so for nucleoside analogs, which cells convert into nucleotides. But they can cause serious toxicities if they get into human DNA or RNA. At the time Schinazi joined Prusoff's lab in 1976, many drug developers shunned them.

After 3 years with Prusoff making nucleoside analogs, Schinazi moved to Emory to study viruses and immunology with his uncle. "I knew that the glory was in biology," he says. "I wanted to save the world." But he was confident that his aptitude for chemistry would help. "I look at structures and they mean something to me," he says. "It's a language."

BRENDAN LARDER MET SCHINAZI in the early 1980s when he exited a herpesvirus conference held at the University of Oxford and stepped into the street. "A car pulled up on the sidewalk, a window came down, and a voice said, 'Get in,' " recalls Larder, who was then working on his Ph.D. in virology. Schinazi knew that Larder was studying acyclovir, a nucleoside analog being developed by Burroughs Wellcome to treat herpesvirus, and wanted to pick his brain. In those days, Larder says, Schinazi "was not at all prominent."

Larder tells me this story at a swank hotel in Key Biscayne, Florida, where 125 researchers gathered in December 2014 for HIV DART, a biennial conference on HIV drug development that Schinazi co-organizes. (He hosts a similar hepatitis meeting in Hawaii.) Many of the attendees wear the colorful meeting T-shirt, sporting an aerial view of Miami that Schinazi shot from his nearby condo. "If you ask a lot of people why did you come here, they'll say, 'Because Ray asked me to,' " says Larder, who for years worked at Wellcome and now heads the HIV Resistance Response Database Initiative, a nonprofit based in London. "It's a way to bring his friends together. Ray does polarize opinions and people's emotions, but more people love him than hate him."

One morning, Schinazi gives the David Barry DART Achievement Award. He sings the praises of the deceased Barry, who once directed research at Wellcome and helped develop AZT, the first anti-HIV drug. He makes no mention of their complicated history. "David Barry was my arch enemy," Schinazi tells me during a meeting break.

Schinazi fishes for big drugs, which are difficult to land.

In 1986, Schinazi—independent of Wellcome—synthesized AZT and gave it to Sommadossi, a pharmacologist then with the University of Alabama, Birmingham. Sommadossi proceeded to show that it had toxic effects on bone marrow cells. Barry, anxious about AZT's imminent approval by the U.S. Food and Drug Administration (FDA), dismissed the results, Schinazi says, asserting that they were due to impurities in the compound he had made. "He was a big shot and I was a nothing," Schinazi says. "He hated me." The toxicity soon surfaced in human studies, but the FDA approved the drug nonetheless in March 1987. That same year, Schinazi helped Prusoff's lab show that another nucleoside analog, d4T, had activity against HIV—and it later would come to market. But it was a third AIDS drug dubbed 3TC that elevated Schinazi to the big leagues.

In 1989, he learned of a potential drug developed by a Canadian biotech, BioChem International. The drug, a synthetic nucleoside, contained an equal mixture of mirror-image "enantiomers"—left- and right-hand versions of the same molecule. Because enantiomers can have different powers and toxicities, Schinazi saw an opportunity. He enlisted Dennis Liotta, a chemist at Emory, to see if they could sort out the enantiomers. "I was a pretty good chemist and Ray had a background in virology," Liotta says. "It turned out to be an excellent combination."

With help from one of Liotta's postdocs, the team found a chemical reaction that efficiently separated the enantiomers. The left-handed enantiomer, 3TC, was more potent, and they then synthesized a closely related compound, FTC, that included a fluorine atom. Subsequent studies showed that the drugs also had activity against hepatitis B virus. Schinazi had to lobby Emory to file patents for their compounds. "He's got natural entrepreneurial talents that most people have to teach themselves," Liotta says. "I think he can smell money."

IN 1993, LARDER LED a Wellcome team that found a remarkable test-tube effect of 3TC and FTC: HIVs that mutated and became resistant to these drugs became more sensitive to AZT. The synergy meant lower, far less toxic doses of AZT, plus it gave 3TC and FTC a new reason for being. Novel combination therapies were in the offing.

The next year, pharmaceutical giant Glaxo merged with Wellcome, leading Barry and a host of his colleagues to defect and form Triangle Pharmaceuticals. They joined forces with Schinazi, Liotta, and Chu, who had potential drugs on their university shelves. "[Barry] probably teamed up with Ray because his enemy became Glaxo," Larder says.

The unusual synergistic features of 3TC and FTC—and their obvious market potentials—led to a tangle of lawsuits, with Emory suing Glaxo and BioChem for patent infringement on 3TC, countersuits, and similar fights over FTC. The cases were all settled, transforming the fortunes of Schinazi and Liotta—and Emory.

Triangle's slow progress frustrated Schinazi, so he and Sommadossi formed two new drug companies in 1998 to focus on nucleoside analogs. "They weren't taking any of our compounds, and I could see my technology sitting on a shelf," Schinazi says.

PHOTO: JON COHEN

"I like speed." Schinazi headed one, Pharmasset, while Sommadossi ran the other, Idenix. "Both companies made some great scientific discoveries when nucleosides were basically considered poor science," Sommadossi says.

Schinazi had a heart attack in 1998 while attending a meeting at Triangle. "Too much stress," he says. "More than 30 years no vacation, in the trenches, writing grants, trying to survive. I work too hard. You can ask my ex-wife." Barry drove him to the hospital, where they discovered that Schinazi, then 48, had an arterial blockage known as a widowmaker. "You try to form two companies simultaneously," he says. "It almost killed me."

Adding to his workload, Schinazi, Sommadossi, and a few other aggrieved researchers launched HIV DART that year because the main annual HIV/AIDS meeting in North America—the Conference on Retroviruses and Opportunistic Infections (CROI)—had repeatedly rejected many of their submissions. "We told the CROI people, 'Next time, if you don't accept our abstracts, we're going to move our meeting to exactly the same date as CROI,' " Schinazi says. HIV DART made its debut in December 1998, in St. Thomas, the U.S. Virgin Islands, while CROI took place in the harsh winter of Chicago. "I know how to play hardball," Schinazi says.

CROI has never invited Schinazi to give an honorary presentation or a plenary talk. He feigns indifference, but he also says the organizers are missing an opportunity to open attendees' eyes to the drug discovery process. He says it is a lot like fishing. During our expedition, I try to reel in the only big fish we hit that day, but I clumsily snap the line at the last moment. Schinazi consoles me by explaining that this is the story of his life. "Drug discovery, you have to hook it and reel it in—and many things happen along the way," he says. "You don't know what you have until the end of the story. You can lose it at any time."

TODAY, POPULAR ANTI-HIV drugs that have the brand names Combivir, Trizivir, Truvada, and Atripla all contain either 3TC or FTC. Add in d4T (its use is being phased out), and Emory estimates that some 94% of the people infected by HIV who have received treatment have taken one of the drugs Schinazi helped develop (see table).

These drugs made Schinazi rich, but the hepatitis drug sofosbuvir made him super rich. Sofosbuvir, a nucleo*tide* analog (it masks the negative charge), must be taken in combination with another drug, but unlike older HCV treatments, it has no serious side effects, works against virtually all variations of the virus, and reduces the time to a cure from 48 to 12 weeks. Gilead bought Pharmasset for $11.4 billion to obtain sofosbuvir, which racked up more than $10 billion in sales last year, second only to one other drug on the market. But in the yin-yang of Schinazi's life, this great success has brought him greater scrutiny than ever.

First and foremost is sofosbuvir's price tag of $1000 per pill. Gilead set the price, he notes, which he calls "obscene." But at the same time, he blasts critics who suggest sofosbuvir's price is not "reasonable" or "rational"—and that he profited too much. "Is it fair to pay $3 for a bottle of water?" he asks. "Do you complain when you're thirsty? This is something that cures you from a disease." And he notes that Gilead has already dropped the price because it now combines the drug with a new HCV drug it makes and sells for $1125 per pill. The company also offers a steep discount for poor countries and allows generic sales; indeed, according to Schinazi—"Look at the irony!"—he helped negotiate a price of about $11 per pill for his home country Egypt, which has the highest prevalence of HCV in the world.

Schinazi's precise role in sofosbuvir's discovery is also contentious. He's the co-author of a 2005 paper that discovered a precursor to the drug. But little of that potential drug reached the liver, where HCV resides. Pharmasset then developed a "prodrug," sofosbuvir, that becomes active in the liver. "I give credit to Ray: He had the vision to start the company," says Michael Sofia, one of Pharmasset's key inventors of the prodrug. But when it comes to sofosbuvir's discovery, he asserts, forget about Schinazi. "Go to the patents, go to publications—there are over 40 in that space," Sofia says. "His name's not there."

Schinazi claims he now has a spectacular HCV drug in the works. "We should be able to cure hepatitis C with just one drug," he asserts. In November 2014, he merged his company RFS Pharma with Cocrystal Pharma, which he says also has strong leads on a hepatitis B cure and influenza drugs that work against all strains of the virus. He predicts Cocrystal will be as profitable as Pharmasset—and promises to give away his profits. "Everything I do now I'm giving to my charity," says Schinazi, who has bankrolled land for a new synagogue in Cabo San Lucas, an exchange program with the University of Bath, and endowed chairs at Emory.

Barbara Stoll, who heads his department at Emory, is astonished that he has not let up. "He could be on a yacht doing nothing, but he is driven to make a contribution," Stoll says. "Money is nothing at this point."

Well, not nothing. Since the merger, he boasts to me, Cocrystal Pharma's stock price has doubled. "Thank you, Raymond Schinazi," Schinazi says. "Somebody likes my drugs. I've got a good reputation."

One day, I have the temerity to suggest that he has also had a great deal of luck. "Don't tell me about luck, because I worked very hard," he all but barks. "Nothing came easy for me. I mean, how many times do I have to be lucky?"

During our 9-hour fishing expedition, luck is definitely not with us. But shortly before we return to dock, one of the rods starts to bend and give out line. A deck hand says it is probably a small tuna. I suggest Schinazi reel it in, but he has no interest. "You take it," he says. "I only want the big ones." ■

All the king's pills

Schinazi had a hand in the development of five FDA-approved drugs, three of which are used in popular combinations.

DRUGS	DISEASE	DEVELOPER	SALES ($ billion)*
d4T (Stavudine)	HIV/AIDS	Yale (BMS)	N/A
3TC (Lamivudine)	HIV/AIDS	Emory/ BioChem (ViiV)	$0.7•
3TC (Lamivudine)	Hepatitis B	Emory (ViiV)	$0.2•
FTC (Emtricitabine)	HIV/AIDS	Emory (Gilead)	$0.3•
LdT (Telbivudine)	Hepatitis B	Idenix (Novartis)	$0.03•
Sofosbuvir (Sovaldi)	HCV	Pharmasset (Gilead)	$10.3
Combination drugs			
3TC + 1 (Combivir)	HIV/AIDS	ViiV	$0.1
3TC + 2 (Trizivir)	HIV/AIDS	ViiV	$0.6
3TC + 1 (Epzicom)	HIV/AIDS	ViiV	$1.3
FTC + 1 (Truvada)	HIV/AIDS	Gilead	$3.3
FTC + 2 (Atripla)	HIV/AIDS	Gilead	$3.5
FTC + 2 (Complera)	HIV/AIDS	Gilead	$1.2
FTC + 3 (Stribild)	HIV/AIDS	Gilead	$1.2
Sofosbuvir + 1 (Harvoni)	HCV	Gilead	$2.1
Total (2014 only)			**$23.6**

*2014 figures with 2013 exceptions marked •

DATA SOURCE: GILEAD AND GLAXOSMITHKLINE EARNINGS REPORTS/IMS HEALTH/FDA

Saving California's calves

After a half-century of research, scientists find a promising solution to mysterious abortions in beef cattle

By **Ingfei Chen**

Veterinarian Tom Talbot of Owens Valley, California, remembers his ranching family's first run-in with the livestock scourge known as foothill abortion. It was about 1970, and his father had bought 200 heifers from elsewhere in the state for breeding. He initially grazed them on leased pastures in the worst possible place for pregnant cattle: the foothill country of California. About a month before the new calves were due, Talbot's father started finding aborted fetuses scattered across his valley ranch. More cropped up each day. "One hundred percent of those animals aborted," recalls Talbot, who is a past president of the California Cattlemen's Association. "It was the absolute most God-awful wreck you can have imagined."

The calves—and his father's business—were victims of a devastating but highly regional cattle disease that causes pregnant heifers to lose their fetuses in the third trimester. Foothill abortion has not abated in the half-century since Talbot witnessed it. Even now it kills an estimated 5% to 10% of California's annual beef calf "crop"—a loss of 45,000 to 90,000 animals, worth many millions of dollars. But the veterinary drug industry has ignored it, concentrating on bigger markets. And researchers have long struggled to find a cause or a cure.

"Foothill abortion's been an enigma. Everything about it has made it difficult to work with," says University of California (UC), Davis, microbiologist Jeffrey Stott. But after years of sleuthing, he and his colleagues identified the odd bacterium responsible, which belongs to a class of soil microbes better known for their swarming, gliding behavior than for causing disease. And by stitching together funding and collaborations, the scientists developed a promising vaccine and are now testing it in thousands of heifers.

ON A HOT, CLOUDLESS March afternoon in Buellton, California, a young Black Angus heifer bellows like a foghorn from inside a holding cage. Stott, in a baseball cap and faded red, long-sleeve shirt, has just injected the vaccine into the cow's neck. A local veterinarian draws a blood sample from its tail, and two cowboys affix bright yellow numbered tags to the animal's ears. In less than a minute, the cage clangs open and the protesting cow bolts away in a cloud of dust, rejoining the nearby herd.

Two hundred and fifty-five cows down, 265 to go. "It moves pretty quick; it's a nonstop process," Stott yells with a grin over the rumble of a generator that powers the hydraulically controlled cage doors. The crew was in a dawn-to-dusk push to administer the injections to more than 500 cattle pastured on the coastal foothills here, 70 kilometers northwest of Santa Barbara.

On the flanks of the Sierras and the coastal mountain ranges in California, southern Oregon, and Nevada, foothill abortion is as much a part of the landscape as the gnarled oaks. Stott's home institution, UC Davis's veterinary school, was founded in 1948 in part to study the disease, which was later named epizootic bovine abortion (EBA). In an early effort to find out what might spread it, pregnant cows were hefted onto "treehouse" platforms, away from anything that crawls on the ground but still within reach of mosquitoes. The cows all produced healthy calves.

PHOTO: REGENTS OF THE UNIVERSITY OF CALIFORNIA/ELENA ZHUKOVA

Heifers in California's foothills country are at risk of an infection that threatens their calves.

By the 1970s, researchers at UC Davis and the UC Cooperative Extension had fingered *Ornithodoros coriaceus*, a brown, soft-bodied tick endemic to foothill regions, as the disease carrier. "The ticks love lying under the oaks," Stott says—and cattle bed down there as well. Also known as the pajaroello (pa-ha-WAY-lo) tick, it is infamous in Native American lore for inflicting a more agonizing bite than a rattlesnake, he says.

Tick-bitten cows don't get sick from the subsequent infection, but if they're pregnant and weren't exposed to the tick before, they often lose their babies. Abortion "storms" can wipe out 50% to 90% of new calves in a herd that lacks immunity—as ranchers such as the Talbots learned the hard way.

By the time Stott joined the UC Davis faculty in 1985, researchers there were immersed in the hunt for a tick-borne pathogen in foothill abortion. Each decade has had its fashionable suspect: a chlamydia bacterium in the '70s, a novel *Borrelia* bacterium (from the same family that causes Lyme disease) in the '80s, and retroviruses in the early '90s. They were all red herrings.

Progress was tough. Conducting studies in pregnant cows, with their 9-month gestation periods, was slow, expensive work. Moreover, deliberately infecting animals for research by exposing them to hordes of ticks works only half the time. And because foothill abortion has a geographically limited impact, funding was scarce and major pharmaceutical companies had no interest, Stott says.

But he and his colleagues Myra Blanchard and Mark Anderson began making headway after joining forces in 1992 with Mark Hall and Donald Hanks at the University of Nevada, Reno (UNR), which had a research cattle herd living in tick-free meadows. The team found they could reliably transmit EBA to the beasts by injecting them with ground-up thymus tissue from aborted bovine fetuses.

In a pivotal experiment published in 2002, the scientists showed that treating pregnant heifers with heavy doses of penicillin and tetra-cycline at the time of the injections prevented the abortions. "That told us it was a bacterial pathogen," Stott recalls.

The pajaroello tick carries the pathogen.

The perpetrator remained elusive. "You couldn't culture it and you couldn't see it" under a microscope, Blanchard says. But with the help of new molecular biology methods, the researchers managed to extract some of the mystery microbe's DNA from infected thymus tissue and identify its bacterial family. In 2005, they pinpointed it as a novel species of *Myxococcus* "slime bacteria," the first pathogen known within that group. The discovery was a triumph of "persistency, systematic approach, and scientific acumen," says entomologist Robert Lane, a professor emeritus at UC Berkeley, who once proposed a *Borrelia* bug as the cause.

"It's a craaazy unusual bacteria," Stott says of foothill abortion, and not just because slime bacteria tend to swarm and glide. He and his colleagues call the pathogen *Pajaroellobacter abortibovis*, and it appears to foment disease in a unique way. Their unpublished work suggests it lives in the immune system cells called macrophages, where it replicates slowly, without triggering symptoms in an infected cow. "It's only if she is pregnant that you see disease," Blanchard says. What kills the bovine fetus is its own immune response to the infection: When the animal's immune system finally matures in the third trimester, it unleashes an attack that causes extensive damage to its tissue and organs, triggering abortion.

Veterinarian Jeffrey Stott spent decades working toward the vaccine he is now testing.

GETTING A VACCINE for foothill abortion to affected beef producers has become a personal mission for Stott, who grew up on cattle ranches in rural Oregon. He and his fellow scientists cobbled together funding for the project, receiving $212,000 from the California Cattlemen's Association and another $205,000 from a UC grant program.

Field trials began in 2011 after pilot studies at UNR saw promising results from the experimental vaccine, which consists of live *P. abortibovis* produced by infecting immunodeficient mice and extracting their spleen cells. Beef producers are a wary lot, but Talbot, the veterinarian, helped recruit ranchers to participate, and the scientists have been testing the vaccine in 4370 cows at about 10 sites, including Buellton, in the past 4 years.

"We became very confident, very quickly, that this vaccine was spectacular," Stott says. Based on their unpublished data, he says, it looks close to 100% effective, keeping cows free of infection and thus protecting their fetuses for at least 18 months. However, ranchers must wait 60 days after inoculating heifers before breeding them, because of a risk that still-lingering bacteria from the vaccine could trigger early fetal deaths, he says.

UC Davis is now in talks with a small vaccine manufacturer that is interested in bringing the preventive to market. Stott and Blanchard plan to make the experimental vaccine available to as many as 6000 more heifers through continuing field trials at 50 other ranches over the next year.

Fifth-generation cattleman Buck Parks, 41, whose family ranch in Modoc County, California, has lost 20 to 35 calves to foothill abortion every year for decades, has no doubt that the vaccine is helping. Parks says he seriously considered selling his business at one point, but this spring, with almost half his breeding cows vaccinated in field trials over the past 3 years, only eight calves aborted. "I don't want to compare it to curing cancer, but it's pretty close," Parks says.

Stott's quest isn't over, however, because many basic mysteries about foothill abortion remain unsolved. Where is the pajaroello tick picking up the pathogen? Could mule deer, which are also hosts for the ticks but don't seem to get the abortion syndrome, be slowly spreading the disease geographically? Once the calves of the California foothills are safe, Stott is eager to explore such questions. "That's what I want to get back to doing," he says. ■

Ingfei Chen is a freelance writer in northern California.

PHOTOS: (TOP TO BOTTOM) REGENTS OF THE UNIVERSITY OF CALIFORNIA/WILL SUCKOW; MEGAN OSBOURN/SIERRA FOOTHILL RESEARCH AND EXTENSION CENTER

INSIGHTS

BOOKS *et al.*

THE ENVIRONMENTAL FILM FESTIVAL IN THE NATION'S CAPITAL

Brave new world

Each March, the museums, embassies, libraries, and local theaters of Washington, D.C., play host to a festival of films that shed light on pressing environmental issues. Many of the screenings are free, and all are open to the public. A number of this year's films sought to draw specific attention to climate change, a move organizers hoped would help the festival "serve as a signpost" on the route to the 2015 United Nations Climate Conference, which will be held later this year in Paris, France. Other films challenged audiences to confront the role of humans in wildlife extinction, invited viewers to think twice about our seemingly insatiable appetites for food and fuel, and encouraged the adoption of more sustainable ways of life. Read on to see what our reviewers thought of nine of this year's films.

The E-Waste Tragedy

Reviewed by **Marc Lavine**

Desktops, laptops, e-book readers, netbooks, tablets, cell phones, and flat panel, HD, and 4K displays—every year, new gadgets call out to us, promising to enhance our lives. But what happens to the old and broken devices we discard, including the large appliances that contain and depend on electronics? Globally, dealing with garbage and waste is a problem, but e-waste adds its own particular challenges due to the toxicity and scarcity of some of the raw materials. Despite our best intentions, when we donate an old piece of equipment to a charity or dispose of it at an authorized recycling center, it often ends up at dump sites in Africa or China. At best, it may just pile up and slowly decompose, but more likely it will be processed under hazardous and uncontrolled conditions to recapture the base metals or disassembled so that the old components can be fraudulently resold as new ones. In *The E-Waste Tragedy*, Cosima Dannoritzer takes us on a journey—one that crisscrosses countries and continents—as e-waste is removed from the legal and controlled recycling streams and finds its way to improper recycling and disposal sites. Despite improved legislation in some countries, including laws that incorporate recycling fees into the purchase of new electronics and ban the exportation of e-waste, too many individuals and companies find ways to profit at the expense of the health of the people and environment where the waste ends up. Dannoritzer hopes that the behavior of consumers will change in order to reduce the quantity of waste being produced, but it seems more likely that the problem will only be solved when the costs associated with the human health risks, the increased scarcity of some raw materials, or the catastrophic failure of falsely labeled recycled parts drives the business and political communities to find better solutions to this growing problem.

The E-Waste Tragedy
Cosima Dannoritzer, director.
Media 3.14, Spain, 2014.
86 minutes.

ILLUSTRATION: OLI WINWARD

Published by AAAS

PHOTO: PEG LEG FILMS (SCENE FROM *JUST EAT IT: A FOOD WASTE STORY*)

Tiger Tiger
George Butler, director.
White Mountain Films, United States, 2015. 90 minutes.

Tiger Tiger

Reviewed by **Laura M. Zahn**

"Unless we do something, tigers are not going to survive." So says Alan Rabinowitz in one of the first lines of this documentary, which focuses on collecting data on the tiger population in protected areas of the Sundarbans mangrove forest of India and Bangladesh. This region may be one of the largest remaining contiguous populations of tigers and thus one of the best places to focus conservation efforts. Highlighting Rabinowitz's research trip, this film offers footage not only of tigers and their likely prey, captured through camera traps, but also of their greatest threat—the encroaching human population. On the basis of his interactions with the locals, it is clear that the people of these areas understand the potential long-term benefits of the tiger preserves. However, it is also apparent that there is a lack of governmental policy and protection, especially in Bangladesh, as well as a large financial incentive driving people to kill the tigers. The mortality of both human and feline are entwined throughout the film as we learn that Rabinowitz has leukemia—a fact that will likely make this his final field expedition. Coupled with the uncertainty of efforts to save the tiger, a sense of melancholy permeates the film. But Rabinowitz's push for tiger conservation lends hope for the survival of the species, and the movie intends for his example to propel others to take up the challenge.

Just Eat It: A Food Waste Story

Reviewed by **Jennifer Sills**

Would it be possible to survive for 6 months on only discarded food? In *Just Eat It*, Grant Baldwin and Jen Rustemeyer set out to do just that, scouring the dumpsters of Vancouver, British Columbia, where they discover a veritable cornucopia of wasted produce, dairy, prepared meals, and more. Interspersed with their experiences, the film provides vignettes about food waste at various junctures in the production system. We visit farms and factories where between 20 and 70% of bananas, celery, and nectarines are thrown away immediately after harvest, simply because they don't meet the stringent cosmetic standards set by supermarkets. At a scrap farm outside Las Vegas, 2500 swine are fed on just 8% of the food waste generated by the city's restaurants and hotels. We learn that a third of the food produced globally is wasted, including 15 to 25% of the food we purchase in our regular trips to the supermarket. The loss of the food itself is compounded by the waste of all the resources that contributed to its production.

Why is the system so flawed? Some of the waste can be traced to economics. Farms can't afford to harvest and ship food for which there is no demand. Food banks lack the infrastructure to accept donations in large quantities. However, the film maintains that culture is equally important. Unlike littering, wasting food is condoned in rich countries. A host with no leftover food is considered a failure. *Just Eat It* offers unsettling statistics—for example, the water required to produce one hamburger is the equivalent of a 90-minute shower—along with striking visuals—a field full of wasted celery stalks, a dumpster filled to the brim with containers of not-yet-expired hummus. After watching, you might just rethink going out to eat while those leftovers sit in the fridge another day.

Just Eat It:
A Food Waste Story
Grant Baldwin, director.
Peg Leg Films, Canada, 2014.
75 minutes.

Grant Baldwin considers a dumpster filled with discarded hummus.

Published by AAAS

Peruvian farmers are working to preserve over 1500 potato varieties that are native to the Andes Mountains.

Seeds of Time
Sandy McLeod, director.
Hungry, United States, 2014.
77 minutes.

Seeds of Time

Reviewed by **Valerie Thompson**

Buried beneath the permafrost on a remote Norwegian archipelago is a vault that holds the seeds of more than 4000 plant species. The Svalbard Global Seed Vault, as it is known, has a passionate advocate in the American agriculturalist Cary Fowler, who provides much of the narration for this compelling film. Through Fowler, we learn that vegetable crops in the United States now have less than 7% of the diversity that existed just a century ago—troubling news for a world in which staple food crops are increasingly vulnerable to disease and climate change. Maintaining crop diversity via seed banking, he argues, is essential to safeguarding our agricultural future.

Woven throughout Fowler's quest to promote seed-banking efforts around the globe is the story of a group of indigenous Peruvian farmers who are working to preserve native potato crops that are threatened by rising global temperatures. Their struggle to save this important food staple serves as a harrowing reminder of just how high the stakes truly are.

In a fascinating flashback to the mid-20th century, we learn that the city of Leningrad once boasted the world's largest seed bank. So dedicated was the group of scientists who tended the collection that they refused to eat any of its contents during the period of intense starvation that accompanied the protracted World War II military blockade known as the Siege of Leningrad. By the end of the blockade, nine of the curators had died of starvation. This vivid example places today's efforts in a broad historical context.

The film ends by discussing the value of collecting and preserving wild relatives of crop species, which, through breeding and genetic engineering, may be able to confer drought and disease resistance to food crops. Ultimately, we will likely need to embrace both traditional and modern techniques for preserving plant biodiversity if we hope to maintain a secure global food system.

Bikes vs Cars

Reviewed by **Valerie Thompson**

More than 20 million people live in Brazil's São Paulo metro area—a fact that is not easily forgotten during the hours of frustrating traffic congestion that define many residents' daily commute. As the title suggests, this thought-provoking film pits car-centric commuting against alternative modes of transportation, including bikes and, to a lesser degree, public transit. The film features a wide range of perspectives—an urban planner in São Paulo, a bike advocate in Los Angeles, a city councilman in Toronto, a taxi driver in Copenhagen—most of whom embrace, or at least pay lip service to, the notion of improving bike-friendly infrastructure. Some of the film's most persuasive arguments focus on the dangers that cars pose to bystanders and cyclists. We learn, for example, that in Toronto, a pedestrian is hit by a car every 3 hours. In another scene, we witness a large crowd gathered to pay tribute to a fallen bike rider in São Paulo, where an average of one cyclist is killed by a motorist every week. Nor does the film neglect the environmental arguments in favor of bike-based commuting. This point is driven home with a scene describing a weekend construction project that shut down a 10-mile stretch of one of Los Angeles's busiest highways in 2011. Taking advantage of this natural experiment, UCLA scientists showed that air quality near the highway improved by 83 percent that day, relative to comparable weekends. Broad in scope, and compellingly presented, this film opens an important dialogue about one possible solution to the commuting conundrum facing growing urban areas today.

Bikes vs Cars
Fredrik Gertten, director.
WG Film, Sweden, 2015.
88 minutes.

Cowspiracy: The Sustainability Secret
Kip Andersen and Keegan Kuhn, directors.
A.U.M. Films and First Spark Media, United States, 2014.
91 minutes.

Cowspiracy: The Sustainability Secret

Reviewed by **Sacha Vignieri**

If you were asked to identify the greatest human impact on the planet, what would you answer? Perhaps our oil and gas consumption and the resulting release of climate-altering greenhouse gases? As filmmakers Kip Andersen and Keegan Kuhn successfully argue in this film, the answer is actually livestock production, which is not only the leading source of greenhouse gases but also the largest consumer of water and other natural resources and the leading driver of habitat destruction. Through a series of interviews with scientists, authors, and activists, the film demonstrates how our current production of livestock for meat, eggs, and dairy is both a major driver of many of the environmental issues we face today and entirely unsustainable. Yet, there appears to be large-scale resistance to discussing its damaging impact on the environment and little thought given to the idea that we may need to change our behavior when it comes to the foods we eat. Andersen and Kuhn explore what might be underlying this resistance, including industry and political pressure, as well as our own denial. Unlike activities

PHOTO: HANK EDELBO

like oil and gas production, diet choices are profoundly personal, and the film leaves one feeling as though we as individuals have great power to foment bottom-up changes with simple actions. In the end, the film is a noble and entertaining discussion of how we can begin to tackle one of the biggest, yet least addressed, human-caused environmental problems.

Return of the River
John Gussman and Jessica Plumb, directors.
Elwhafilm LLC, United States, 2014. 70 minutes.

Return of the River

Reviewed by **Julia Fahrenkamp-Uppenbrink**

In 1914, the Elwha Dam on the Olympic Peninsula in Washington state began to generate power, bringing energy to the town of Port Angeles. Upriver, Glines Canyon Dam followed in 1927. Told in a poetic style and beautifully shot, this film shows how the dams, seen by many as an essential element of "conquering" the wild countryside, changed the river and the surrounding ecosystem. Clams disappeared as fine sediment no longer washed down to the river's mouth. Salmon and other migrating fish populations collapsed as the spawning grounds that were still accessible deteriorated. Salmon hatcheries set up to mitigate falling fish numbers were a poor replacement for natural salmon runs.

In the end, community engagement was key to the momentous decision to remove both dams. The film tells the story of the environmentalists, politicians, and members of the Lower Elwha Klallam Tribe who fought for decades for the removal of the dams and the restoration of the river. As the Elwha Dam turbines stopped on 1 June 2011, the camera zooms in on the last, handwritten entry in the dam's record book: "Elwha P.H. Shut Down—Final." Then the dams come crashing down.

Replanting the former reservoirs will take several years; ecological changes will unfold over decades. But as salmon are traveling up the Elwha River again to spawn, Senator Bill Bradley captures the importance of this dam removal—the largest in history—when he says hope is "the great gift of the Elwha."

For more information on the ecological effects of dam removals, see J. E. O'Connor, J. J. Duda, G. E. Grant, *Science* **348**, 496 (2015).

Who Owns Water

Reviewed by **Nick Wigginton**

Tracking water as it flows downstream is usually a straightforward task. But as a river flows through communities and across political boundaries, who should be able to divert, pump, drink, or fish in that water? Does it change on one side of the riverbank versus the other? These are difficult questions to answer, but as access to fresh water diminishes in some regions of the world, they will become more common.

In *Who Owns Water*, filmmaker David Hanson and his brother Michael paddle down the Chattahoochee River in the southeastern United States, from its spring-fed origin through cities and national parks to the Gulf of Mexico. The often breathtaking views from the river change constantly, from canyons to massive reservoirs to flooded forests. At times, the water is rough enough to tip the most expert paddler. Yet at other times, the water levels are so shallow, they are barely navigable by canoe at high water. The river also serves as the primary battleground between communities, landowners, and three U.S. states, who are fighting over the dwindling freshwater reserves in this growing region.

Along their journey, the brothers interview several residents spanning a range of interests, from environmentalists to oyster farmers, all of whom claim a reasonable stake in the river. In isolation, each of their stories about the changing river seems to require simple solutions and often justifiably direct blame upstream or shift consequences downstream. As the film highlights, however, the river is more than a shared resource connecting communities in one watershed in one small corner of the world. Answering the question of who owns water remains difficult, but it is a question that we still need to ask.

Who Owns Water
David Hanson, Michael Hanson, Andrew Kornylak, directors.
MoDoc and Fourmile Media, United States, 2014. 50 minutes.

Kendall Shoelles harvests oysters in Apalachicola Bay.

PHOTO: MODOC STORIES

Gambling on Extinction
Jakob Kneser, director.
Real to Reel Productions Inc., Germany, 2014.
52 minutes.

Gambling on Extinction

Reviewed by **Barbara Jasny**

The film *Gambling on Extinction* describes what many see as a war on the rapidly declining populations of rhinos and elephants in Africa. Certainly, the facts presented are horrifying: If poaching continues at its current rate, there could be no more wild elephants within two decades. However, what makes the film memorable is not so much that it presents new data but that it reveals the dimensions of the problem. Investigations of fly-covered carcasses reveal that parts have been carved from still-living animals and that the equipment used indicts outsiders who cross borders to decimate native populations. To the poachers, the lives of the animals are irrelevant; they just see them as the "white man's toys." Through investigative journalists and undercover agents, we meet rhino horn users (who believe the myths that this material, made from the same material as fingernails, has healing properties) and an ivory carver. We see sellers who have catalogs of illegal animal parts for sale and who disguise the horns and tusks as wood to escape customs officials.

Much of the ivory loads from African ports are sent to China, where carved ivory is considered to be an investment whose value can only go up as more and more elephants are killed. Part of the problem in China is that there is a legal supply, based on government stockpiles, which acts as a cover for the illegal trade. However, in a recent survey, 60% of the Chinese respondents said that they would not have the products if the government instituted a universal ban. Ten countries have destroyed their ivory stockpiles, demonstrating a growing global commitment to conservation efforts. As Grace Gabriel from the International Fund for Animal Welfare declares, "There are things money shouldn't buy."

MATERIALS SCIENCE

Understanding friction in layered materials

A scanning probe technique provides a clearer picture of friction at the nanometer scale

By **Kenneth M. Liechti**

As we move to the digital age, we may forget that a lot of correspondence was accomplished by pencil and paper. Nonetheless, when we do still write with "lead" pencils, we are making use of the weak interlayer forces in graphite to strip off tiny flakes of graphite and deposit them on paper in a complex interplay between adhesion and friction. Understanding the nature of such weak interlayer forces and the attendant opportunities afforded by such understanding are becoming more important with the advent of nano- and microelectromechanical systems (NEMS/MEMS); machines whose moving components are at the nanometer and micrometer scales embodied in their names. Because the surface area of such components is much larger than their volume, surface forces (for example, van der Waals, electrostatic, and capillary forces) become the dominant loading to be considered in the design and reliability of NEMS and MEMS devices (*1*). On page 679 of this issue, Koren *et al.* (*2*) have devised an innovative experiment that quantifies our day-to-day experience with lead pencils, but with much higher fidelity than we might expect. They show that two adjacent planes of carbon atoms can be sheared in highly ordered pyrolytic graphite (HOPG) and observe the interplay between adhesion and friction forces in this layered material. This experiment with HOPG can be considered as a model for two planes of graphene or other so-called two-dimensional materials sliding over one another. The findings are exciting because they point to new ideas for data storage at small scales, as well as novel actuation concepts in electromechanical devices.

Center for the Mechanics of Solids, Structures and Materials, Department of Aerospace Engineering and Engineering Mechanics, University of Texas at Austin, Austin TX 78712, USA. E-mail: kml@mail.utexas.edu

The challenge of measuring relatively weak forces between components has been addressed by a number of instrumented indentation and lateral loading devices, which all make use of probes that are brought into contact or near contact with the target surface while the normal and lateral (friction) load on and displacement of the probe are measured. With sharp enough probes, it is possible to observe oscillations in the lateral force-displacement response whose maxima and minima, respectively, coincide with the onset of slipping and attachment of the probe to the target surface and were commensurate with the interatomic spacing of the mica surface that was being probed (*3*). The novelty of the experiment by Koren *et al.* lies in the use of an atomic force microscope to apply a lateral shear force to disks (mesas) of HOPG. The disks, 50 nm thick and with radii that ranged from 50 to 300 nm, were sheared along the basal plane of the graphite, about 10 nm from their bases. A classic frictional lateral load-displacement response was observed, which was largely reversible except for dynamic dissipative events that occurred during sliding. They can be seen as slight differences in the force-displacement response during sliding in opposite directions. These latter events were related to slight rotational misalignments between the graphite lattices above and below the slip plane. In addition, in a second set of experiments, when a torque was applied to the mesas, stable orientations were observed every 60°, in registration with the sixfold symmetry of the hexagonal carbon atom lattice. A third set of experiments, with a structure exhibiting mechanical bistability, demonstrated the potential to produce cell structures for memory devices that are entirely mechanical in operation. The various equilibrium states of these tiny cells could then be used as switches in such memory devices.

Taking a measure of friction

Illustrating the method of Koren *et al.* with a toy model of a layered system under lateral shear and torque.

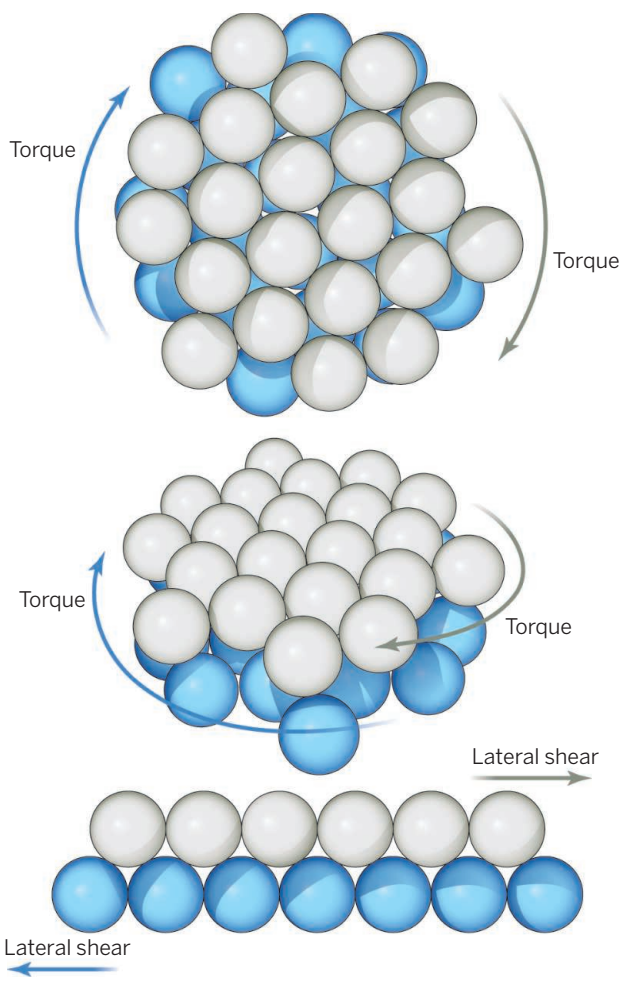

ILLUSTRATION: P. HUEY/*SCIENCE*

The idea behind the method developed by Koren *et al.* can be illustrated more easily if we consider, for example, a toy system consisting of ping-pong balls glued together in a hexagonal pattern (close packed) in two planes that are placed on top of one another (see the figure). The in-plane attachment is much stronger than the interaction between the planes, just as in layered, two-dimensional materials. One can imagine sliding or rotating the planes relative to one another and finding a series of equilibrium positions.

Another opportunity afforded by the experiment of Koren *et al.* is that it may present a close

link to multiscale modeling from atomistic to continuum scales in that the interface or slip plane was free of any contamination and the geometry was relatively simple, which is not usually the case for contact pairs. Although atomistic or molecular analyses have provided insights into deformation and dissipation mechanisms and other effects that are difficult to separate out experimentally, one-to-one comparisons are limited by the high shear velocities and nanometer-scale probe tips that are currently accessible to analysis. Some progress in this direction has been provided by quartz microbalance experiments (*4*) and molecular analyses (*5*) of krypton monolayers sliding on gold, where the close agreement between simulation and experiment identified mechanisms for phononic contributions to friction. Molecular self-assembled monolayers provide another, slightly more complex avenue for linking experiments and analysis in addition to having technological relevance to MEMS. The issue of time and spatial scaling in atomistic analyses of friction between self-assembled monolayers has been identified as one of the current challenges in single asperity friction (*6*). One possible way of addressing this issue is through hybrid analyses with schemes that combine molecular analyses with phenomenological potentials (*7*, *8*) that have allowed typical sliding speeds to be accessed.

Koren *et al.* have come up with a novel experiment that provides a better understanding of friction in layered materials. Although graphite was the subject of this study, the extension to the plethora of two-dimensional materials that are becoming available is clear. The authors have also provided much food for thought in developing potential applications of the observed phenomena to novel memory devices and machines. ■

REFERENCES AND NOTES

1. B. Bhushan, J. N. Israelachvili, U. Landman, *Nature* **374**, 607 (1995).
2. E. Koren, E. Lörtscher, C. Rawlings, A. W. Knoll, U. Duerig, *Science* **348**, 679 (2015).
3. R. W. Carpick, N. Agraït, D. F. Ogletree, M. Salmeron, *Langmuir* **12**, 3334 (1996).
4. J. Krim, D. H. Solina, R. Chiarello, *Phys. Rev. Lett.* **66**, 181 (1991).
5. M. Cieplak, E. D. Smith, M. O. Robbins, *Science* **265**, 1209 (1994).
6. I. Szlufarska, M. Chandross, R. W. Carpick, *J. Phys. D Appl. Phys.* **41**, 123001 (2008).
7. T. Ohzono, J. N. Glosli, M. Fujihira, *Jpn. J. Appl. Phys.* **37** (part 1, no. 12A), 6535 (1998).
8. T. Ohzono, J. N. Glosli, M. Fujihira, *Jpn. J. Appl. Phys.* **38** (part 2, no. 6A/B), L675 (1999).

ACKNOWLEDGMENTS

Supported by the National Science Foundation and the Basic Energy Sciences program of the U.S. Department of Energy.

10.1126/science.aab0930

ILLUSTRATION: C. SMITH/*SCIENCE*

INFECTIOUS DISEASE

More than just bugs in spit

Advances in imaging help to explain tuberculosis treatment failures and develop better drugs

By **Clifton Barry**[1,2,3]

The development of new drugs for tuberculosis (TB) is not for the faint of heart. In addition to all the typical hurdles to developing a new anti-infective, additional complications result from the complex pathology induced by the disease. Because the bacillus is surrounded by a thick, waxy coat, hit rates in whole-cell screens are typically low; the resulting hits are typically so lipophilic that they do not offer good chemical starting points. Despite extensive research efforts, no TB drug has been developed using target-based approaches. Advances in imaging at both a macroscopic and microscopic level offer new insights and strategies for getting urgently needed new drugs to the clinic.

TB is a disease of the lungs: It is transmitted by inhalation of an aerosol droplet containing the bacterium, which implants in small alveoli and then invades and multiplies in the interstitial spaces in the lung. Here, it forms granulomas—that is, nodules of immune cells recruited as the body attempts to wall off the invading bacteria. Eventually, the granulomas undergo necrosis to form cavities and leak out into the airways, spilling bacteria into the lungs and inducing coughing to enable transmission to a new host. A single patient with TB can have dozens of individual lesions, all at different stages of maturation.

TB therapy is often very protracted. Standard medical care for pulmonary TB patients globally involves 6 months of treatment. Although full treatment is successful in 95% of patients, in reality many patients fail to complete such a long course of therapy; mobilizing the resources to ensure full compliance is nearly impossible in resource-poor countries where the disease is endemic. Shorter courses of treatment are one of the major goals of global research efforts because they would allow for more supervision, less recurrent disease, and correspondingly less opportunity for developing drug resistance.

U.S. and European regulatory bodies mandate that end points in phase 3 clinical trials of new TB drugs focus on achieving disease-free status in patients 1 year after completion of treatment. Because determining relapse-free cure requires such a long time, end points in phase 2 clinical trials focus on killing bacteria in expectorated sputum over the first few months of treatment. It has long been clear that the end points in these two different stages of clinical evaluation are not well correlated, as emphasized again recently by the failure of three large phase 3 studies that aimed to shorten the standard 6-month regimen to four months by including a fluoroquinolone as part of a four-drug regimen (*1*–*3*). Despite achieving earlier sterilization of sputum than conventional therapy in preceding phase 2 studies and in the phase 3 trials themselves, more patients in the 4-month fluoroquinolone arms suffered relapse after treatment was discontinued. The fact that these patients were obviously not cured shows that bacteria in the sputum do not tell a complete story. Nor would one expect them to do so, given that only certain lesions produce bacteria that are represented in the airways.

> ***"All these exciting techniques have tremendous potential to accelerate TB drug development by improving the quality of drugs and drug combinations used in clinical trials to target specific lesion types."***

Curing all patients with a shortened TB treatment regimen requires developing an understanding of what leads to a relapse—defined as recurrent disease with the same bacterial strain after apparent initial cure—in a subset of treated patients. There are two main hypotheses for why relapse occurs. One argues that relapse is due to a subset of bacteria with unique physiology (imposed by drugs,

INFECTIOUS DISEASE SERIES

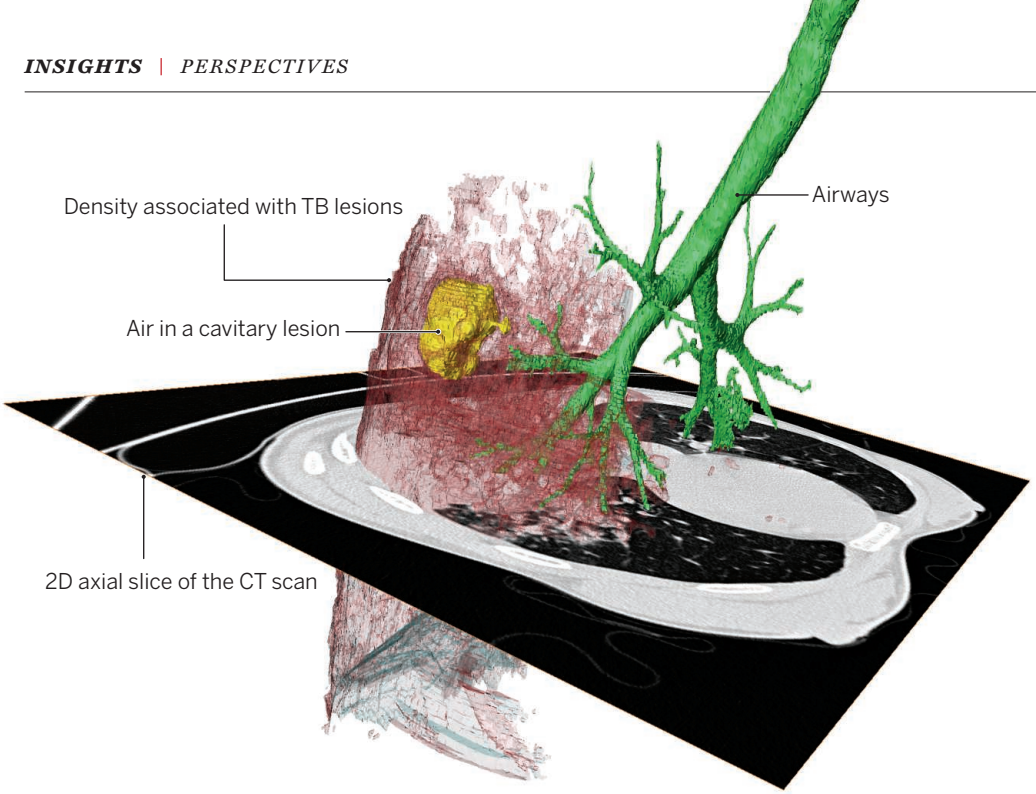

Abnormal CT density in the lungs of a patient with pulmonary TB. A three-dimensional map generated from a CT scan shows abnormal density in TB lesions at millimeter resolution. These computationally segmented lung regions can be precisely quantified and monitored over time, allowing a real-time quantitative evaluation of response to a given drug regimen. Produced in Amira 5.6.0 (FEI Visualization Sciences Group).

the immune system, physical properties of the local environment, or subpopulations that arise stochastically) (*4*). The other maintains that relapse is due to bacteria in an area of unique pathology where their exposure to antibiotics is limited (*5*). Experimental data exist in support of both theories, and it is likely that each has some validity. Recently, translational studies have started to move beyond simple measurements of bacteria in sputum to elucidate the metabolism and status of bacteria that are buried in lesions that are not shedding bacteria into the sputum.

Advances in radiologic imaging and computational image analysis enable precise quantitation of all types of lesion pathology present in the lungs of TB patients. Computed tomography (CT) can generate three-dimensional (3D) maps of every voxel of the lung at millimeter resolution (see the figure). In a recent study, changes in abnormal CT lung density after 2 months of treatment were shown to accurately predict how patients would fare 2 years later, after they had completed treatment (*6*). Positron-emission tomography (PET) scanning involves administering a radioactive probe and collecting information about the location of positron emission and hence location of the probe. TB lesions (and likely lesions from many pathogens) are sites of intense inflammation; quantification of changes in the extent of inflammation during the first 2 months of treatment predicted ultimate treatment outcome just as well as CT changes (*6*).

Both approaches have also been applied to nonhuman primates, offering a smooth pathway between a realistic animal model and clinical trials (*7*). The initial studies in humans were done 2 months after treatment started, but results in rabbits suggest that radiographic changes as a result of chemotherapy are quantifiable as early as 1 week after initiation. Furthermore, PET probes that report on processes specific to TB are under development, potentially providing a quantitative means of assessing bacterial numbers in specific lesions (*8*, *9*).

The search for markers to determine when treatment is complete has also been advanced by looking at changes in circulating levels of immunologically active molecules in blood from patients on treatment (*10*), as well as by analyzing changes in metabolites in urine during the first month of treatment (*11*). Both approaches offer potential surrogate markers that might be used to rapidly cycle through new drug compounds and combinations in order to identify the most promising drug candidates. Larger cohorts of patient samples, preferably from trials designed to attempt treatment shortening, are urgently needed for all these techniques to assess the predictive validity of such markers.

Imaging mass spectrometry (IMS) is another technique that advances the understanding of persisting bacterial populations. IMS creates 2D ion maps from excised tissue samples, allowing the evaluation of drug distribution across relatively large areas. The lung has long been thought to be a "blood organ," suggesting that the circulating concentration of drug in the bloodstream approximates that in TB lesions. Recent work with IMS in animal models of disease clearly shows this assumption to be false in most cases (*5*, *12*); some drugs penetrate lesions poorly or not at all, whereas others freely diffuse into and out of affected areas. Better knowledge of the physicochemical properties of molecules that favor lesion penetration to get to where the bacteria are will help to achieve successful shorter TB therapies. These sorts of tools may also find application in other diseases with potential latent phases associated with distinct pathology.

All these exciting techniques have tremendous potential to accelerate TB drug development by improving the quality of drugs and drug combinations used in clinical trials to target specific lesion types. Whole-body imaging can also affect the speed and accuracy of clinical trials by providing quantitative end points. For example, serial CT allows changes in bacterial load and hence in the volume of disease in specific lesion types to be measured. At the same time, changes in the extent of inflammation can be monitored with PET. These tools could be as transformative in TB clinical trials as viral load and CD4 counts were to HIV/AIDS. ■

[1]*Tuberculosis Research Section, National Institute of Allergy and Infectious Diseases, National Institutes of Health, Bethesda, MD, USA.* [2]*Department of Clinical Laboratory Sciences, University of Cape Town, Cape Town, South Africa.* [3]*Department of Molecular Biology and Human Genetics, Stellenbosch University, Stellenbosch, South Africa.*
E-mail: cbarry@niaid.nih.gov

REFERENCES

1. A. Jindani *et al.*, *N. Engl. J. Med.* **371**, 1599 (2014).
2. C. S. Merle *et al.*, *N. Engl. J. Med.* **371**, 1588 (2014).
3. S. H. Gillespie *et al.*, *N. Engl. J. Med.* **371**, 1577 (2014).
4. J. D. McKinney, *Nat. Med.* **6**, 1330 (2000).
5. V. Dartois, *Nat. Rev. Microbiol.* **12**, 159 (2014).
6. R. Y. Chen *et al.*, *Sci. Transl. Med.* **6**, 265ra166 (2014).
7. M. T. Coleman *et al.*, *Sci. Transl. Med.* **6**, 265ra167 (2014).
8. B. L. Urbanek *et al.*, *ChemBioChem* **15**, 2066 (2014).
9. K. M. Backus *et al.*, *Nat. Chem. Biol.* **7**, 228 (2011).
10. G. Walzl, K. Ronacher, W. Hanekom, T. J. Scriba, A. Zumla, *Nat. Rev. Immunol.* **11**, 343 (2011).
11. S. Mahapatra *et al.*, *BMC Infect. Dis.* **14**, 53 (2014).
12. M. C. Kjellsson *et al.*, *Antimicrob. Agents Chemother.* **56**, 446 (2012).

10.1126/science.aaa2886

ILLUSTRATION: CLIFTON BARRY/NATIONAL INSTITUTE OF ALLERGY AND INFECTIOUS DISEASES, NATIONAL INSTITUTES OF HEALTH

A closer mimic of the oxygen evolution complex of photosystem II

An inorganic cluster replicates many of the structural aspects of the complex that photosplits water and powers photosynthesis

By **Licheng Sun**

The oxygen evolution complex (OEC) in photosystem II (PSII) catalyzes the photosplitting of water. The resulting electrons and protons are then ultimately used to create adenosine triphosphate to convert carbon dioxide (CO_2) into organic compounds. An artificial catalyst that mimics the small inorganic OEC cluster within the much larger PSII enzyme could be used to create fuels such as hydrogen from water via sunlight (*1*). Although tremendous efforts have been spent on artificial photosynthesis systems (*2*), synthetic water oxidation catalysts that closely mimic the structure and function of OEC in PSII have been very limited. Now, on page 690 of this issue, Zhang *et al.* (*3*) describe the closest structural mimic of the OEC in PSII reported to date.

The naturally occurring OEC contains a cluster of manganese, calcium, and oxygen, Mn_4CaO_5. Several crystal structures of PSII have been reported since 2001 (*4*, *5*), but these had insufficient resolution to elucidate the atomic structure of the OEC. In 2011, Shen and co-workers reported a crystal structure of PSII at a resolution of 1.90 Å by x-ray diffraction using synchrotron radiation (*6*). Although much detailed structural information was revealed, extended x-ray absorption fine structure (EXAFS) studies showed that the Mn cations in the OEC are easily reduced (*7*), leading to slight differences in the Mn-Mn distances determined by different techniques.

Very recently, Shen and collaborators (*8*) used femtosecond x-ray pulses to obtain a high-resolution (1.95 Å) "radiation damage–free" crystal structure of PSII in the dark-stable S1 state. In this Mn_4CaO_5 cluster (see the figure, panel A), five oxo-bridged O atoms form a twisted cubane with three Mn atoms and 1 Ca atom on the corners, and a fourth Mn atom outside the cubane held by two of the five oxo bridges. Because one of the oxo-bridged oxygens, O5, is much farther away from the Mn atoms than are the other oxo-oxygen atoms, the O5 is likely a hydroxide ion instead of a normal oxygen dianion. Thus, O5 may serve as one of the substrate O atoms and be involved in the O-O bond formation step (*9*, *10*).

> ***"Making the synthetic models work as real water oxidation catalysts will require consideration of other structural features."***

Artificial molecular water oxidation catalysts based on other transition metal complexes [for example, ruthenium (*11*)] can be very active in chemical, electrochemical, and even photochemical reactions, but efficient biomimetic water oxidation catalysts based on Mn complexes have so far shown very limited success. In 2011, Agapie and coworkers synthesized a Mn_3CaO_4 cluster that structurally mimics the subsite of the OEC in PSII (*12*). However, the Mn_4CaO_4 cluster that Zhang *et al.* have synthesized has the core cubane structure Mn_3CaO_4 linked to a dangling Mn via one oxo bridge on the cubane (see the figure, panel B) and structurally mimics the full site of the OEC in PSII more closely.

The x-ray crystal analysis of this synthetic Mn_4CaO_4 cluster revealed structural similarities to the OEC of PSII. First, both structures have the core cubane Mn_3CaO_4 and the dangling Mn atom. Second, for the first coordination sphere, both structures have one nitrogen-based ligand, with 6 carboxylates in the OEC and 10 carboxylates in the synthetic model. Third, the valence states of the Mn ions—Mn(III), Mn(IV), Mn(IV), and Mn(III)—are identical in both structures.

The main difference in structural features is that in the OEC of PSII, there are

Natural versus artificial

The structure of the Mn_4CaO_5 cluster in photosystem II (**A**) (*6*) and the structure of the synthetic Mn_4CaO_4 cluster (**B**) prepared by the group of Zhang *et al.*; ^{t}Bu is tert-butyl and Me is methyl.

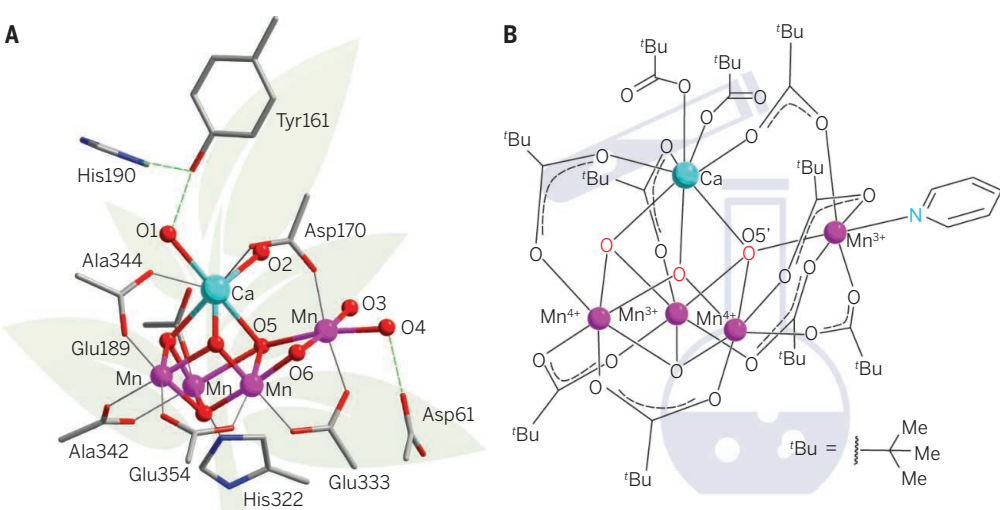

State Key Laboratory of Fine Chemicals, DUT-KTH Joint Education and Research Center on Molecular Devices, Dalian University of Technology (DUT), Dalian 116024, China, and Department of Chemistry, KTH Royal Institute of Technology, 10044 Stockholm, Sweden.
E-mail: lichengs@kth.se

Published by AAAS

two oxo bridges (O5 and O6 in the figure, panel A) between the dangling Mn and the core cubane, but in the synthetic cluster there is only one oxo bridge (O5′ in the figure, panel B). The lack of the second oxo bridge (O6′) might be a fatal weakness for this synthetic model to work as a real catalyst for water oxidation. In the OEC of PSII, the O-O bond formation involves O5, and the second oxo bridge O6 can keep the dangling Mn at the correct position and redox potential after O5 has left during the O-O bond formation. In contrast, the dangling Mn in the synthetic model might detach from the core cubane after O5′ has left during the O-O bond formation if it follows a similar reaction pathway, which would inactivate the catalyst. Another difference is the lack of a potentially open coordination site in the synthetic model because of the short bond length between O5′ and the Mn (2.28 Å) on the corner of the core cubane, relative to the related bond length of 2.7 Å in the OEC of PSII.

The work of Zhang *et al.* constitutes an important step toward a full structural mimic of the OEC in PSII. Further improvement of synthetic model complexes must address the second oxo bridge between the dangling Mn and the core cubane. Making the synthetic models work as real water oxidation catalysts will require consideration of other structural features. For example, longer distances between the corner Mn(III) and O5′, and between O5′ and the dangling Mn(III), need to be enforced via rational ligand design to provide a potentially open site for substrate water molecules to coordinate. This change also would allow the introduction of a pendent base in the second or third coordination sphere to facilitate the proton-coupled electron-transfer process during the O-O formation. ■

REFERENCES AND NOTES

1. L. Sun, L. Hammarström, B. Åkermark, S. Styring, *Chem. Soc. Rev.* **30**, 36 (2001).
2. M. D. Kärkäs, O. Verho, E. V. Johnston, B. Åkermark, *Chem. Rev.* **114**, 11863 (2014).
3. C. Zhang *et al.*, *Science* **348**, 690 (2015).
4. A. Zouni *et al.*, *Nature* **409**, 739 (2001).
5. K. N. Ferreira, T. M. Iverson, K. Maghlaoui, J. Barber, S. Iwata, *Science* **303**, 1831 (2004).
6. Y. Umena, K. Kawakami, J. R. Shen, N. Kamiya, *Nature* **473**, 55 (2011).
7. J. Yano *et al.*, *Proc. Natl. Acad. Sci. U.S.A.* **102**, 12047 (2005).
8. M. Suga *et al.*, *Nature* **517**, 99 (2015).
9. N. Cox *et al.*, *Science* **345**, 804 (2014).
10. P. E. M. Siegbahn, *Biochim. Biophys. Acta* **1827**, 1003 (2013).
11. L. Duan *et al.*, *Nat. Chem.* **4**, 418 (2012).
12. J. S. Kanady, E. Y. Tsui, M. W. Day, T. Agapie, *Science* **333**, 733 (2011).

ACKNOWLEDGMENTS

I thank L. Duan at KTH for assistance with the drawing of the figure.

10.1126/science.aaa9094

NEURODEVELOPMENT

"RASopathic" astrocytes constrain neural plasticity

The cellular pathology of a complex neurodevelopmental disorder is teased apart

By **Lei Xing, Xiaoyan Li, William D. Snider**

Over the past decade, mutations in genes encoding RAS family members, other components of an intracellular signaling cascade that RAS controls, and proteins that modify the cascade have been recognized as causes of developmental syndromes. Collectively, these syndromes are often referred to as "RASopathies." Not surprisingly, RASopathies have numerous manifestations, including propensity to cancer, craniofacial abnormalities, cardiac defects, cutaneous abnormalities, neurodevelopmental delay, and varying degrees of cognitive dysfunction. Uncovering the causes and developing treatments for the neurodevelopmental abnormalities are a challenge because of the myriad cellular elements in the brain and the complexity of nervous system function. A recent study by Krencik *et al.* (*1*) takes a major step toward identifying the cellular pathology underlying Costello syndrome, a RASopathy that is characterized by delayed development, craniofacial and heart problems, and cognitive impairment. The latter appears to be linked to abnormal development and function of a population of nonneuronal cells (astrocytes) in the brain.

The extracellular signal–regulated kinase/mitogen-activated protein kinase (ERK/MAPK) signaling cascade (also known as the RAS-RAF-MEK-ERK pathway) is among the most important cellular pathways, transducing effects of external signals and regulating key cellular responses such as proliferation, differentiation, and morphological development. Interestingly, most RASopathies exhibit gain of function in ERK signaling with exact clinical manifestations varying with the specific mutation (*2*). Dysregulation of ERK signaling in RASopathy mouse models leads to premature differentiation and overproduction of astrocytes (*3*, *4*). Astrocytes and other glial cells, including oligodendroglia, are thought to represent more than 50% of the cellular elements in the human brain and are increasingly recognized as having important roles in regulating the development of brain circuits (*5*, *6*).

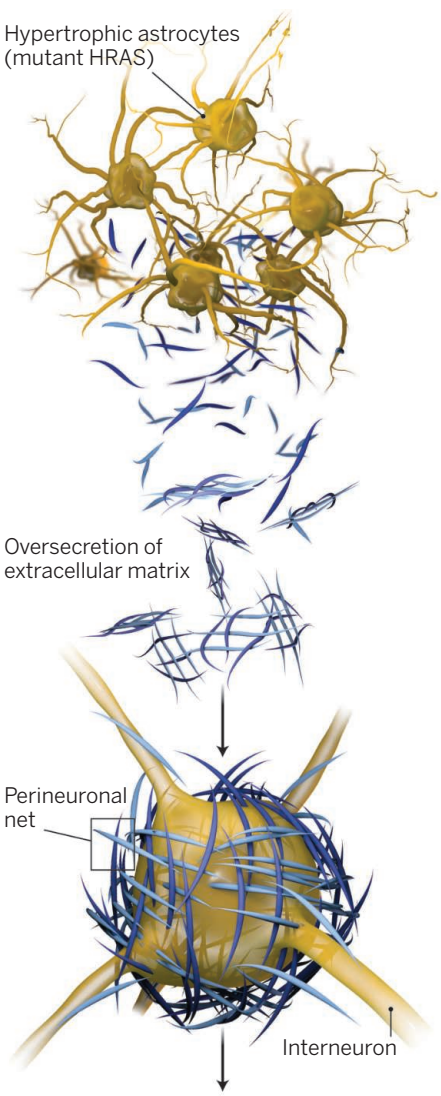

ILLUSTRATION: V. ALTOUNIAN/*SCIENCE*

Altering neural plasticity. Astrocytes derived from fibroblasts of Costello syndrome patients harboring the $HRAS^{G12S}$ mutation exhibit premature differentiation, increased proliferation, and larger size compared to controls. They also express more extracellular matrix components, resulting in the formation of perineuronal nets around interneurons (in a mouse model of Costello syndrome). Premature formation of perineuronal nets may accelerate neuron maturity and "close" the critical period of plasticity.

Costello syndrome is caused by at least 15 different mutations in the gene encoding the RAS family member HRAS (*7*). Disease-associated mutations cause constitutive activation of this protein. Krencik *et al.* explored the function of one particular mutation, $HRAS^{G12S}$ (in which glycine at amino acid 12 is changed to serine) in gliogenesis. From dermal fibroblasts derived from Costello syndrome patients, the authors generated human induced pluripotent stem cells (iPSCs). These iPSCs were then induced to give rise to neuroepithelial cells, the precursor to both neurons and glia. When these neuroepthelial cells were exposed to epidermal growth factor and fibroblast growth factor 2 (FGF2), which act through the RAS-ERK signaling pathway, they expressed astrocytic markers indicative of glial differentiation. Fewer control neuroepithelial cells expressed astrocytic markers, indicating that mutant HRAS leads to premature astrocyte differentiation.

Astrocytes expressing $HRAS^{G12S}$ were apparently healthy, hyperproliferative, markedly larger in size than controls, and also displayed more elaborate neural processes. The hypertrophic nature was also observed when these astrocytes were cultured on mouse hippocampal organotypic slices (a more realistic environment than dissociated cells), as well as in a mouse model in which a different Costello syndrome mutant, $HRAS^{G12V}$ (where glycine at amino acid 12 is changed to valine), was expressed in astrocytes. These findings are in line with a recent study in the fly *Drosophila melanogaster* showing that FGF signaling elicits similar morphological changes in astrocytes. Importantly, astrocytes are closely associated with developing synapses (astrocytes can create a tripartite structure at neuronal synapses) (*8*). The implication is that hypertrophy of astrocytes could produce an enlarged brain and might account for the macrocephaly seen in many Costello syndrome patients.

Astrocytes derived from Rett syndrome and Down syndrome patients have been observed to have growth-inhibiting effects on developing neurons (*9*, *10*). By contrast, astrocytes expressing the mutant $HRAS^{G12S}$ secreted factors that were notably more potent than those released by control astrocytes in promoting neuronal process outgrowth and synaptic development (*1*). During normal mammalian brain development, astrocytes release constituents of the extracellular matrix that influence maturation of synapses and other neurodevelopmental processes. Consistent with premature astrocyte differentiation, transcripts and proteins of extracellular matrix components (such as proteoglycans and fibrous collagens) were markedly increased in astrocytes derived from $HRAS^{G12S}$ iPSCs compared to controls. The expression of regulators and effectors of the RAS-ERK signaling pathway and regulators of synaptogenesis was also increased. The transcription factor SNAI2 is required for the increased expression of the extracellular matrix constituents.

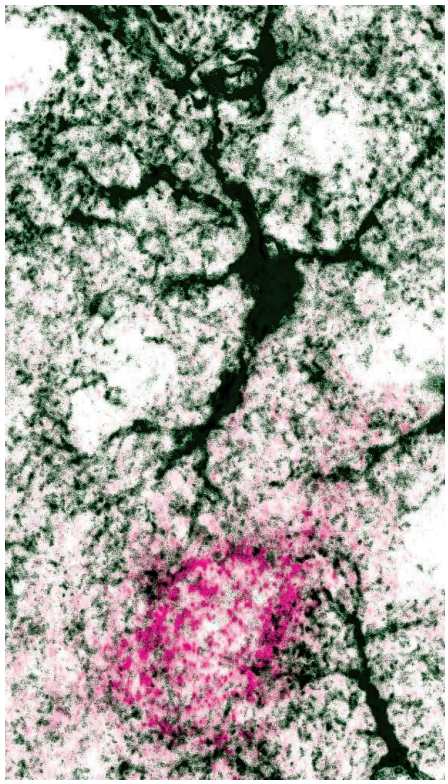

Perineuronal net. A perineuronal net of extracellular matrix protein (magenta) surrounds an interneuron in the visual cortex of a mouse model of Costello syndrome. The elaborate processes of astrocytes are shown in black.

A critical function of glial-secreted proteoglycans is to form "perineuronal nets" that influence neural plasticity regulated by experience (*11*) (see the first figure). They are found around neuronal cell bodies and neurites and stabilize established neuronal connections by restricting neuronal morphological plasticity. Importantly, Krencik *et al.* found that higher amounts of perineuronal nets accumulate around inhibitory neurons expressing parvalbumin in the visual cortex of the $HRAS^{G12V}$ mouse model of Costello syndrome (compared to controls) at 14 days after birth. Parvalbumin-expressing neurons control the "critical period" in early brain development, a window of dynamic synaptic rearrangement and change in synaptic efficacy (*11*). Accelerated deposition of perineuronal nets around these neurons could enhance their maturation, resulting in premature critical-period closure and altered neuronal output (see the second figure). Indeed, the authors observed changes in synaptic potentials onto cortical excitatory neurons in the $HRAS^{G12V}$ mouse model at later developmental stages. Although this study did not investigate potential alterations of brain functions, it is plausible that disrupting synaptic development during the critical period may produce long-term effects on neuronal circuits. Overall, the results of Krencik *et al.* suggest that "RASopathic" astrocytes may have potent effects on neural plasticity that contribute to cognitive dysfunction. A variety of standard paradigms could be used to test this idea, including formation of ocular dominance columns, tests of the physiological effects of monocular deprivation, and studies of patterning in the sensory cortex.

The results of Krencik *et al.* are important not only for understanding pathogenesis, but also for developing effective treatments. Owing to the importance of the RAS-ERK pathway in cancer, many inhibitors of pathway components have been developed for treating various malignancies. In mouse models of RASopathies, MEK (MAPK kinase) inhibitors reversed cardiac defects (*12*) and some abnormalities of brain development, including increased gliogenesis (*3*). The use of RAS and MEK inhibitors in a Noonan syndrome mouse model demonstrated reversibility of synaptic dysfunction without obviously altering the behavior of control animals (*13*). However, there are many reasons for caution, including that RAS-ERK signaling regulates higher-order processes involved in learning (*14*), and that other signaling pathways are likely activated downstream of pathogenic RAS (*15*). The implication that there is premature closure of critical periods in brain development due to hyperactive HRAS provides another plasticity paradigm that might be further explored in preclinical studies. ■

UNC Neuroscience Center, University of North Carolina School of Medicine, Chapel Hill, NC 27599, USA.
E-mail: william_snider@med.unc.edu

IMAGE: R. KRENCIK

REFERENCES AND NOTES

1. R. Krencik *et al.*, *Sci. Transl. Med.* **7**, 286ra66 (2015).
2. K. A. Rauen, *Annu. Rev. Genomics Hum. Genet.* **14**, 355 (2013).
3. Y. Wang *et al.*, *Cell* **150**, 816 (2012).
4. X. Li *et al.*, *Neuron* **75**, 1035 (2012).
5. L. E. Clarke, B. A. Barres, *Nat. Rev. Neurosci.* **14**, 311 (2013).
6. A. V. Molofsky *et al.*, *Nature* **509**, 189 (2014).
7. K. W. Gripp, A. E. Lin, in *GeneReviews* (2006, updated 2012), www.ncbi.nlm.nih.gov/books/NBK1507/?log$=activity.
8. T. Stork *et al.*, *Neuron* **83**, 388 (2014).
9. E. C. Williams *et al.*, *Hum. Mol. Genet.* **23**, 2968 (2014).
10. C. Chen *et al.*, *Nat. Commun.* **5**, 4430 (2014).
11. A. E. Takesian, T. K. Hensch, *Prog. Brain Res.* **207**, 3 (2013).
12. X. Wu *et al.*, *J. Clin. Invest.* **121**, 1009 (2011).
13. Y. S. Lee *et al.*, *Nat. Neurosci.* **17**, 1736 (2014).
14. G. M. Thomas, R. L. Huganir, *Nat. Rev. Neurosci.* **5**, 173 (2004).
15. A. L. Lin, D. H. Gutmann, *Nat. Rev. Clin. Oncol.* **10**, 616 (2013).

ACKNOWLEDGMENTS

W.D.S. is supported by NIH grant RO1 NS031768.

10.1126/science.aab3738

CONSERVATION

Committing to ecological restoration

Efforts around the globe need legal and policy clarification

By **Katharine Suding,[1]* Eric Higgs,[2] Margaret Palmer,[3] J. Baird Callicott,[4] Christopher B. Anderson,[5] Matthew Baker,[6] John J. Gutrich,[7] Kelly L. Hondula,[8] Matthew C. LaFevor,[8] Brendon M. H. Larson,[9] Alan Randall,[10,11] J. B. Ruhl,[12] Katrina Z. S. Schwartz[13]**

At the September 2014 United Nations Climate Summit, governments rallied around an international agreement—the New York Declaration on Forests—that underscored restoration of degraded ecosystems as an auspicious solution to climate change. Ethiopia committed to restore more than one-sixth of its land. Uganda, the Democratic Republic of Congo, Guatemala, and Colombia pledged to restore huge areas within their borders. In total, parties committed to restore a staggering 350 million hectares by 2030.

The ambition affirms restoration's growing importance in environmental policy. These new commitments follow the 2010 Aichi Convention on Biological Diversity (to restore at least 15% of degraded ecosystems globally) and the 2011 Bonn Challenge (to restore 150 million hectares). Particularly when accompanied by policies to reduce further losses (as in the New York Declaration), restoration of such magnitude holds promise to address global environmental concerns.

POLICY

Achieving this promise requires careful thought about how we restore ecosystems (*1*, *2*). We outline four core principles of scientifically based, workable, and comprehensive restoration (*3*) that can provide appropriate best practice guidelines in legal, policy, and planning efforts.

There is little question that ecological restoration can provide substantial benefits that enhance quality of life (*4*). A considerable body of science suggests that restoration can guide establishment of complex self-sustaining interactions between biota, biophysical features, and processes that compose an ecosystem (*5*, *6*). The science also emphasizes the challenging nature of the endeavor: Our interventions rarely achieve full recovery, and uncertainty is to be expected in dealing with natural recovery processes (*7*, *8*). Continuing environmental change further challenges the notion of recovery (*9*).

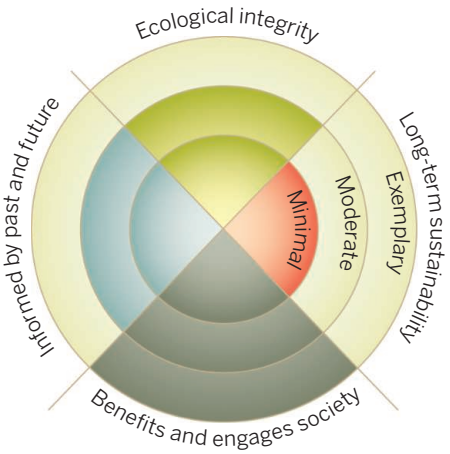

Four principles for planning restoration. The use of four principles identifies trade-offs in the planning process and the extent of departure from the full opportunities presented by comprehensive ecological restoration [example after (*25*)].

Some have thus questioned whether declarations of intent to restore will in fact result in substantive restoration of degraded land (*10*, *11*). Others have cautioned that these declarations may spur actions that compromise biodiversity: for instance, by replacing ancient grassy biomes with forest plantations (*12*) or by planting species in climatic zones where they may not persist (*13*). Others emphasize that a focus on one specialized goal (e.g., climate change mitigation) might not deliver intended benefits because of complexity in ecosystem dynamics in ways and over time scales not fully understood (*14*, *15*).

Specialized programs such as compensatory mitigation, endangered species conservation, and ecosystem service delivery can be a useful contribution to—but are not synonymous with—ecological restoration (*16*, *17*). Such distinctions are not trivial because projects undertaken in the name of restoration may in fact be something different and, in many cases, have been demonstrated to achieve neither restoration nor their intended purposes (*17*, *18*). Delivery of diverse benefits will depend on how on-the-ground efforts are conceived and implemented (*7*, *8*). Avoiding mistakes on a grand scale requires clear practice principles (*10*).

FOUR PRINCIPLES. We advocate considering four principles when planning restoration. The degree to which each principle is achievable will vary on the basis of social and ecological context. By taking into account these comprehensive principles, trade-offs inherent in specialized projects are avoided, which increases the prospect of sustainable and valuable overall outcomes (see the figure).

1. Restoration increases ecological integrity. Restoration initiates or accelerates recovery of degraded areas by prioritizing the complexity of biological assemblages, including species composition and representation of all functional groups, as well as the features and processes needed to sustain these biota and to support ecosystem function (*3*, *4*).

2. Restoration is sustainable in the long term. Restoration aims to establish systems that are self-sustaining and resilient; thus, they must be consistent with their environmental context and landscape setting. Once a restoration project is complete, the goal should be to minimize human intervention over the long term. When intervention is required, it should be to simulate natural processes that the landscape no longer provides (e.g., fire or invasive species removal) or to support traditional practices of local communities (*8*, *9*).

3. Restoration is informed by the past and future. Historical knowledge, in its many forms, can indicate how ecosystems functioned in the past and can provide references for identifying potential future trajectories and measuring functional and compositional success of projects (*19*). However, the unprecedented pace and spatial extent of anthropogenic changes in the present era can create conditions that depart strongly from historical trends (*9*). Often, then, history serves less as a template and more as a guide for determining appropriate restoration goals (*19*, *20*).

[1]*University of Colorado Boulder, Boulder, CO 80309, USA.* [2]*University of Victoria, Victoria, British Columbia V8W 2Y2, Canada.* [3]*University of Maryland, College Park, MD 20742, USA.* [4]*University of North Texas, Denton, TX 76203, USA.* [5]*Consejo Nacional de Investigaciones Científicas y Técnicas and National University of Tierra del Fuego, Ushuaia, TDF 9410, Argentina.* [6]*University of Maryland Baltimore County, Baltimore, MD 21250, USA.* [7]*Southern Oregon University, Ashland, OR 97520, USA.* [8]*National Socio-Environmental Synthesis Center, University of Maryland, Annapolis, MD 21401, USA.* [9]*University of Waterloo, Waterloo, Ontario N2L 3G1, Canada.* [10]*Ohio State University, Columbus, OH 43210, USA.* [11]*University of Sydney, Sydney, New South Wales 2006, Australia.* [12]*Vanderbilt University Law School, Nashville, TN 37203, USA.* [13]*Woodrow Wilson International Center for Scholars, Washington, DC 20004, USA.*
**Corresponding author. suding@colorado.edu*

4. Restoration benefits and engages society. Restoration focuses on recovering biodiversity and supporting the intrinsic value of nature (*21*). It also provides a suite of ecosystem services (e.g., improved water quality, fertile and stable soils, drought and flood buffering, genetic diversity, and carbon sequestration) that enhance human quality of life (e.g., clean water, food security, enhanced health, and effective governance) (*22*). Restoration engages people through direct participation and, thus, increases understanding of ecosystems and their benefits and strengthens human communities (*4*).

Parties to the U.N. Declaration will consider a variety of ways to achieve the new restoration commitments. We advocate adoption of all four principles as normative standards that assess intent at the planning stage, developed in conjunction with consideration of levels of uncertainty (in both the means and ends), the degree to which each principle could be attained, and legal or regulatory frameworks (*23*). Components that constitute ecological integrity will differ across ecosystems; they will need to be described and made practical through best practice guidelines (*4*). The degree to which restoration can be self-sustaining will depend on landscape context; ongoing interventions may be required in some cases to ensure ecological goals consistent with local context are met (*6*). Flexibility regarding the degree of historical fidelity will be needed to ensure success in rapidly changing environments (*9*). Ethical considerations can supersede direct societal benefits, particularly when ecocentric ideals are followed (*21*).

"Our four principles provide a necessary foundation to achieve sustainability and resilience into the future."

To achieve new restoration commitments, it will be tempting to consider specialized projects that emphasize one principle rather than attending to the full suite of potential opportunities. Degraded lands could be converted to carbon farms, where monocultures of fast-growing tree species are planted and managed to optimize carbon sequestration (*24*). Green infrastructure could provide vegetation that fixes carbon and increases permeable surfaces (*25*). As valuable as these strategies may be, they alone do not constitute comprehensive ecological restoration. To contribute to our commitment to restore, the scope of these strategies should be broadened to include all restoration principles (see the table).

We urge parties to utilize all principles in their planning and to maintain a broad purpose. Although a comprehensive plan may require a more integrative approach than one aimed toward a specialized purpose, considering all four guiding principles is most consistent with ecological and social science and most likely to realize accepted benefits of restoration without net ecological loss.

Our four principles provide a necessary foundation to achieve sustainability and

Application of guiding principles for restoration

Consideration of a comprehensive set of principles, with each principle situated along a continuum of effectiveness, should be a necessary provision of global restoration efforts.

	Four guiding principles			
EXAMPLES	**ECOLOGICAL INTEGRITY**	**LONG-TERM SUSTAINABILITY**	**BENEFITS AND ENGAGES SOCIETY**	**INFORMED BY PAST AND FUTURE**
Mitigation Compensatory mitigation for mountaintop mining impacts on streams, Appalachia, USA (*26*)	**Minimal** Project implementation most often based only on physical structure	**Minimal** Ongoing maintenance often required. Large changes in environmental context unaccounted for	**Minimal** Net loss of aquatic resources. Economic value of mining placed above environmental losses	**Minimal** Historical or reference ecosystems evaluated by length or oversimplified stream "units" rather than functional metrics
Ecosystem services Global Partnership on Forest and Landscape Restoration, Pamu Berekum, Ghana (*27*)	**Minimal** Tree-planting focus, with little attention to diversity or other processes and functions. Planting targets in ha/year of plantations	**Moderate** Increased rural livelihoods will decrease probability of unsustainable harvesting	**Exemplary** Increased carbon sequestration and food production. Participatory planning. Better income and rural livelihoods	**Minimal** Most focus on plantation methods, some attention to including valued indigenous tree species
Urban greening Cheonggyecheon stream restoration, Seoul, South Korea (*25*)	**Moderate** Increased biodiversity sixfold, including marsh plants, fish, and birds, but at considerable capital cost given central location in large urban region	**Minimal** To keep river flowing, water must be pumped from Han River and underground reserves at a cost of >200 million yen per year	**Exemplary** Reduced urban heat island effect and small-particle air pollution. Increased property values. Provided critical natural habitat for recreation in urban core	**Moderate** Redirected underground waterways. Historically, an intermittent stream with strong cultural significance
Endangered species El Segundo blue butterfly (*Euphilotes battoides allyni*), California, USA (*28*)	**Moderate** Focus on host plant, coast buckwheat (*Eriogonum parvifolium*)	**Minimal** Habitat protection and conservation	**Moderate** Intrinsic value of species preservation	**Exemplary** Preservation of last remaining coastal dunes in butterfly range
Habitat restoration Postlogging stream restoration, Lyell Island, Gwaii Haanas, Haida Gwaii, British Columbia, Canada (*4*)	**Exemplary** Integrated approach to habitat restoration that focused on several aspects of diversity and function	**Exemplary** Cessation of logging, relative absence of invasive species, cultural engagement, and assisted succession techniques ensure long-term success	**Exemplary** Significant cultural value in recovery of a focal group (salminoid fish), an important food source	**Exemplary** Clear use of intact contemporary reference ecosystems; goals included ecological and cultural continuity

resilience into the future. Ecosystems that are structurally and functionally diverse are more likely to be durable and capable of adapting to future challenges of climate change, introduced species, and land-use change and they can be sustained with a declining investment of human and financial capital over time. Involving people through multiple avenues—from participation to consumption of ecosystem services to cultural renewal—can promote public engagement and stewardship of local ecosystems. Adherence to these principles will add clarity, accountability, and accomplishment in this new era of embracing ecological restoration as an environmental policy tool. ■

REFERENCES AND NOTES

1. N. Shackelford *et al.*, *Restor. Ecol.* **21**, 297 (2013).
2. L. M. Hallett *et al.*, *Restor. Ecol.* **21**, 312 (2013).
3. Science and Policy Working Group, Society for Ecological Restoration, *SER International Primer on Ecological Restoration* (SER, Washington, DC, 2004).
4. K. Keenleyside *et al.*, Eds., *Ecological Restoration for Protected Areas* (International Union for Conservation of Nature, IUCN, Gland, Switzerland, 2012).
5. D. A. Falk, M. A. Palmer, J. B. Zedler, *Foundations of Restoration Ecology* (Island Press, Washington DC, 2007).
6. K. N. Suding, *Annu. Rev. Ecol. Evol. Syst.* **42**, 465 (2011).
7. R. L. Chazdon, *Second Growth: The Promise of Tropical Forest Regeneration in an Age of Deforestation* (Univ. of Chicago Press, Chicago, 2014).
8. E. Higgs, *Nature by Design* (MIT Press, Cambridge, MA, 2003).
9. R. J. Hobbs, L. M. Hallett, P. R. Ehrlich, H. A. Mooney, *Bioscience* **61**, 442 (2011).
10. C. Biron, Inter Press Service, 3 October 2014.
11. M. H. M. Menz, K. W. Dixon, R. J. Hobbs, *Science* **339**, 526 (2013).
12. J. W. Veldman *et al.*, *Science* **347**, 484 (2015).
13. Afforestation in China: Great green wall, *Economist*, 23 August 2014).
14. L. L. Bremer, K. A. Farley, *Biodivers. Conserv.* **19**, 3893 (2010).
15. L. Ciccarese, A. Mattsson, D. Pettenella, *New For.* **43**, 543 (2012).
16. M. A. Palmer, S. Filoso, R. M. Fanelli, *Ecol. Eng.* **65**, 62 (2014).
17. A. Telesetsky, *Vermont J. Environ. Law* **14**, 494 (2013).
18. J. Salzman, J. B. Ruhl, *Stanford Law Rev.* **53**, 607 (2000).
19. E. Higgs *et al.*, *Front. Ecol. Environ.* **12**, 499 (2014).
20. L. Balaguer, A. Escudero, J. F. Martín-Duque, I. Mola, J. Aronson, *Conserv. Biol.* **176**, 12 (2014).
21. J. B. Callicott, *Principles of Conservation Biology* (Sinauer Assoc., Sunderland, MA, 2006)
22. R. S. De Groot *et al.*, *Conserv. Biol.* **27**, 1286 (2013).
23. R. K. Craig, *HELR Harvard Environ. Law Rev.* **34**, 9 (2010).
24. B. B. Lin *et al.*, *Bioscience* **63**, 793 (2013).
25. V. M. Temperton *et al.*, *Restor. Ecol.* **22**, 271 (2014).
26. M. A. Palmer, K. L. Hondula, *Environ. Sci. Technol.* **48**, 10552 (2014).
27. Global Partnership on Forest and Landscape Restoration, Pamu Berekum site; www.forestlandscaperestoration.org/learning-site-pamu-berekum.
28. K. Suckling, N. Greenwald, T. Curry, *On Time, on Target: How the Endangered Species Act Is Saving America's Wildlife* (Center for Biological Diversity, Tucson, AZ, 2012).

ACKNOWLEDGMENTS

We thank anonymous reviewers, N. Barger, R. Hobbs, and S. Murphy for comments. This work was supported by the National Socio-Environmental Synthesis Center (SESYNC) under funding received from the U.S. National Science Foundation DBI-1052875.

10.1126/science.aaa4216

HUMAN GENETICS

GTEx detects genetic effects

The genetic basis for variation among individuals in transcript abundance across tissues is analyzed

By **Greg Gibson**

One of the lessons from the past several years of genomic analysis is that well-conceived, ambitious, and thoughtfully analyzed genetic studies carried out by large consortia can advance the field in giant leaps. They do so both by providing new insight and by generating data sets that are widely accessible to all investigators. It is thus remarkable that, even though we now know that the vast majority of common polymorphisms (variants of a particular DNA sequence) that are associated with disease risk act by modulating gene expression, "big science" transcription analyses have been lacking. This deficit is now addressed with the publication of the first results from the Genotype-Tissue Expression (GTEx) Consortium (*1*), which also includes the findings of Melé *et al.* (*2*) and Rivas *et al.* (*3*), on pages 648, 660, and 666, respectively, in this issue.

GTEx is an effort coordinated by the U.S. National Human Genome Research Institute to understand the genetic basis for variation among individuals in transcript abundance across many tissues (*4*). Hitherto, our knowledge of the genetics of gene expression in humans has derived mostly from studies of blood (*5*), lymphoblast cell lines (*6*), and isolated studies of accessible tissues such as fat or skin (*7*). The plan for GTEx is to associate whole-genome sequence variation with RNA sequencing data for more than 50 tissue types from almost 1000 next-of-kin consented postmortem donors. This knowledge will provide direct evidence addressing the function of the many thousands of disease-associated variants supplied by genome-wide association studies (GWAS) and will illuminate mechanisms of variation for disease risk among healthy people. The pilot phase results (*1*–*3*) are based on data from the first 237 donors, of whom around 100 have RNA samples analyzed in 9 tissues, with data from smaller subsets of donors available for 33 other tissues. The main GTEx Consortium article reports on the genetic regulation of gene expression, whereas Melé *et al.* provide an overview of differences between the "transcriptome"—all RNA molecules, including messenger RNA, ribosomal RNA, transfer RNA, and other long noncoding RNA transcripts—across tissues and individuals. Rivas *et al.* report on the effect that protein-truncating variants have on human transcription, generating a quantitative model of how nonsense-mediated decay (the elimination of transcripts that contain a premature stop codon) varies across tissues and may be genetically regulated.

Previous studies in many organisms have established that common regulatory polymorphisms (expression quantitative trait loci, or cis-eQTLs) located within a few hundred kilobases of a gene significantly influence the expression of at least half of all genes in one tissue or another (*8*). They act locally to influence expression of a nearby gene, and may explain anywhere from a few percent to more than half the variance in abundance of the specific transcript among individuals. These effects are much larger than those typically associated with disease, so the largest eQTL effects can be detected with sample sizes of as few as 100 individuals (*9*). It is to be expected that rare variants also contribute to disease, although their discovery is in its infancy. Epigenetic influences such as chromatin modification and microRNA regulation certainly also explain substantial amounts of the variance. A critical feature of transcriptional variation is the very high degree of co-regulation, sometimes of thousands of genes. This can be attributed to the collective effects of trans-acting regulatory factors (transcription factors, hormones, environmental agents) as well as variation in the abundance of cell types within tissues.

> ***"This knowledge will ... illuminate mechanisms of variation for disease risk..."***

One of the major contributions of these first GTEx papers is quantification of the relative contributions of cis-eQTLs in different tissues, suggesting (for example) that thyroid and tibial nerve have twice the number of genes regulated by local polymorphisms than blood or heart (*1*). However, blood seems to have a relatively high level of allele-specific expression (transcription predomi-

School of Biology, Georgia Institute of Technology, Atlanta, GA 30332, USA. E-mail: greg.gibson@biology.gatech.edu

nantly from one of the two chromosomes), whereas brain samples are depleted for this phenomenon. Interestingly, it appears that allele-specific expression is more strongly conserved among tissues within individuals than is overall transcript abundance (*1*).

There has been much debate on how much shared genetic variation for gene expression there is across tissues. Different analytical methods applied to comparisons of different data sets have led to diverse conclusions (*7*, *10*). The GTEx Consortium tackles the issue by studying a common set of individuals with two different analytical approaches: pairwise linear models and joint Bayesian analysis. The conclusion is striking, namely that around half of all cis-eQTLs—particularly those proximal to a promoter—are active in the majority of tissues, whereas the other half tend to be specific to one or two tissues (*1*). Variants that affect splicing, namely the generation of alternative transcript isoforms, also tend to be conserved across tissues with more than 80% detected in multiple tissues, but with a wide range of similarity among pairwise comparisons: Whole blood shares fewer than 10% of its splicing QTLs with Sun-exposed skin, but almost 50% with the heart's left ventricle.

One of the big surprises reported (*1*) is the discovery of module QTLs (modQTLs), which are regulatory variants that influence the co-regulation of gene expression. The idea is that most genes are organized into expression modules. Even though they are located on different chromosomes, they tend to be have similar expression levels (*11*). Often, many genes in a module share a function such as controlling the cell division cycle. The reported analysis finds 117 modules of between 25 and 414 transcripts each. Some of these are observed in multiple tissues, but not necessarily with the same expression profiles across tissues. It turns out that quite a few genes switch module "membership" between individuals (see the figure). These switches can be associated with local regulatory variants (modQTLs), only about half of which were detected as cis-eQTLs in the relevant tissues (*1*). Because genes in modules often share regulatory motifs for a common set of transcription factors, and these motifs tend to harbor regulatory polymorphisms, the implication is that the full GTEx project will uncover new principles accounting for variation in the co-regulation of genes within and between tissues.

What are the implications for personalized medicine? These are barely hinted at in the studies (*1*–*3*), but the most obvious is validation of inferences from bioinformatics processing of GWAS data and information from the Encyclopedia of DNA Elements (ENCODE) project (which identified functional elements in the human genome sequence) (*12*). The measurement of chromatin features designed to annotate enhancers and other regulatory elements has led to the realization that disease-associated variants tend to be enriched in the vicinity of genes that are more likely to be active in disease-relevant tissues, such as lymphoid cells in autoimmune disease or neurons in psychiatric disorders (*13*, *14*). GTEx provides direct evidence that this is the case, and the project's accompanying portal allows anyone to look up in which tissue a disease variant influences the expression of a nearby gene in a particular direction. Notably, very often, "nearby" does not mean the most adjacent. Additionally, the important point is made (*1*, *3*) that profiling gene expression across 50 tissues demonstrates that genes encoding protein-truncating variants are actually not even expressed in the most relevant tissue. This implies that variants predicted to be deleterious on the basis of DNA sequence may actually be highly unlikely to contribute to a disease.

Within the next 2 years, the full GTEx data should be available. There is no question that with an order of magnitude more data, the analyses will greatly exceed verification of the findings reported in the pilot studies. Vastly more cis-eQTLs will be found, intricacies of allele-specific expression and splicing will be worked out, and mechanisms responsible for switches in modularity inferred. We can also expect more complete integration of the GTEx data with the ENCODE analyses (*13*), using statistical approaches yet to be conceived, and a pilot ENCODE Tissue Expression (EnTEx) project will report chromatin profiling of some GTEx samples. Such analyses will allow us to sift through the suggestive GWAS peaks and explain more of the variance for disease and attribute it to appropriate cell types. Yet more ambitious GTEx projects might be conceived, evaluating how genetic regulatory effects vary in the context of disease ("GTEx-D") and across environments ("GTEx-E"), if investments are made in the research of genotype-tissue expression from patients who have chronic diseases or have lived with different lifestyles or environmental exposures such as toxins or severe socioeconomic stress (*15*).

Perhaps most important, we can begin to outline an enhanced program of genome-enabled precision medicine. Although there is justifiable excitement about the ability of DNA sequencing to identify the causes of congenital abnormalities, to predict the progression of tumors, and to personalize the prescription of drugs, the static genome has its limitations. If, 20 years from now, gene expression profiling is incorporated side-by-side with genotype analysis as a standard component of medical diagnostics, the GTEx project will be seen to have brought us closer to realization of this vision. ■

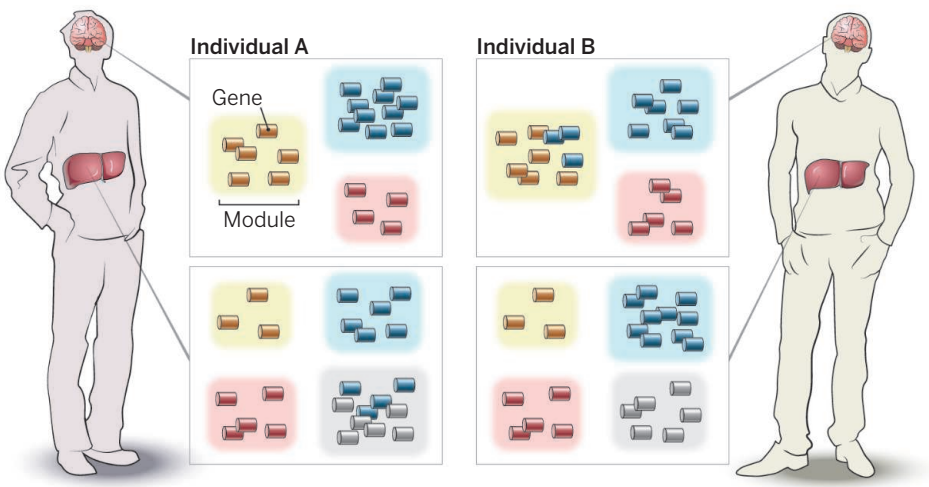

Switches in modularity. Many genes tend to be coexpressed in modules. Modules may differ in their presence (gray) or size (yellow) among tissues and between individuals (blue). Some genes switch between modules [from the blue to yellow module in the brain (right); from the blue to gray module in the liver (left)].

ILLUSTRATION: V. ALTOUNIAN/*SCIENCE*

REFERENCES

1. GTEx Consortium, *Science* **348**, 648 (2015).
2. M. Melé *et al.*, *Science* **348**, 660 (2015).
3. M. A. Rivas *et al.*, *Science* **348**, 666 (2015).
4. GTEx Consortium, *Nat. Genet.* **45**, 580 (2013).
5. H. J. Westra *et al.*, *Nat. Genet.* **45**, 1238 (2013).
6. T. Lappalainen *et al.*, *Nature* **501**, 506 (2013).
7. A. C. Nica *et al.*, MuTHER Consortium, *PLOS Genet.* **7**, e1002003 (2011).
8. F. W. Albert, L. Kruglyak, *Nat. Rev. Genet.* **16**, 197 (2015).
9. M. Morley *et al.*, *Nature* **430**, 743 (2004).
10. T. Flutre *et al.*, *PLOS Genet.* **9**, e1003486 (2013).
11. E. Segal *et al.*, *Nat. Genet.* **34**, 166 (2003).
12. ENCODE Project Consortium, *Nature* **489**, 57 (2012).
13. M. T. Maurano *et al.*, *Science* **337**, 1190 (2012).
14. A. Gusev *et al.*, *Am. J. Hum. Genet.* **95**, 535 (2014).
15. S. W. Cole, *PLOS Genet.* **10**, e1004601 (2014).

10.1126/science.aab3002

LETTERS

Edited by **Jennifer Sills**

Promises and perils for the panda

AS A GLOBAL conservation icon and China's national treasure, the endangered giant panda has received exceptional attention worldwide. Between 2003 and 2013, giant pandas in the wild increased from 1596 to 1864, according to the results from the latest survey released by the State Forestry Administration (*1*). About two-thirds of the wild giant pandas and 53.8% of panda habitat are within nature reserves (*1*). Pandas in captivity are also thriving.

However, there are long-term threats to panda survival and reproduction, including virus infection ("Captive pandas succumb to killer virus," M. Hvistendahl, In Depth, 13 February, p. 700), habitat fragmentation, low genetic diversity, and human activities. As some old threats have diminished, new threats have emerged. Harvesting forests for fuelwood and timber has declined drastically (*2*), but livestock grazing has increased (*3*). Although illegal poaching has dwindled, climate change is becoming a potential threat. For example, climate change could bring a substantial reduction in the distributional ranges of the dominant bamboo species that comprise almost the entire diet of the panda population in Qinling Mountains of Shaanxi Province (the region with the highest panda density across the panda range) (*4*).

To ensure long-term panda survival, it is important to expand from short-term to long-term strategies from the perspective of coupled human and natural systems (*5*). For example, the State Forestry Administration plans to prohibit encroachments on existing reserves for economic development, but only for the next 2 years. It is imperative to reduce human pressure in the long run by providing local residents with incentives to conserve pandas and panda habitat (*6*) and by providing educational opportunities that will enable young people living in the panda range to find jobs and settle in the cities (*7*). Creating nature reserves in areas where no pandas currently live (such as the northern side of the current panda range) might provide a safer haven for future pandas as the climate changes.

To respond to the Chinese government's call for more panda conservation, detailed data from the panda surveys should be made readily available. Releasing the data can help to analyze how and why panda populations have changed in a particular region that was covered in different surveys. Sharing the data respects the hard work by more than 2000 people surveying in the rugged mountains over 3 years in the latest panda survey alone. Most important, it can help boost promises and reduce perils for the panda.

Jianguo Liu

Center for Systems Integration and Sustainability, Department of Fisheries and Wildlife, Michigan State University, East Lansing, MI 48823, USA.
E-mail: liuji@msu.edu

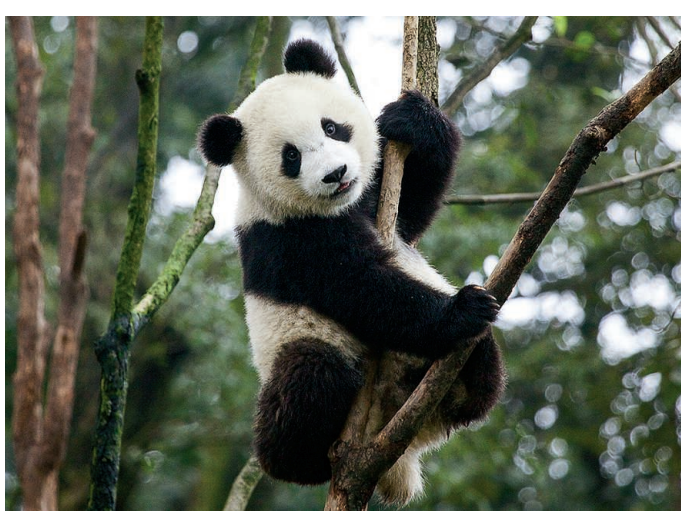

PHOTO: MARTHA DE JONG-LANTINK/FLICKR

REFERENCES

1. State Council Information Office of China (2015); www.scio.gov.cn/xwfbh/gbwxwfbh/fbh/Document/1395514/1395514.htm [in Chinese].
2. G. He *et al.*, *Landscape Urban Plan.* **92**, 1 (2009).
3. V. Hull *et al.*, *Biol. Conserv.* **144**, 3028 (2011).
4. M.-N. Tuanmu *et al.*, *Nat. Clim. Change* **3**, 249 (2013).
5. J. Liu *et al.*, *Science* **347**, 1258832 (2015).
6. X. Chen *et al.*, *Conserv. Biol.* **24**, 1469 (2010).
7. J. Liu *et al.*, *Science* **300**, 1240 (2003).

NEXTGEN VOICES

Postdocs reimagined: Last call

You have one more week to respond to the NextGen VOICES survey! Share your thoughts about this question:

Is the idea of the postdoc position obsolete in today's scientific landscape? If so, what should replace it? If not, what one change would you make to improve it?

To submit, go to http://scim.ag/NG_15

Deadline for submissions is 15 May. A selection of the best responses will be published in the 3 July 2015 issue of *Science*. Submissions should be 200 words or less. Anonymous submissions will not be considered.

The potential of secondary forests

TROPICAL FORESTS ARE increasingly modified by human activities. Centuries of human–forest interactions have led to a diverse array of forest areas in different phases of succession. In recent decades, forest conversion to cattle pasture or agricultural fields, followed by land abandonment, has led to large areas of second-growth forest in the Amazon. These forests grow rapidly and sequester large amounts of carbon in their biomass, but they tend to be ignored, as most of the debate on the carbon balance of the Amazon basin tends to revolve around old-growth forests.

For example, a recent study has shown that the net carbon uptake of Amazonian old-growth forests has declined by a third per decade from 1990 to 2010 (*1*, *2*). When extrapolated over the whole Amazon basin, these results translate into a reduced role of intact tropical forests in climate change mitigation. This alarming conclusion, however, completely ignores the important role of regenerating forests as carbon sinks. For instance, in 2010 about 25% of formerly deforested areas in Para, Brazil, were occupied by second-growth forests. Although re-growing forests have lower carbon stocks (45 to 48% of old growth forest), their net carbon sequestration rate is up to 20 times higher (4.6 to 5.8 Mg carbon ha^{-1} $year^{-1}$) (*3*) than old-growth forests (*1*). Additionally, about one-quarter of the forests in the Amazon basin are managed for timber production. Net carbon sequestration rates after timber extraction are high, and the application of reduced-impact logging techniques further increases carbon sequestration rates (2.8 Mg ha^{-1} $year^{-1}$ compared with 0.5 for conventionally logged areas) (*4*). Consequently, it is essential to incorporate the carbon sequestration potential of second-growth, logged, and managed forests in future

assessments of the Amazon basin as a global carbon sink.

F. Bongers,[1]* R. Chazdon,[2] L. Poorter,[1] M. Peña-Claros[1]

[1]Forest Ecology and Management Group, Wageningen University. 6700AH, Wageningen, Netherlands. [2]Department of Ecology and Evolutionary Biology, University of Connecticut, Storrs, CT 06269–3043, USA.

*Corresponding author. E-mail: Frans.Bongers@wur.nl

REFERENCES

1. R. J. W. Brienen *et al.*, *Nature* **519**, 344 (2015).
2. E. Kintisch, "Amazon rainforest ability to soak up carbon dioxide is falling" (2015); http://news.sciencemag.org/climate/2015/03/amazon-rainforest-ability-soak-carbon-dioxide-falling.
3. Y. Pan *et al.*, *Science* **333**, 988 (2011).
4. T. A. P. West, E. Vidal, F. E. Putz, *Forest Ecol. Manage.* **314**, 59 (2014).

Naming diseases: First do no harm

IN RECENT YEARS, the world has seen the emergence of several new human infectious diseases. Given the rapid and global communication through social media and other electronic means, diseases are now often given common names by stakeholders outside as well as inside the scientific community. The use of names such as "swine influenza" and "Middle Eastern Respiratory Syndrome" has had unintentional negative economic and social impacts by stigmatizing certain industries or communities. Disease names, once given, are difficult to change later even if an inappropriate name is being used. Therefore, it is important that an appropriate name is assigned to a newly identified human disease by whoever first reports it.

In response to such concerns, the World Health Organization (WHO), in close collaboration with the World Organisation for Animal Health (OIE) and the Food and Agriculture Organization of the United Nations (FAO), and in consultation with the International Classification of Diseases (ICD) (*1*), has developed a set of standard best practices for naming new human infectious diseases, with the aim of minimizing unnecessary negative effects on nations, economies, people, and animals. A full description of these best practices is available on the WHO Web site (*2*).

These best practices apply to new infections, syndromes, and diseases of humans that have never been recognized or reported before in humans, that have potential public health impact, and for which no disease name is yet established in common usage. They do not replace the existing ICD system, but rather provide an interim solution prior to the assignment of a final ICD disease name. As these best practices only apply to disease names for common usage, they also do not affect the work of existing international authoritative bodies responsible for scientific taxonomy and nomenclature of microorganisms.

WHO, OIE, and FAO strongly encourage all national, regional, and international stakeholders, including scientists, national authorities, and media, to follow these best practices in the event of the emergence of a new human disease, so that inappropriate disease names do not become established.

K. Fukuda,[1]* R. Wang,[2] B. Vallat[3]

[1]World Health Organization, 1211, Geneva, Switzerland. [2]Food and Agriculture Organization of the United Nations, 00153, Rome, Italy. [3]World Organisation for Animal Health, 75017, Paris, France.

*Corresponding author. E-mail: infectiousdiseasenaming@who.int

REFERENCES

1. World Health Organization, International Classification of Diseases (www.who.int/classifications/icd/en).
2. www.int/topics/infectious_diseases/naming-new-diseases/en.

The views expressed in this Letter are those of the authors and do not necessarily reflect the views or policies of the signatory organizations.

RESEARCH

Molybdenum nanostructures convert natural gas

Gao et al., *p. 686*

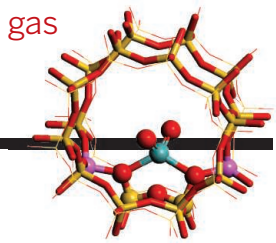

IN *SCIENCE* JOURNALS

Edited by **Stella Hurtley**

The whispering gallery at St. Paul's

PHYSICS

A circular route to confine electrons

Physical barriers are used to confine waves. Whether it is harbor walls for sea waves, a glass disk for light, or the "whispering gallery" circular chamber walls in St. Paul's Cathedral for sound, the principle of confinement—reflection—is the same. Zhao *et al*. used that same principle to confine electrons in a nanoscale circular cavity in graphene. Periodic patterns within the cavity were associated with an electronic wave version of whispering gallery modes. The tunability of the cavity size may provide a route for the manipulation of electrons in graphene and similar materials. — ISO

Science, this issue p. 672

HUMAN GENOMICS

Expression, genetic variation, and tissues

Human genomes show extensive genetic variation across individuals, but we have only just started documenting the effects of this variation on the regulation of gene expression. Furthermore, only a few tissues have been examined per genetic variant. In order to examine how genetic expression varies among tissues within individuals, the Genotype-Tissue Expression (GTEx) Consortium collected 1641 postmortem samples covering 54 body sites from 175 individuals. They identified quantitative genetic traits that affect gene expression and determined which of these exhibit tissue-specific expression patterns. Melé *et al.* measured how transcription varies among tissues, and Rivas *et al.* looked at how truncated protein variants affect expression across tissues. — LMZ

Science, this issue p. 648, p. 660, p. 666; see also p. 640

GEOPHYSICS

Silent slip events get shallow

Clues to help better predict the likelihood of devastating earthquakes and tsunamis may be embedded in a more gentle type of rumbling. Using ocean-bottom seismometers, Yamashita *et al*. report rare observations of migrating tremors in the shallow part of a subduction zone off southern Kyushu, Japan. The tremors appear to be linked to a very low-frequency earthquake and seem to migrate to the region where big earthquakes are generated. The tremors may be tracing how and where stress gets concentrated onto the earthquake-producing portion of the fault. — BG

Science, this issue p. 676

SURFACE SCIENCE

Using friction to guide fabrication

Ultralow friction found in certain layered materials such as graphite is important in the construction of nanomechanical devices. Koren *et al.* combined measurements and modeling to characterize the interaction of sliding graphite planes (see the Perspective by Liechti). This helped them to make small graphite devices that featured rotational pivots and multiple locking positions. — BG

Science, this issue p. 679

BIOENGINEERING

Keeping tabs on tiny worms

Filarial nematodes—tiny parasitic worms that can enter the bloodstream—are common in some parts of Africa. One of these worms, *Loa loa*, causes loiasis but is not compatible with current ivermectin-based mass drug administration (MDA) programs. These programs aim to eliminate other worms that cause onchocerciasis and lymphatic filariasis. To pinpoint people to exclude from MDA, D'Ambrosio *et al.* devised a mobile phone–based strategy for quantifying *Loa* microfilariae in whole blood. A mobile phone video camera and a custom algorithm tracked the worm's "wriggling" motion.

Published by AAAS

The device was packaged for point-of-care use—including its own smartphone "app"—and successfully diagnosed *Loa*-infected people in Cameroon, Africa. — MLF

Sci. Transl. Med. **7**, 286re4 (2015).

OPTOGENETICS

An optogenetic tool to silence neurons

Potassium channels in the cell membrane open and close in response to molecular signals to alter the local membrane potential. Cosentino *et al*. linked a light-responsive module to the pore of a potassium channel to build a genetically encoded channel called BLINK1 that is closed in the dark and opens in response to low doses of blue light. Zebrafish embryos expressing BLINK1 in their neurons changed their behavior in response to blue light. — VV

Science, this issue p. 707

VACCINES

Extra dividends from measles vaccine

Vaccination against measles has many benefits, not only lifelong protection against this potentially serious virus. Mina *et al*. analyzed data collected since mass vaccination began in high-income countries when measles was common. Measles vaccination is associated with less mortality from other childhood infections. Measles is known to cause transient immunosuppression, but close inspection of the mortality data suggests that it disables immune memory for 2 to 3 years. Vaccination thus does more than safeguard children against measles; it also stops other infections taking advantage of measles-induced immune damage. — CA

Science, this issue p. 694

TISSUE REGENERATION

Inhibiting Hippo to mend broken hearts

Activation of the Hippo signaling pathway prevents organ overgrowth. The pathway inhibits the activity of the transcriptional coactivator Yap, which is important during development. However, this same activity limits the ability of some organs to regenerate after injury. Morikawa *et al.* found that Yap target genes not only included cell cycle genes but also genes encoding cytoskeletal remodeling proteins or proteins that link the cytoskeleton to the extracellular matrix. Cardiomyocytes from Hippo signaling–deficient mice formed cellular protrusions typical of migrating cells and more readily moved toward scar sites after cardiac injury. Thus, inhibiting the Hippo pathway could help with heart regeneration. — WW

Sci. Signal. **8**, ra41 (2015).

MALARIA

A way to dissect malaria's secrets

Malaria has exerted a strong selective force on the human genome. However, efforts to identify host susceptibility factors have been hindered by the absence of a nucleus in red blood cells. Egan *et al*. developed an approach involving blood stem cells to discover host factors critical for *Plasmodium falciparum* infection of red blood cells. The authors identified an essential host receptor for parasite invasion that could provide a target for malaria therapeutics. — SMH

Science, this issue p. 711

Measles vaccination

PHOTOS: (LEFT TO RIGHT) TEK IMAGE/SCIENCE SOURCE; J. C. CRONK *ET AL. IMMUNITY* **42**, 4 (21 APRIL 2015) © 2015 ELSEVIER INC.

IN OTHER JOURNALS

Edited by **Sacha Vignieri** *and* **Jesse Smith**

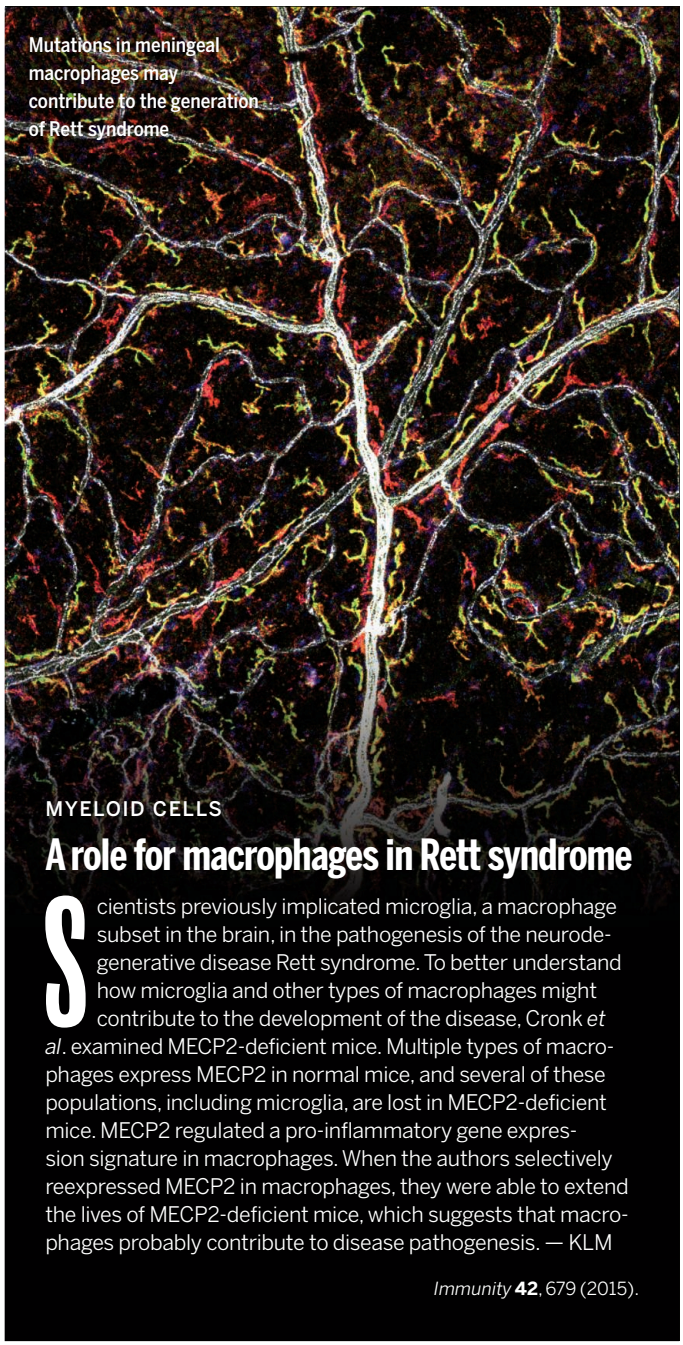

Mutations in meningeal macrophages may contribute to the generation of Rett syndrome

MYELOID CELLS

A role for macrophages in Rett syndrome

Scientists previously implicated microglia, a macrophage subset in the brain, in the pathogenesis of the neurodegenerative disease Rett syndrome. To better understand how microglia and other types of macrophages might contribute to the development of the disease, Cronk *et al*. examined MECP2-deficient mice. Multiple types of macrophages express MECP2 in normal mice, and several of these populations, including microglia, are lost in MECP2-deficient mice. MECP2 regulated a pro-inflammatory gene expression signature in macrophages. When the authors selectively reexpressed MECP2 in macrophages, they were able to extend the lives of MECP2-deficient mice, which suggests that macrophages probably contribute to disease pathogenesis. — KLM

Immunity **42**, 679 (2015).

PROTEIN BINDING

Methyl-C binding may explain Rett late onset

Girls with Rett syndrome develop normally for the first 1 or 2 years of life before suffering from progressive neurological problems, perhaps due to mutations in methyl-CpG–binding protein 2 (MeCP2). Chen *et al.* analyzed the binding of MeCP2 to genomic DNA in the mouse brain and found that before birth, MeCP2 binds predominantly to methylated CG sequences. After birth, there is an increase in the genome of methylated C in a non-CG context (mCH). MeCP2 binds to many of these mCH sites, which are enriched in genes with neuronal functions. MeCP2

ALSO IN *SCIENCE* JOURNALS

Edited by **Stella Hurtley**

SOIL SCIENCE

Global soil resources under stress

The future of humanity is intertwined with the future of Earth's soil resources. Soil provides for agriculture, improves water quality, and buffers greenhouse gases in the atmosphere. Yet human activities, including agricultural soil erosion, are rapidly degrading soil faster than it is naturally replenished. At this rate, human security over the next century will be severely threatened by unsustainable soil management practices. Amundson *et al.* review recent advances in understanding global soil resources, including how carbon stored in soil responds to anthropogenic warming. Translating this knowledge into practice is the biggest challenge remaining. — NW

Science, this issue p. 647

SUPERNOVAE

Stellar metals shine toward our eyes only

Taking a different look at a familiar star may still yield surprises. Boggs *et al*. trained the x-ray vision of the NuSTAR observatory on the well-studied supernova 1987A. Core-collapse explosions such as SN 1987A produce a titanium isotope, ^{44}Ti, whose radioactive decay yields hard x-ray emission lines. All the emission associated with ^{44}Ti appears to be from material moving toward us, with none moving away. This implies that the explosion was not symmetric. These findings help to explain the mechanics of SN 1987A and of core-collapse supernovae in general. — MMM

Science, this issue p. 670

SOLAR CELLS

Going toward the grains

Great strides have been made in improving the efficiency of organic-inorganic perovskite solar cells. Further improvements are likely to depend on understanding the role of film morphology on charge-carrier dynamics. deQuilettes *et al*. correlated confocal fluorescence microscopy images with those from scanning electron microscopy to spatially resolve the photoluminescence and carrier decay dynamics from films of organic-inorganic perovskites. Carrier lifetimes varied widely even between grains, and chemical treatments could improve lifetimes — PDS

Science, this issue p. 683

CATALYSIS

Waste not, want not

Natural gas often escapes or is deliberately burned at remote exploration sites because there is no economical way to transport it to markets. One route proposed for converting its main component, methane, into a more readily transported liquid is conversion to benzene over zeolites containing molybdenum (Mo). However, this method suffers from low conversion efficiency. Gao *et al*. identified the active Mo nanostructures as well as deactivated carbide species that form during this reaction. They were also able to recover and even enhance the zeolite catalytic activity after oxygen treatments. — PDS

Science, this issue p. 686

INORGANIC CHEMISTRY

Mimicking the oxygen evolution center

Making a synthetic analog of plant photosynthesis is a key goal for exploiting solar energy and replacing fossil fuels. Zhang *et al.* synthesized a manganese-calcium cluster that looks and acts like the oxygen evolution center in photosystem II (see the Perspective by Sun). The mimic structurally resembles the biological complex, with the notable exception of bridging protein ligands and water-binding sites on a dangling Mn atom. Functionally, however, the cluster's metal center readily undergoes four redox transitions, which contribute to splitting water into oxygen. This and other synthetic mimics will pave the way for developing more efficient catalysts for artificial photosynthesis. — NW

Science, this issue p. 690; see also p. 635

CHROMOSOMES

Building stable centromeres

Each of our chromosomes has a single centromere, seen as a constriction during cell division, which is required for accurate chromosome segregation to daughter cells. Falk *et al*. show that the special histone protein known as CENP-A, which forms part of the nucleosomes at centromeres, makes the chromatin at these constrictions very stable and long-lived. This stability is conferred by a protein-binding partner, CENP-C, recruited to the centromere by the CENP-A histone. Binding of CENP-C to CENP-A–containing nucleosomes alters the behavior of the macromolecular centromere complex to help it maintain its identity — GR

Science, this issue p. 699

STRUCTURAL VIROLOGY

Measles virus capsid at high resolution

Viruses rely on their capsid proteins to package and protect their genome. For measles virus and other Mononegavirales family members, multiple capsid proteins together form a helical shell around the viral RNA (collectively called the nucleocapsid). Gutsche *et al*. now report a high-resolution cryoelectron microscopy structure of the measles virus nucleocapsid. The structure reveals how the nucleocapsid assembles and how the nucleoprotein and viral RNA interact, both of which may inform drug design — KLM

Science, this issue p. 704

INFECTIOUS DISEASES

Lung imaging for better TB treatments

Tuberculosis treatments typically take 6 months to complete. Although the success rate is high for full treatment, many patients do not complete the treatment course. Attempts to develop drugs with shorter treatment times have not been successful. In a Perspective, Barry highlights the role that recent imaging advances can play in assessing the success of drug candidates. For example, serial computed tomography imaging can be used to map the lung at millimeter resolution and monitor changes in particular lung regions in response to treatment. This and other imaging methods have the potential to improve the quality of clinical trials by defining quantitative target outcomes. — JFU

Science, this issue p. 633

SEMICONDUCTORS

Oriented mesostructure for energy conversion

The orientation-controlled growth of mesoporous channels in single-crystal semiconductors is extremely difficult but highly desirable in optical devices. Zhao *et al.* used a simple evaporation process to synthesize three-dimensional open mesoporous titanium dioxide microspheres with uniform size (~800 nm), well-controlled radially oriented mesoporous channels, and "single-crystal"–like walls. Dye-sensitized solar cells using such microspheres showed good power conversion efficiency up to 12%. This evaporation-driven approach may provide a path for tailoring the orientation and self-assembly of other mesoporous metallic oxides and open the door for their potential use in optoelectronic devices. — ZHK

Sci. Adv. 10.1126/sciadv.1500166 (2015).

The device was packaged for point-of-care use—including its own smartphone "app"—and successfully diagnosed *Loa*-infected people in Cameroon, Africa. — MLF

Sci. Transl. Med. **7**, 286re4 (2015).

OPTOGENETICS

An optogenetic tool to silence neurons

Potassium channels in the cell membrane open and close in response to molecular signals to alter the local membrane potential. Cosentino *et al*. linked a light-responsive module to the pore of a potassium channel to build a genetically encoded channel called BLINK1 that is closed in the dark and opens in response to low doses of blue light. Zebrafish embryos expressing BLINK1 in their neurons changed their behavior in response to blue light. — VV

Science, this issue p. 707

VACCINES

Extra dividends from measles vaccine

Vaccination against measles has many benefits, not only lifelong protection against this potentially serious virus. Mina *et al*. analyzed data collected since mass vaccination began in high-income countries when measles was common. Measles vaccination is associated with less mortality from other childhood infections. Measles is known to cause transient immunosuppression, but close inspection of the mortality data suggests that it disables immune memory for 2 to 3 years. Vaccination thus does more than safeguard children against measles; it also stops other infections taking advantage of measles-induced immune damage. — CA

Science, this issue p. 694

TISSUE REGENERATION

Inhibiting Hippo to mend broken hearts

Activation of the Hippo signaling pathway prevents organ overgrowth. The pathway inhibits the activity of the transcriptional coactivator Yap, which is important during development. However, this same activity limits the ability of some organs to regenerate after injury. Morikawa *et al.* found that Yap target genes not only included cell cycle genes but also genes encoding cytoskeletal remodeling proteins or proteins that link the cytoskeleton to the extracellular matrix. Cardiomyocytes from Hippo signaling–deficient mice formed cellular protrusions typical of migrating cells and more readily moved toward scar sites after cardiac injury. Thus, inhibiting the Hippo pathway could help with heart regeneration. — WW

Sci. Signal. **8**, ra41 (2015).

MALARIA

A way to dissect malaria's secrets

Malaria has exerted a strong selective force on the human genome. However, efforts to identify host susceptibility factors have been hindered by the absence of a nucleus in red blood cells. Egan *et al*. developed an approach involving blood stem cells to discover host factors critical for *Plasmodium falciparum* infection of red blood cells. The authors identified an essential host receptor for parasite invasion that could provide a target for malaria therapeutics. — SMH

Science, this issue p. 711

Measles vaccination

PHOTOS: (LEFT TO RIGHT) TEK IMAGE/SCIENCE SOURCE; J. C. CRONK *ET AL. IMMUNITY* **42**, 4 (21 APRIL 2015) © 2015 ELSEVIER INC.

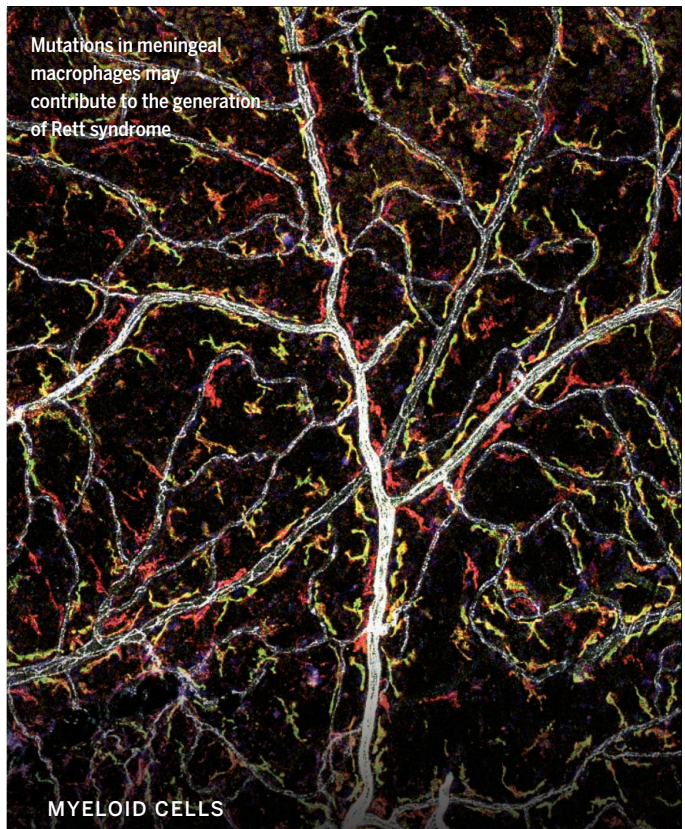

Mutations in meningeal macrophages may contribute to the generation of Rett syndrome

MYELOID CELLS

A role for macrophages in Rett syndrome

Scientists previously implicated microglia, a macrophage subset in the brain, in the pathogenesis of the neurodegenerative disease Rett syndrome. To better understand how microglia and other types of macrophages might contribute to the development of the disease, Cronk *et al*. examined MECP2-deficient mice. Multiple types of macrophages express MECP2 in normal mice, and several of these populations, including microglia, are lost in MECP2-deficient mice. MECP2 regulated a pro-inflammatory gene expression signature in macrophages. When the authors selectively reexpressed MECP2 in macrophages, they were able to extend the lives of MECP2-deficient mice, which suggests that macrophages probably contribute to disease pathogenesis. — KLM

Immunity **42**, 679 (2015).

PROTEIN BINDING

Methyl-C binding may explain Rett late onset

Girls with Rett syndrome develop normally for the first 1 or 2 years of life before suffering from progressive neurological problems, perhaps due to mutations in methyl-CpG–binding protein 2 (MeCP2). Chen *et al.* analyzed the binding of MeCP2 to genomic DNA in the mouse brain and found that before birth, MeCP2 binds predominantly to methylated CG sequences. After birth, there is an increase in the genome of methylated C in a non-CG context (mCH). MeCP2 binds to many of these mCH sites, which are enriched in genes with neuronal functions. MeCP2

ECOLOGY

Thirty new fly species in Los Angeles

Urban environments are not usually considered to be rich in biodiversity; surveys of urban biodiversity often report limited and declining numbers of species. Hartop *et al.* show that they can nevertheless yield surprises, at least when it comes to insect diversity. Studying thousands of samples from private backyards in Los Angeles, CA, the authors have discovered 30 previously unknown species of *Megaselia* flies. Possible reasons for this unexpected diversity may be the wide range of geography in the Los Angeles area and the introduction of invasive species via its large container ports. It remains unclear, however, whether this diversity represents native or invasive species. — JFU

Zootaxa 10.11646/zootaxa.3941.4.1 (2015).

Six of 30 new fly species discovered in Los Angeles

binding modulates the transcription of these genes, some of which are implicated in Rett syndrome, potentially explaining the late onset of the disease. — GR

Proc. Natl. Acad. Sci. U.S.A. doi/10.1073/pnas.1505909112 (2015).

NEUROSCIENCE

Sleeping while awake

Sleep deprivation affects our behavior and performance. Bernardi *et al.* demonstrate the connection between task-specific performance decrease and local sleep in relevant parts of the human brain. During 24 hours of wakefulness, individuals participated in driving simulations and executive function exercises. Their task-related abilities, such as visuomotor control and response inhibition, were tested alongside electroencephalography (EEG) recordings and functional magnetic resonance imaging (fMRI). Local EEG theta waves, normally observed during sleep, coincided with times of slower movements, visual inaccuracies, and decreased impulse control. The fMRI scans exposed cognitive fatigue in the form of regional neuronal disconnections in the task-relevant brain areas in addition to the general deficiencies. — MSM

J. Neurosci. **35**, 4487 (2015)

PHYSICS

Tilting the field to expose a fraction

In extremely clean, flat, and cold conductors, turning on an external magnetic field can produce the so-called quantum Hall effect (QHE), with the voltage across the sample exhibiting plateaus. The plateaus reflect the discrete energy levels of electrons in a magnetic field and can sometimes appear when only part of the level is filled: the fractional QHE. The most exotic of these states have filling factors with even denominators and may be useful in topological quantum computing. Falson *et al.* observed even-denominator states with filling factors 3/2 and 7/2 at the interface of MgZnO and ZnO. Interestingly, one of the states was only observable when the researchers tilted the magnetic field from the normal to the sample. — JS

Nat. Phys. **11**, 347 (2015).

MEDICINAL CHEMISTRY

Proteins take steps to bind larger ligands

In medicinal chemistry, optimizing the binding of a small molecule to a protein target often involves incremental changes to the small molecule. The design process may involve simulations of how a series of molecules binds to the target, but there is little experimental data to inform this analysis. Merski *et al.* determined the structures of eight benzene compounds, each differing by a single methyl group, binding to the model protein T4 lysozyme. Instead of gradually changing structure, T4 lysozyme transitions between three conformations with different-sized ligand-binding sites. A search of the protein data bank revealed other examples of discrete changes in response to ligand size. Modeling such discrete conformations may be important in drug design. — VV

Proc. Natl. Acad. Sci. U.S.A. 10.1073/pnas.1500806112 (2015).

FLOW CHEMISTRY

Round and round with a precious catalyst

When manufacturing pharmaceuticals, it is crucial to make just one of two possible mirror-image structures. Soluble precious metal catalysts can facilitate that objective, but they're often hard to collect and reuse after the reaction is over. O'Neal *et al.* present a laboratory-scale flow and filtration protocol to keep a ruthenium hydrogenation catalyst in continuous use for 24 hours. A membrane incorporated into the flow apparatus retains the catalyst in the reaction loop while releasing the product, all the while withstanding hydrogen pressure and a strongly basic co-catalyst. Less than 200 parts per billion of ruthenium escapes into the product stream. — JSY

ACS Catal. **5**, 2615 (2015).

PHOTO: KELSEY BAILEY

REVIEW SUMMARY

SOIL SCIENCE

Soil and human security in the 21st century

Ronald Amundson,* Asmeret Asefaw Berhe, Jan W. Hopmans, Carolyn Olson, A. Ester Sztein, Donald L. Sparks

BACKGROUND: Earth's soil has formed by processes that have maintained a persistent and expansive global soil mantle, one that in turn provided the stage for the evolution of the vast diversity of life on land. The underlying stability of soil systems is controlled by their inherent balance between inputs and losses of nutrients and carbon. Human exploitation of these soil resources, beginning a few thousand years ago, allowed agriculture to become an enormous success. The vastness of the planet and its soil resources allowed agriculture to expand, with growing populations, or to move, when soil resources were depleted. However, the practice of farming greatly accelerated rates of erosion relative to soil production, and soil has been and continues to be lost at rates that are orders of magnitude greater than mechanisms that replenish soil. Additionally, agricultural practices greatly altered natural soil carbon balances and feedbacks. Cultivation thus began an ongoing slow ignition of Earth's largest surficial reservoir of carbon—one that, when combined with the anthropogenic warming of many biomes, is capable of driving large positive feedbacks that will further increase the accumulation of atmospheric greenhouse gases and exacerbate associated climate change.

ADVANCES: The study of soil is now the domain of diverse schools of physical and biological science. Rapid advances in empirical and theoretical understanding of soil processes are occurring. These advances have brought an international, and global, perspective to the study of soil processes and focused the implications of soil stewardship for societal well-being. Major advances in the past decade include our first quantitative understanding of the natural rates of soil production, derived from isotopic methods developed by collaboration of geochemists and geomorphologists. Proliferation of research by soil and ecological scientists in the northern latitudes continues to illuminate and improve estimates of the magnitude of soil carbon storage in these regions and its sensitivity and response to warming. The role of soil processes in global carbon and climate models is entering a period of growing attention and increasing maturity. These activities in turn reveal the severity of soil-related issues at stake for the remainder of this century—the need to rapidly regain a balance to the physical and biological processes that drive and maintain soil properties, and the societal implications that will result if we do not.

OUTLOOK: Both great challenges and opportunities exist in regards to maintaining soil's role in food, climate, and human security. Erosion continues to exceed natural rates of soil renewal even in highly developed countries. The recent focus by economists and natural scientists on potential future shortages of phosphorus fertilizer offers opportunities for novel partnerships to develop efficient methods of nutrient recycling and redistribution systems in urban settings. Possibly the most challenging issues will be to better understand the magnitude of global soil carbon feedbacks to climate change and to mitigating climate change in a timely fashion. The net results of human impacts on soil resources this century will be global in scale and will have direct impacts on human security for centuries to come. ■

ON OUR WEB SITE

Read the full article at http://dx.doi.org/10.1126/science.1261071

The list of author affiliations is available in the full article online.
*Corresponding author. E-mail: earthy@berkeley.edu
Cite this article as R. Amundson *et al.*, *Science* **348**, 1261071 (2015). DOI:10.1126/science.1261071

CREDIT: BRENT STIRTON/GETTY IMAGES

Large-scale erosion forming a gully system in the watershed of Lake Bogoria, Kenya. Accelerated soil erosion here is due to both overgrazing and improper agricultural management, which are partially due to political-social impacts of past colonization and inadequate resources and infrastructure. The erosion additionally affects the long-term future of Lake Bogoria because of rapid sedimentation. This example illustrates the disruption of the natural balance of soil production and erosion over geological time scales by human activity and the rapidity of the consequences of this imbalance.

REVIEW

SOIL SCIENCE

Soil and human security in the 21st century

Ronald Amundson,[1]* Asmeret Asefaw Berhe,[2] Jan W. Hopmans,[3] Carolyn Olson,[4] A. Ester Sztein,[5] Donald L. Sparks[6]

Human security has and will continue to rely on Earth's diverse soil resources. Yet we have now exploited the planet's most productive soils. Soil erosion greatly exceeds rates of production in many agricultural regions. Nitrogen produced by fossil fuel and geological reservoirs of other fertilizers are headed toward possible scarcity, increased cost, and/or geopolitical conflict. Climate change is accelerating the microbial release of greenhouse gases from soil organic matter and will likely play a large role in our near-term climate future. In this Review, we highlight challenges facing Earth's soil resources in the coming century. The direct and indirect response of soils to past and future human activities will play a major role in human prosperity and survival.

Soil is the living epidermis of the planet (*1*). Globally, soil is the medium through which a number of atmospheric gases are biologically cycled and through which waters are filtered and stored as they pass through the global hydrological cycle (*2*). Soil is a large and dynamic reservoir of carbon and the physical substrate for most of our food production. Profound changes are on the horizon for these interconnected functions—particularly sparked by changes to climate and food production—that will likely reverberate through society this century. Ultimately, the way in which we directly and indirectly manage our planet's soil will be interwoven within our future success as a species.

Soil is commonly thought of as the ~1-m-thick layer of biogeochemically altered rock or sediment at Earth's surface that has acquired numerous qualities during its exposure to the atmosphere that greatly distinguish it from its geological sources (*3*). Soil-forming chemical reactions create micrometer-sized electrically negative clay minerals that impart soil with plant nutrient retention capabilities (*4*). The electrical charge characteristics of soil, combined with its small particle size and high surface area, allow it to temporarily store rain and snow melt for plant use and provide sufficient residence time for a multitude of chemical reactions to occur that may remove or reduce the toxicity of contaminants. The water stored in soil—termed green water (*5*)—serves as the source for 90% of the world's agricultural production and represents ~65% of global fresh water (*5*). Last, the intimate intermingling of life—plant, animal, and microbial—within the soil matrix drives redox reactions that control many elemental cycles (*6*) and creates a reservoir of organic C that greatly exceeds the C in the global atmosphere and biosphere (*7*). The microbial communities that mediate these redox reactions are now believed to represent much of Earth's total biodiversity (*8*), but the nature, function, and economic potential of this soil biosphere is only beginning to be probed (*6*).

Soil, due to global variations in climate, geology, and biota (*3*), has tremendous spatial diversity. More than 20,000 soil types (or soil series) have been identified and mapped in the United States alone (*9*), and the number identified increases as land area investigated increases. If the soil series–to–land area relationship (*10*) is extrapolated to global ice-free land area, the results suggest that there are more than 300,000 series on the planet. The response of these soils to perturbations can be extremely varied because of their diverse chemical, physical, and biological characteristics, suggesting the importance, as a simple precautionary principle, of maintaining segments of this diversity for the stability and resilience of global biogeochemical systems in the face of anthropogenic disturbances.

Human Imprint on Soil

Humans altered the ecosystems they encountered as they began their spread across the globe. However, the most momentous development in human landscape change occurred with the invention and adoption of agriculture (*11*). Most agricultural practices involve the removal of the natural flora, the simplification of biodiversity to favor monocultures, and the physical disruption of the soil. Since the Industrial Revolution, expanding populations have relied on the exploitation of more and more soil for a corresponding growth in food production. Today, ~12% of ice-free land is in cropland, and 38% is used for combined cropping and grazing (*12*), an area roughly equivalent to the land area covered by ice and scoured or otherwise disturbed during the last glacial maximum (Fig. 1A). In addition to the similarity in area, the agricultural impact on soil processes rivals or exceeds the effect of those ice sheets in both rapidity and magnitude.

Undisturbed soils have the characteristic, as result of a number of feedback mechanisms, of being able to retain many of their features indefinitely over time—their thickness, C content, and nutrients, for example—a condition that is equatable to sustainability (Fig. 2). Cultivated soils are highly modified forms of their wild predecessors and may thus be viewed as domesticated soils (*9*). One key characteristic is that domesticated soils seldom are able to maintain the qualities of their original conditions, and these changes greatly affect their productivity and their impact on surrounding geochemical cycles. The efforts to improve the management and conservation of these domesticated soils, and the preservation of portions of their remaining wild ancestral stock, will be among the most important challenges this century (*9*, *13*). Analyses of the combined agricultural and urban impact on soil series in the United States, for example, revealed large areas in the agricultural heartland where more than 50% of the soil series had been domesticated. Soil diversity, like biodiversity (*14*), provides an array of human-valued goods and services. Among the most apparent issues is the ability of soil to provide sustained agricultural production.

The domesticated soil landscape is one of Earth's most valuable commodities. For example, nearly $3816 billion (U.S. dollars) in agricultural products were produced globally in 2012 (*15*). However, agriculture is competing with increasing urban and suburban soil demands. The conversion of soil to urban land is largely irreversible on human time scales. There is uncertainty both in the present and the future distribution of urban land on Earth (Fig. 1B). A recent meta-analysis suggests that between 1970 and 2000, an area greater than the size of Denmark was urbanized, and that in the next 20 years, 1.5 million km^2 of land (the size of Mongolia) will be urbanized (*16*). The conversion of farmland to urban areas must be weighed against the fact that our most productive soils have already been exploited and that demand for food production will continue to increase.

Soil and Climate Security

A relatively stable climate has been the stage on which the great human inventions of agriculture and industrialization have evolved, and direct or indirect human impacts on soil C cycling processes will have much to do with atmospheric greenhouse gas concentrations and the associated climate implications by the end of this century.

[1]Department of Environmental Science, Policy, and Management, University of California, Berkeley, CA 94720, USA. [2]Life and Environmental Sciences Unit, University of California, Merced, CA 95343, USA. [3]Land, Air, and Water Resources, One Shields Avenue, Davis, CA 95616, USA. [4]Climate Change Program Office, Office of the Chief Economist, U.S. Department of Agriculture (USDA), 14th and Independence SW, Washington, DC 20013, USA. [5]Board on International Scientific Organizations, National Academy of Sciences, 500 Fifth Street NW, Washington, DC 20001, USA. [6]Plant and Soil Science, Chemistry and Biochemistry, Civil and Environmental Engineering, and Marine Science and Policy, University of Delaware, Newark, DE 19716, USA.
*Corresponding author. E-mail: earthy@berkeley.edu

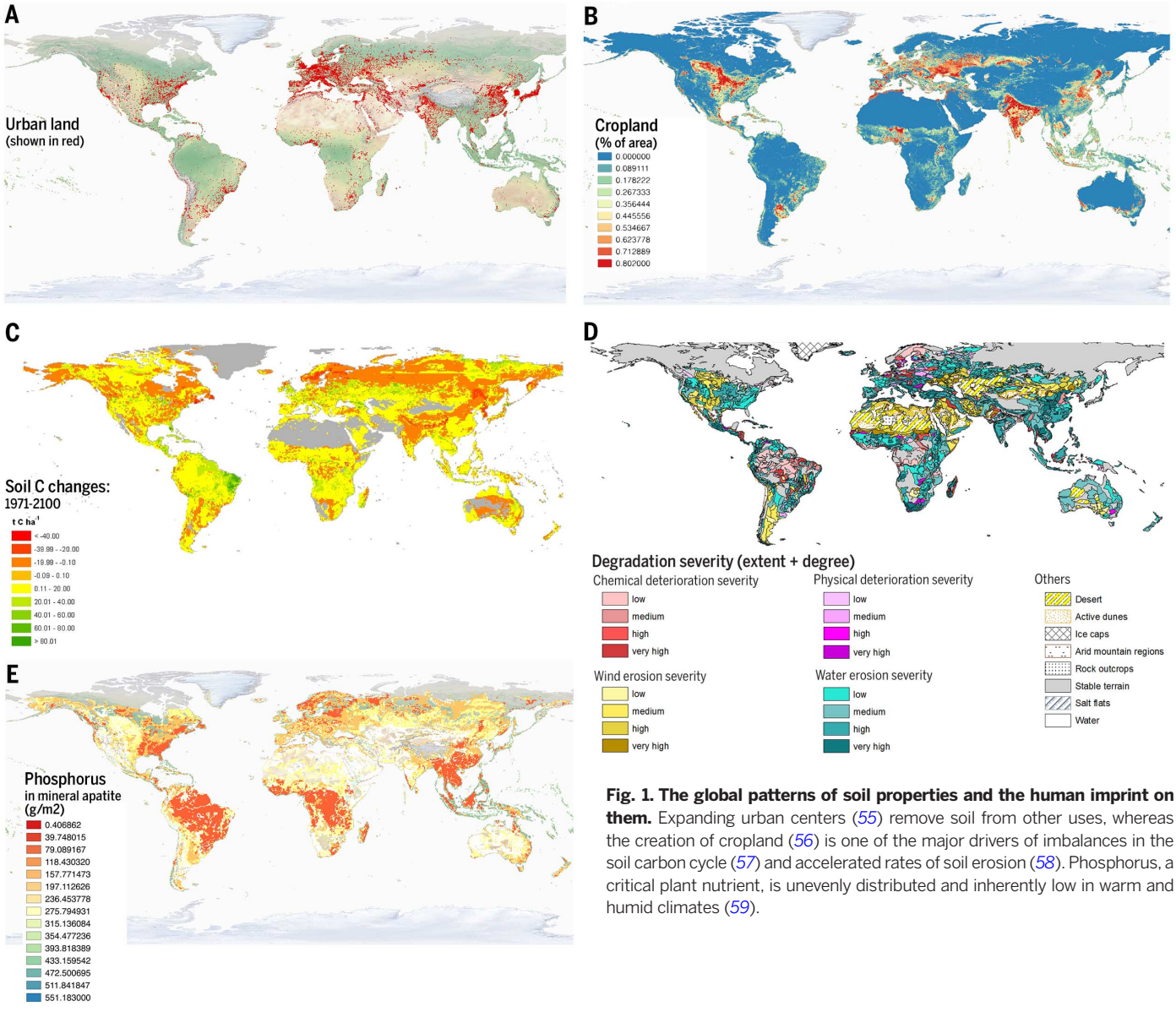

Fig. 1. The global patterns of soil properties and the human imprint on them. Expanding urban centers (*55*) remove soil from other uses, whereas the creation of cropland (*56*) is one of the major drivers of imbalances in the soil carbon cycle (*57*) and accelerated rates of soil erosion (*58*). Phosphorus, a critical plant nutrient, is unevenly distributed and inherently low in warm and humid climates (*59*).

Organic C stored in soil is the balance between plant inputs and microbially mediated metabolic losses as CO_2 (Fig. 2). In unperturbed conditions, soils achieve steady-state C pools on time scales of centuries to a few millennia. The total store of soil organic carbon is still uncertain, but recent estimates suggest pools on the order of 2300 gigatons (Gt) in the upper 3 m (*7*). Soil cultivation and clearing has caused a major fraction of total anthropogenic greenhouse gas emissions since the 19th century (*17*). Cultivation is a major disruption to the natural C balance in soil, one that alters the physical and biological structure of soil, effectively igniting, through microbially mediated processes, a vast store of labile C that has accumulated over millennia (*18*). During the first few decades that soil is cultivated, up to 50% of the carbon pool is oxidized to CO_2; eventually, a quasi-steady-state soil C pool is achieved (*19*). Based on the global agricultural land area, cultivation has likely released between 50 and 70 Gt of C to the atmosphere over the course of human history (*20*), and the combined cultivation and biomass burning contributions to atmospheric CO_2 exceeded that of fossil fuel emissions well into the 20th century (*17*). However, the agricultural imprint on atmospheric greenhouse gas concentrations appeared much earlier in the Holocene (*21*). Early spikes in atmospheric CO_2 and CH_4 corresponded to agricultural expansion in Mesopotamia and in China (*22*). Much of the historical C loss was from the soils of forests and grasslands of the northern latitudes. However, today the locus of land alteration has shifted to the equatorial latitudes, and up to 10% of global anthropogenic CO_2 emissions are from a combination of biomass burning and soil cultivation in the humid and subhumid tropics (*23*).

Under changed management or through land abandonment, global agricultural soils have the capacity to reapproach their original C storage and regain up to a half a decade of present fossil fuel emissions (over a multidecade period). Better stewardship of domesticated soils that leads to higher organic matter contents is a valuable practice from an ecological perspective and from an agronomic point of view (*24*). There is now a large body of research on the rates of C sequestration under differing management practices. However, there are limits to these practices as a means of mitigating continued fossil fuel emissions. First, a serious concern with management-based soil C sequestration strategies is that they are dependent on restricted management options in a highly decentralized and economically driven agricultural sector (*25*). A change in land ownership, or a change in factors driving agricultural practices, can rapidly release much of regained C. Second, the effectiveness of soil C sequestration is time dependent. For example, if all potential soil sequestration strategies were established, they would initially serve as a sink of about 1.3 Gt of C $year^{-1}$ (Table 1) (*26*), but this sink term would be expected to decline nonlinearly to low

sequestration rates over a period of several decades as a new soil C steady state is reached (27). Equally as important is the difficulty of actually achieving this maximum potential, which involves multiple governments and millions of individual land managers. Last, soil management effects on the global C balance are inherently small relative to the climate-driven changes to soil C storage that will occur in this century.

Soil C storage is well documented to decline with increasing temperature and decreasing soil moisture, and soil C storage patterns mirror global climate zones (28, 29), with secondary impacts by bedrock, topography, and soil age (20). Soil C pools are the balance between plant inputs and microbial decomposition (Fig. 3), and the responses of these processes to anthropogenic climate change are considered to be large, (in the case of inputs) poorly constrained (30), and complicated by temperature and moisture interactions. Anthropogenic increases in atmospheric CO_2 may drive increased net primary production (NPP) as long as nutrient and water limitations do not occur (31), which ultimately may have a negative feedback on atmospheric CO_2 through increased inputs to soil C (Fig. 3). On the other hand, increasing air temperatures warm soil, melt permafrost, and stimulate biological metabolism of soil carbon pools, driving what appears to be a large positive feedback process (32) (Figs. 1C and 3). Based on current earth system modeling, additions of soil C by increased NPP (relative to an 1850 BCE reference date) are projected to be between 160 and 1230 Gt by 2100, whereas C losses by increased decomposition are projected to be between 104 and 629 Gt (31). Overall, models suggest net soil C changes from a loss of 72 Gt to gains of 253 Gt by 2100 (31). However, such exercises include great uncertainties in both projected gains (by CO_2-enhanced photosynthesis) and losses (by soil warming) and in assumptions about long-term ecosystem response to ever-increasing CO_2 concentrations. One important uncertainty is the response of northern latitude soils to warming, which could result in net soil C losses between 50 to 150 Gt (32, 33). Last, the current generation of earth system models has difficulty in matching present-day soil carbon storage patterns (34), and tuning the models is challenged by empirical uncertainties in the global soil C pool of more than 770 Gt (34), an uncertainty similar in size to the present atmospheric C pool.

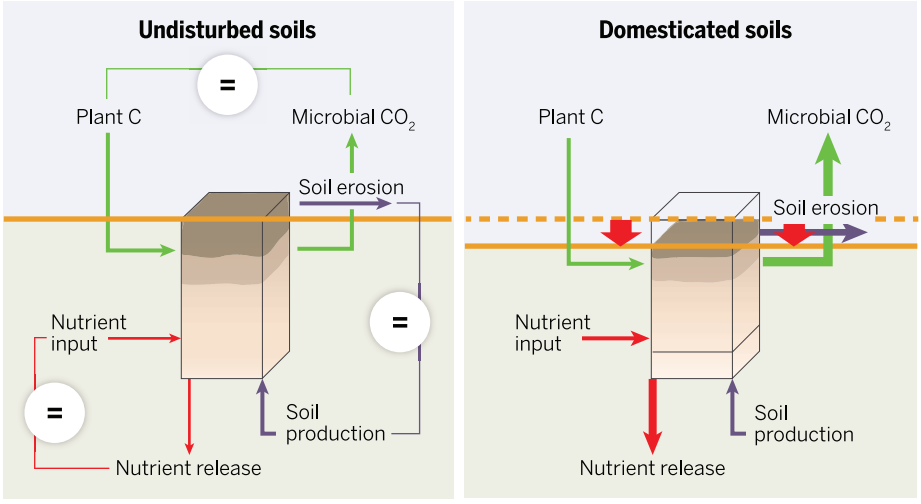

Fig. 2. Changes in the balance of important soil processes caused by human disturbance. Many soil characteristics are the balance or the result of a number of processes that respond to changes in environmental variables (3). However, properties such as hillslope soil thickness, organic carbon storage, N content, and other features attain steady state in intervals of a few centuries to millennia and appear capable of regaining stability. Human intervention in soil processes many times exceeds natural perturbations and thus exceeds the resiliency of soil to recover to its original condition. Viewed broadly, steady state is a quantitative measure of soil sustainability.

Table 1. Published estimates of soil C sources and sinks for the 21st century.

Management Type	Maximum Flux (Gt of C $year^{-1}$)	Reference	Cumulative Flux (Gt)
	Carbon Sinks		
Increased net primary production		(31)	160 to 1230
Erosion	0.40	(37)	40
	Management		
Cropland management	0.36	(26, 27)	
Grazing land management	0.37	(26, 27)	
Restore degraded land	0.18	(26, 27)	
Restore organic soils	0.36	(26, 27)	
Total for management	1.26		16.4*
	Carbon Sources		
Land clearing†			250
Soil warming			
Boreal regions		(32)	50–270
Globe		(34)	104–629
Total			
Net balance			–188 to +137

*Based on maximum new cropland by 2050 (10 billion ha) (68) and assumed loss of 25% of an average C content of 10 kg m^{-2} (29). †Calculated assuming exponential decline to an ultimate landscape saturation after 50 years.

Still debated is the impact of soil erosion on the global C cycle. When agricultural soil is lost by water or wind erosion, the surficial, and most C-rich, material is preferentially removed, which accelerates the decline in the soil C pool. Rates of soil C replacement by crops and plants are rapid enough in certain situations to maintain soil C levels at a steady state under the condition of constant erosion—e.g., creating an ongoing sink (35). This sink represents a net reduction in atmospheric CO_2 only if the eroded C is not re-oxidized. Because some depositional environments are conducive to partial preservation of buried C (lakes, reservoirs, basins, floodplains), the net effect of accelerated agricultural erosion was first suggested to be a global C sink of 0.6 to 1.5 Gt $year^{-1}$, a rate similar to the total global land sink (35). If the eroded C is largely oxidized, however, it may result in no net sink (or possibly even a net source) (36). The most recent estimates suggest that agricultural erosion of soil C may be 0.40 ±0.20 Gt of C $year^{-1}$ (37). If we benefit from an unintended C sink due to soil erosion, any benefits must be clearly balanced against the related losses of nutrients and reduction of environmental quality that require fossil fuel energy to remediate (38).

The global soil C cycle has been greatly perturbed by human activity, both directly through farming and indirectly through anthropogenic climate change. All projected soil C gains and losses this century are highly uncertain because of economic, population, and political influences (which will largely affect carbon sequestration efforts) and uncertainties in the magnitude of the soil response to warming (because of the complexity of the soil C pool structure) (Fig. 3). Human changes to the global atmosphere and climate are likely to simultaneously drive both very large gains and losses of soil C—fluxes that are equivalent to decades of emissions at present

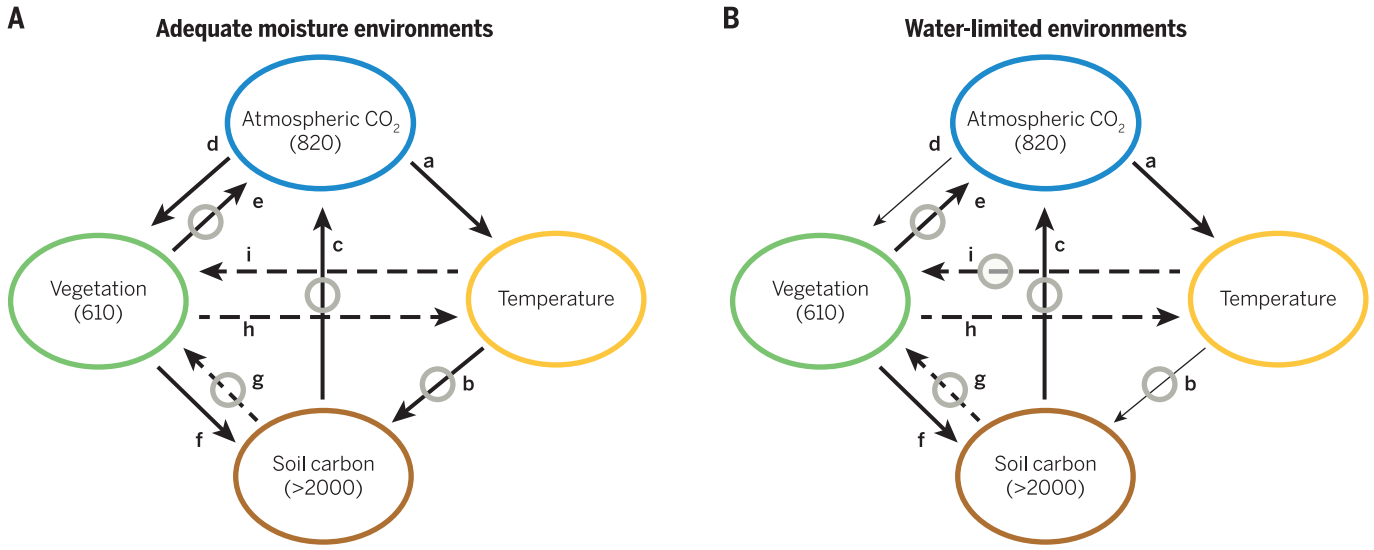

Fig. 3. A cause-effect diagram of the major soil-atmospheric CO_2 feedback processes. The values in parentheses, in the circles, are the approximate pool sizes (Gt) of C. A solid arrow represents a direct response (e.g., as CO_2 increases, temperature increases); an arrow with a circle indicates an inverse response (e.g., as temperature increases, soil carbon storage decreases). Dashed lines are for processes that are less well understood. (**A**) Environments with adequate moisture. (**B**) Water-limited environments. In (A), the a-b-c loop is a positive feedback process (even number of inverse relationship arrows), one especially important in regions of melting permafrost. The d-f-c loop is a negative feedback, one with less certain feedbacks between vegetation and soil (f-g loop) and temperature (h-i). The strength of the a-b-c- versus d-f-c loops on soil carbon pools will likely determine whether soil carbon losses in northern latitudes serve as a major source of CO_2 and CH_4 this century, a balance that also hinges on the ability of the soils to supply nutrients to plants (arrow g) in order to respond to the increases in CO_2 (arrow d). In (B), regions with limited moisture, the strengths of vegetation response to CO_2 (d) and soil carbon response to temperature (b) may be weakened (thinner arrow). In addition, the vegetation response to increasing temperature may become negative. These figures reveal the importance of soil carbon to the global CO_2 balance this century, as well as the uncertainties in the strength and direction of important processes. Arrow references are as follows: a, (*60*); b, (*32*, *33*); c, CO_2 loss by respiration is the overwhelming pathway of C removal from soils; d, water efficiency response in (*61*); f, soil C is the balance between plant inputs and decomposition losses; g, not well constrained, but see discussion in (*62*); h, (*63*); i, e.g., (*64*).

rates of fossil fuel consumption. The presently unknown balance, and most importantly its sign, between the large fluxes represent considerable uncertainty for climate security (Table 1).

Soil and Food Security

The late 20th and early 21st centuries have been, for industrialized countries, an unprecedented era of increasingly low food prices (*39*). There are numerous factors that may reverse this trend—such as increased global demand; climate change (*40*); and competition for soil by nonagricultural uses, such as biofuels or urbanization. Abundant energy has been the key driving force behind our ability to maintain food production apace with an expanding population that is estimated to reach 11 billion by 2100 (*41*). Low-cost energy, which led to advanced agricultural machinery replacing human labor, is causing migration to urban centers. Energy is used to replace the soil nutrients removed or lost by agricultural perturbations of soil. Energy transforms atmospheric N_2 to the bioavailable NH_4 fertilizer through the energy-intensive Haber-Bosch process—constituting the first and most important green revolution (*42*) (Fig. 4A), one that allows us to feed the increasing global population (Fig. 4A). Before the industrial fixation of N, any increase in food production for a given country was largely due to increased soil used for production (*43*), and only after the advent of N fertilizer (Fig. 4A) did yields per area of major crops begin their upward trajectory (*43*).

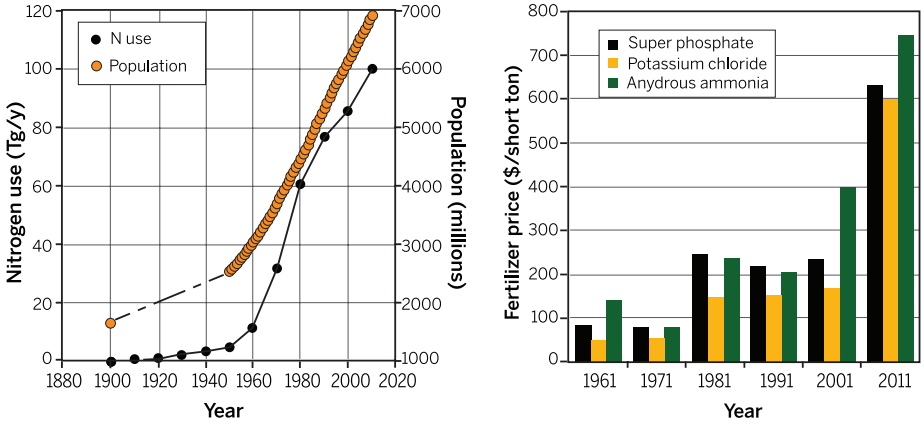

Fig. 4. The post–World War II rise in fertilizer production and cost coincides with the spike in global human populations. The growth in world population in the late 20th century (*65*) mirrors the increasing use of industrially derived N fertilizer. Before N fertilization, for major U.S. crops (*66*), wheat and other grain yields per acre increased only following World War II, coincident with the rise in the use of N fertilizer produced by the Haber-Bosch process. Prices have sharply risen (*67*) because global demand is straining the supplies.

Last, energy is essential to mine and transport essential plant nutrients, such as P and K, that can only be accessed from limited geological reservoirs.

Agricultural soil erosion is one of the most destructive human perturbations to soil sustainability. Given little opportunity or desirability for further agricultural expansion, stewardship of our existing domesticated soil is essential for sustained human prosperity. Yet despite the importance of soil conservation, the implementation of practices to minimize soil erosion has not followed apace with the severity of the problem. The most pervasive mechanism of soil erosion is via water. Before European contact and the removal of native vegetation by plowing and cultivation, the geological mechanism of soil erosion on most

uplands was by slow, biologically driven creep (*44*). The removal of plant cover allows the mechanism of erosion to change to raindrop dislodgment of soil particles and their subsequent removal by overland flow, which is a far more rapid erosional process. For example, recent analyses of U.S. erosion rates before European contact place the average rate at about 21 m My^{-1} (My, million years) (*45*). Today, erosion rates in the central United States can exceed 2000 m My^{-1} (*45*), whereas the rates of soil erosion in portions of the loess plateau of China approach 10,000 m My^{-1} (*46*) (Fig. 1D). This eroded sediment is ultimately replaced by the conversion of the underlying sediment or rock into new soils with the addition of organic matter and nutrients through biological mechanisms. Until the past decade, the pace of this replacement process was poorly known, and the acceptable rates of soil erosion on agricultural lands were placed at 400 m My^{-1} or more (*47*). Numerous studies of natural rates of soil production now suggest rates between 50 to 200 m My^{-1} for many environments, indicating that the pace of erosion in numerous agricultural areas is, or until recently has been, unsustainable (*47*). Not only does the loss of soil remove nutrients from the site of agricultural production (*38*), but the sediment generated adversely affects local drainages, water bodies, and regional aquatic ecology. Last, the maintenance (or even the improvement) of agricultural production in the face of accelerated rates of soil erosion is energy intensive. Although microbial symbiosis with plants can fix atmospheric N to bioavailable forms and can substitute for N fixed by the Haber-Bosch process, there is no biological or atmospheric source for rock-derived nutrients, such as P, K, and Ca.

Although natural processes of soil production and formation replace or release nutrients, the paces of these processes are slow relative to our anthropogenic use rate (Fig. 2). The transport of crops from the site of production to other locations remove plant-essential nutrients from the soil, potentially causing deficiencies that limit potential production levels (*48*). This further drives a dependence on the mining and distribution of macronutrients from geological sources, which can create economic inequalities or geopolitical conflicts between nations (*49*) (Fig. 1E). The growing demand for P has recently caused an increase in the cost of rock phosphate from about $80 per U.S. ton in 1961 to up to $450 per ton in 2008. Prices since then have fluctuated but are now at about $700 per ton (*50*) (Fig. 4). In addition to cost is the related issue of access. Morocco is estimated to have the world's largest geological P reserves, much of it in disputed territory (*49*). The United States, on the other hand, has only about 2% of global P resources (*51*). At current rates of retrieval, the most productive mine in the United States will be depleted in 20 years (*49*), which will force it to become increasingly reliant on imports to sustain its agricultural and industrial sectors.

Because most other P-reliant countries lack the geological resources to indefinitely sustain current use, the only means to confront the decline in reserves (other than conversion from domestic to imported P) is to develop a more coherent and integrated program of P (and other nutrient) recycling. The loss of nutrients in our human and animal waste streams is environmentally damaging and economically problematic. Regaining control of these resources, now largely considered waste, would go far toward substantially lowering the demand for imported nutrients and other resources (*52*). In addition to P, other soil nutrients appear to be entering periods of limitation or high demand (Fig. 1F). For example, K (potash) prices were ~$875 per metric ton in 2009 and are expected to reach $1500 by 2020.

The 21st Century Challenge

Humans have domesticated our soil resources and the planet (*12*, *53*). This domestication has in turn perturbed a number of soil cycles such that they are no longer in balance, and the imbalance is changing soil in ways that will affect future generations and their climate (Fig. 2). Soil management must be geared toward passing a habitable, albeit highly altered, landscape to the generations that follow—one where our exploitation of, and impacts on, soil resources is adjusted to the pace of our planet's renewal. These strategies should focus on regaining a balance in (i) organic C inputs and losses, (ii) soil erosion and production, and (iii) release and loss of nutrients. Soil sustainability—based on quantitative principles and measurements of soil erosion and production, soil nutrient loss and release, and soil carbon loss and return—must be the ultimate goal for managing the global soil resource and should serve as the driving principle for soil research that will support this management.

These are challenging goals that will be difficult to achieve. The solutions will require an effort commensurate with the magnitude of the problems. First, effective solutions to soil sustainability, much like the approaches required to contend with climate change (*54*), must involve highly multidisciplinary research in novel intellectual settings or institutions. Second, the ultimate success of any innovation requires a dialog and interface with policy makers and public institutions, the ultimate "deciders" in broad-scale social change. These linked efforts will depend on continued, and arguably much greater, investments in knowledge and innovative knowledge transfer and simply different ways of conceptualizing and approaching problems. From our vantage point, the future of Earth's soil resources is tenuously in our control or within our ability to sustain it into the future. Only those on Earth in 2100 will know how well we succeeded.

REFERENCES AND NOTES

1. "We might say that the earth has a spirit of growth; that its flesh is the soil." From (*69*).
2. A. Koch *et al.*, Soil security: Solving the global soil crisis. *Glob. Policy* **4**, 434–441 (2013). doi: 10.1111/1758-5899.12096
3. H. Jenny, *Factors of Soil Formation: A System of Quantitative Pedology* (McGraw-Hill, New York, 1941).
4. G. Sposito *et al.*, Surface geochemistry of the clay minerals. *Proc. Natl. Acad. Sci. U.S.A.* **96**, 3358–3364 (1999). doi: 10.1073/pnas.96.7.3358; pmid: 10097044
5. G. Sposito, Green water and global food security. *Vadose Zone J.* **12**, 0 (2013). doi: 10.2136/vzj2013.02.0041
6. R. D. Bardgett, W. H. van der Putten, Belowground biodiversity and ecosystem functioning. *Nature* **515**, 505–511 (2014). doi: 10.1038/nature13855; pmid: 25428498
7. E. G. Jobbágy, R. B. Jackson, The vertical distribution of soil organic carbon and its relation to climate and vegetation. *Ecol. Appl.* **10**, 423–436 (2000). doi: 10.1890/1051-0761(2000)010[0423:TVDOSO]2.0.CO;2
8. D. H. Wall, R. D. Bardgett, E. Kelly, Biodiversity in the dark. *Nat. Geosci.* **3**, 297–298 (2010). doi: 10.1038/ngeo860
9. R. Amundson, Y. Guo, P. Gong, Soil diversity and landuse in the United States. *Ecosystems* **6**, 470–482 (2003). doi: 10.1007/s10021-002-0160-2
10. Y. Guo, P. Gong, R. Amundson, Pedodiversity in the United States. *Geoderma* **117**, 99–115 (2003). doi: 10.1016/S0016-7061(03)00137-X
11. J. Diamond, Evolution, consequences and future of plant and animal domestication. *Nature* **418**, 700–707 (2002). doi: 10.1038/nature01019; pmid: 12167878
12. J. A. Foley *et al.*, Solutions for a cultivated planet. *Nature* **478**, 337–342 (2011). doi: 10.1038/nature10452; pmid: 21993620
13. M. Tennesen, Rare earth. *Science* **346**, 692–695 (2014). doi: 10.1126/science.346.6210.692; pmid: 25378604
14. P. R. Ehrlich, E. Wilson, Biodiversity studies: Science and policy. *Science* **253**, 758–762 (1991). doi: 10.1126/science.253.5021.758; pmid: 17835492
15. FAOSTAT production, http://faostat.fao.org/site/613/DesktopDefault.aspx?PageID=613#ancor.
16. K. C. Seto, M. Fragkias, B. Güneralp, M. K. Reilly, A meta-analysis of global urban land expansion. *PLOS ONE* **6**, e23777 (2011). doi: 10.1371/journal.pone.0023777; pmid: 21876770
17. E. T. Sundquist, The global carbon dioxide budget. *Science* **259**, 934–941 (1993). doi: 10.1126/science.259.5097.934
18. L. B. Guo, R. M. Gifford, Soil carbon stocks and land use change: A meta analysis. *Glob. Change Biol.* **8**, 345–360 (2002). doi: 10.1046/j.1354-1013.2002.00486.x
19. U. Stockmann *et al.*, The knowns, known unknowns and unknowns of sequestration of soil organic carbon. *Agric. Ecosyst. Environ.* **164**, 80–99 (2013). doi: 10.1016/j.agee.2012.10.001
20. R. Amundson, The carbon budget in soils. *Annu. Rev. Earth Planet. Sci.* **29**, 535–562 (2001). doi: 10.1146/annurev.earth.29.1.535
21. W. F. Ruddiman, The Anthropocene. *Annu. Rev. Earth Planet. Sci.* **41**, 45–68 (2013). doi: 10.1146/annurev-earth-050212-123944
22. W. F. Ruddiman, The early anthropogenic hypothesis: Challenges and responses. *Rev. Geophys.* **45**, RG4001 (2007).
23. P. Cias *et al.*, in *Climate Change 2013: The Physical Basis. Contributions of Working Group 1 to the Fifth Assessment Report of the Intergovernmental Panel on Climate Change* (Cambridge Univ. Press, Cambridge, 2013), pp. 465–570.
24. R. B. Jackson, W. H. Schlesinger, Curbing the U.S. carbon deficit. *Proc. Natl. Acad. Sci. U.S.A.* **101**, 15827–15829 (2004). doi: 10.1073/pnas.0403631101; pmid: 15514026
25. P. Smith, An overview of the permanence of soil organic carbon stocks: Influence of direct human-induced, indirect and natural effects. *Eur. J. Soil Sci.* **56**, 673–680 (2005). doi: 10.1111/j.1365-2389.2005.00708.x
26. P. Smith *et al.*, "Agriculture," in *Climate Change 2007: Mitigation. Contribution of Working Group III to the Fourth Assessment Report on the International Panel of Climate Change* (Cambridge Univ. Press, Cambridge, 2007).
27. P. Smith *et al.*, Greenhouse gas mitigation in agriculture. *Philos. Trans. R. Soc. London Ser. B* **363**, 789–813 (2008). doi: 10.1098/rstb.2007.2184; pmid: 17827109
28. Center for Sustainability and the Global Environment (SAGE), Nelson Institute for Environmental Studies at the University of Wisconsin - Madison, *The Atlas of the Biosphere*, www.sage.wisc.edu/atlas/maps.php?datasetid=21&includerelatedlinks=1&dataset=21.
29. W. M. Post, W. R. Emanuel, P. J. Zinke, A. G. Stangenberger, Soil carbon pools and world life zones. *Nature* **298**, 156–159 (1982). doi: 10.1038/298156a0
30. P. Friedlingstein *et al.*, Climate-carbon cycle feedback analysis: Results from the C4MIP model intercomparison. *J. Clim.* **19**, 3337–3353 (2006). doi: 10.1175/JCLI3800.1
31. K. E. O. Todd-Brown *et al.*, Changes in soil organic carbon storage predicted by Earth system models during the 21st century. *Biogeosciences* **11**, 2341–2356 (2014). doi: 10.5194/bg-11-2341-2014
32. E. J. Burke, I. P. Hartley, C. D. Jones, Uncertainties in global temperature change caused by carbon release from

permafrost thawing. *The Cryosphere* **6**, 1063–1076 (2012).
33. E. A. G. Schuur *et al*., Expert assessment of vulnerability of permafrost carbon to climate change. *Clim. Change* **119**, 359–374 (2013). doi: 10.1007/s10584-013-0730-7
34. K. E. O. Todd-Brown *et al*., Causes of variation in soil carbon simulations from CMIP5 Earth system models and comparison with observations. *Biogeosciences* **10**, 1717–1736 (2013). doi: 10.5194/bg-10-1717-2013
35. R. F. Stallard, Terrestrial sedimentation and the carbon cycle: Coupling weathering and erosion to carbon burial. *Global Biogeochem. Cycles* **12**, 231–257 (1998). doi: 10.1029/98GB00741
36. R. Lal *et al*., Soil erosion: A carbon sink or source? *Science* **319**, 1040–1042 (2008). doi: 10.1126/science.319.5866.1040; pmid: 18292324
37. S. Doetterl, K. Van Oost, J. Six, Towards constraining the magnitude of global agricultural sediment and soil organic carbon fluxes. *Earth Surf. Process. Landf.* **37**, 642–655 (2012). doi: 10.1002/esp.3198
38. J. N. Quinton, G. Govers, K. Van Oost, R. Bardgett, The impact of agricultural erosion on biogeochemical cycling. *Nat. Geosci.* **3**, 311–314 (2010). doi: 10.1038/ngeo838
39. USDA Economic Research Service data for 2014, www.ers.usda.gov/data-products/food-expenditures.aspx#.U2vmj17INZF.
40. FAO, *FAO in the 21st Century: Ensuring Food Security in a Changing World* (Food and Agriculture Organization of the United Nations, Rome, 2011).
41. P. Gerland *et al*., World population stabilization unlikely this century. *Science* **346**, 234–237 (2014). doi: 10.1126/science.1257469; pmid: 25301627
42. V. Smil, Nitrogen cycle and world food production. *World Agriculture* **2**, 9–13 (2011).
43. USDA, Economic Research Service; www.ers.usda.gov/data-products/wheat-data.aspx.
44. M. J. Kirkby, Measurement and theory of soil creep. *J. Geol.* **75**, 359–378 (1967). doi: 10.1086/627267
45. B. H. Wilkinson, B. J. McElroy, The impact of humans on continental erosion and sedimentation. *Geol. Soc. Am. Bull.* **119**, 140–156 (2007). doi: 10.1130/B25899.1
46. W. Sun, Q. Shao, J. Liu, J. Zhai, Assessing the effects of land use and topography on soil erosion in the Loess Plateau in China. *Catena* **121**, 151–163 (2014). doi: 10.1016/j.catena.2014.05.009
47. D. R. Montgomery, Soil erosion and agricultural sustainability. *Proc. Natl. Acad. Sci. U.S.A.* **104**, 13268–13272 (2007). doi: 10.1073/pnas.0611508104; pmid: 17686990
48. D. L. Jones *et al*., Nutrient stripping: The global disparity between food security and soil nutrient stocks. *J. Appl. Ecol.* **50**, 851–862 (2013). doi: 10.1111/1365-2664.12089
49. D. Cordell, J.-O. Drangert, W. White, The story of phosphorus: Global food security and food for thought. *Glob. Environ. Change* **19**, 292–305 (2009).
50. USDA Economic Research Service, www.ers.usda.gov/data-products/fertilizeruse-and-price.aspx.
51. http://minerals.usgs.gov/minerals/pubs/commodity/
52. J. Elser, E. Bennett, Phosphorus cycle: A broken biogeochemical cycle. *Nature* **478**, 29–31 (2011). doi: 10.1038/478029a; pmid: 21979027
53. E. C. Ellis *et al*., Used planet: A global history. *Proc. Natl. Acad. Sci. U.S.A.* **110**, 7978–7985 (2013). doi: 10.1073/pnas.1217241110; pmid: 23630271
54. National Research Council, "Advancing the science of climate change," in *America's Climate Choices: Panel on Advancing the Science of Climate Change* (National Academies Press, Washington, DC, 2010).
55. Center for International Earth Science Information Network (CIESIN), Columbia University; International Food Policy Research Institute (IFPRI); the World Bank; and Centro Internacional de Agricultura Tropical (CIAT), Global Rural-Urban Mapping Project, Version 1 (GRUMPv1): Urban Extents Grid [Socioeconomic Data and Applications Center (SEDAC), Columbia University. Palisades, NY, 2011]; available at http://sedac.ciesin.columbia.edu/data/dataset/grump-v1-urban-extents.
56. N. Ramankutty, A. T. Evan, C. Monfreda, J. A. Foley,. *Global Agricultural Lands: Pastures, 2000* (2010), http://sedac.ciesin.columbia.edu/es/aglands.html.
57. P. Gottschalk *et al*., How will organic carbon stocks in mineral soils evolve under future climate? Global projections using RothC for a range of climate change scenarios. *Biogeosciences* **9**, 3151–3171 (2012). doi: 10.5194/bg-9-3151-2012
58. L. R. Odelman, R. T. A. Hakkeling, W. G. Sombroek, *Global Assessment of Soil Degradation GLASOD*, International Soil Reference and Information Centre (1991).
59. Yang, X., W.M. Post, P.E. Thornton, A. Jain. 2014. *Global Gridded Soil Phosphorus Distribution Maps at 0.5-Degree Resolution* (data set). doi: http://dx.doi.org/
60. IPCC,: *Climate Change 2013: The Physical Science Basis. Contribution of Working Group I to the Fifth Assessment Report of the Intergovernmental Panel on Climate Change*, T. F. Stocker *et al*., Eds. (Cambridge Univ. Press, Cambridge, 2013).
61. N. Gedney *et al*., Detection of a direct carbon dioxide effect in continental river runoff records. *Nature* **439**, 835–838 (2006). doi: 10.1038/nature04504; pmid: 16482155
62. C. D. Koven *et al*., The effect of vertically resolved soil biogeochemistry and alternate soil C and N models on C dynamics of CLM4. *Biogeosciences* **10**, 7109–7131 (2013). doi: 10.5194/bg-10-7109-2013
63. L. Cao, G. Bala, K. Caldeira, R. Nemani, G. Ban-Weiss, Importance of carbon dioxide physiological forcing to future climate change. *Proc. Natl. Acad. Sci. U.S.A.* **107**, 9513–9518 (2010). doi: 10.1073/pnas.0913000107; pmid: 20445083
64. H. Lieth, Primary production: Terrestrial ecosystems. *Hum. Ecol.* **1**, 303–332 (1973). doi: 10.1007/BF01536729
65. "World Population Prospects: The 2012 Revision" (XLS), Population Division of the Department of Economic and Social Affairs of the United Nations Secretariat, June 2013.
66. www.ers.usda.gov/data-products/wheat-data.aspx#.U2ktw17INZE
67. www.ers.usda.gov/data-products/fertilizer-use-and-price.aspx#.U2kz-17INZE
68. H. K. Gibbs *et al*., Tropical forests were the primary sources of new agricultural land in the 1980s and 1990s. *Proc. Natl. Acad. Sci. U.S.A.* **107**, 16732–16737 (2010). doi: 10.1073/pnas.0910275107; pmid: 20807750
69. Jean Paul Richter, Ed., *The Notebooks of Leonardo Da Vinci* (Dover Publications, New York, 1970).

ACKNOWLEDGMENTS

The paper resulted from discussions within the U.S. National Committee for Soil Sciences, P. Bertsch, Chair. We thank I. Fung, C. Koven, and G. Sposito for discussions and P. Gottschalk for figure data.

10.1126/science.1261071

RESEARCH ARTICLE

HUMAN GENOMICS

The Genotype-Tissue Expression (GTEx) pilot analysis: Multitissue gene regulation in humans

The GTEx Consortium*†

Understanding the functional consequences of genetic variation, and how it affects complex human disease and quantitative traits, remains a critical challenge for biomedicine. We present an analysis of RNA sequencing data from 1641 samples across 43 tissues from 175 individuals, generated as part of the pilot phase of the Genotype-Tissue Expression (GTEx) project. We describe the landscape of gene expression across tissues, catalog thousands of tissue-specific and shared regulatory expression quantitative trait loci (eQTL) variants, describe complex network relationships, and identify signals from genome-wide association studies explained by eQTLs. These findings provide a systematic understanding of the cellular and biological consequences of human genetic variation and of the heterogeneity of such effects among a diverse set of human tissues.

Over the past decade, there has been a marked increase in our understanding of the role of genetic variation in complex traits and human disease, especially via genome-wide association studies (GWAS) that have cataloged thousands of common genetic variants affecting human diseases and other traits (*1*–*3*). However, the molecular mechanisms by which this genetic variation predisposes individuals to disease are still poorly characterized, impeding the development of therapeutic interventions.

The majority of GWAS variants are noncoding, likely manifesting their effects via the regulation of gene expression (*4*, *5*). Thus, characterization of the regulatory architecture of the human genome is essential, not only for understanding basic biology but also for interpreting GWAS loci. Expression quantitative trait locus (eQTL) analysis (*6*–*8*) is the most common approach used to dissect the effects of genetic variation on gene expression. However, comprehensive eQTL data from a range of human tissues are lacking, and eQTL databases are biased toward the most accessible tissues. Additionally, although many regulatory regions act in a tissue-specific manner (*9*, *10*), it is unknown whether genetic variants in regulatory regions have tissue-specific effects as well. Complex diseases are often caused by the dysfunction of multiple tissues or cell types, such as pancreatic islets, adipose, and skeletal muscle for type 2 diabetes (*11*, *12*), so it is not obvious a priori what the causal tissue(s) are for any given GWAS locus or disease. Hence, understanding the role of regulatory variants, and the tissues in which they act, is essential for the functional interpretation of GWAS loci and insights into disease etiology. The Genotype-Tissue Expression (GTEx) Project was designed to address this limitation by establishing a sample and data resource to enable studies of the relationship among genetic variation, gene expression, and other molecular phenotypes in multiple human tissues (*13*). To facilitate the collection of multiple different tissues per donor, the project obtains recently deceased donors through consented next-of-kin donation, from organ donation and rapid autopsy settings. The results described here were generated during the project's pilot phase, prior to scaling up collection to 900 donors. All project data are made available at regular intervals to qualified researchers through dbGaP. Summary data are available on the GTEx Portal (http://gtexportal.org).

*A list of authors and affiliations appears at the end of the paper.
†Corresponding author: Kristin G. Ardlie (kardlie@broadinstitute.org) or Emmanouil T. Dermitzakis (emmanouil.dermitzakis@unige.ch)

Study design

During the pilot, we recruited 237 postmortem donors, collecting an average of 28 tissue samples per donor spanning 54 distinct body sites (fig. S1 and tables S1 and S2). Blood-derived DNA samples were genotyped at approximately 4.3 million sites, with additional variants imputed using the 1000 Genomes phase I, resulting in ~6.8 million single-nucleotide polymorphisms (SNPs) with minor allele frequency (MAF) of ≥5% after quality control (tables S3 to S5) (*14*).

RNA was extracted from all tissues, but quality varied widely, with tissue site and sample specific ischemic time accounting for ~40% of the variance in RNA quality (fig. S2). To maximize statistical power, we prioritized RNA sequencing of samples from nine tissues that were most frequently collected and that routinely met minimum RNA quality criteria: adipose (subcutaneous), tibial artery, heart (left ventricle), lung, muscle (skeletal), tibial nerve, skin (Sun-exposed), thyroid, and whole blood (Table 1) (*14*).

We performed 76–base pair (bp) paired-end mRNA sequencing on a total of 1749 samples, of which 1641 samples from 43 sites, and 175 donors, constituted our final "pilot data freeze" reported on here (*14*). Median sequencing depth was 82.1 million mapped reads per sample (fig. S3A). The final data freeze included samples from 43 body sites: 29 solid-organ tissues, 11 brain subregions (with two duplicated regions), a whole-blood sample, and two cell lines derived from donor blood [EBV-transformed lymphoblastoid cell lines (LCLs)] and skin samples (cultured fibroblasts) (Table 1 and tables S1 and S2). Median sample size for the nine high-priority tissues was 105; median sample size for the other 34 sampled sites was 18.5.

Gene expression across tissues

We examined the patterns of expression of 53,934 transcribed genes across tissues [on the basis of Gencode V12 annotations] (*14*, *15*). The number of biotypes [protein-coding genes, pseudogenes, and long noncoding RNAs (lncRNAs)] that were transcribed above a minimal threshold [reads per kilobase per million mapped reads (RPKM) > 0.1] was similar for most tissues (average of 20,940) (fig. S3B). Testis was an outlier, with substantially more transcribed regions detected than other tissues (31,240 on average), many of which are lncRNAs. Whole blood was also an outlier, exhibiting the fewest detected transcribed regions (17,160 on average).

Hierarchical clustering demonstrated that expression profiles accurately recapitulate tissue type, with blood samples forming the primary outgroup (Fig. 1A). The multiple brain regions cluster strongly together as a single unit, but among those the 11 individual subsampled regions are less distinct (Fig. 1A and fig. S4A). The most distinct brain region is the cerebellum (fig. S4A) (*16*), with preservation method having little impact on that signal (fig. S4B). The distribution of gene expression across tissues is described by Melé *et al.* (*17*), who show that tissue-specific transcription is typically dominated by a few genes that vary from tissue to tissue.

We quantified splicing events (splice junctions, exons, transcripts) by estimating exon inclusion levels, measured as PSI (percent spliced in) scores (*14*, *18*). Clustering samples by PSI scores also largely, although less clearly, recapitulates tissue type. Samples from the brain, not blood, form the primary outgroup (Fig. 1B), which is divided into two groups: A group of 227 samples (from the cerebellum and cortex) forms an independent subcluster (cluster 1), and a smaller group of 97 samples (cluster 2, dominated by the remaining subregions) clusters closer to samples from the rest of the tissues.

Table 1. GTEx pilot samples. Characteristics of the 1641 RNA-sequenced samples included in the pilot data freeze. The second and third columns show the tissue abbreviation and color assigned to each tissue (used throughout). The nine tissues prioritized for sequencing are indicated by red stars. Boxes highlight two regions of the brain that were sampled in duplicate. A region each from the cerebellum and cortex (BRNCHA and BRNCTXA) was sampled on site during initial tissue collection, and again after the brain was received by the brain bank (BRNCHB and BRNCTXB). Cell lines included are an EBV-transformed lymphoblastoid cell line from blood (LCL) and a cultured primary fibroblast cell line from fresh skin (FIBRBLS). RIN, RNA integrity number.

				RIN		Sample Ischemic Time (min)		Age
Tissue Site Detail	Abbreviation	Color	n	Mean	SD	Mean	SD	Mean
★ Adipose - Subcutaneous	ADPSBQ		94	6.9	0.6	421.9	318.3	48.2
Adipose - Visceral (Omentum)	ADPVSC		19	7.2	0.6	401.4	303.1	46.9
Adrenal Gland	ADRNLG		12	8.3	0.8	172.8	107.2	51.4
Artery - Aorta	ARTAORT		24	7.8	0.8	262.0	178.3	50.8
Artery - Coronary	ARTCRN		9	7.5	0.7	312.4	307.9	55.3
★ Artery - Tibial	ARTTBL		112	7.5	0.7	486.7	350.0	47.9
Brain - Amygdala	BRNAMY		23	6.9	0.8	NA	NA	51.2
Brain - Anterior cingulate cortex (BA24)	BRNACC		17	7.0	0.7	NA	NA	51.4
Brain - Caudate (basal ganglia)	BRNCDT		36	7.5	0.8	NA	NA	52.5
Brain - Cerebellum [PAXgene]	BRNCHA		30	7.4	1.0	868.9	300.9	51.6
Brain - Cerebellar Hemisphere [Frozen]	BRNCHB		24	7.6	1.1	NA	NA	49.7
Brain - Cortex [PAXgene]	BRNCTXA		23	7.1	0.9	837.2	280.3	51.3
Brain - Frontal Cortex (BA9) [Frozen]	BRNCTXB		24	7.5	0.9	NA	NA	55.1
Brain - Hippocampus	BRNHPP		24	6.9	0.7	NA	NA	51.1
Brain - Hypothalamus	BRNHPT		23	7.0	0.9	NA	NA	51.4
Brain - Nucleus accumbens (basal ganglia)	BRNNCC		28	7.4	0.6	NA	NA	53.4
Brain - Putamen (basal ganglia)	BRNPTM		20	7.3	0.9	NA	NA	49.5
Brain - Spinal cord (cervical c-1)	BRNSPC		16	7.1	0.7	NA	NA	52.5
Brain - Substantia nigra	BRNSNG		25	6.8	0.7	NA	NA	53.8
Breast - Mammary Tissue	BREAST		27	7.0	0.7	645.6	425.4	50.3
Cells - EBV-transformed lymphocytes	LCL		39	9.9	0.2	59.7	502.0	46.2
Cells - Transformed fibroblasts	FIBRBLS		14	9.5	0.5	544.5	478.4	49.2
Colon - Transverse	CLNTRN		12	7.5	0.8	236.5	137.0	46.3
Esophagus - Mucosa	ESPMCS		18	8.6	0.7	330.9	219.6	51.7
Esophagus - Muscularis	ESPMSL		20	7.9	0.6	310.6	273.3	48.5
Fallopian Tube	FLLPNT		1	6.1	NA	520.0	NA	51.0
Heart - Atrial Appendage	HRTAA		25	7.5	0.7	492.3	323.9	51.0
★ Heart - Left Ventricle	HRTLV		83	7.9	0.9	380.9	334.4	48.0
Kidney - Cortex	KDNCTX		3	6.8	0.4	583.0	585.0	56.3
Liver	LIVER		5	7.6	0.9	365.2	321.8	42.8
★ Lung	LUNG		119	7.6	0.9	447.0	380.4	48.9
★ Muscle - Skeletal	MSCLSK		138	7.9	0.6	486.1	358.1	49.2
★ Nerve - Tibial	NERVET		88	7.0	0.7	463.8	315.6	49.4
Ovary	OVARY		6	7.3	0.7	401.0	248.4	43.5
Pancreas	PNCREAS		19	6.8	0.7	200.4	115.3	49.3
Pituitary	PTTARY		13	7.3	0.6	841.3	305.5	51.9
Prostate	PRSTTE		9	6.8	0.7	231.1	84.0	50.2
Skin - Not Sun Exposed (Suprapubic)	SKINNS		23	7.2	0.7	557.2	388.2	48.7
★ Skin - Sun Exposed (Lower leg)	SKINS		96	7.0	0.7	498.5	364.0	49.0
Stomach	STMACH		12	7.4	0.9	250.0	131.6	47.8
Testis	TESTIS		14	7.0	0.9	293.6	236.3	52.4
★ Thyroid	THYROID		105	7.0	0.7	428.5	391.7	49.2
Uterus	UTERUS		7	7.4	1.0	313.3	184.3	48.7
Vagina	VAGINA		6	7.8	1.1	414.5	234.4	54.0
★ Whole Blood	WHLBLD		156	8.1	0.8	238.4	498.2	49.7
All			**1641**	**7.5**	**0.9**	**418.9**	**394.2**	**50.2**

This is consistent with isoform regulation playing a comparatively larger role in defining cellular specificity in the brain (*18*, *19*). These analyses are extended in Melé *et al.* (*17*) to define tissue-specific splicing signatures and to investigate in depth the role of individual variation in splicing.

eQTL analyses: Single-tissue eQTL analysis

A primary goal of the GTEx project is to identify eQTLs for all genes for a range of human tissues. Past studies, hampered by the difficulties of obtaining human tissue samples, have typically examined no more than three tissues (*8*, *20*). Although our pilot sample sizes are modest for eQTL discovery, the breadth of tissues provides an opportunity to assess differential eQTL discovery among tissues. Because of our small sample sizes, we primarily examined eQTLs that act in cis to the gene (cis-eQTLs; see box S1), as the expected effect size of trans-eQTLs (box S1) is too low to be efficiently detected at this time. We calculated cis-eQTLs separately for each of the nine tissues with sufficient sample sizes (>80 donors) for all SNPs within ±1 Mb of the transcriptional start site (TSS) of each gene (*14*). Significance correlations between genotypes and gene expression levels were determined by linear regression on quantile normalized gene-level expression values, after correction for known and inferred technical covariates (fig. S8) (*14*), using Matrix eQTL (*21*). To obtain gene-specific significance levels while correcting for testing multiple SNPs per gene, we computed permutation-adjusted *P* values for each gene for the most significant

SNP per gene (*14*). We defined "eGenes" as genes with at least one SNP in cis significantly associated, at a false discovery rate (FDR) of ≤0.05, with expression differences of that gene (box S1) (*14*). A list of the significant SNP-gene pairs detected per eGene can be found on the GTEx Portal (http://gtexportal.org).

The number of eGenes ranged from 919 in heart to 2244 in thyroid, with a total of 6486 unique eGenes across the nine tissues (Fig. 2A). Rerunning the analysis on successively downsampled donor subsets from each tissue showed an approximately linear relationship between eGenes and sample size (slope of ~21 eGenes per sample; Fig. 2A). Interestingly, thyroid and nerve share a steeper slope with ~29 significant eGenes per sample, whereas muscle and blood share a shallower trajectory with ~15 eGenes per sample, which may reflect the lower transcript complexity observed for these two tissues (*17*). The number of eGenes identified showed no signs of plateauing at current sample sizes in any of the tissues.

Consistent with previous work (*20*, *22*), the majority of the significant cis-eQTLs clustered around the TSS of target genes in all nine tissues (fig. S9, A and B, and fig. S10). The eQTL signals also tended to show an upstream bias (fig. S10 and tables S6 and S7); an average of ~80% of significant eQTLs fell within ±100 kb around the TSS, and ~60% of all eQTLs were upstream despite testing a similar fraction of SNPs upstream and downstream of the TSS (tables S6 and S7) (*23*). A slight but distinct overrepresentation of nonsignificant eQTLs around the TSS (relative to other SNPs near the gene; red versus black line in figs. S9A and S11A) supports the existence of additional eGenes, which did not meet significance with current sample sizes.

To investigate the sensitivity and validity of our study, in particular because we used tissues from deceased donors, we compared the GTEx blood eQTLs to a previously reported eQTL study of whole blood samples in ~5300 individuals (*7*). Although many experimental and processing differences exist between these studies, a considerable fraction of GTEx eGenes (68%) were replicated in this study at FDR < 5% (*14*). Given the incomplete overlap in variants tested, we also compared our eQTLs against a smaller study of 911 blood samples taken from the Estonian Biobank, where we were able to apply a similar eQTL analysis pipeline to that used in GTEx and hence get better SNP coverage (fig. S11) (*14*). Notably, 98% of GTEx blood eQTLs at FDR < 5% showed consistent allelic direction with those eQTLs ($P < 10^{-200}$, binomial test) (*14*).

Multitissue joint discovery of eQTLs: Tissue specificity and sharing of eQTLs

The specificity or sharing of eQTLs among different tissues and cell types is of considerable biological interest (*8*, *22*, *24*), yielding insights into differential genetic regulation among tissues. Furthermore, cross-referencing tissue-specific eQTLs with disease genetic associations could help identify tissues most relevant to disease biology. We used the GTEx pilot data to examine eQTL sharing across multiple tissues and leveraged the large tissue range to discover weak but constitutively active eQTLs.

We investigated patterns of eQTL sharing using 22,286 genes (with RPKM > 0.1 in at least 10 samples) for each of the nine tissues with both a simple non–model-based analysis of every pair of tissues (*22*) and more sophisticated Bayesian models for joint analysis of

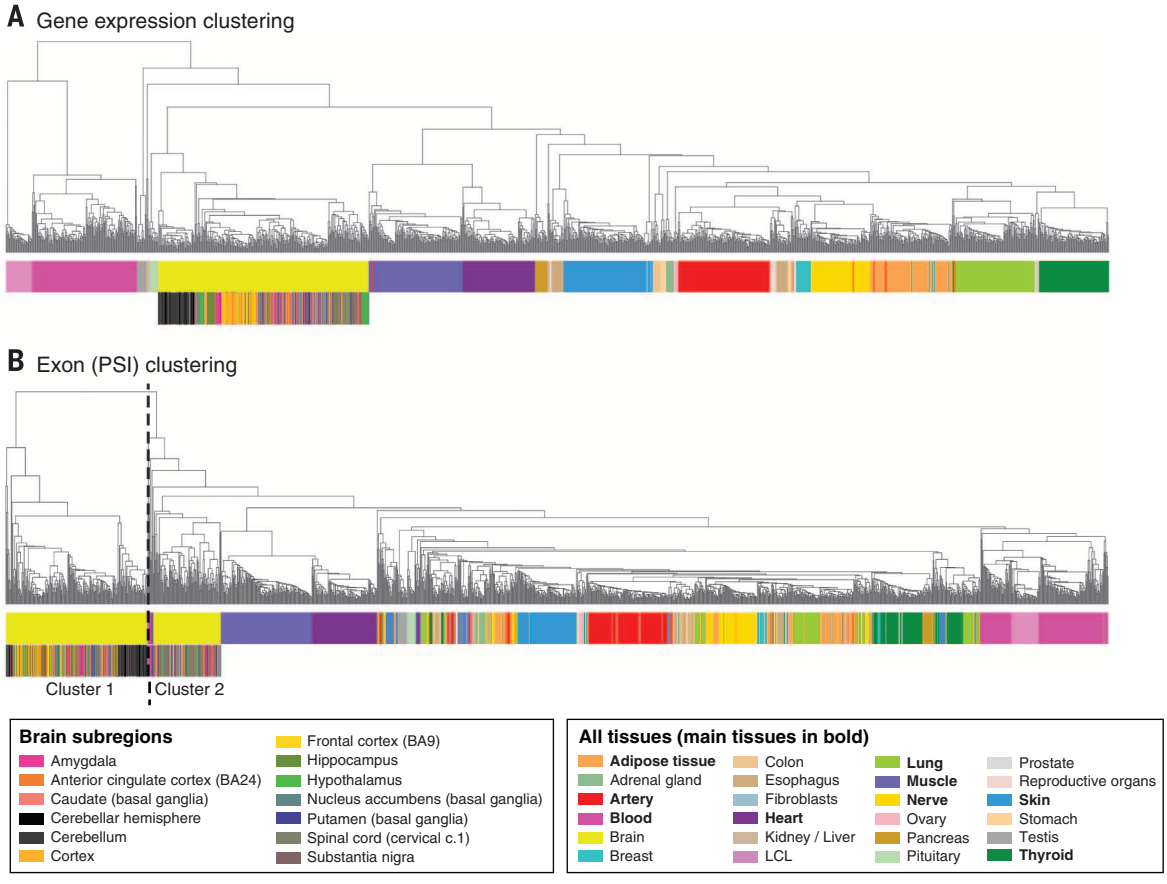

Fig. 1. Sample clustering based on gene expression and exon splicing profiles. (**A**) Clustering performed on the basis of gene expression values for all genes from Gencode v12 annotation. Tissue type is the primary driver of expression differences, with the nonsolid tissues (blood and LCL cell lines) clustering separately from solid tissues. Hierarchical clustering was performed using as distance = 1 – Pearson correlation, and average method. (**B**) Sample clustering based on the "percent spliced in" (PSI) values for exons across samples. Tissue differentiation is less clearly a driver, and brain is now the main outgroup, driven largely by a cluster comprised of cerebellum and cortex samples.

all nine tissues (*24*, *25*). Analyses focused on a ±100-kb window surrounding the TSS for each gene, which is smaller than used for the single-tissue analysis, as this is where we observe the highest eQTL density.

The non–model-based pairwise analysis method identifies significant SNP-gene pairs in a first tissue, and then uses the distribution of the *P* values for these pairs in the second tissue to estimate π_1, the proportion of non-null associations in the second tissue (*22*, *26*). Estimated values of π_1 ranged from 0.54 to 0.90 (Fig. 2B). For every pair of tissues, we observed a high level of sharing of eQTLs, and this pairwise sharing of eQTL among tissues roughly mirrored the tissue gene expression correlations (fig. S12).

To assess patterns of sharing beyond tissue pairs, we applied two Bayesian methods that assess, for each SNP-gene pair, the evidence for each of the 512 (2^9) possible null/alternative eQTL configurations. The first method (*24*) is "gene-based" and assumes a single causal eQTL per gene. We extended the model to (i) support the fact that not all tissues were sampled across all GTEx donors; (ii) calculate a gene-level FDR without requiring permutations (*27*); and (iii) include a fine mapping approach across multiple tissues (*28*). We also used a "SNP-based" approach (*25*), which assesses association of each SNP-gene pair separately, working directly with the *z*-statistics for each SNP-gene pair within each tissue [see also (*29*)]. We summarized the estimates of tissue specificity using marginal posterior probabilities for the number of tissues in which a randomly selected gene (gene-based model) or SNP-gene pair (SNP-based model) is active (Fig. 2C). Both approaches show a U-shaped pattern, with high tissue specificity (activity in a single tissue) or tissue ubiquity (activity in all nine tissues) more common than profiles involving only a few tissues, despite many more possible combinatorial patterns for intermediate specificity. Notably, both methods indicate that more than 50% of all detected eQTLs are common to all nine tissues. Reassuringly, both Bayesian methods produce pairwise tissue sharing probabilities that show agreement with the non–model-based analysis (fig. S13). Figure S14 illustrates the value of the multitissue analysis for an example in which the tissue specificity of an eQTL supports *NDRG4* as a candidate to influence QT interval in the heart (*30*). Despite superficial similarity between patterns of tissue-tissue gene expression and eQTL sharing, extensive comparisons of eQTL evidence to expression levels indicate that the tissue-specific patterns are only modestly correlated with average tissue expression levels (fig. S15).

We also examined effect size estimates for eQTLs that are shared between tissues. The vast majority of shared eQTLs show consistent effect directions in different tissues. However, some SNPs showed apparent opposite effect directions in different tissues (fig. S16). A number of examples that we investigated using multi-SNP multitissue analyses (*28*) appeared to be due to pairs of SNPs, in LD with one another, that were separate eQTLs in different tissues (fig. S17) rather than being a single eQTL with opposite effects.

Beyond the biological interest of eQTL sharing among tissues, the availability of multiple tissues can also increase the power to detect eQTLs active in multiple tissues by combining information across tissues (*24*). To investigate, we conducted a permutation analysis by holding the expression data fixed and permuting the genotypes. In this manner, we identified the significant eGenes per tissue (as in the single-tissue analysis above, but for a smaller window near the TSS), or jointly for any combination of tissues by considering the minimum *P* value across tissues under each permutation. With this approach, the number of eGenes identified for individual tissues was similar to the single-tissue eQTL analysis (Fig. 2A). Next, the minimum *P* value for each gene across all nine tissues was used to test for eQTL evidence, and subjected to gene-level false discovery control. A total of 7425 eGenes with FDR < 0.05 were identified, representing a factor of 3 increase relative to the maximum number of significant eGenes for any single tissue. The Bayesian models, which leverage the high proportion of tissue-common eQTLs, increase the power to detect eQTLs for an individual tissue by borrowing strength from the remaining tissues. Thus, of the original 22,286 expressed genes, 10,030 showed a significant eQTL (FDR < 0.05) with the gene-based Bayesian multitissue model

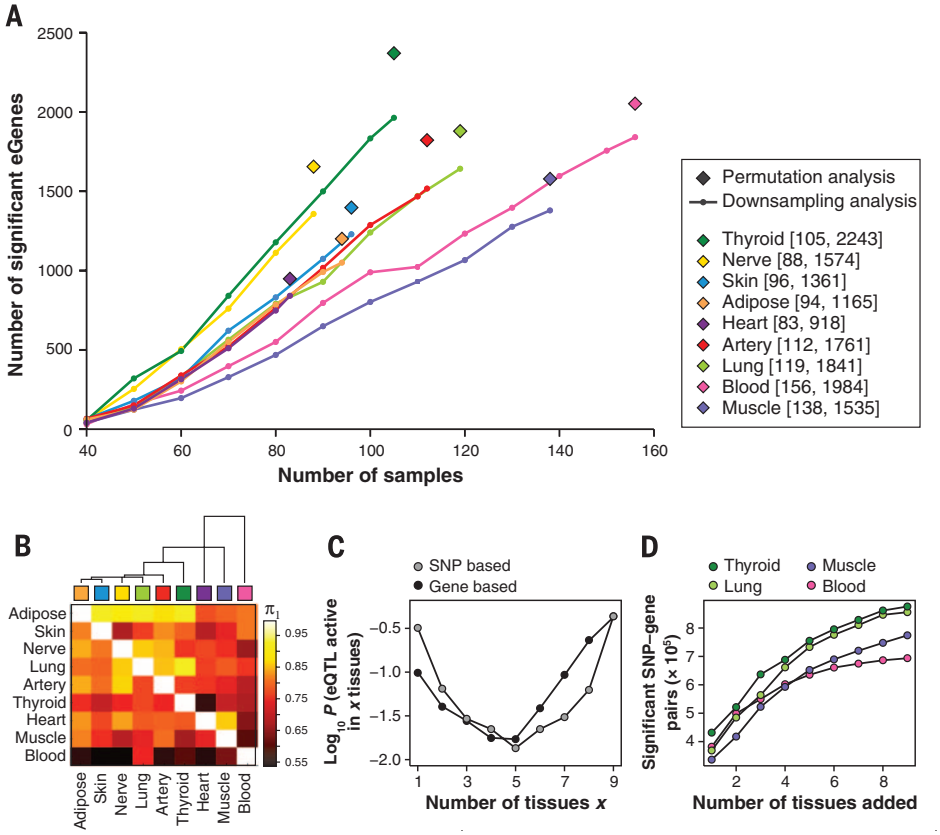

Fig. 2. Number and sharing of significant cis-eQTLs per tissue. (**A**) Numbers of significant cis-eQTL genes (eGenes) per tissue according to single-tissue analysis. For each gene, the minimum nominal *P* value was used as the test statistic and an empirical *P* value was computed to correct for number of tests per gene, based on either permutation analysis of genotype sample labels applied to the full set of samples per tissue (♦) or Bonferroni correction, used for downsampling (line) to reduce computational burden (*14*). In the range of sample sizes tested, the number of identified eGenes increases linearly with sample size. (**B**) Dendrogram and heat map of pairwise eQTL sharing using the method of Nica *et al*. (*22*). Values are not symmetrical, since each entry in row *i* and column *j* is an estimate of $\pi_1 = Pr$(eQTL in tissue *i* given an eQTL in tissue *j*). Blood has the lowest levels of eQTL sharing with other tissues while adipose shows higher levels of sharing. (**C**) Activity probabilities for both multitissue modeling approaches, applied to all nine tissues, indicate that the most likely configurations are for eQTLs that are active in only a few tissues or in many tissues. (**D**) For eQTLs in each tissue considered separately, analyzing multiple tissues jointly increases the number of discovered eQTL associations (FDR < 0.05), as assessed by the SNP-based multitissue model.

(approximately 35% more than by joint permutation). Using the SNP-based Bayesian model, we selected four of the tissues with the largest sample sizes, and computed the marginal eQTL probability for each tissue alone after adding one to eight additional tissues in a fixed sequence. This resulted in a marked increase in the number of significant SNP-gene pairs (*FDR* < 0.05) (Fig. 2D). For downstream analyses using the multitissue results, a single SNP with highest posterior probability was chosen as representative across all tissues, recognizing that multiple causal SNPs would be difficult to resolve with the current sample size. Posterior probability profiles for both Bayesian models, as well as marginal posterior probabilities that an eQTL is active in each tissue, based on summing the probabilities across all configurations, are available for these genes (http://gtexportal.org).

Allele-specific expression analysis

To complement eQTL analysis, we used allele-specific expression (ASE) of genes to indirectly estimate the overall effect of cis-regulatory variants on the expression of nearby genes. Individuals that are heterozygous for a cis-regulatory variant may differentially express each of the two alleles of the affected gene. In these cases, assuming no other causes for allele-specific expression, imbalanced allelic expression of a gene can be used to infer the effect of cis regulation on the gene even without necessarily identifying the specific regulatory variant(s). In addition to the subtle cis-regulatory effects described here, ASE of premature stop variants is also informative of nonsense-mediated decay (*31*), and consistent monoallelic expression of specific genes can be used to detect epigenetic silencing by imprinting.

ASE can be estimated from the abundance of RNA-seq reads supporting each of the gene's alleles, measured at heterozygous sites within the transcribed region. We identified a median of 6385 sites per sample (across all tissues and all individuals) that were both heterozygous for a transcript SNP in the imputed genotype data of the associated individual and well expressed in that sample (SNP covered by ≥ 30 RNA-seq reads) (fig. S18). Of these sites, a median of 390 sites per sample had significant ASE (binomial $P < 0.005$, or 144 sites with FDR 21%, after rigorous quality control of ASE sites and after downsampling to exactly 30 reads at each site to ensure equal power to detect ASE) (Fig. 3A and table S8A) (*14*). To assess whether different tissues vary in terms of the overall effect of cis-regulatory variation in them, we estimated the proportion of those sites with significant ASE in each of the tissues (combining data from all individuals) (*14*) and found that the fraction of significant ASE sites varied widely across tissues, with a range of 1.7 to 3.7% (median 2.3%). Brain regions appeared depleted for allelic effects (2.0% ASE in brain versus 2.7% in other tissues combined; $P < 2 \times 10^{-16}$, Fisher's exact test) (Fig. 3A), consistent with the hypothesis that brain-specific genes exhibit reduced genetic diversity (*32*). Our results generally support our eQTL findings; in thyroid, where we observed a high number of eQTLs (Fig. 2A), we also see an increased amount of ASE (Fig. 3B). Blood and LCLs have a higher proportion of allelic effects (3.6% versus 2.3% in others; $P < 2 \times$

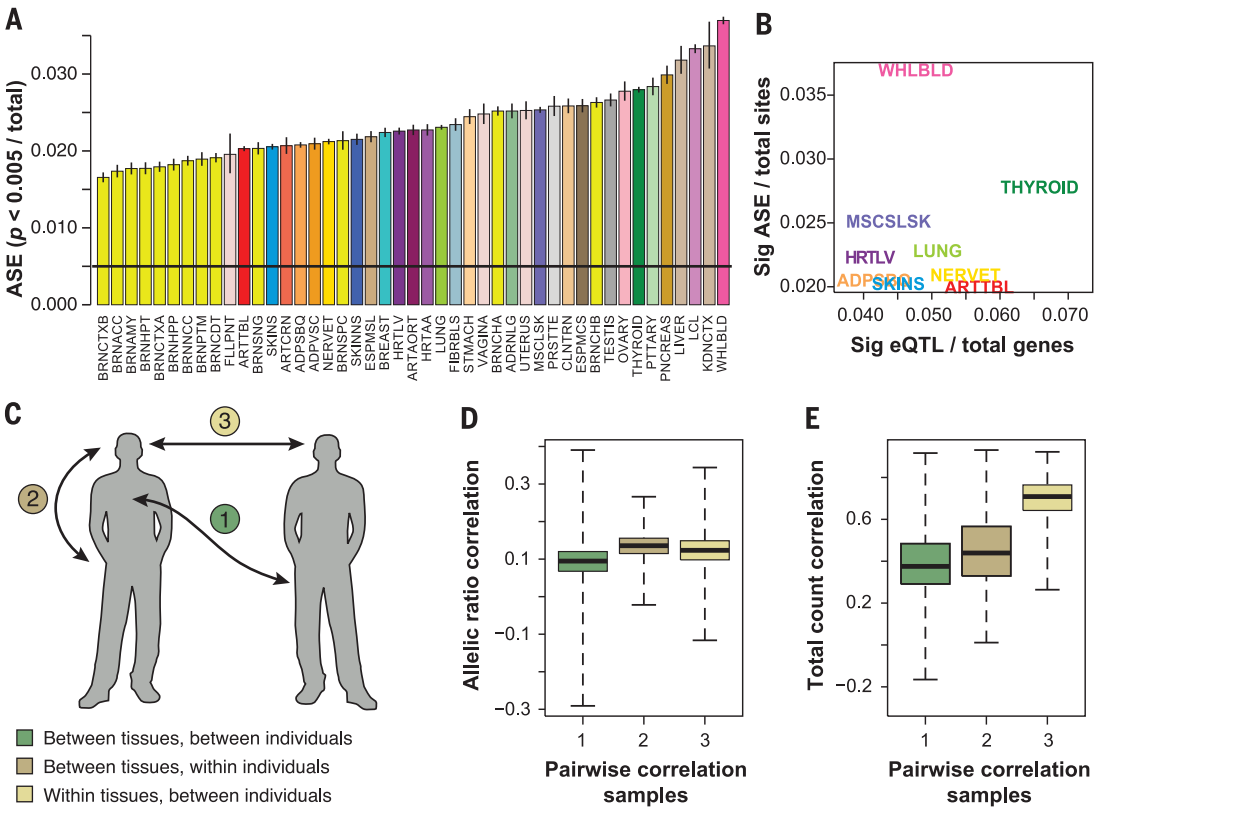

Fig. 3. Quantification of regulatory diversity by ASE. (**A**) Proportion of sites with significant ASE ($P < 0.005$) in each tissue (colored and labeled as in Table 1), with binomial confidence intervals. (**B**) Proportion of significant ASE sites for the nine tissues with eQTL data as a function of the proportion of eQTLs after regressing out the log of sample size. (**C**) Partitioning variation in allelic and total gene expression within and between individuals and tissues. We calculated pairwise Spearman rank correlations between all the samples using two metrics [(D) and (E)]. (**D**) Allelic ratios over sites (sampled to 30 reads each), which captures similarity in allelic effects that are a proxy for cis-regulatory variation. (**E**) Total read counts over the same sites, which captures similarity in total gene expression levels. The plots show the distributions of pairwise correlations for sample pairs that are from (1) different tissues and different individual, (2) different tissues within an individual, or (3) same tissues in different individuals. Gene expression levels are highly correlated within the same tissue (E3) (see Fig. 1A). However, allelic ratios show highest correlation among different tissues of the same individual that share the same genome (D2).

10^{-16}, Fisher's exact test) (Fig. 3B), suggesting nongenetic sources of monoallelic expression possibly due to the more clonal nature of these cells (*33*).

To compare between-sample and between-tissue sharing of ASE with the overall similarity of gene expression, we constructed two Spearman rank correlation matrices between all pairs of samples. In one, we correlated ASE ratios, capturing sharing of cis regulation; in the other, we correlated total coverage of the same sites, capturing similarity of overall gene expression levels, analyzing genes that are expressed in both tissues (both matrices used counts of reads covering heterozygous sites shared between the compared pair of samples) (*14*). The two matrices of tissue medians were highly correlated (Mantel test, $r = 0.772$, $P < 0.0001$; fig. S19), indicating that tissues with similar gene expression profiles also have a higher degree of sharing of genetic regulatory effects.

Interestingly, when partitioning the full sample-level matrix into correlations between samples from different tissues of the same individual, the same tissue across individuals, or different individuals and different tissues (Fig. 3C), we found more complex relationships between total expression and allelic ratios. As expected, expression levels are determined by tissue, and samples cluster by tissue (75.6% of variance; Fig. 3E and table S8B). However, allelic ratios show the opposite pattern (Fig. 3D), with higher correlation among tissues within the same individual (17.9% of variance) than among individuals for the same tissue (8.6%). These results indicate that ASE is primarily determined by the common genome among different tissues of the same individual (*34*). This suggests that the two dimensions of gene expression variability, gene expression levels and allelic ratios, are largely defined by independent factors.

ASE analysis can also be used as orthogonal confirmation of eQTL effects, on the basis of the expectation that individuals who are heterozygous for a cis-eQTL variant should manifest biased allelic ratios in the eQTL target gene. We performed this analysis at the genome-wide level across all the tissues in the GTEx data set, including the tissues with sample sizes that were too small for eQTL analysis. Examining the significant eQTLs identified by single-tissue analysis for the nine main tissues, we looked at their ASE effects separately in each of the 42 tissues, calculating the odds ratio of significant versus nonsignificant ASE for eQTL heterozygote versus homozygote individuals (e.g., for thyroid eQTLs we looked for ASE in all 42 tissues, then for blood eQTLs and so on) (figs. S20 and S21). In addition to replication of eQTL signals in the discovery tissue, we can estimate how relevant our eQTL findings from nine tissues are to a wide variety of other tissues (independent of sample size or allele frequency) and then assess which tissue is the best proxy for capturing regulatory effects in another tissues of interest.

We found that the overall tissue specificity of the eQTL sets varies. For example, eQTLs identified in skeletal muscle were less active in other tissues. Some tissues, such as brain, were not well captured by any of the nine eQTL sets here. ASE analysis also allows quantification of genome-wide tissue sharing of cis-regulatory signals without relying on eQTL discovery, but instead by measuring how often a site with a significant ASE signal in one tissue is significant in another tissue of the same individual. The proportion of shared ASE effects between tissue pairs within an individual varies between 36% and 58% (mean 46%), with slightly increased sharing observed between closely related tissues (conditioning on each site being measurable in both of the tissues) (fig. S22A). This relatively high degree of sharing is consistent with the eQTL results described above. If we relax the constraint of requiring a gene to be expressed in both tissues, then the proportion of shared ASE effects is substantially lower (0.85 to 39%, mean 11%; fig. S22B). This finding represents the total probability of detecting a regulatory effect in another tissue, and highlights a high degree of apparent tissue specificity that derives from the fact that a gene expressed in one tissue is often simply not expressed in another. This is particularly pronounced in brain, where the large proportion of genes showing tissue-specific isoform expression in that organ (*17*) drives a lower degree of overall sharing. Whole blood and skeletal muscle are partial outliers, relative to other tissues,

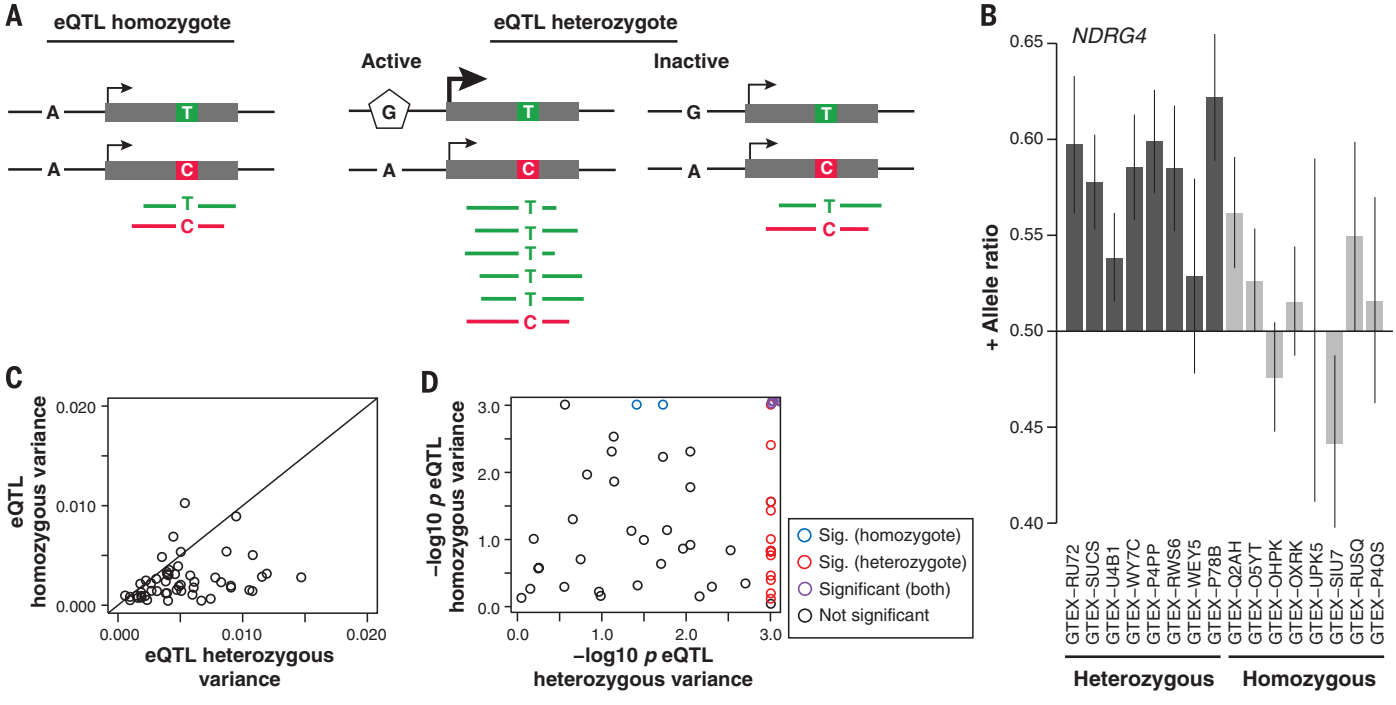

Fig. 4. Cis-regulatory effects in individuals that are not explained by detected eQTLs. (**A**) An eQTL showing individual homozygous (AA) for the eQTL SNP (left panel) or heterozygous (AG) (right panel). ASE is measured at the TC SNP. (**B**) An example of replication of an eQTL signal in ASE analysis in the *NDRG4* gene, with eQTL heterozygotes showing higher ASE in the eQTL target gene than eQTL homozygotes (only a subset of individuals shown; linear regression $P = 5.69 \times 10^{-6}$). The error bars are from a binomial test for the allelic ratio. (**C**) For each eQTL gene where the eQTL signal was replicated in ASE (linear regression $P < 0.05$ after Bonferroni correction), the eQTL heterozygotes show higher variance in allelic ratio (Mann-Whitney $P = 2.13 \times 10^{-7}$). (**D**) Permuted *P* value for the variance between individuals, which is higher than expected in 22/53 genes (9 genes in homozygotes, 20 in heterozygotes).

with lower sharing of eQTLs and lower average replication in other tissues (Fig. 2A, fig. S12, and figs. S20 to S22).

Although eQTL analysis and other association-based analyses are efficient for identifying common variants with phenotypic effects in populations, the genotype of those variants may not be a good indicator of the gene expression phenotype at an individual level. We investigated this using ASE analysis to estimate how consistent the allelic effect of single-tissue eQTL variants are across individuals that share the same genotype for the best associated eQTL variant per gene. We tested a subset of 606 eQTLs that had high read coverage and a large number of samples for transcript heterozygous sites in the eQTL discovery tissue. We identified 53 eQTLs with significant replication of the eQTL signal in ASE, as inferred by higher allelic imbalance in eQTL heterozygotes than in homozygotes (linear regression $P < 0.05$ after Bonferroni correction; Fig. 4, A and B). Further, for 22 of the 53 eQTL genes, individuals show variability in their allelic ratios that cannot be accounted for by the eQTL genotype or sampling error (Bonferroni corrected $P < 0.05$ from permutation of read counts; Fig. 4, C and D). These results highlight that common eQTLs do not explain all of the cis-regulatory effects in individuals and are inadequate predictors of allelic expression variance at the individual level. The higher variance in eQTL heterozygotes than in homozygotes (Mann-Whitney $P = 2.13 \times 10^{-7}$; Fig. 4B) suggests that part of this variance might originate from modification of the main eQTL effect by environmental or trans effects, or due to additional, independent regulatory variants (*34*).

Analysis of splicing QTLs

Beyond estimating overall levels of gene expression, RNA-seq data also allow for the quantification of expression levels of individual transcript isoforms, as well as components of these, such as exons, splice junctions, and untranslated regions. We refer to the quantitative variation of gene structure due to genetic variation as splicing QTLs (sQTLs) (Fig. 5A). To identify sQTLs, we used Altrans (*35*), a method that identifies SNPs that are associated with variation in the expression levels of exon junctions (sjQTLs; box S1) (*14*), and sQTLSeekeR (*36*), a method that identifies SNPs associated with the variation in the relative abundances of gene transcript isoforms (srQTLs; box S1) (*14*). Altrans identifies both novel and annotated splicing events, while sQTLSeekeR tests only annotated isoforms. Altrans, however, is restricted to changes in the usage of splice junctions, while sQTLSeekeR can in principle detect any variation in the relative abundance of transcript isoforms (fig. S23). Altrans was run using a ±1 Mb region around the TSS, while for sQTLseekeR, we tested within the body of the gene ±5 kb (*14*).

We detected an average of ~1900 genes with Altrans, and ~250 with sQTLseekeR, with at least one cis-sQTL per tissue (FDR = 0.05; table S9). The greater genomic window tested around the TSS for Altrans, and the capacity to detect novel splicing events, explains the much larger number of sQTLs detected by Altrans than by sQTLseekeR (about 70% of Altrans sQTLs correspond to novel events, and only about 10% map within 5 kb of

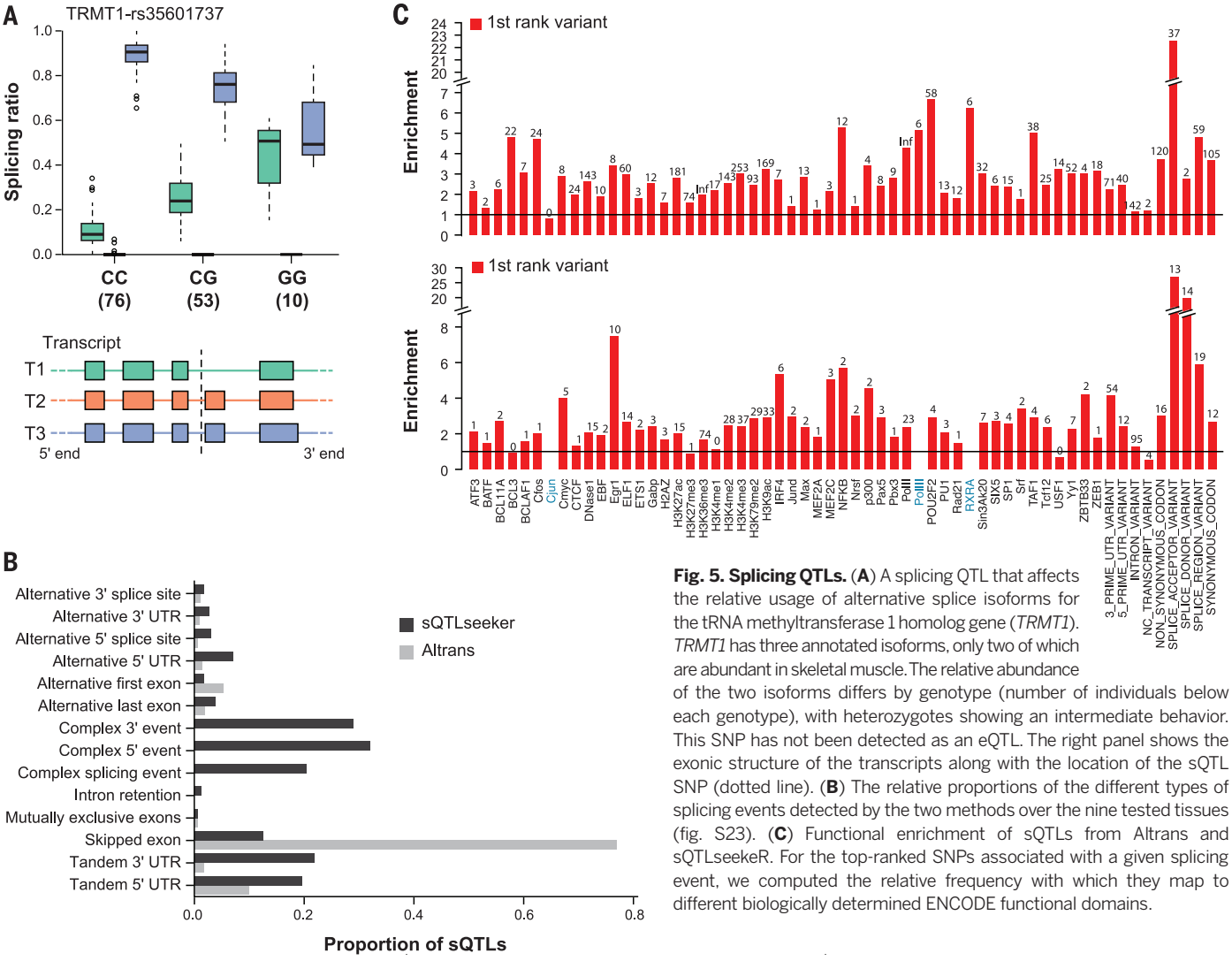

Fig. 5. Splicing QTLs. (**A**) A splicing QTL that affects the relative usage of alternative splice isoforms for the tRNA methyltransferase 1 homolog gene (*TRMT1*). *TRMT1* has three annotated isoforms, only two of which are abundant in skeletal muscle. The relative abundance of the two isoforms differs by genotype (number of individuals below each genotype), with heterozygotes showing an intermediate behavior. This SNP has not been detected as an eQTL. The right panel shows the exonic structure of the transcripts along with the location of the sQTL SNP (dotted line). (**B**) The relative proportions of the different types of splicing events detected by the two methods over the nine tested tissues (fig. S23). (**C**) Functional enrichment of sQTLs from Altrans and sQTLseekeR. For the top-ranked SNPs associated with a given splicing event, we computed the relative frequency with which they map to different biologically determined ENCODE functional domains.

annotated genes). Despite the difference, Altrans and sQTLseekeR show strong complementarity, detecting variants that are associated with very different types of alternative splicing events. Most of the splice events detected by Altrans (80%) are exon-skipping events, while 60% of those detected by sQTLseekeR correspond to complex splice events, such as mutually exclusive exons (Fig. 5B and fig. S23). If we consider only sQTLs associated with exon-skipping events, the overlap in sQTLs identified by both methods is substantial (36% of sQTLseekeR are also found by Altrans, $P = 0.004$) (figs. S23 to S25). An example of an sQTL that we identified with potential biological relevance is shown in Fig. 5A (further examples are in fig. S26).

Significant sQTLs show a high degree of sharing among tissue pairs, with tissue-specific sQTLs accounting only for 7 to 21% of the total depending on the tissue (figs. S27 and S28). The highest degree of sharing is between heart left ventricle and whole blood, whereas the two tissues that share the fewest sQTLs are whole blood and Sun-exposed skin. In general, sQTLs identified in whole blood are shared at lower levels with other tissues, as was observed for eQTLs (Fig. 2A and fig. S12, A and B). Although we observe the same enrichment of sQTLs around the TSS as seen for eQTLs, the sQTLs that are shared across multiple tissues tend to be closer to the TSS than those that are tissue-specific (fig. S28). On average, 20% of sQTLs associated with changes in exon junction abundance by Altrans were also predicted to be eQTLs (π_1 = 0.20, π_1 = 0.14 to 0.27; table S10). An even larger fraction (48%) of sQTLs detected by sQTLseekeR associated with changes in relative abundances of gene transcript isoforms, were identified as eQTLs (π_1 = 0.48, π_1 = 0.13 to 0.70; table S10). This enrichment of eQTLs among sQTLs is larger than expected at FDR < 0.05, but a substantial fraction of sQTLs are unique and not detected by standard eQTL analysis.

Functional annotation of eQTLs in noncoding regions

Genetic variants affecting gene expression and splicing patterns have been shown to fall within regulatory elements, providing a potential molecular basis for their effects (*37*–*39*). To assess whether the eQTLs discovered across the nine tissues were enriched in regulatory regions, we used a set of regulatory annotations from the ENCODE project (*10*) and the Epigenomics Roadmap project (*40*), including regulator-bound locations, DNase I hypersensitivity sites, and maps of histone modifications for proximal and distal regulatory regions (*14*). For each tissue, we chose the top significant SNP per gene from the single-tissue eQTL analysis (14,431 eQTL SNPs). Discarding SNPs that were within annotated genes resulted in 4085 intergenic eQTL SNPs, which were compared to our regulatory annotations (*14*). Intergenic eQTL SNPs were enriched for transcription factor-bound sites, open chromatin, promoters, and enhancers ($P = 4.3 \times 10^{-18}$, 2.9×10^{-8}, 1.7×10^{-19}, and 0.003, respectively) relative to the density of these features within a 2.5-kb window of the tested eQTLs (fig. S29 and table S11). This enrichment was even more pronounced in a subset of 91 unambiguous intergenic eQTL SNPs (fig. S29). In contrast, we found sQTLs to be enriched within annotated splice junctions relative to other functional regions (Fig. 5C).

We also asked whether the specific SNP-gene links ("genetic links") predicted by our eQTL analysis were supported by enhancer-gene links based on functional correlation ("functional links") (*14*). We found that open chromatin regions containing an eQTL SNP show higher correlation to the corresponding gene, relative to open chromatin regions without an eQTL at similar distances and linked to genes also containing an independent eQTL ($r = 0.037$ versus 0.030, paired Mann-Whitney two-sided $P = 4.3 \times 10^{-11}$, SE = 0.00114, $n = 32{,}168$ eQTL-SNP pairs).

This demonstrates the value of eQTL information to establish functional links between regulatory elements and genes in the genome, an analysis that will increase in power as additional tissues and subjects are added to the data set.

Gene network inference within tissues using cross-individual expression variation

To provide a view of coordinated gene regulation arising from both cis and trans genetic effects and nongenetic sources, we inferred gene-gene coexpression networks within tissues. Studying each of the nine tissues in isolation and examining variation of gene expression across individuals, we linked pairs of genes that show correlated expression (top 1% of pairs by Pearson correlation) (*14*), revealing similar patterns of coexpression across tissue pairs (Fig. 6A). The median π_1 statistic (fraction of true positive results) (*26*), estimating the total fraction of coexpressed gene pairs identified in one tissue that are replicated in a second tissue, is 0.44, ranging from 0.30 to 0.58 (Fig. 6A). Furthermore, the specific tissue pairs with higher overlap of coexpressed genes also have a greater overlap of cis-eQTLs than other tissue pairs, indicating a similar pattern of tissue relatedness underlying both results ($P < 0.05$ for correlation between similarity matrices of Figs. 2B and 6A). Thus, although coexpression networks primarily capture non-cis mechanisms, including trans regulation and environmental factors, the overall level of sharing and the specific patterns of tissue relatedness agree with the patterns observed from cis-eQTLs, which suggests that regulatory mechanisms beyond cis effects may be shared across tissues.

We also used a weighted gene coexpression network analysis (WGCNA) approach (*41*) to construct coexpression networks and extract gene modules for each tissue (Fig. 6B). The clustering of coexpressed genes into modules allows us to identify active biological processes across tissues (Fig. 6C). Modules enriched for common Gene Ontology (GO) biological processes were observed in all nine tissues (e.g., cell cycle, protein transport), while other biological processes were only seen in specific tissues (e.g., fatty-acyl-CoA metabolic process enrichment seen only in adipose, Benjamini-Hochberg corrected $P = 2.6 \times 10^{-7}$) (*14*). In addition to functional annotation, the identified coexpression networks also enabled us to search for potential transcriptional regulators of these modules (Fig. 6D). We found enrichment of transcription factor binding in promoter regions of genes in the same module using ENCODE chromatin immunoprecipitation (ChIP)–seq data (*42*), suggesting that some modules could be regulated by a large number of transcription factors (fig. S30A). Finally, we compared coexpression modules learned in each tissue individually to those learned in other tissues, based on common gene membership and correlation of first principal components of expression variation across individuals (fig. S30B). Many modules showed correlation between principal components to other modules across tissues but lacked common genes, demonstrating that similarity in patterns of variation is sometimes only visible at the module level.

Gene network inference within individuals using cross-tissue expression variation

The availability of multiple tissues per individual further allowed us to define modules of co-regulated genes within each individual, by correlating gene expression across tissues for the same individual (*14*). Merging modules across individuals produced 117 modules (fig. S6E), containing between 25 and 414 genes. Each of these modules corresponds to a multitissue expression pattern for a gene, enabling us to study changes in the regulatory program of genes that affect multiple tissues at a time.

We used these modules to identify instances of coordinated variation in multitissue expression patterns across individuals. For each gene, we estimated the proximity of each individual's expression pattern to the median expression pattern of each module, corresponding to a "module membership score" (Fig. 6F and fig. S31A). We then calculated a module membership score for each individual (Fig. 6G) (*14*). Cases where depletion in membership of one module was accompanied by a corresponding increase in membership of a different module are called "module switching events." The majority of genes showed conserved multitissue gene expression patterns among individuals, remaining in the same module or switching between modules with similar expression patterns (correlation distance < 0.5). However, we identified 3965 genes (21%) that show switching between dissimilar modules (correlation distance > 0.5), which may have important biological consequences (fig. S31B). Using module membership scores as a quantitative trait, we searched for neighboring SNPs that are correlated with these module membership scores (Fig. 6H), which we call module-switching QTLs (modQTLs). Searching a window of 1Mbp around each gene in cis, we found a total of 2102 modQTLs associated with statistically significant switching (FDR < 0.05) between dissimilar gene modules (correlation

distance > 0.5), suggesting that genetic variation for those genes leads to changes in multitissue regulatory programs. For example, the *ZFP57* gene shows three distinct patterns of multitissue expression across individuals, and three nearby SNPs are associated with these changes, suggesting a genetic basis for these multitissue differences (Fig. 6H).

We compared the 2102 modQTLs with eQTLs discovered by both the single-tissue and multitissue eQTL analyses. At all correlation levels of stringency, the modQTLs capture 53% of tissue-specific eQTLs (calculated as the percentage of lead SNPs in LD r^2 > 0.8 with lead modQTLs) and 60% of multitissue eQTLs, and these two

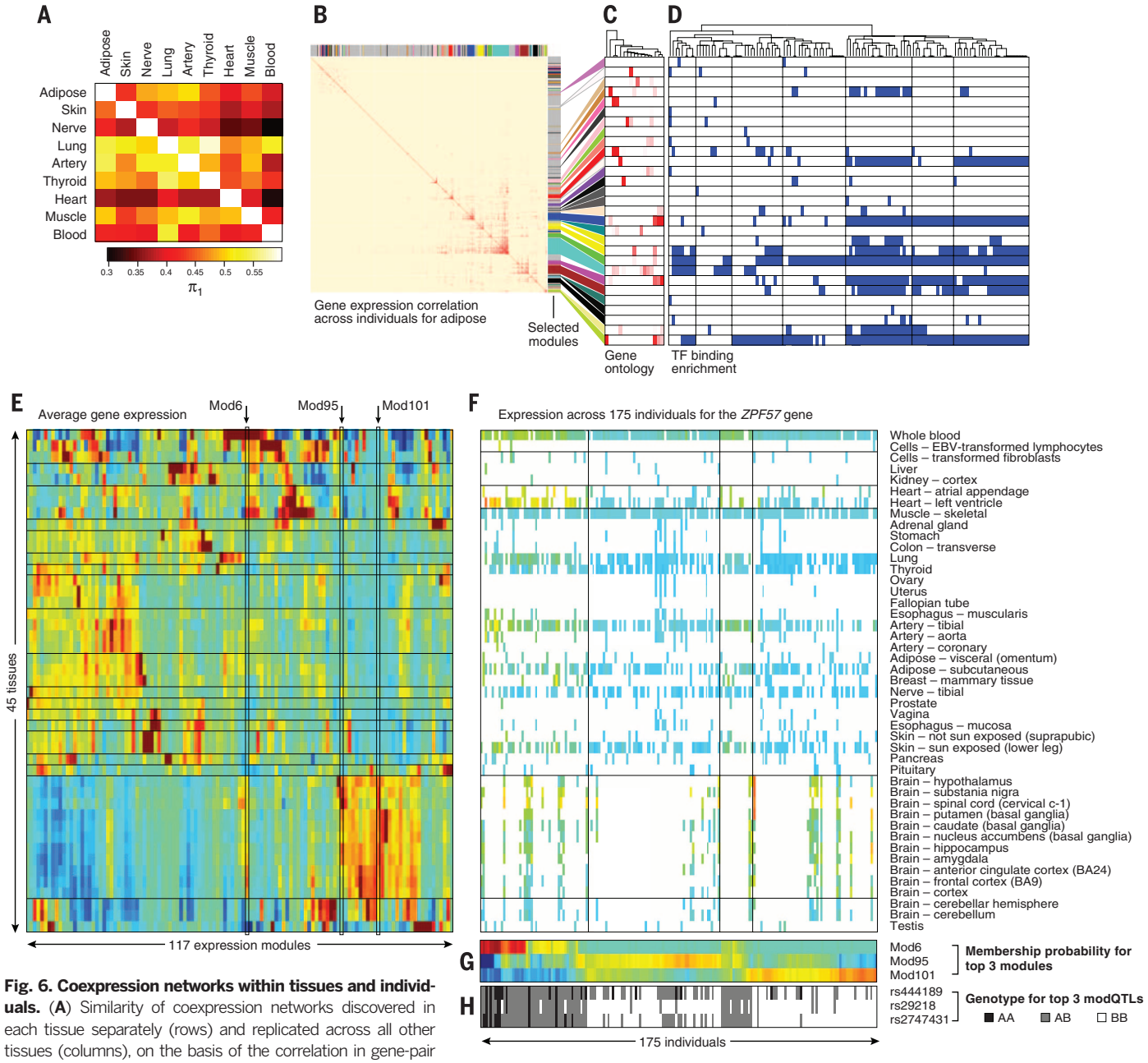

Fig. 6. Coexpression networks within tissues and individuals. (**A**) Similarity of coexpression networks discovered in each tissue separately (rows) and replicated across all other tissues (columns), on the basis of the correlation in gene-pair expression levels across all individuals for a given tissue, as quantified by the π_1 statistic. The tissues in this heat map are ordered as in Fig. 2B. (**B**) Coexpression modules learned within adipose tissue on the basis of weighted gene coexpression network analysis (WGCNA). The heat map shows the similarity in gene expression patterns (across individuals) for each pair of genes expressed within adipose tissue (red = high correlation, blue = low correlation). Non-gray colors highlight separate modules. (**C** and **D**) Genes in the same adipose coexpressed module [(C), rows] show enrichment for similar gene ontology (GO) categories (columns) and are co-bound by the same transcription factors (TF) [(D), columns] in their transcription start site (blue = Benjamini-Hochberg corrected P < 0.01). Dendrogram (top) denotes TF-to-TF similarity in module targeting. (**E**) Average expression level (red = high, blue = low) in each tissue (rows) across 117 expression modules (columns). Modules highlighted include Mod6, showing highest expression in whole blood and cortex; Mod95, showing highest expression in noncortex brain; and Mod101, showing brainwide expression. (**F**) Expression pattern of 175 individuals (columns) across 45 tissues (rows) for the *ZFP57* gene encoding a KRAB domain transcription factor. Colored entries denote expression levels (heat map). White entries denote missing expression measurements for an individual in a given tissue. (**G**) Probability of membership of each individual (columns) in each expression module (rows) for the three most significant modules [highlighted in (E)]. (**H**) Genotype of the three top modQTL SNPs (rows) across individuals (columns) shows correlation with module membership probability.

together account for only 42% of modQTL SNPs. Hence, 58% of modQTLs are not discovered by other methods, which suggests that the approach has the potential to reveal novel genetic effects on the modulation of genes across tissues (fig. S31C).

Personal transcriptomics and implications for human disease

The in-depth analysis of multitissue transcriptomes enables both an understanding of the population-level properties of the transcriptome as well as individual level properties inferred from analyses of single transcriptomes or the transcriptomes of multiple tissues from a single individual. As is the case for personalized genomics, this individual-level transcriptome analysis is likely to become a crucial addition to the personalized assessment of an individual's biology and likely disease status.

Impact of individual gene-disrupting variants on splicing and expression

Assessing the functional impact of DNA sequence variants identified in whole-genome and exome sequencing studies remains a major challenge. Variants predicted to result in the truncation of proteins (splice, stop-gain SNVs, or frame-shift indels) may have large effects on biochemical function, but are also highly enriched for annotation artifacts (*43*). Errors in predicting the true functional impact of these and other variants can substantially reduce discovery power in common complex diseases and, more important, can affect disease diagnosis in clinical settings (*44*).

The GTEx multitissue expression data provide an opportunity to assess the real impact of protein-truncating variants (PTVs) on the human

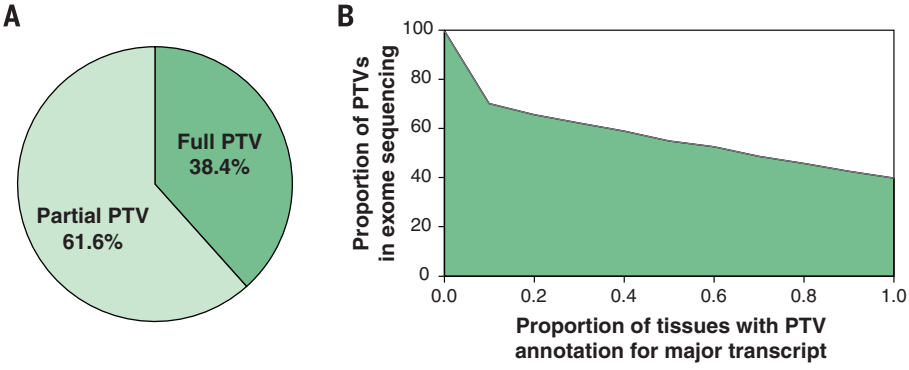

Fig. 7. Integration of transcriptome data improves annotation of putative protein truncating variants (PTVs). (**A**) The majority of annotated PTV variants are partial PTV, meaning that only a fraction of the RNA-seq transcripts support PTV annotation. (**B**) For all the predicted PTV variants, we ask what percentage of variants maintain a PTV annotation if we require that a fixed percentage of the dominant isoforms across all sequenced tissues support a PTV prediction; 70% of PTV variants are relevant if the threshold is 10%, whereas only 40% of PTV variants are relevant if the threshold is 100%.

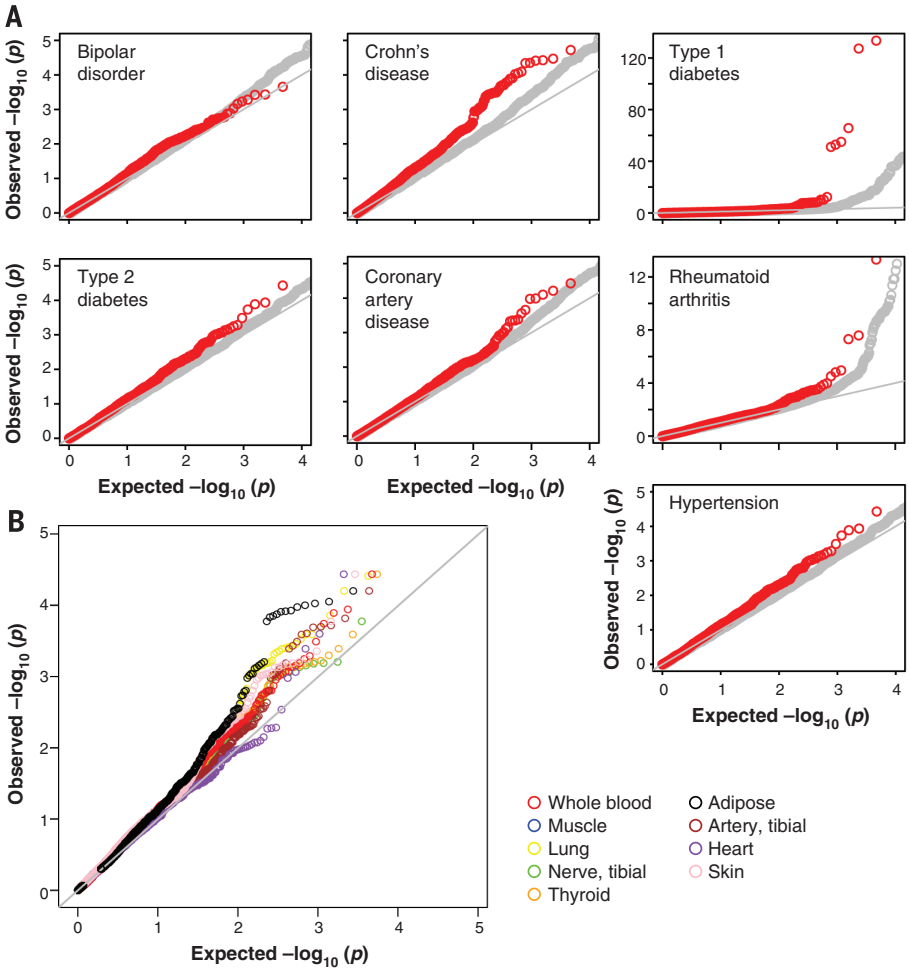

Fig. 8. Tissue-dependent GWAS eQTL enrichment Q-Q plots. (**A**) eQTLs are enriched for trait associations with an important class of complex diseases. eQTLs discovered in whole blood (plotted in red) show significant enrichment for SNPs associated with autoimmune disorders from the WTCCC study (type 1 diabetes, Crohn's disease, and rheumatoid arthritis) relative to null expectation (shown in gray) defined by non-eQTLs. (**B**) Enrichment of eQTLs for disease associations is tissue-dependent. Single-tissue eQTL annotation can be used to increase power to detect associations with hypertension, a disease for which the WTCCC study failed to yield significant associations. Notably, eQTLs discovered in adipose are enriched relative to muscle, lung, thyroid, skin, heart, and tibial artery ($P < 0.05$, Kolmogorov-Smirnov test) for known SNP associations with the hypertension.

transcriptome [see also (*31*)]. We combined exome sequencing and RNA-seq data from 173 GTEx individuals to assess the global properties of predicted high-confidence PTVs (*14*). PTVs are enriched in alternatively spliced exons, with just 38.4% of high-confidence PTVs having annotation support across all reported transcripts (Fig. 7A), and only 51 to 55% supported by the major transcript of at least one tissue (for all tissues with at least 10 samples). These numbers highlight the need for careful transcript-specific assessment of functional annotation for all classes of variation. Furthermore, if we require that a fixed percentage of the dominant isoforms across all sequenced tissues support this annotation, we find that the percentage of predicted PTVs with annotation support of PTV decreases as we increase the threshold for the proportion of tissues with major transcript isoform support for PTV prediction (Fig. 7B). This highlights the need for empirically derived reference transcript sets across a broad array of tissues to enhance clinical interpretation for personal genome sequencing and disease studies. An example with clinical ramifications is shown in fig. S32.

GWAS and eQTLs

The ultimate goal of the GTEx project is to provide a framework for biological interpretation of disease-related variants. To evaluate the relevance of the discovered eQTLs in disease mapping studies, we tested the eQTLs identified in each tissue for association with disease using the Wellcome Trust Case Control Consortium (WTCCC) studies of seven complex disorders (*45*) (see Fig. 8A). Using eQTLs identified in whole blood, we found an enrichment for top associations with autoimmune diseases (shown as a leftward shift from the null distribution in the Q-Q plot in Fig. 8A), for Crohn's disease, rheumatoid arthritis, and type 1 diabetes among eQTLs ($P < 2.2 \times 10^{-16}$ for each disease), consistent with the utility of blood and lymphoblastoid cell lines (LCLs) in trait mapping for autoimmune disorders (*46*, *47*). In contrast to the autoimmune disorders, we found no enrichment for association (no shift in P value distribution) with bipolar disorder or type 2 diabetes among the blood eQTLs ($P > 0.05$) (Fig. 8A). This tissue specificity of autoimmune enrichment results suggests they are not due to the confounding effects that result from similar underlying genomic properties between eQTL and disease association regions. More generally, we observed trait-specific levels of enrichment for the WTCCC disease traits among the nine different single-tissue eQTL sets.

Remarkably, the use of eQTLs increased power to detect associations with hypertension (Fig. 8B). In particular, eQTLs in subcutaneous adipose were significantly enriched for multiple associations with hypertension relative to muscle, lung, thyroid, skin, heart, and tibial artery ($P < 0.05$, Kolmogorov-Smirnov test) (Fig. 8B). This is particularly noteworthy because the WTCCC GWAS of this disease did not yield any genome-wide significant associations, which suggests that larger sample sizes were required to identify highly significant SNP associations in the absence of functional data. Because the majority of GWAS-identified variants (~95%) lie in non-coding regions of the genome, we determined

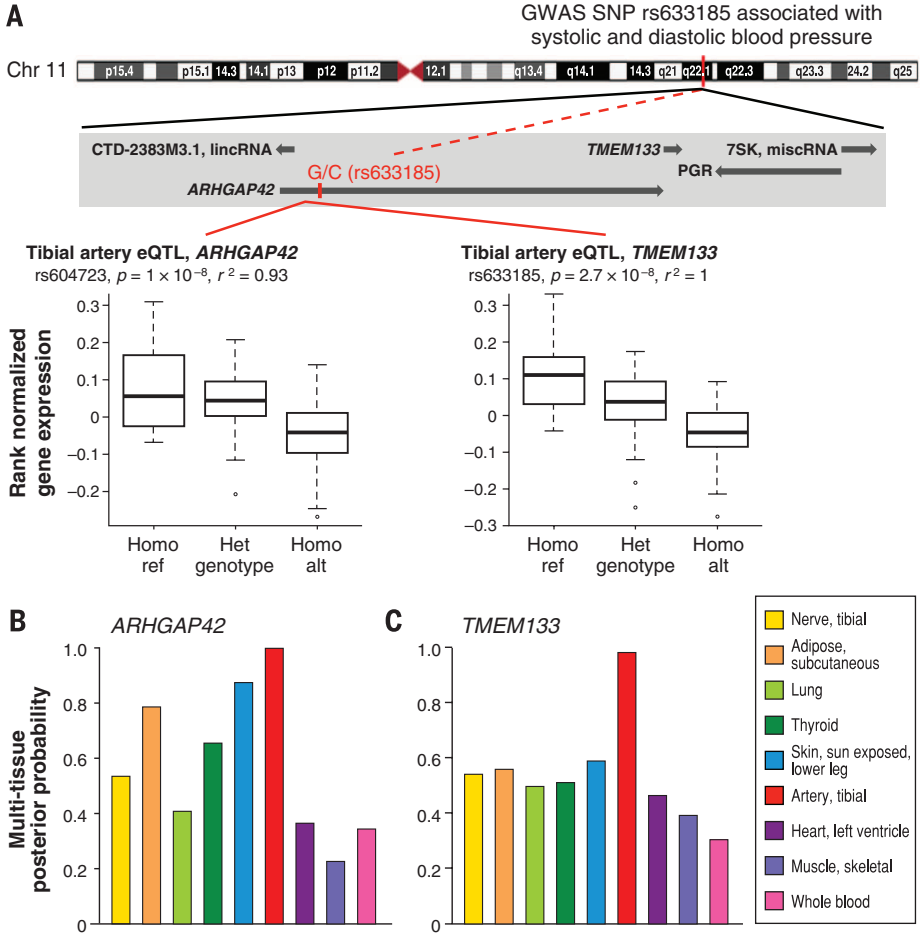

Fig. 9. A blood pressure-associated SNP is a significant eQTL in tibial artery, for *ARHGAP42* and *TMEM133*. (**A**) The GWAS SNP, rs633185 in the intron of *ARHGAP42*, is associated with systolic blood pressure ($P = 1.2 \times 10^{-17}$) and diastolic blood pressure ($P = 2 \times 10^{-15}$). This GWAS SNP is in tight LD ($r^2 = 0.93$) with the most significant eQTL for *ARHGAP42* in tibial artery, rs604723 ($P = 1 \times 10^{-8}$), and is the most significant eQTL for *TMEM133* in tibial artery ($P = 2.7 \times 10^{-8}$). Tibial artery was the only significant tissue at FDR < 0.05 according to the single-tissue eQTL discovery method. (**B**) Average posterior probability of the most significant cis-eQTL, rs607562 for *ARHGAP42* at FDR < 0.05 from the multitissue eQTL methods. (**C**) Similar plot for *TMEM133*. The most significant cis-eQTL for *TMEM133* from the multitissue methods at FDR < 0.05 is the GWAS SNP, rs633185, in tibial artery.

which genome-wide significant trait associations ($P < 5 \times 10^{-8}$) reported to date are in LD with at least one GTEx-identified eQTL. We merged NCBI's Phenotype-Genotype Integrator (PheGenI) (*48*) and the NHGRI GWAS catalog (*49*), yielding 10,129 genome-wide significant SNP associations with nearly 630 distinct complex traits. In total, 5195 "independent" SNPs were identified after LD pruning at $r^2 \geq 0.8$ and counting SNPs only once (*14*). Of these, 308 (~6%) are in strong LD ($r^2 \geq 0.8$), with a "best eQTL per gene" (at FDR < 0.05) from either the single-tissue or multitissue eQTL discovery analysis (table S12) in at least one of the nine tissues tested. For two-thirds of these cases (211 SNPs), no putative deleterious coding variants (nonsynonymous or splice variants) in the target gene product lie in LD ($r^2 \geq 0.8$) with the GWAS SNP; this finding suggests that regulatory effects may underlie the causal mechanism, although additional work is needed to prove causality. GWAS SNPs in LD with an eQTL show a factor of 2 higher representation in coding regions relative to all GWAS SNPs (11% versus 4.6%; table S13). Notably, about one-third of the eQTLs in LD with GWAS SNPs were detected only with methods that leverage the multitissue nature of GTEx data. Increasing both sample sizes and the range of tissues will likely increase the number of detected GWAS-eQTL loci.

Annotating a GWAS SNP with an eQTL can help to highlight candidate causal genes within a locus (i.e., the eQTL target gene). We found that proximity-based and eQTL-based gene assignments for GWAS SNPs were often discordant (*47*). A surprising proportion of trait-associated SNPs in LD ($r^2 \geq 0.80$) with a GTEx eQTL showed disagreement between the strongest eQTL-derived target gene and the genes that were physically proximal to the GWAS SNP (table S14). Of 190 GWAS loci ($P < 5 \times 10^{-8}$) where the lead SNP is an eQTL from the single-tissue analysis (FDR < 0.05) with only a single target gene, in 65 cases (~34%) this eQTL target gene differs from any of the genes that were closest to the SNPs in LD. These results were also observed when we restricted the target genes to protein-coding genes, when we pruned the GWAS SNPs for each trait examined ($r^2 \geq 0.80$), and when we used the eQTLs identified from the multitissue joint eQTL analysis.

In addition to prioritizing causal genes in GWAS loci, an eQTL catalog from multiple human tissues can highlight the relevant tissue(s) of action, evaluate the tissue specificity of GWAS loci, and characterize pleiotropic associations. We demonstrate the value of multitissue data to explore and resolve these issues for the GWAS intronic SNP, rs633185, located in *ARHGAP42* (Fig. 9). This GWAS SNP is in high LD ($r^2 = 0.93$) with the best cis-eQTL (rs604723) targeting *ARHGAP42*, and the best cis-eQTL for a neighboring gene, *TMEM133* in tibial artery. Evaluating eQTL significance in all nine tissues shows that although the eQTL's significance is indeed strongest in tibial artery, several other tissues may merit consideration in exploring the causal function of this locus, such as subcutaneous adipose and skin (Fig. 9, B and C, and fig. S33). This supports the need to explore the genetic basis of disease in the fuller context of a wide range of human tissues. The GTEx eQTLs may also be useful in highlighting the role of noncoding genes in disease risk and other complex traits (fig. S34). We found that ~13% of candidate genes proposed by GTEx eQTLs, and in LD to genome-wide significant GWAS SNPs, are noncoding genes (table S15).

Conclusions

We have described a large in-depth data set of multitissue human gene expression. We assessed the variability of the transcriptome among individuals in a large number of tissues at a resolution that provides unique insights in to the diversity and regulation of gene expression among tissues. This analysis provides a unified view of genetic effects on gene expression across a broad range of tissue types, most of which have not been studied for eQTLs previously. We look forward to scaling up the resource to create a data set that will transform our understanding of how genetic variability influences different tissues and biological systems and ultimately complex diseases.

REFERENCES AND NOTES

1. D. Welter *et al.*, *Nucleic Acids Res.* **42**, D1001–D1006 (2014).
2. P. M. Visscher, M. A. Brown, M. I. McCarthy, J. Yang, *Am. J. Hum. Genet.* **90**, 7–24 (2012).
3. B. E. Stranger, E. A. Stahl, T. Raj, *Genetics* **187**, 367–383 (2011).
4. L. D. Ward, M. Kellis, *Nat. Biotechnol.* **30**, 1095–1106 (2012).
5. M. T. Maurano *et al.*, *Science* **337**, 1190–1195 (2012).
6. M. Morley *et al.*, *Nature* **430**, 743–747 (2004).
7. H. J. Westra *et al.*, *Nat. Genet.* **45**, 1238–1243 (2013).
8. E. Grundberg *et al.*, *Nat. Genet.* **44**, 1084–1089 (2012).
9. J. Ernst *et al.*, *Nature* **473**, 43–49 (2011).
10. ENCODE Project Consortium, *Nature* **489**, 57–74 (2012).
11. B. F. Voight *et al.*, *Nat. Genet.* **42**, 579–589 (2010).
12. K. S. Small *et al.*, *Nat. Genet.* **43**, 561–564 (2011).
13. GTEx Consortium, *Nat. Genet.* **45**, 580–585 (2013).
14. See supplementary materials on *Science* Online.
15. J. Harrow *et al.*, *Genome Res.* **22**, 1760–1774 (2012).
16. H. J. Kang *et al.*, *Nature* **478**, 483–489 (2011).
17. M. Melé *et al.*, *Science* **348**, 660–665 (2015).
18. N. L. Barbosa-Morais *et al.*, *Science* **338**, 1587–1593 (2012).
19. G. Yeo, D. Holste, G. Kreiman, C. B. Burge, *Genome Biol.* **5**, R74 (2004).
20. A. S. Dimas *et al.*, *Science* **325**, 1246–1250 (2009).
21. A. A. Shabalin, *Bioinformatics* **28**, 1353–1358 (2012).
22. A. C. Nica *et al.*, *PLOS Genet.* **7**, e1002003 (2011).
23. J. B. Veyrieras *et al.*, *PLOS Genet.* **4**, e1000214 (2008).
24. T. Flutre, X. Wen, J. Pritchard, M. Stephens, *PLOS Genet.* **9**, e1003486 (2013).
25. G. Li, A. A. Shabalin, I. Rusyn, F. A. Wright, A. B. Nobel, http://arxiv.org/abs/1311.2948 (2013).
26. J. D. Storey, R. Tibshirani, *Proc. Natl. Acad. Sci. U.S.A.* **100**, 9440–9445 (2003).
27. X. Wen, http://arxiv.org/abs/1311.3981 (2013).
28. X. Wen, *Biometrics* **70**, 73–83 (2014).
29. J. H. Sul, B. Han, C. Ye, T. Choi, E. Eskin, *PLOS Genet.* **9**, e1003491 (2013).
30. C. Newton-Cheh *et al.*, *Nat. Genet.* **41**, 399–406 (2009).
31. M. A. Rivas *et al.*, *Science* **348**, 666–669 (2015).
32. E. Khurana *et al.*, *Science* **342**, 1235587 (2013).
33. A. Chess, *Nat. Rev. Genet.* **13**, 421–428 (2012).
34. A. Buil *et al.*, *Nat. Genet.* **47**, 88–91 (2015).
35. H. Ongen, E.T. Dermitzakis, http://biorxiv.org/content/early/2015/01/22/014126 (2015).
36. J. Monlong, M. Calvo, P. G. Ferreira, R. Guigó, *Nat. Commun.* **5**, 4698 (2014).
37. L. D. Ward, M. Kellis, *Nucleic Acids Res.* **40**, D930–D934 (2012).
38. D. J. Gaffney *et al.*, *Genome Biol.* **13**, R7 (2012).
39. A. Battle *et al.*, *Genome Res.* **24**, 14–24 (2014).
40. B. E. Bernstein *et al.*, *Nat. Biotechnol.* **28**, 1045–1048 (2010).
41. B. Zhang *et al.*, *Cell* **153**, 707–720 (2013).
42. M. B. Gerstein *et al.*, *Nature* **489**, 91–100 (2012).
43. D. G. MacArthur *et al.*, *Science* **335**, 823–828 (2012).
44. F. E. Dewey *et al.*, *JAMA* **311**, 1035–1045 (2014).
45. Wellcome Trust Case Control Consortium, *Nature* **447**, 661–678 (2007).
46. D. L. Nicolae *et al.*, *PLOS Genet.* **6**, e1000888 (2010).
47. A. C. Nica *et al.*, *PLOS Genet.* **6**, e1000895 (2010).
48. E. M. Ramos *et al.*, *Eur. J. Hum. Genet.* **22**, 144–147 (2014).
49. L. A. Hindorff *et al.*, *Proc. Natl. Acad. Sci. U.S.A.* **106**, 9362–9367 (2009).

ACKNOWLEDGMENTS

We thank the donors and their families for their generous gifts of organ donation for transplantation and tissue donations for the GTEx research study; the Genomics Platform at the Broad Institute for data generation; J. Nedzel, K. Huang, and K. Hadley for work on the GTEx Portal; L. Gaffney for help with figures; and members of the Analysis Working Group for scientific editing and feedback. The primary and processed data used to generate the analyses presented here are available in the following locations: all primary sequence and clinical data files, and any other protected data, are deposited in and available from dbGaP (www.ncbi.nlm.nih.gov/gap) (phs000424.v3.p1, except for whole-exome sequencing data, which are part of phs000424.v5.p1); derived analysis files are available on the GTEx Portal (www.gtexportal.org). Biospecimens remaining from the study may be requested for research studies. The sample request form, biospecimen access policy, and material transfer agreement (MTA) are available on the GTEx Portal (www.gtexportal.org/home/samplesPage). Supported by the Common Fund of the Office of the Director, U.S. National Institutes of Health, and by NCI, NHGRI, NHLBI, NIDA, NIMH, NIA, NIAID, and NINDS through NIH contracts HHSN261200800001E (Leidos Prime contract with NCI), 10XS170 (NDRI), 10XS171 (Roswell Park Cancer Institute), 10X172 (Science Care Inc.), 12ST1039 (IDOX), 10ST1035 (Van Andel Institute), and HHSN268201000029C (Broad Institute) and through NIH grants R01 DA006227-17 (Univ. of Miami Brain Bank), R01 MH090941 (Univ. of Geneva), R01 MH090951 and R01 MH090937 (Univ. of Chicago), R01 MH090936 (Univ. of North Carolina–Chapel Hill), R01 MH090948 (Harvard Univ.), R01 GM104371 (Massachusetts General Hospital), and R01AG046170, R01CA163772, and U01AI111598-01 (Icahn School of Medicine, Mount Sinai). Additional support: European Research Council, Swiss National Science Foundation, and Louis-Jeantet Foundation (E.T.D.); Wellcome Trust grant 098381 (M.I.M.); Clarendon Scholarship, a NDM Studentship, and a Univ. of Oxford Green Templeton College Award (M.A.R.). J.K.P. is compensated for his work on the scientific advisory board for 23andMe and computational advisory board for DNANexus; W.W. is an employee and shareholder of Novartis Inc.; A. Battle is a shareholder of Google, Inc.; J. Fleming is executive director of the American Medical and Research Association; and J.B.V. and R. Little serve on the board of NDRI. Author contributions: The GTEx Consortium contributed collectively to this study. Biospecimens were provided by the Biospecimen source sites and the brain bank operations, and processed by the LDACC and comprehensive biospecimen resource. Pathological review of specimens was conducted by the pathology resource center, and all donor data entry and review by the comprehensive data resource. Data generation was undertaken by the Laboratory, Data Analysis and Coordinating Center (LDACC), and analyses were performed by all members of the Analysis Working Group. Project activities were coordinated by caHUB operations and overseen by the NHGRI, NIMH, and NCI project teams. We acknowledge the following investigators of the Analysis Working Group who contributed substantially to analyses presented here. Transcriptome variation: D.S.D., P.G.F. Single-tissue eQTL analysis: A.A.S., D.S.D., A.V.S. Multitissue eQTL analysis: T.F., X.W., A.A.S., G.L. Allele-specific expression: T.L. Splice QTLs: J.M., H.O. Functional annotation: L.D.W., P.K. Network Analyses: A. Battle, S.M., Z.T., T.H., B.I. Protein-truncating analyses: M.A.R., M.L. GWAS analysis: E.R.G., A.V.S., L.D.W.

The GTEx Consortium

Authorship of this paper should be cited as "GTEx Consortium"; participants are arranged by area of contribution and then by institution. **Analysis Working Group** *LDACC:* Kristin G. Ardlie,[1]

David S. DeLuca,[1] Ayellet V. Segrè,[1] Timothy J. Sullivan,[1] Taylor R. Young,[1] Ellen T. Gelfand,[1] Casandra A. Trowbridge,[1] Julian B. Maller,[1,2] Taru Tukiainen,[1,2] Monkol Lek,[1,2] Lucas D. Ward,[1,3] Pouya Kheradpour,[1,3] Benjamin Iriarte,[3] Yan Meng,[1] Cameron D. Palmer,[1,4] Tõnu Esko,[1,4,5] Wendy Winckler,[1] Joel N. Hirschhorn,[1,4] Manolis Kellis,[1,3] Daniel G. MacArthur,[1,2] Gad Getz[1,6]; *UNC/NCSU:* Andrey A. Shabalin,[7] Gen Li,[8] Yi-Hui Zhou,[9] Andrew B. Nobel,[8] Ivan Rusyn,[10,11] Fred A. Wright[9]; *Univ. of Geneva:* Tuuli Lappalainen,[12,13,14,15,16,17] Pedro G. Ferreira,[12,13,14] Halit Ongen,[12,13,14] Manuel A. Rivas,[18] Alexis Battle,[19,20] Sara Mostafavi,[19] Jean Monlong,[21,22,23] Michael Sammeth,[21,22,24] Marta Melé,[21,22,25] Ferran Reverter,[21,26] Jakob M. Goldmann,[21,27] Daphne Koller,[19] Roderic Guigó,[21,22,28] Mark I. McCarthy,[18,29,30] Emmanouil T. Dermitzakis[12,13,14]; *Univ. of Chicago:* Eric R. Gamazon,[31,32] Hae Kyung Im,[31] Anuar Konkashbaev,[31,32] Dan L. Nicolae,[31] Nancy J. Cox,[31,32] Timothée Flutre,[33,34] Xiaoquan Wen,[35] Matthew Stephens,[33,36] Jonathan K. Pritchard[33,37,38]; *Harvard:* Zhidong Tu,[39,40] Bin Zhang,[39,40] Tao Huang,[39,40] Quan Long,[39,40] Luan Lin,[39,40] Jialiang Yang,[39,40] Jun Zhu,[39,40] Jun Liu[41]

Biospecimen and data collection, processing, quality control, storage, and pathological review *caHUB Biospecimen Source Sites, National Disease Research Interchange (NDRI):* Amanda Brown,[42] Bernadette Mestichelli,[42] Denee Tidwell,[42] Edmund Lo,[42] Michael Salvatore,[42] Saboor Shad,[42] Jeffrey A. Thomas,[42] John T. Lonsdale[42]; *Roswell Park:* Michael T. Moser,[43] Bryan M. Gillard,[43] Ellen Karasik,[43] Kimberly Ramsey,[43] Christopher Choi,[43] Barbara A. Foster[43]; *Science Care Inc.:* John Syron,[44] Johnell Fleming,[44] Harold Magazine,[44]; *Gift of Life Donor Program:* Rick Hasz[45]; *LifeNet Health:* Gary D. Walters[46]; *UNYTS:* Jason P. Bridge,[47] Mark Miklos,[47] Susan Sullivan[47]

caHUB ELSI study *VCU:* Laura K. Barker,[48] Heather M. Traino,[48,49] Maghboeba Mosavel,[48] Laura A. Siminoff[48,49]

caHUB comprehensive biospecimen resource *Van Andel Research Institute:* Dana R. Valley,[50] Daniel C. Rohrer,[50] Scott D. Jewell[50]

caHUB pathology resource center *NCI:* Philip A. Branton[51]; *Leidos Biomedical Research Inc.:* Leslie H. Sobin,[52] Mary Barcus[52]

caHUB comprehensive data resource *Leidos Biomedical Research Inc.:* Liqun Qi,[52] Jeffrey McLean,[52] Pushpa Hariharan,[52] Ki Sung Um,[52] Shenpei Wu,[52] David Tabor,[52] Charles Shive[52]

caHUB operations management *Leidos Biomedical Research Inc.:* Anna M. Smith,[52] Stephen A. Buia,[52] Anita H. Undale,[52] Karna L. Robinson,[52] Nancy Roche,[52] Kimberly M. Valentino,[52] Angela Britton,[52] Robin Burges,[52] Debra Bradbury,[52] Kenneth W. Hambright,[52] John Seleski,[53] Greg E. Korzeniewski[52]; *Sapient Government Services:* Kenyon Erickson[54]

Brain bank operations *University of Miami:* Yvonne Marcus,[55] Jorge Tejada,[55] Mehran Taherian,[55] Chunrong Lu,[55] Margaret Basile,[55] Deborah C. Mash[55]

Program management *NHGRI:* Simona Volpi,[56] Jeffery P. Struewing,[56] Gary F. Temple,[56] Joy Boyer,[57] Deborah Colantuoni[56]; *NIMH:* Roger Little,[58] Susan Koester[59]; *NCI:* Latarsha J. Carithers,[51] Helen M. Moore,[51] Ping Guan,[51] Carolyn Compton,[51] Sherilyn J. Sawyer,[51] Joanne P. Demchok,[60] Jimmie B. Vaught,[51] Chana A. Rabiner,[51] Nicole C. Lockhart[51,57]

Writing committee Kristin G. Ardlie,[1] Gad Getz,[1,6] Fred A. Wright,[9] Manolis Kellis,[1,3] Simona Volpi,[56] Emmanouil T. Dermitzakis[12,13,14]

[1]Broad Institute of MIT and Harvard, Cambridge, MA 02142, USA. [2]Analytic and Translational Genetics Unit, Massachusetts General Hospital, Boston, MA 02114, USA. [3]MIT Computer Science and Artificial Intelligence Laboratory, Massachusetts Institute of Technology, Cambridge, MA 02139, USA. [4]Center for Basic and Translational Obesity Research and Division of Endocrinology, Boston Children's Hospital, Boston, MA 02115, USA. [5]Estonian Genome Center, University of Tartu, Tartu, Estonia. [6]Cancer Center and Department of Pathology, Massachusetts General Hospital, Boston, MA 02114, USA. [7]Center for Biomarker Research and Personalized Medicine, Virginia Commonwealth University, Richmond, VA 23298, USA. [8]Department of Statistics and Operations Research and Department of Biostatistics, University of North Carolina, Chapel Hill, NC 27599, USA. [9]Bioinformatics Research Center and Departments of Statistics and Biological Sciences, North Carolina State University, Raleigh, NC 27695, USA. [10]Department of Environmental Sciences and Engineering, University of North Carolina, Chapel Hill, NC 27599. [11]Department of Veterinary Integrative Biosciences, Texas A&M University, College Station, TX 77843, USA. [12]Department of Genetic Medicine and Development, University of Geneva Medical School, 1211 Geneva, Switzerland. [13]Institute for Genetics and Genomics in Geneva (iG3), University of Geneva, 1211 Geneva, Switzerland. [14]Swiss Institute of Bioinformatics, 1211 Geneva, Switzerland. [15]Department of Genetics, Stanford University, Stanford, CA 94305, USA. [16]New York Genome Center, New York, NY 10011, USA. [17]Department of Systems Biology, Columbia University Medical Center, New York, NY 10032, USA. [18]Wellcome Trust Centre for Human Genetics Research, Nuffield Department of Clinical Medicine, University of Oxford, Oxford OX3 7BN, UK. [19]Department of Computer Science, Stanford University, Stanford, CA 94305, USA. [20]Department of Computer Science, Johns Hopkins University, Baltimore, MD 21218, USA. [21]Centre for Genomic Regulation (CRG), 08003 Barcelona, Catalonia, Spain. [22]Universitat Pompeu Fabra, 08003 Barcelona, Catalonia, Spain. [23]Human Genetics Department, McGill University, Montréal, Quebec H3A 0G1, Canada. [24]National Institute for Scientific Computing, Petropolis 25651-075, Rio de Janeiro, Brazil. [25]Department of Stem Cell and Regenerative Biology, Harvard University, Cambridge, MA 02138, USA. [26]Universitat de Barcelona, 08028 Barcelona, Spain. [27]Radboud University Nijmegen, Netherlands. [28]Institut Hospital del Mar d'Investigacions Mèdiques (IMIM), 08003 Barcelona, Spain. [29]Oxford Centre for Diabetes, Endocrinology and Metabolism, University of Oxford, Churchill Hospital, Oxford OX3 7LJ, UK. [30]Oxford NIHR Biomedical Research Centre, Churchill Hospital, Oxford OX3 7LJ, UK. [31]Section of Genetic Medicine, Department of Medicine and Department of Human Genetics, University of Chicago, Chicago, IL 60637, USA. [32]Division of Genetic Medicine, Department of Medicine, Vanderbilt University, Nashville, TN 37232, USA. [33]Department of Human Genetics, University of Chicago, Chicago, IL 60637, USA. [34]INRA, Department of Plant Biology and Breeding, UMR 1334, AGAP, Montpellier, 34060, France. [35]Department of Biostatistics, University of Michigan, Ann Arbor, MI 48109, USA. [36]Department of Statistics, University of Chicago, Chicago, IL 60637, USA. [37]Department of Genetics and Biology, Stanford University, Stanford, CA 94305, USA. [38]Howard Hughes Medical Institute, Chicago, IL, USA. [39]Department of Genetics and Genomic Sciences, Icahn School of Medicine at Mount Sinai, New York, NY 10029, USA. [40]Icahn Institute of Genomics and Multiscale Biology, Icahn School of Medicine at Mount Sinai, New York, NY 10029, USA. [41]Department of Statistics, Harvard University, Cambridge, MA 02138. [42]National Disease Research Interchange, Philadelphia, PA 19103, USA. [43]Roswell Park Cancer Institute, Buffalo, NY 14263, USA. [44]Science Care Inc., Phoenix, AZ, USA. [45]Gift of Life Donor Program, Philadelphia, PA 19103, USA. [46]LifeNet Health, Virginia Beach, VA 23453, USA. [47]UNYTS, Buffalo, NY 14203, USA. [48]Virginia Commonwealth University, Richmond, VA 23298, USA. [49]Department of Public Health, Temple University, Philadelphia, PA 19122, USA. [50]Van Andel Research Institute, Grand Rapids, MI 49503, USA. [51]Biorepositories and Biospecimen Research Branch, National Cancer Institute, Bethesda, MD 20892, USA. [52]Biospecimen Research Group, Clinical Research Directorate, Leidos Biomedical Research, Inc., Rockville, MD 20852, USA. [53]iDoxSolutions Inc., Bethesda, MD 20814, USA. [54]Sapient Government Services, Arlington, VA 22201, USA. [55]Brain Endowment Bank, Department of Neurology, Miller School of Medicine, University of Miami, Miami, FL 33136, USA. [56]Division of Genomic Medicine, National Human Genome Research Institute, Bethesda, MD 20892, USA. [57]Division of Genomics and Society, National Human Genome Research Institute, Bethesda, MD 20892, USA. [58]Office of Science Policy, Planning, and Communications, National Institute of Mental Health, Bethesda, MD 20892, USA. [59]Division of Neuroscience and Basic Behavioral Science, National Institute of Mental Health, Bethesda, MD 20892, USA. [60]Cancer Diagnosis Program, National Cancer Institute, Bethesda, MD 20892, USA.

SUPPLEMENTARY MATERIALS

www.sciencemag.org/content/348/6235/648/suppl/DC1
Materials and Methods
Box S1
Figs. S1 to S34
Tables S1 to S15
References (*50*–*86*)

3 October 2014; accepted 3 April 2015
10.1126/science.1262110

REPORTS

HUMAN GENOMICS

The human transcriptome across tissues and individuals

Marta Melé,[1,2]* Pedro G. Ferreira,[1,3,4,5]* Ferran Reverter,[1,6,7]* David S. DeLuca,[8] Jean Monlong,[1,7,9] Michael Sammeth,[1,7,10] Taylor R. Young,[8] Jakob M Goldmann,[1,7,11] Dmitri D. Pervouchine,[1,7,12] Timothy J. Sullivan,[8] Rory Johnson,[1,7] Ayellet V. Segrè,[8] Sarah Djebali,[1,7] Anastasia Niarchou,[3,4,5] The GTEx Consortium, Fred A. Wright,[13] Tuuli Lappalainen,[3,4,5,14,15] Miquel Calvo,[6] Gad Getz,[8,16] Emmanouil T. Dermitzakis,[3,4,5] Kristin G. Ardlie,[8]† Roderic Guigó[1,7,17,18]†

Transcriptional regulation and posttranscriptional processing underlie many cellular and organismal phenotypes. We used RNA sequence data generated by Genotype-Tissue Expression (GTEx) project to investigate the patterns of transcriptome variation across individuals and tissues. Tissues exhibit characteristic transcriptional signatures that show stability in postmortem samples. These signatures are dominated by a relatively small number of genes—which is most clearly seen in blood—though few are exclusive to a particular tissue and vary more across tissues than individuals. Genes exhibiting high interindividual expression variation include disease candidates associated with sex, ethnicity, and age. Primary transcription is the major driver of cellular specificity, with splicing playing mostly a complementary role; except for the brain, which exhibits a more divergent splicing program. Variation in splicing, despite its stochasticity, may play in contrast a comparatively greater role in defining individual phenotypes.

Gene expression is the key determinant of cellular phenotype, and genome-wide expression analysis has been a mainstay of genomics and biomedical research, providing insights into the molecular events underlying human biology and disease. Whereas expression data sets from tissues/primary cells (*1*, *2*) and individuals (*3*) have accumulated over recent years, only limited expression data sets have allowed analysis across tissues and individuals

simultaneously (*4*). The Genotype-Tissue Expression Project (GTEx) is developing such a resource (*5*, *6*), collecting multiple "nondiseased" tissues sampled from recently deceased human donors. We analyzed the GTEx pilot data freeze (*6*), which comprised RNA sequencing (RNA-seq) from 1641 samples from 175 individuals representing 43 sites: 29 solid organ tissues, 11 brain subregions, whole blood, and two cell lines: Epstein-Barr virus–transformed lymphocytes (LCL) and cultured fibroblasts from skin [table S1 and (*7*)].

The identification and characterization of genetic variants that are associated with gene expression are extensively discussed in (*6*). Here we use the GTEx data to investigate the patterns of transcriptome variation across individuals and tissues and how these patterns associate with human phenotypes. RNA-seq performed on the GTEx pilot samples produced an average of 80 million paired-end mapped reads per sample (fig. S1) (*7*, *8*). We used the mapped reads to quantify gene expression using Gencode V12 annotation (*9*), which includes 20,110 protein-coding genes (PCGs) and 11,790 long noncoding RNAs (lncRNAs). Comparison with microarray-based quantification for a subset of 736 samples showed concordance between the two technologies (average correlation coefficient = 0.83, fig. S2). At the threshold defined for expression quantitative trait loci (eQTL) analysis [reads per kilobase per million mapped reads (RPKM) > 0.1, see (*7*)], at which 88% of PCGs and 71% of lncRNAs are detected in at least one sample, the distribution of gene expression across tissues is U-shaped and complementary between PCGs (generally ubiquitously expressed) and lncRNAs (typically tissue-specific or not expressed, Fig. 1A).

Tissues show a characteristic transcriptional signature, as revealed by multidimensional scaling, of both PCG and lncRNA expression (figs. 1B, S3, and S4), with individual phenotypes contributing little (fig. S5). The primary separation, as observed in prior studies (*10*), is between nonsolid (blood) and solid tissues and, within solid tissues, brain is the most distinct. Brain subregions are not well differentiated, with the exception of cerebellum (fig. S6). Postmortem ischemia appears to have little impact on the characteristic tissue transcriptional signatures, as previously noted (*11*). In a comparison of 798 GTEx samples with 609 "nondiseased" samples obtained from living (surgical) donors (table S2), we found that GTEx samples clustered with surgical samples of the same tissue type (Fig. 1C and table S3) (*12*).

Tissue transcription is generally dominated by the expression of a relatively small number of genes. Indeed, we found that for most tissues, about 50% of the transcription is accounted for by a few hundred genes (*13*). In many tissues, the bulk of transcription is of mitochondrial origin (Fig. 1D and table S4) (*14*). In kidney, for instance, a highly aerobic tissue with many mitochondria, a median of 51% (>65% in some samples) of the transcriptional output is from the mitochondria (fig. S7). Other tissues show nuclear-dominated expression; in blood, for example, three hemoglobin genes contribute more than 60% to total transcription. Genes related to lipid metabolism in pancreas, actin in muscle, and thyroglobulin in thyroid are other examples of nuclear genes contributing disproportionally to tissue-specific transcription. Because RNA samples are generally sequenced to the same depth, in tissues where a few genes dominate expression, fewer RNA-seq reads are comparatively available to estimate the expression of the remaining genes, decreasing the power to estimate expression variation. These tissues—i.e., blood, muscle, and heart (Fig. 1E)—are, consequently, those with less power to detect eQTLs (*6*). Because most eQTL analyses are performed on easily accessible samples, such as blood, this highlights the relevance of the GTEx multitissue approach.

Although thousands of genes are differentially expressed between tissues (fig. S8) or show tissue-preferential expression (fig. S9 and table S5), fewer than 200 genes are expressed exclusively in a given tissue (figs. S10 and S11 and tables S6 and S7, A to E). The vast majority (~ 95%) are exclusive to testis and many are lncRNAs. This may reflect low-level basal transcription common to all cell types or result from general tissue heterogeneity, with few primary cell types being specific to a given tissue.

Expression of repetitive elements also recapitulates tissue type (table S8 and fig. S12A). We identified 3046 PCGs whose expression, in at least one tissue, was correlated with the expression of the closest repeat element (on average 2827 base pairs away, fig. S12B). In about half of these cases, the repeat was also significantly coexpressed with other repeats of its same family (table S8 and fig. S13). LncRNA expression can be regulated by specific repeat families (*15*), and we found evidence that testis-specific expression could be regulated by endogenous retrovirus L repeats (ERVL and ERVL-MaLR) (fig. S12C).

Using linear mixed models, we found that variation in gene expression is far greater among tissues (47% of total variance in gene expression) than among individuals (4% of total variance, Fig. 2A and table S9), and very similar for PCGs and lncRNAs when controlling for gene expression (Fig. 2A). Genes that show high expression variance across individuals and low variance across tissues include genes on the sex chromosomes, as well as autosomal genes, such as the *RHD* gene that determines Rh blood group.

We identified 92 PCGs and 43 lncRNAs with global sex-biased expression [false discovery rate (FDR) < 0.05, Fig. 2B and table S10]. Genes overexpressed in males are predominantly located on the Y chromosome. Conversely, many genes on the X chromosome are overexpressed in females, suggesting that more genes might escape X inactivation than previously described (*16*). Among these, we found *XIST* and *JPX*, known to participate in X inactivation, as well as the lncRNAs RP11-309M23.1 and RP13-216E22.4, the expression of which shows enrichment in the nucleus in female cell lines from ENCODE (*17*) and hence could be candidates to also participate in X inactivation (fig. S14) (*16*). Among autosomal PCGs, *MMP3*, linked to susceptibility to coronary heart disease [Online Mendelian Inheritance in Man (OMIM) no. 614466] and more prevalent in males, shows the strongest expression bias (Fig. 2B).

We detected 221 PCGs and 153 lncRNAs globally differentially expressed between individuals of European and African-American ancestry (FDR < 0.05, Fig. 2C and table S11). There is a slight enrichment of lncRNAs ($P < 1 \times 10^{-6}$), among which we identified the RP11-302J23.1 gene, highly expressed in cardiac tissue in African Americans only, and located in a region that harbors weak associations to heart disease (*18*). Additionally, some genes showing differential expression by ethnicity lie in genomic regions under positive selection in European or sub-Saharan African populations (Fig. 2C and fig. S15).

Finally, we detected 1993 genes that globally change expression with age (FDR < 0.05, Fig. 2D and table S12). Genes that decrease expression are enriched in functions and pathways related to neurodegenerative diseases such as Parkinson's and Alzheimer's diseases, among which eight harbor single-nucleotide polymorphisms (SNPs) for these diseases identified from genome-wide association studies ($P < 0.05$). Among the genes that increase expression with age is *EDA2R*, whose ligand, EDA, has been associated with age-related phenotypes (*19*).

We also identified 753 genes with tissue specific sex-biased expression (FDR < 0.05, table S13) predominantly in breast tissue (92%), and 31 genes with tissue-specific ethnicity-biased expression, many in the skin (FDR < 0.05, Table 1 and table S14). Among the sex-differentially expressed genes, five show biased expression specifically in heart and are of interest given the differing

[1]Center for Genomic Regulation (CRG), Barcelona, Catalonia, Spain. [2]Harvard Department of stem cell and regenerative biology, Harvard University, Cambridge, MA, USA. [3]Department of Genetic Medicine and Development, University of Geneva, Geneva, Switzerland. [4]Institute for Genetics and Genomics in Geneva (iGE3), University of Geneva, Geneva, Switzerland. [5]Swiss Institute of Bioinformatics, Geneva, Switzerland. [6]Facultat de Biologia, Universitat de Barcelona (UB), Barcelona, Catalonia, Spain. [7]Universitat Pompeu Fabra (UPF), Barcelona, Catalonia, Spain. [8]Broad Institute of MIT and Harvard, Cambridge, MA, USA. [9]McGill University, Montreal, Canada. [10]National Institute for Scientific Computing (LNCC), Petropolis, Rio de Janeiro, Brazil. [11]Radboud University, Nijmegen, Netherlands. [12]Faculty of Bioengineering and Bioinformatics, Moscow State University, Leninskie Gory 1-73, 119992 Moscow, Russia. [13]North Carolina State University, Raleigh, NC, USA. [14]New York Genome Center, New York, NY, USA. [15]Department of Systems Biology, Columbia University, New York, NY, USA. [16]Cancer Center and Department of Pathology, Massachusetts General Hospital, Boston, MA 02114, USA. [17]Institut Hospital del Mar d'Investigacions Mèdiques (IMIM), Barcelona, Catalonia, Spain. [18]Joint CRG-Barcelona Super Computing Center (BSC)–Institut de Recerca Biomedica (IRB) Program in Computational Biology, Barcelona, Catalonia, Spain. *These authors contributed equally to this work. **†Corresponding author. E-mail: kardlie@broadinstitute.org (K.G.A.); roderic.guigo@crg.cat (R.G.)**

prevalence of cardiovascular disease between males and females. One of these genes, *PLEKHA7* (fig. S15C), contains SNPs associated with risk for cardiovascular disease.

Overall, tissue specificity is likely to be driven by the concerted expression of multiple genes. Thus, we performed sex-based differential analysis of coexpression networks. We identified 42 coexpression modules in males and 46 in females (fig. S16). Among male-specific modules, we found one related to spermatid differentiation and development (FDR = 9.0×10^{-4}, fig. S16B), and among female-specific modules, we found one related to epidermis and ectoderm development (FDR = 4.6×10^{-14}, fig. S16C). Differential network expression, therefore, distinguishes differences between male and females not well captured by analysis of individual genes.

Split-mapped RNA-seq reads predict about 87,000 novel junctions with very strong support

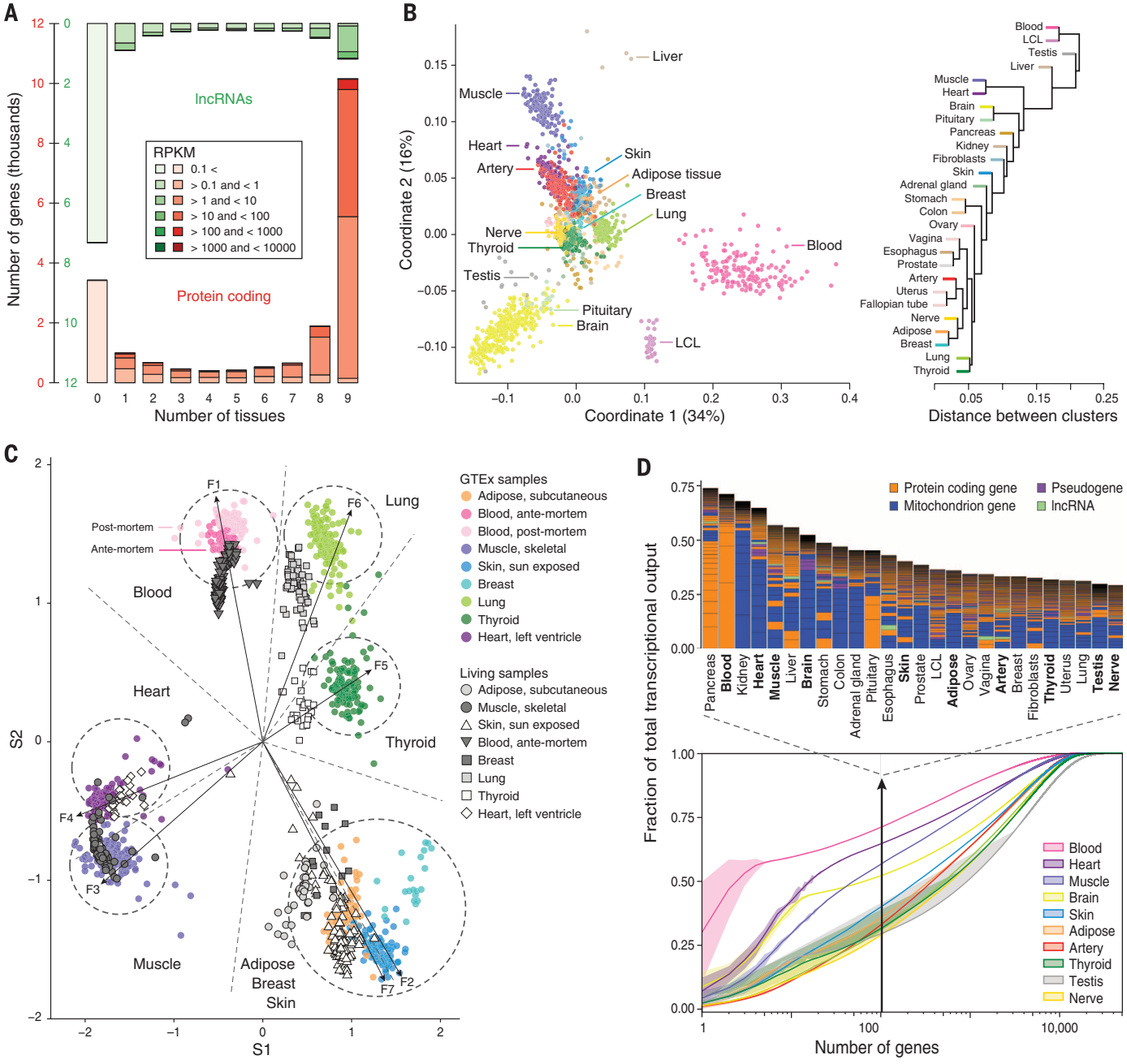

Fig. 1. The GTEx multitissue transcriptome. (**A**) Gene expression levels and number of tissues in which genes are expressed (>0.1 RPKM in at least 80% of the samples). RPKMs are averaged over all genes expressed in a given number of tissues. (**B**) Sample and tissue similarity on the basis of gene expression profiles. Left: Multidimensional scaling Right: Tissue hierarchical clustering. (**C**) Expression values from eight GTEx tissues (colored circles) plotted radially along seven metagenes extracted from expression data. Antemortem samples curated from the Gene Expression Omnibus (GEO) cluster strongly with GTEx tissues. (**D**) Transcriptome complexity. Bottom: Cumulative distribution of the average fraction of total transcription contributed by genes when sorted from most-to-least expressed in each tissue (*x* axis). Lines represent mean values across samples of the same tissue, and lighter-color surfaces around the mean represent dispersion calculated as the standard deviation divided by the cumulative sum of all means. Top: Biological type and relative contribution to total transcription of the hundred most expressed genes. Height of the bars is proportional to the fraction that these genes contribute to total transcription.

(fig. S17). These tend to be more tissue specific, detected in fewer samples, and less conserved than previously annotated junctions (only 2.6% of novel junctions can be detected as orthologous in mouse, compared to 65% for annotated junctions). Multidimensional scaling based on exon inclusion levels again largely recapitulates tissue type (Fig. 3A). However, samples from brain cluster as the primary outgroup, supporting the existence of a distinct splicing program in the brain (*20*). Furthermore, preferential gene expression of RNA-binding proteins and both differential and preferential exon inclusion are enriched in the brain (figs. S18 and S19 and table S15). We found very few exons exclusively included or excluded in a given tissue (fig. S20 and table S16), 40% of which show exclusive inclusion in the brain. We also found that micro-exons (<15 bp) are overwhelmingly used in the brain compared to other tissues (Wilcoxon test, $P < 1 \times 10^{-7}$, Fig. 3B). This pattern is not obvious in short exons longer than 15 bp ($P = 0.3$, fig. S21). This observed brain-specific splicing pattern may result from differential splicing in the cerebellum, because expression clustering of the brain regions reveals a general up-regulation of RNA-binding proteins specifically in the cerebellum (Fig. 3C). This is also the brain region exhibiting the largest proportion of novel splicing events (fig. S22).

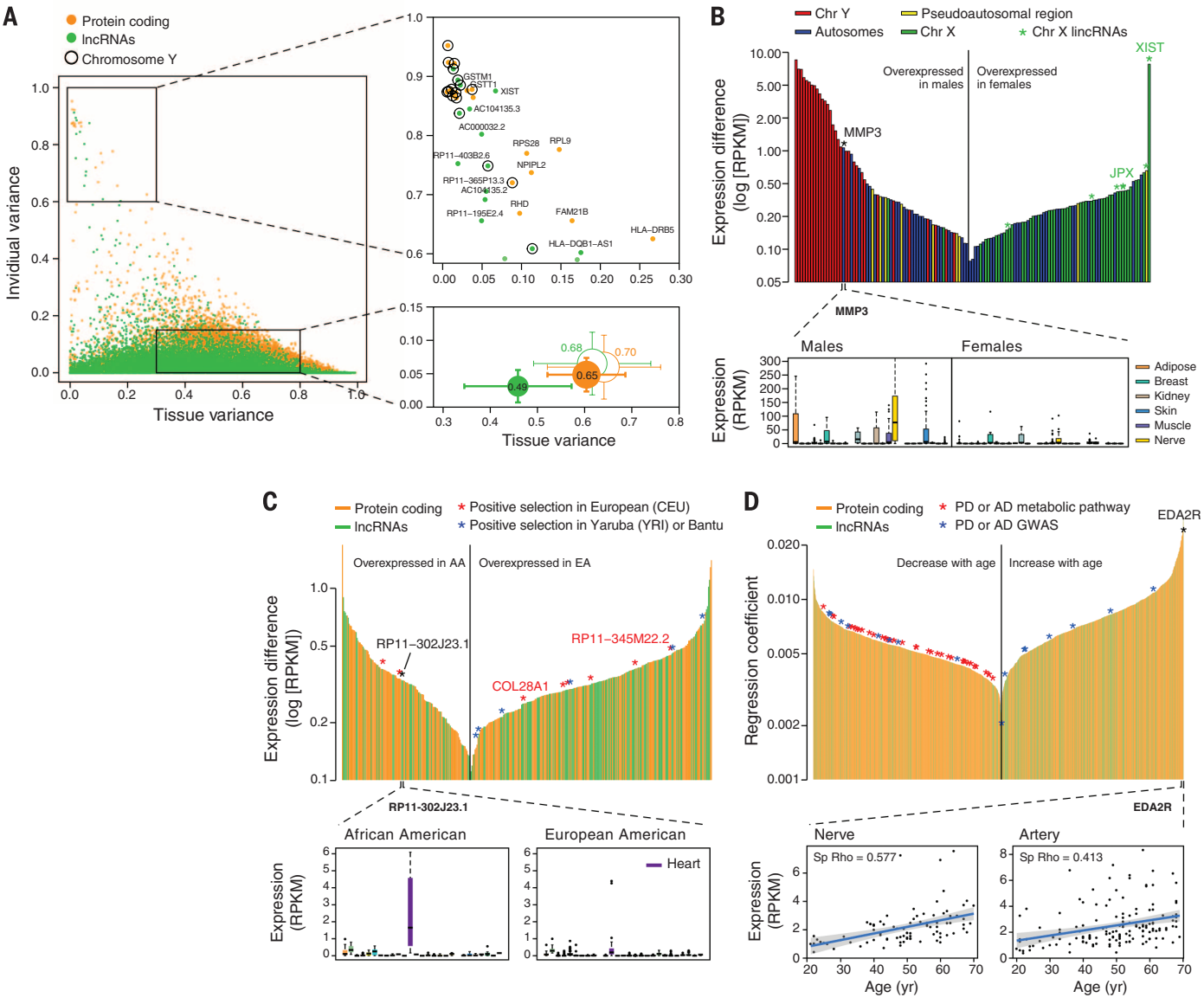

Fig. 2. Gene expression across tissues and individuals. (**A**) Left: Contribution of tissue and individual to gene expression variation of PCGs and lncRNAs. Bottom right: Mean ± SD over all genes (filled circles) and over genes with similar expression levels in PCGs and lncRNAs (unfilled circles). Circle size is proportional to the sum of tissue and individual variation, and segment length corresponds to 0.5 SD. Top right: genes with high individual variation and low tissue variation. (**B**) Sex differentially expressed genes. Top: differentially expressed genes (FDR < 0.05) sorted according to expression differences between males and females. Genes in the Y chromosome are sorted according to the expression in males. Bottom: *MMP3* gene expression in males and females. (**C**) Genes differentially expressed with ethnicity. Top: differentially expressed genes (FDR < 0.05) between African Americans (AA) and European Americans (EA) sorted according to expression differences. A few of these genes lie in regions reported to be under positive selection in similar populations. Bottom: expression of RP11-302J23.1. (**D**) Genes differentially expressed with age. Top: Genes sorted according to the regression coefficient. Bottom: expression of EDAR2 gene in nerve and artery as a function of age. Shaded area around the regression line represents 95% confidence interval.

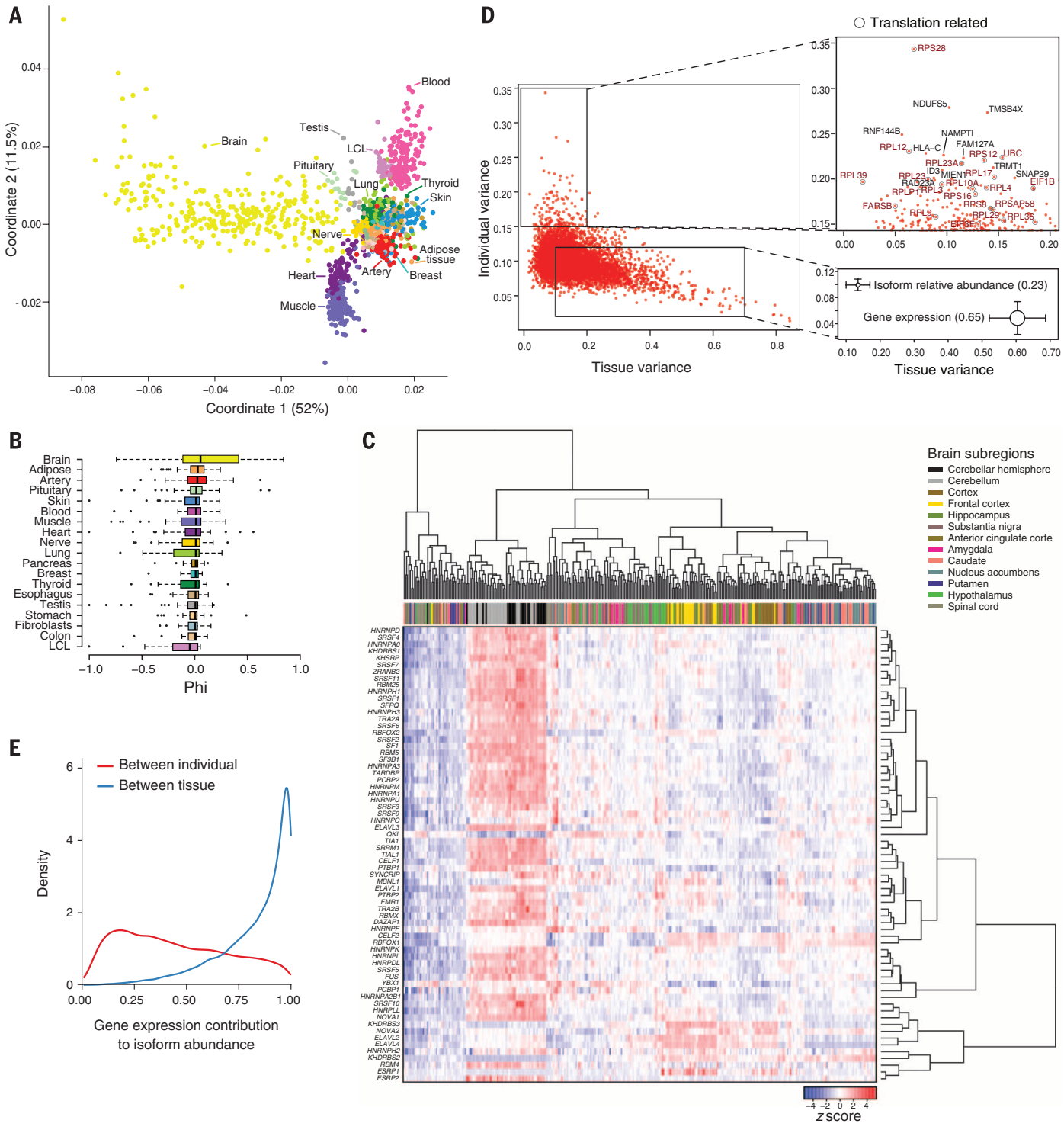

Fig. 3. Splicing across tissue and individuals. (**A**) Multidimensional scaling of all samples on the basis of exon inclusion levels (Percent spliced in, PSI). (**B**) Microexon inclusion across tissues. Values of tissue exon inclusion close to 1 (–1) indicate that the microexon is included (excluded), in nearly all samples from the tissue, and excluded (included) in nearly all samples from the rest of the tissues. Tissues are sorted according to tissue exon inclusion (phi) median value. (**C**) Clustering of brain samples on the basis of the normalized expression levels of 67 RNA binding proteins involved in splicing. The order of samples and genes is obtained by biclustering the expression matrix. (**D**) Left: Contribution of tissue and individual to splicing variation in PCGs. Bottom right: Mean ± SD of individual and tissue contributions to splicing and to gene expression variation. Circle size is proportional to the sum of tissue and individual variation and segment length corresponds to 0.5 SD. Top right: Genes with high splicing variation across individuals. (**E**) Contribution of gene expression to the between-individual and between-tissue variation in isoform abundance

Table 1. Genes with sex-biased and ethnicity-biased expression in GTEx tissues. Differentially expressed genes between males (M) and females (F) and between African American (AA) and European American (EA) in those tissues with at least 10 samples per group. Median fold change (on autosomal genes) was calculated for tissues with more than two significant genes.

	Sex										Ethnicity					
	No. of samples		No. of genes							Med. fold change	No. of samples		No. of genes			Med. fold change
	M	F	All genes	PCGs	lncRNA	Y chrom.	X chrom.	Pseudo-autosomal region	Autosomal		AA	EA	All genes	PCGs	lncRNA	
Adipose	76	37	45	29	16	28	4	1	12	2.8	17	95	0	0	0	–
Artery	88	57	40	21	19	29	2	0	9	2.3	21	121	3	0	0	2.9
Blood	99	57	20	12	8	18	1	0	1	–	24	129	0	0	0	–
Breast	14	13	762	567	195	26	21	0	715	4.2	5	22	–	–	–	–
Esophagus	27	11	23	14	9	22	1	0	0	–	5	33	–	–	–	–
Heart	74	34	27	15	12	23	1	0	3	3	11	95	2	1	1	–
LCL	26	13	23	11	12	21	1	1	0	–	9	30	–	–	–	–
Lung	76	43	34	17	17	31	1	0	2	–	14	104	4	3	1	3
Muscle	87	51	42	27	15	24	6	0	12	2.7	18	117	2	2	0	–
Nerve	54	34	38	24	14	25	5	1	7	2.3	13	73	2	1	1	–
Skin	76	43	47	32	15	31	5	0	11	2.3	14	103	14	13	1	2.9
Thyroid	65	40	42	25	17	27	5	1	9	1.9	13	90	13	7	6	3.5
No. of samples	942	566									172	1307	35	27	8	
No. of individuals	111	64	847	628	219	41	34	1	771		24	148				

In contrast to gene expression, variation of splicing, measured either from relative isoform abundance or exon inclusion, is similar across tissues and across individuals, but exhibits a much larger proportion of residual unexplained variation (Fig. 3D, fig. S23, and table S17). This could arise from nonadditive interactions between individuals and tissues, but might also reflect stochastic, nonfunctional fluctuations that are more common in splicing than in expression (*21*). Among the genes that show high interindividual splicing variability, we found an enrichment of ribosomal proteins and genes related to translation and protein biosynthesis (Fig. 3D and table S18). Higher variability between individuals may also partially reflect an effect of ischemic time on splicing, which we observed when clustering samples by exon inclusion within each tissue (fig. S24).

The abundance of splicing isoforms reflects the actions of both primary transcription and posttranscriptional processing—mostly alternative splicing. To determine the relative contribution of each process, we estimated the proportion of variance in isoform abundance that can be simply explained by variance in gene expression. We found that gene expression explains only 45% of the variance between individuals, but 84% of the variance between tissues (Fig. 3E and fig. S25). This strongly suggests that primary transcription is the main driver of cellular specificity, with splicing playing a complementary role. Although this may be unexpected, given the magnitude of the effect, it is consistent with recent findings of low proteomic support for alternatively spliced isoforms (*22*) and few shifts in major protein isoforms across cell types (table S19) (*23*).

Overall, our results underscore the value of monitoring the transcriptome of multiple tissues and individuals in order to understand tissue-specific transcriptional regulation and to uncover the transcriptional determinants of human phenotypic variation and disease susceptibility.

REFERENCES AND NOTES

1. FANTOM Consortium and the RIKEN PMI and CLST (DGT) *et al*., *Nature* **507**, 462–470 (2014).
2. ENCODE Project Consortium, *Nature* **489**, 57–74 (2012).
3. T. Lappalainen *et al*., *Nature* **501**, 506–511 (2013).
4. E. Grundberg *et al*., *Nat. Genet.* **44**, 1084–1089 (2012).
5. T. J. Lonsdale *et al*., *Nat. Genet.* **45**, 580–585 (2013).
6. The GTEx Consortium, *Science* **348**, 648–660 (2015).
7. Materials and methods are available in the supplementary materials on *Science* Online.
8. D. S. DeLuca *et al*., *Bioinformatics* **28**, 1530–1532 (2012).
9. J. Harrow *et al*., *Genome Res.* **22**, 1760–1774 (2012).
10. M. Lukk *et al*., *Nat. Biotechnol.* **28**, 322–324 (2010).
11. A. C. Birdsill, D. G. Walker, L. Lue, L. I. Sue, T. G. Beach, *Cell Tissue Bank.* **12**, 311–318 (2011).
12. J. P. Brunet, P. Tamayo, T. R. Golub, J. P. Mesirov, *Proc. Natl. Acad. Sci. U.S.A.* **101**, 4164–4169 (2004).
13. P. Carninci *et al*., *Genome Res.* **10**, 1617–1630 (2000).
14. R. D. Kelly, A. Mahmud, M. McKenzie, I. A. Trounce, J. C. St John, *Nucleic Acids Res.* **40**, 10124–10138 (2012).
15. D. Kelley, J. Rinn, *Genome Biol.* **13**, R107 (2012).
16. L. Carrel, H. F. Willard, *Nature* **434**, 400–404 (2005).
17. S. Djebali *et al*., *Nature* **489**, 101–108 (2012).
18. V. Regitz-Zagrosek, U. Seeland, *Wien. Med. Wochenschr.* **161**, 109 (2011).
19. M. Yan *et al*., *Science* **290**, 523–527 (2000).
20. G. Yeo, D. Holste, G. Kreiman, C. B. Burge, *Genome Biol.* **5**, R74 (2004).
21. J. K. Pickrell, A. A. Pai, Y. Gilad, J. K. Pritchard, *PLOS Genet.* **6**, e1001236 (2010).
22. I. Ezkurdia *et al*., *Mol. Biol. Evol.* **29**, 2265–2283 (2012).
23. M. Gonzàlez-Porta, A. Frankish, J. Rung, J. Harrow, A. Brazma, *Genome Biol.* **14**, R70 (2013).

ACKNOWLEDGMENTS

We acknowledge and thank the donors and their families for their generous gifts of organ donation for transplantation and tissue donations for the GTEx research study. We thank the Genomics Platform at the Broad Institute for data generation; L. Gaffney for help with figures; E. Gelfand and C. Trowbridge for project support and members of the Analysis Working Group for feedback; and D. MacArthur, J. Maller, and B. Neale for critical reading of the manuscript. The primary and processed data used to generate the analyses presented here are available in the following locations: All primary sequence files are deposited in and available from dbGaP (phs000424.v3.p1); gene and transcript quantifications are available on the GTEx Portal (www.gtexportal.org). The Genotype-Tissue Expression (GTEx) Project was supported by the Common Fund of the Office of the Director of the National Institutes of Health (http://commonfund.nih.gov/GTEx). Additional funds were provided by the National Cancer Institute (NCI); National Human Genome Research Institute; National Heart, Lung, and Blood Institute; National Institute on Drug Abuse; National Institute of Mental Health; and National Institute of Neurological Disorders and Stroke. This work was supported by the following grants and contracts from the United States National Institutes of Health: contract HHSN261200800001E (Leidos Prime contract with NCI); contracts 10XS170 [National Disease Research Interchange (NDRI)], 10XS171 (Roswell Park Cancer Institute), 10X172 (Science Care Inc.), and 12ST1039 (IDOX); contract 10ST1035 (Van Andel Institute); contract HHSN268201000029C (Broad Institute); R01 DA006227-17 (University of Miami Brain Bank); R01 MH090941 (University of Geneva), European Research Council, Swiss National Science Foundation, and Louis-Jeantet Foundation to E.T.D.; R01 MH090936 (University of North Carolina–Chapel Hill); and grants BIO2011-26205 from the Spanish Ministerio de Ciencia e Innovación (MICINN), 2014 SGR 464 and 2014 SGR 1319 from the Generalitat de Catalunya, and 294653 from the European Research Council–European Commission.

SUPPLEMENTARY MATERIALS

www.sciencemag.org/content/348/6235/660/suppl/DC1
Materials and methods
Figs. S1 to S25
Tables S1 to S20
References (*24*–*72*)
Data tables S4 to S7 and S9 to S18

20 October 2014; accepted 2 April 2015
10.1126/science.aaa0355

HUMAN GENOMICS

Effect of predicted protein-truncating genetic variants on the human transcriptome

Manuel A. Rivas,[1*†] Matti Pirinen,[2‡] Donald F. Conrad,[3‡] Monkol Lek,[4,5‡] Emily K. Tsang,[6,7,8] Konrad J. Karczewski,[4,5] Julian B. Maller,[4,5] Kimberly R. Kukurba,[6,7] David S. DeLuca,[4] Menachem Fromer,[4,5,9] Pedro G. Ferreira,[10,11,12] Kevin S. Smith,[6,7] Rui Zhang,[6] Fengmei Zhao,[4,5] Eric Banks,[4] Ryan Poplin,[4] Douglas M. Ruderfer,[9,13] Shaun M. Purcell,[4,5,9,13] Taru Tukiainen,[4,5] Eric V. Minikel,[4,5] Peter D. Stenson,[14] David N. Cooper,[14] Katharine H. Huang,[4] Timothy J. Sullivan,[4] Jared Nedzel,[4] The GTEx Consortium, The Geuvadis Consortium, Carlos D. Bustamante,[6] Jin Billy Li,[6] Mark J. Daly,[4,5] Roderic Guigo,[15] Peter Donnelly,[1,16] Kristin Ardlie,[4] Michael Sammeth,[15,17] Emmanouil T. Dermitzakis,[10,11,12] Mark I. McCarthy,[1,18] Stephen B. Montgomery,[6,7] Tuuli Lappalainen,[6,10,11,12,19,20*†] Daniel G. MacArthur[4,5,21*†]

Accurate prediction of the functional effect of genetic variation is critical for clinical genome interpretation. We systematically characterized the transcriptome effects of protein-truncating variants, a class of variants expected to have profound effects on gene function, using data from the Genotype-Tissue Expression (GTEx) and Geuvadis projects. We quantitated tissue-specific and positional effects on nonsense-mediated transcript decay and present an improved predictive model for this decay. We directly measured the effect of variants both proximal and distal to splice junctions. Furthermore, we found that robustness to heterozygous gene inactivation is not due to dosage compensation. Our results illustrate the value of transcriptome data in the functional interpretation of genetic variants.

Genetic variants predicted to shorten the coding sequence of genes—termed protein-truncating variants (PTVs)—are typically expected to have large effects on gene function. These variants are enriched for disease-causing mutations (*1*, *2*), but some may be protective against disease (*3*). However, PTVs are abundant in the genomes of healthy individuals (*4*), indicating that they often do not have major phenotypic consequences. In addition, although PTVs are often described as loss-of-function (LOF) variants, in most cases their precise molecular effect has not been characterized and in other cases show gain-of-function effects (*1*). Clinical interpretation of PTVs will thus require direct characterization of their biochemical effects.

We cataloged predicted PTVs and their transcriptomic effect in 462 healthy individuals with DNA and mRNA sequencing (RNA-seq) from lymphoblastoid cell lines (LCLs) in the Geuvadis study (*5*, *6*) and 173 individuals with exome sequencing and RNA-seq from a total of 1634 samples from multiple tissues in the Genotype-Tissue Expression (GTEx) study [supplementary materials section S1 (SM S1)] (*7*, *8*). Each GTEx individual has RNA-seq data from 1 to 30 tissues, with 9 tissues having >80 samples. We defined PTVs (*4*) (table S1) as single-nucleotide

[1]Wellcome Trust Centre for Human Genetics, Nuffield Department of Clinical Medicine, University of Oxford, Oxford, UK. [2]Institute for Molecular Medicine Finland (FIMM), University of Helsinki, Helsinki, Finland. [3]Washington University in St. Louis, St. Louis, MO, USA. [4]Broad Institute of MIT and Harvard, Cambridge, MA, USA. [5]Analytical and Translational Genetics Unit, Massachusetts General Hospital, Boston, MA, USA. [6]Department of Genetics, Stanford University, Stanford, CA, USA. [7]Department of Pathology, Stanford University, Stanford, CA, USA. [8]Biomedical Informatics Program, Stanford University, Stanford, CA, USA. [9]Department of Psychiatry, Mt. Sinai Hospital, NY, USA. [10]Department of Genetic Medicine and Development, University of Geneva, Geneva, Switzerland. [11]Institute for Genetics and Genomics in Geneva (iGE3), University of Geneva, Geneva, Switzerland. [12]Swiss Institute of Bioinformatics, Geneva, Switzerland. [13]Division of Psychiatric Genomics, Department of Psychiatry, Icahn School of Medicine at Mount Sinai, NY, USA. [14]Institute of Medical Genetics, School of Medicine, Cardiff University, Heath Park, Cardiff, UK. [15]Center for Genomic Regulation (CRG), Universitat Pompeu Fabra (UPF), Barcelona, Catalonia, Spain. [16]Department of Statistics, University of Oxford, Oxford, UK. [17]National Institute for Scientific Computing (LNCC), Petropolis, Rio de Janeiro, Brazil. [18]Oxford Center for Diabetes Endocrinology and Metabolism, University of Oxford, Oxford, UK. [19]New York Genome Center, New York, NY, USA. [20]Department of Systems Biology, Columbia University, New York, NY, USA. [21]Department of Medicine, Harvard Medical School, Boston, MA, USA.
***Corresponding author. E-mail: rivas@well.ox.ac.uk (M.A.R.); tlappalainen@nygenome.org (T.L.); macarthur@atgu.mgh.harvard.edu (D.G.M.)** †These authors contributed equally to this work. ‡These authors contributed equally to this work.

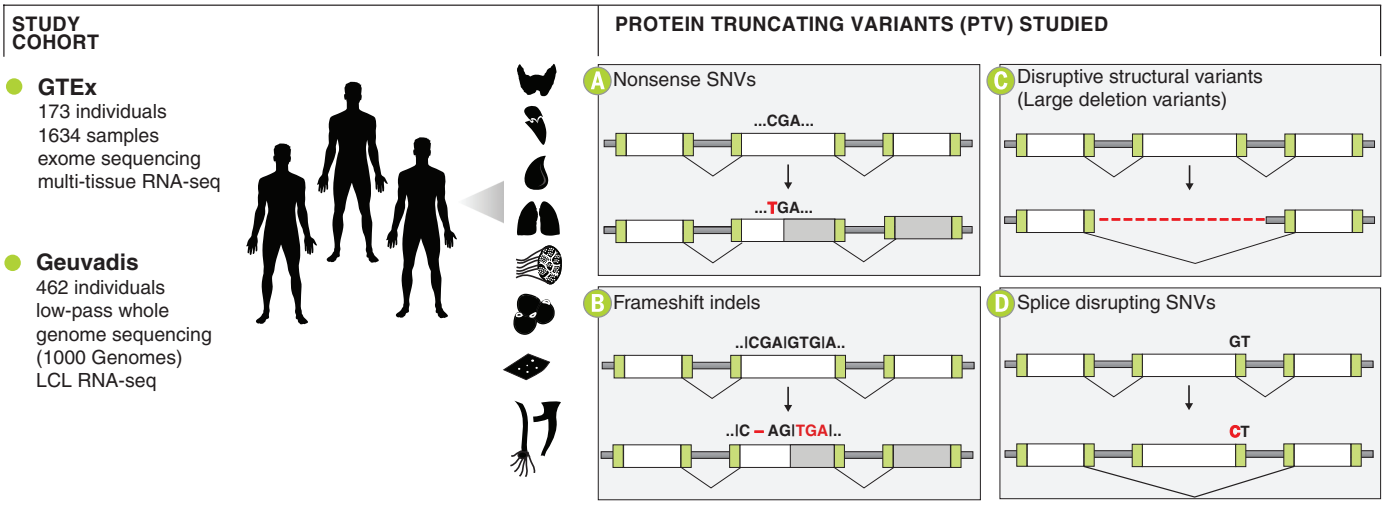

Fig. 1. Schematic overview of the study. We prepared an integrated DNA and RNA sequencing data set by combining the pilot phase of the GTEx project of 173 individuals with up to 30 tissues per individual (total of 1634 samples) and the Geuvadis project of LCL DNA and RNA sequencing in 462 individuals. From these data, we analyzed the effect of predicted protein-truncating genetic variants on the human transcriptome, including (**A**) nonsense SNVs, (**B**) frameshift indels, (**C**) large deletion variants, and (**D**) splice-disrupting SNVs.

variants (SNVs) predicted to introduce a premature stop codon or to disrupt a splice site, small insertions or deletions (indels) predicted to disrupt a transcript's reading frame, and larger deletions that remove the full protein coding sequence (CDS) (SM S2, Fig. 1, and figs. S1 and S2). We identified 13,182 candidate PTVs using phase 1 data of the 1000 Genomes Project (*9*) of the 421 individuals included in the Geuvadis RNA-seq project, as well as 4584 candidate PTVs in the GTEx data, for a combined total of 16,286 candidate variants (table S2).

We measured total gene expression levels in reads per kilobase of exon per million mapped reads, allele-specific expression (ASE) detecting different expression levels of two haplotypes of an individual, and split mappings across annotated exon junctions to quantify splicing (SM S3 and S4). Transcripts containing common PTVs are more weakly expressed and more tissue-specific than transcripts that do not contain common PTVs (SM S5 and figs. S3 to S7), consistent with previous work (*4*).

PTVs that generate premature stop codons may trigger nonsense-mediated decay (NMD). Such variants are often recessive and may protect against detrimental phenotypic effects but also may cause disease via haploinsufficiency (*1*). Variants that escape NMD may create a truncated protein with dominant-negative or gain-of-function effects (*1*). We compared transcript levels between the PTV and the non-PTV alleles within the same individual (SM S6) (*4*, *5*, *10*) for a total of 1814 PTVs (SM S6, figs. S8 to S12, and table S3) and validated the allelic ratios obtained from RNA-seq data (figs. S13 to S18 and table S4) (*11*). We also generated a method to assess the ASE effect of frameshift indels (SM S6 and figs. S8 to S12), which were not previously examined (*5*, *10*) due to the technical challenges of mapping bias (*12*–*14*).

Allelic count data were analyzed with a Bayesian statistical method to address whether a variant exhibits ASE in a given tissue and whether this signal is shared across multiple tissues of the same individual (SM S7 and figs. S19 to S26) (*15*). We observe a higher proportion of strong or moderate allelic imbalance in rare and singleton nonsense SNVs compared with common nonsense variants (54.3%, 55.4%, and 35.7%, respectively), suggesting that rare PTVs are more likely to trigger NMD (fig. S19).

Rare nonsense SNVs predicted to trigger NMD according to the 50-bp (base pair) rule (SM S7) (*16*) have a larger proportion of ASE than SNVs that escape NMD (69.5% versus 31.9%,

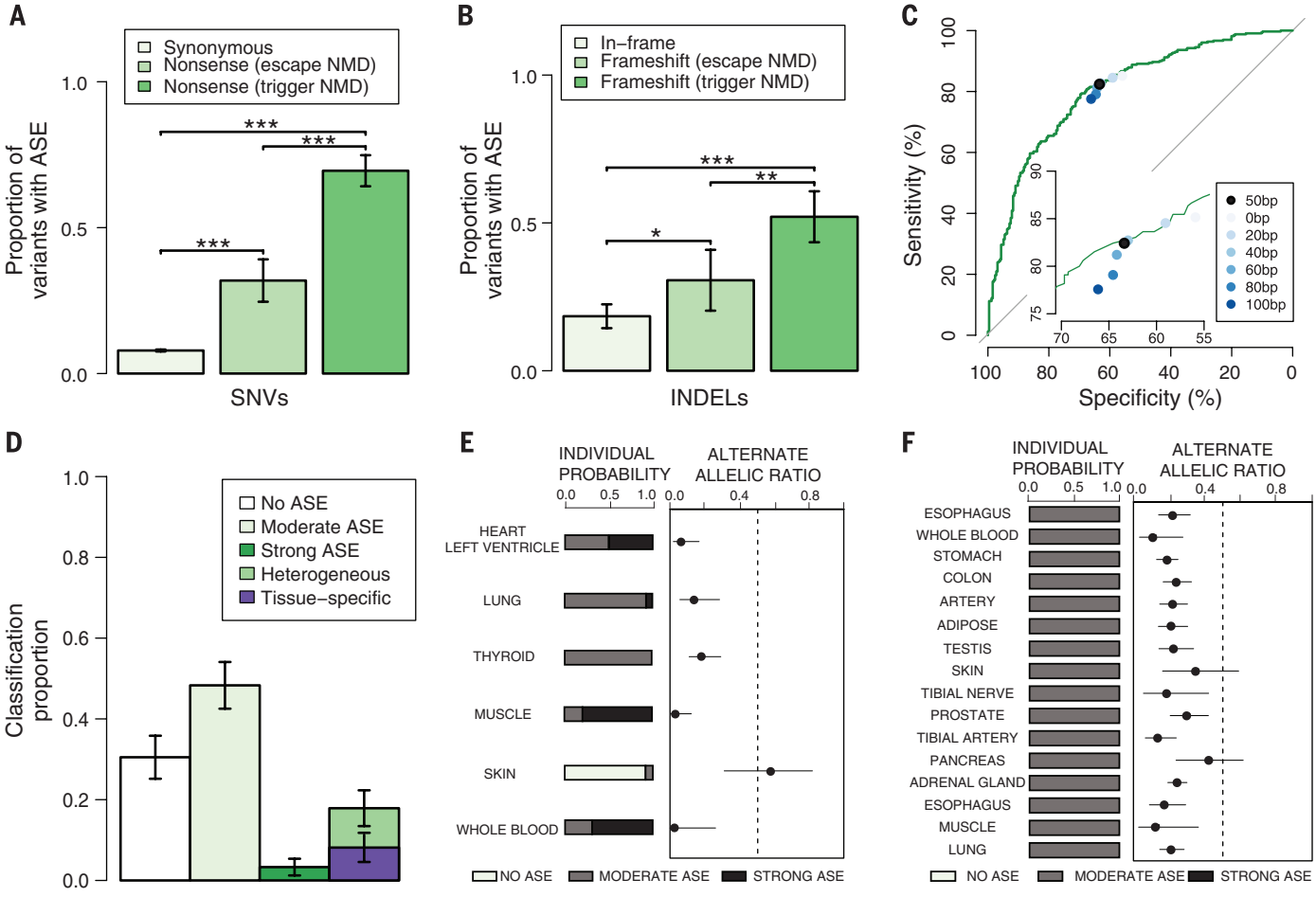

Fig. 2. Allele-specific expression analysis. (**A**) Proportion of rare SNVs with allele-specific expression (ASE) for synonymous variants (n = 25,233) and nonsense variants predicted to escape (n = 158) or trigger (n = 287) NMD. (**B**) Proportion of rare indels with ASE for in-frame (n = 355) and frameshift indel variants predicted to escape (n = 77) or trigger (n = 129) NMD. Due to different quality filters, the proportions are not directly comparable to those in (A). (**C**) Receiver operating characteristic curve for predicting NMD with binary classification defined as no ASE (escape) and moderate, strong, or heterogeneous ASE (trigger). The filled circles show the specificity and sensitivity for NMD prediction with alternative simple distance rules (inset). (**D**) Multitissue ASE classification for rare nonsense variants predicted to trigger NMD (n = 287). (**E**) Example of ASE data across six tissues for a heterozygous carrier of the nonsense variant rs149244943 in gene *PHKB* (phosphorylase kinase, beta) classified as having heterogeneous ASE effects across the six tissues. We confirmed that this effect is not driven by a common tissue-specific expression quantitative trait locus. (**F**) Example of ASE data across 16 tissues for a heterozygous carrier of the nonsense variant rs119455955, a disease mutation for recessive late-infantile neuronal ceroid lipofuscinosis in gene *TPP1* (tripeptidyl peptidase I), classified as having moderate ASE across all tissues. For all plots, 95% CIs are shown.

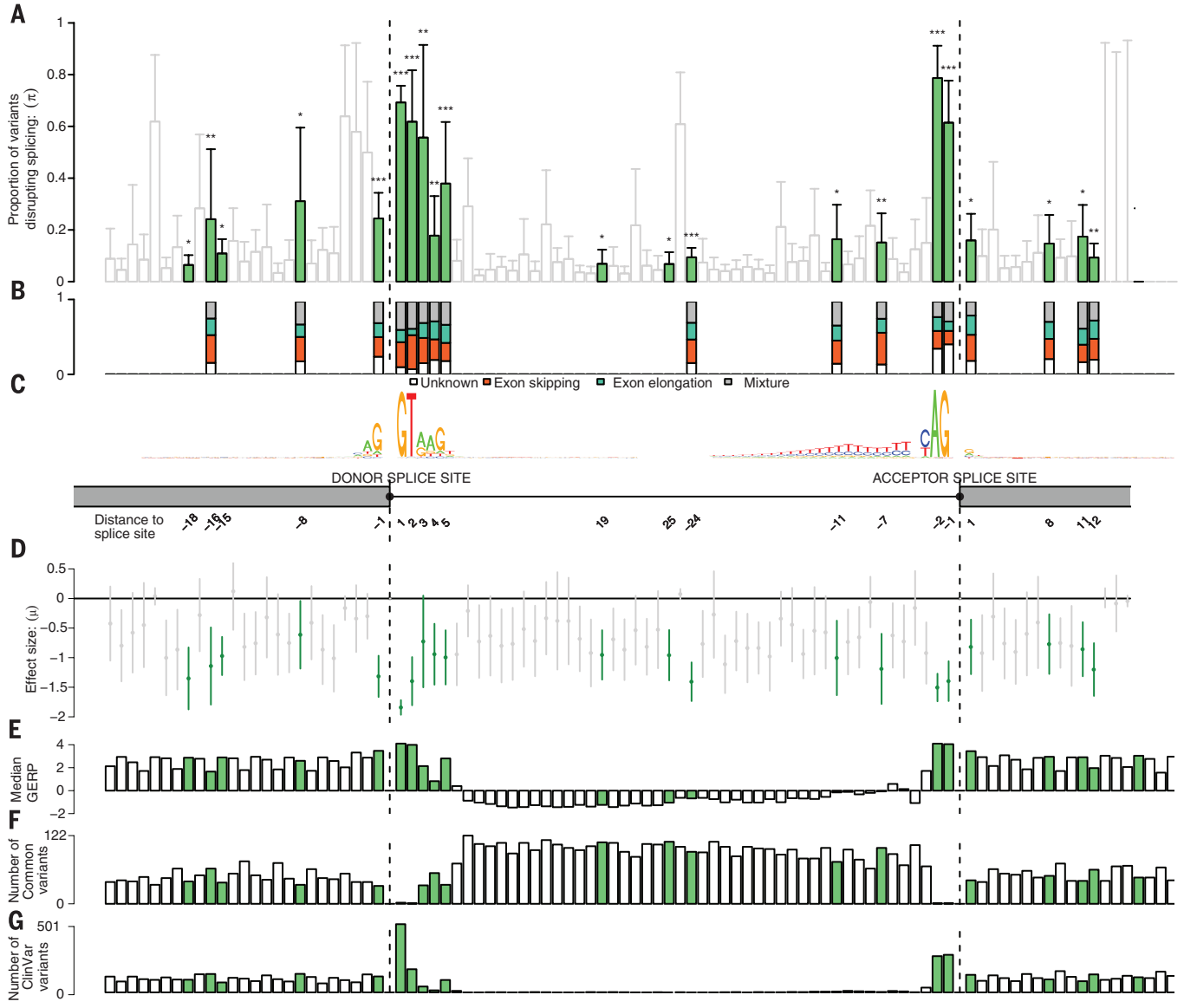

Fig. 3. Splicing disruption. (**A**) Proportion of variants disrupting splicing at each distance ±25 bp from donor and acceptor site (*P < 0.05, **P < 0.01, ***P < 0.001; green for P < 0.05; upper limit of 95% CI is shown; P value evaluated using the estimated proportion of variants supporting the alternative distribution times the effect size of the alternative distribution). (**B**) Classification of splice disruption events: exon skipping (low exon quantification value, no effect on intron quantification), exon elongation (high intron quantification value, no effect on exon quantification), and mixture (high intron and low exon quantification values). (**C**) Diagram of donor and acceptor splice junctions and sequence logo of represented sequences. (**D**) Effect size estimates (in standard deviations from the population distribution; 95% CI is shown) of the variants on splice junction quantification value. (**E**) Median genomic evolutionary rate profiling score (GERP) of all variants. (**F**) Distribution of common variants identified in an independent exome sequencing study of 4500 Swedish individuals. (**G**) Distribution of reported disease-causing variants in ClinVar.

respectively), and both classes demonstrate ASE more often than synonymous variants (7.9%, P < 0.001 across all comparisons, two-proportion z test) (Fig. 2A). A higher proportion of ASE is also observed for frameshift indels predicted to trigger NMD (52.1%) compared with those predicted to escape NMD (30.6%) and at higher levels than that predicted for in-frame indels (18.4%) (Fig. 2B). Testing alternative simple distance rules showed that the 50-bp rule has the highest predictive value (Fig. 2C).

We next generated an improved predictive model for no ASE versus strong/moderate ASE for all nonsense SNVs (SM S7). Our model predicts NMD better than the 50-bp rule, with an area under the curve (AUC) of 80.8% [95% confidence interval (CI) 77.3 to 84.4%] compared to a 50-bp rule AUC of 72.9% (69.3 to 76.5% CI) (Fig. 2C and figs. S21 and S22). Our results provide a quantitative estimate of the value of NMD predictions and illustrate that the 50-bp rule (*16*) remains a valuable heuristic. Nonetheless, our model improves NMD prediction, allows a more flexible analysis of the probability that a variant will trigger NMD from variant data (fig. S21), and provides data for understanding the molecular mechanisms of NMD (fig. S22).

The GTEx study design allows us to study variation in NMD across tissues. We applied a Bayesian hierarchical model (SM S7) (*15*) to rare nonsense variants predicted to trigger NMD, according to the 50-bp rule, with ASE data from at least two tissues. We estimate that 30.5% of these nonsense variants have no ASE in any tissue, and 48.3% and 3.3% have moderate or strong ASE across all tissues, respectively. Finally, 17.9% have heterogeneous effects across tissues, and 8.1% of ASE effects

are specific to a single tissue (Fig. 2, D to F, and figs. S23 to S26). The tissue specificity of NMD implies that the same PTV may have different effects across tissues, which could contribute to tissue-specific effects of disease-causing mutations (*17*).

We examined whether heterozygous carriers of PTVs exhibit compensatory up-regulation of the functional allele, which could contribute to tolerance of PTVs and partially explain the widespread haplosufficiency of human genes (*18*). Dosage compensation has been reported to correlate with gene expression levels (*19*) and occur in over 80% of deleted genes in *Drosophila melanogaster* (*20*). To minimize the effect of genotyping error, we focused only on biallelic whole-gene deletions with strong experimental support and manual curation (SM S2 and figs. S27 to S29). We first analyzed the few examples of common whole-gene deletion polymorphisms (SM S8). For 5/6 of these genes, an additive model relating gene expression to gene copy number provided a better fit than a dominant model, providing no evidence for dosage compensation (table S6). Additionally, heterozygous carriers of rare deletions also had consistently decreased expression of the respective gene compared with the population median ($P = 1.37 \times 10^{-5}$, one-sided binomial test of 11 rare PTV deletions in 25 genes) (figs. S27 and S28). Similar results were obtained for 53 nonsense PTVs with strong ASE signals ($P = 2.90 \times 10^{-9}$, one-sided binomial test) (figs. S30 and S31). These results suggest that full dosage compensation is rare for human genes.

Disruption of splicing can result in changes in protein structure either via in-frame changes in exon structure or by introducing a premature stop codon (*21*). Splicing variant annotation tools typically focus only on the two bases at either end of a spliced intron, "essential splice sites" (*22*), despite the fact that more distant sites are also known to affect splicing (*21*, *23*, *24*).

Variation around splice junctions tends to be rare (minor allele frequencies ≤ 0.01). We standardized the population distribution of each splice-junction quantification per tissue and grouped variants by their distance from their respective donor and acceptor sites. We then analyzed whether individuals carrying variants in these positions differ from the population in the quantification of the splice junction and the proximal exon and intron (Fig. 3, A to D).

In the Geuvadis data set, up to 79% of variants in the four essential splice-site loci cause splice disruptions ($P < 0.01$, Fig. 3A; GTEx results, figs. S33 to S37). We also find evidence of splice disruption from variants outside these regions, especially at positions 1 to 5 bp downstream of intronic donor splice sites, 1 bp into the adjacent exon, and also more distally—including the −24 position from the acceptor site, which likely reflects the branch-point position required for pre-mRNA splicing (*25*).

These patterns are consistent with other estimates of functional effects (Fig. 3E), depletion of common variants in exome sequencing data sets (Fig. 3F) (*26*), and a higher prevalence of disease-causing mutations (Fig. 3G). Analyses of common variants did not capture these patterns of enrichment (table S7, figs. S38 to S40, and SM S9). Our posterior probability estimates for sites with significant alternative distributions ($P < 0.05$) provide a resource for analyses (figs. S41 and 42 and SM S9 and S10).

By drawing on data from a wide range of adult tissues across 635 individuals, we provide a systematic assessment of the effect of predicted PTVs on the human transcriptome. Furthermore, this study indicates that nonsense-mediated decay has heterogeneous effects across tissues and also shows how to better detect splice-disrupting variants outside the "essential" sites at the splice junction.

We find no evidence for widespread dosage compensation maintaining normal expression levels of genes affected by heterozygous PTVs. This, together with the fact that most human genes are haplosufficient (*18*), suggests that homeostatic mechanisms at the cellular level, possibly as proposed in the theory of dominance (*27*), maintain biological function in the face of heterozygous, or even homozygous (*4*), inactivation of human genes.

The resource made available with this study provides a starting point for cataloging variants affecting protein function, but larger data sets will be required to increase our power to predict molecular consequences of variants from sequence data alone. These results highlight the benefits of direct RNA sequencing of either patient tissue or genetically engineered cell lines for interpretation of genetic variation and suggest that personal transcriptomics will become an important complement to genome analysis.

REFERENCES AND NOTES

1. J. A. Holbrook, G. Neu-Yilik, M. W. Hentze, A. E. Kulozik, *Nat. Genet.* **36**, 801–808 (2004).
2. P. D. Stenson *et al.*, *Hum. Genet.* **133**, 1–9 (2014).
3. J. C. Cohen, E. Boerwinkle, T. H. Mosley Jr., H. H. Hobbs, *N. Engl. J. Med.* **354**, 1264–1272 (2006).
4. D. G. MacArthur *et al.*, *Science* **335**, 823–828 (2012).
5. T. Lappalainen *et al.*, *Nature* **501**, 506–511 (2013).
6. P. A. C. 't Hoen *et al.*, *Nat. Biotechnol.* **31**, 1015–1022 (2013).
7. J. Lonsdale *et al.*, *Nat. Genet.* **45**, 580–585 (2013).
8. The GTEx Consortium, *Science* **348**, 648–660 (2014).
9. The 1000 Genomes Consortium, *Nature* **491**, 56–65 (2012).
10. K. R. Kukurba *et al.*, *PLOS Genet.* **10**, e1004304 (2014).
11. R. Zhang *et al.*, *Nat. Methods* **11**, 51–54 (2014).
12. S. B. Montgomery *et al.*, *Genome Res.* **23**, 749–761 (2013).
13. D. A. Skelly, M. Johansson, J. Madeoy, J. Wakefield, J. M. Akey, *Genome Res.* **21**, 1728–1737 (2011).
14. K. R. Stevenson, J. D. Coolon, P. J. Wittkopp, *BMC Genomics* **14**, 536 (2013).
15. M. Pirinen *et al.*, *Bioinformatics* **2015**, btv074 (2015).
16. E. Nagy, L. E. Maquat, *Trends Biochem. Sci.* **23**, 198–199 (1998).
17. J. F. Bateman, S. Freddi, G. Nattrass, R. Savarirayan, *Hum. Mol. Genet.* **12**, 217–225 (2003).
18. N. Huang, I. Lee, E. M. Marcotte, M. E. Hurles, *PLOS Genet.* **6**, e1001154 (2010).
19. A. A. McAnally, L. Y. Yampolsky, *Genome Biol. Evol.* **2**, 44–52 (2010).
20. J. Zhou, B. Lemos, E. B. Dopman, D. L. Hartl, *Genome Biol. Evol.* **3**, 1014–1024 (2011).
21. N. A. Faustino, T. A. Cooper, *Genes Dev.* **17**, 419–437 (2003).
22. D. J. McCarthy *et al.*, *Genome Medicine* **6**, 26 (2014).
23. C. B. Burge, T. Tuschl, P. A. Sharp, *Cold Spring Harbor Monogr. Arch.* **37**, 525–560 (1999).
24. H. Y. Xiong *et al.*, *Science* **347**, 1254806 (2015).
25. A. Corvelo, M. Hallegger, C. W. Smith, E. Eyras, *PLOS Comput. Biol.* **6**, e1001016 (2010).
26. S. M. Purcell *et al.*, *Nature* **506**, 185–190 (2014).
27. H. Kacser, J. A. Burns, *Genetics* **97**, 639–666 (1981).

ACKNOWLEDGMENTS

We thank all the members of the GTEx and Geuvadis consortia and L. Solomon for assistance with the figures. This work was supported by the National Institutes of Health (NIGMS R01GM104371 to D.G.M.; NIMH R01MH101814 to E.T.D, C.D.B., S.B.M., R.G., T.L., and M.I.M.; R01MH090941 to E.T.D. and M.I.M.; U01HG007593 to J.B.L. and S.B.M.; and R01MH101810 to D.F.C.); Academy of Finland (257654 to M.P.); a Hewlett-Packard Stanford Graduate Fellowship and a doctoral fellowship from the Natural Science and Engineering Research Council of Canada to E.K.T.; a National Defense Science and Engineering Graduate Fellowship (NDSEG) from the United States Department of Defense (DoD) to K.R.K.; European Research Council, Swiss National Science Foundation, and Louis-Jeantet Foundation to E.T.D.; Wellcome Trust (095552/Z/11/Z and 090532/Z/09/Z to P.D. and 098381 to M.I.M.); and a Clarendon Scholarship, NDM Studentship, and Green Templeton College Award from University of Oxford to M.A.R. The Genotype-Tissue Expression (GTEx) project was supported by the Common Fund of the Office of the Director of NIH. Additional funds were enrolled at Biospecimen Source sites funded by NCI/SAIC-Frederick, Inc. (SAIC-F) subcontracts to the National Disease Research Interchange (10XS170), Roswell Park Cancer Institute (10XS171), and Science Care, Inc. (X10S172). The Laboratory, Data Analysis, and Coordinating Center (LDACC) was funded through a contract (HHSN268201000029C) to the Broad Institute, Inc. Biorepository operations were funded through an SAIC-F subcontract to Van Andel Institute (10ST1035). Additional data repository and project management were provided by SAIC-F (HHSN261200800001E). The Brain Bank was supported by a supplement to University of Miami grant DA006227. Statistical methods development grants were made to the University of Geneva (MH090941), the University of Chicago (MH090951 and MH090937), the University of North Carolina–Chapel Hill (MH090936), and Harvard University (MH090948). The primary and processed data used to generate the analyses presented here are available in the following locations: All primary sequence and clinical data files, and any other protected data, are deposited in and available from the database of Genotypes and Phenotypes (www.ncbi.nlm.nih.gov/gap) (phs000424.v3.p1, except for whole-exome sequencing data in phs000424.v5.p1 and mmPCR-seq data and processed ASE data in phs000424.v6.p1); derived analysis files are available on the GTEx Portal (www.gtexportal.org). Biospecimens remaining from the study may be requested for research studies. The sample request form, biospecimen access policy, and material transfer agreement are available on the GTEx Portal (www.gtexportal.org/home/samplesPage). The Geuvadis data are available in ArrayExpress accession E-GEUV-1. Further details and links to data and software are available in www.well.ox.ac.uk/~rivas/ptv2015. C.D.B. is a paid member of the Scientific Advisory Boards of Personalis, InVitae, and Ancestry.com; he is founder and chair of the SAB of Identify Genomics, LLC; he also owns stock options in Personalis, Invitae, and Identify Genomics, LLC.

SUPPLEMENTARY MATERIALS

www.sciencemag.org/content/348/6235/666/suppl/DC1
Materials and Methods
Figs. S1 to S42
Tables S1 to S7
Data File S1
References (*28*–*56*)

29 September 2014; accepted 2 April 2015
10.1126/science.1261877

SUPERNOVAE

^{44}Ti gamma-ray emission lines from SN1987A reveal an asymmetric explosion

S. E. Boggs,[1]* F. A. Harrison,[2] H. Miyasaka,[2] B. W. Grefenstette,[2] A. Zoglauer,[1] C. L. Fryer,[3] S. P. Reynolds,[4] D. M. Alexander,[5] H. An,[6] D. Barret,[7,8] F. E. Christensen,[9] W. W. Craig,[1,10] K. Forster,[2] P. Giommi,[11] C. J. Hailey,[12] A. Hornstrup,[9] T. Kitaguchi,[13] J. E. Koglin,[14] K. K. Madsen,[2] P. H. Mao,[2] K. Mori,[12] M. Perri,[11,15] M. J. Pivovaroff,[10] S. Puccetti,[11,15] V. Rana,[2] D. Stern,[16] N. J. Westergaard,[9] W. W. Zhang[17]

In core-collapse supernovae, titanium-44 (^{44}Ti) is produced in the innermost ejecta, in the layer of material directly on top of the newly formed compact object. As such, it provides a direct probe of the supernova engine. Observations of supernova 1987A (SN1987A) have resolved the 67.87- and 78.32–kilo–electron volt emission lines from decay of ^{44}Ti produced in the supernova explosion. These lines are narrow and redshifted with a Doppler velocity of ~700 kilometers per second, direct evidence of large-scale asymmetry in the explosion.

Supernova 1987A (SN1987A) in the Large Magellanic Cloud provides a unique opportunity to study a nearby (50 kpc) core collapse supernova (CCSN) explosion and its subsequent evolution into a supernova remnant. SN1987A has validated some of our most basic assumptions about CCSN. The burst of neutrinos observed on Earth that preceded the visible emission confirmed that the overall explosion is driven by the collapse of the central core to a neutron star (*1*, *2*). The direct gamma-ray detections of 0.07 solar mass ($M_\odot$) of ^{56}Co (*3*, *4*) and 0.003 $M_\odot$ of ^{57}Co (*5*), and the correlation between the exponential decay of the optical light curve and lifetime of these isotopes (*6*, *7*), confirmed that the light curve is driven by radioactive decay of these nuclei.

SN1987A, however, held a few surprises. Models and light curves supported red supergiant progenitors for CCSN, but the SN1987A progenitor was blue (*8*). The ^{56}Co gamma-ray lines emerged from the explosion several months before expected, implying that some of the innermost heavy nuclear products had been mixed into the outer envelope (*3*). The ^{56}Co gamma-ray line spectroscopy showed mixing to velocities of ~3000 km s^{-1}, several times higher than expected from spherically symmetric models, and also a net redshift of ~500 km s^{-1}, which indicated large-scale asymmetry (*9*, *10*). Although subsequent x-ray observations have revealed expanding, brightening ejecta, there has been no evidence of the compact object created in the explosion (*11*, *12*).

Here we present observations of ^{44}Ti emission from SN1987A with the Nuclear Spectroscopic Telescope Array (NuSTAR) focusing high-energy x-ray telescope (*13*). ^{44}Ti production occurs deep inside the supernova near the dividing line between ejecta and material that falls back on the compact object, and is sensitive to the CCSN explosion energy and asymmetries (*14*, *15*). The decay of ^{44}Ti (85.0 years) results in the production of photons at 67.87 keV (93.0% of decays) and 78.32 keV (96.4% of decays) (*16*). NuSTAR observed SN1987A for multiple epochs between September 2012 and July 2014 with a total exposure of 2596 ks, at an average time of ~26.6 years after explosion. A full list of the observations is provided in table S1. Both the 67.87-keV line and the 78.32-keV lines of ^{44}Ti are clearly seen in the NuSTAR spectrum (Fig. 1). The lines are well fit with a simple Gaussian line shape plus the underlying continuum, demonstrated through the chi-square test. All uncertainties are quoted here at the 90% confidence level unless otherwise stated. In the combined analysis, we measure a 67.87-keV line flux of $3.5^{+0.7}_{-0.7} \times 10^{-6}$ photons cm^{-2} s^{-1}, corresponding to a ^{44}Ti yield of $1.5^{+0.3}_{-0.3} \times 10^{-4} M_\odot$. This derived yield assumes the decay rate measured in the laboratory and nearly neutral ^{44}Ti. The NuSTAR optics response cuts off at 78.39 keV, potentially cutting off any blueshifted emission. However, examination of the 67.87-keV line reveals a net redshift, allowing us to combine the lines for optimal analysis and use the individual lines to check for consistency (*17*). The signal-to-noise ratio for the detection of these combined lines is ~8.5σ. The line widths are consistent with the NuSTAR spectral resolution, and the corresponding upper limit on any Doppler broadening is 4100 km s^{-1} full width at half-maximum (FWHM). The 67.87-keV line centroid is redshifted by $0.23^{+0.09}_{-0.09}$ keV. Corrections due to recession velocity and the look-back effect (*17*) are ≤ 340 km s^{-1} combined. Taking these corrections into account, the redshift velocity of the ^{44}Ti lines in the rest frame of SN1987A is 700^{+400}_{-400} km s^{-1}.

The NuSTAR yield can be compared to previous measurements, indirect estimates, and theoretical predictions. The International Gamma Ray Astrophysics Laboratory (INTEGRAL) observatory reported first detection of the ^{44}Ti 67.87-keV and 78.32-keV lines from SN1987A (*18*). INTEGRAL could not spectrally resolve these lines, but measured a combined flux for both lines of $(1.7 \pm 0.4) \times 10^{-5}$ photons cm^{-2} s^{-1}, corresponding to an initial mass of synthesized ^{44}Ti of $(3.1 \pm 0.8) \times 10^{-4} M_\odot$. The yield measured by NuSTAR is inconsistent with the high yield found by INTEGRAL. Chandra X-ray Observatory Advanced CCD Imaging Spectrometer (ACIS) limits on Sc Kα emission have been used to set an upper limit on the ^{44}Ti mass of $<2 \times 10^{-4} M_\odot$ (*19*), consistent with the NuSTAR yield. Between 1994 and 2001, the ultraviolet, optical, and infrared (UVOIR) emission was dominated by the radioactive decay of ^{44}Ti, which led to a number of estimates of the ^{44}Ti yield based on detailed modeling of the UVOIR spectra (*20*–*22*) and bolometric luminosity (*23*, *24*). These observational studies do not all agree within their uncertainties, but generally fall in the range of (0.5 to 2) × $10^{-4} M_\odot$ of ^{44}Ti produced in the explosion (*24*). The ^{44}Ti yield measured by NuSTAR is in good agreement with most estimates based on the UVOIR bolometric light curves and spectroscopic modeling, providing support for the detailed models underlying these estimates; however, our measured redshift reveals a more complicated explosion structure than assumed in these models. Finally, theoretical predictions of the ^{44}Ti yield for SN1987A fall roughly within this same range of (0.5 to 2) × $10^{-4} M_\odot$, with lower yields generally corresponding to spherically symmetric models, and yields increasing with larger asymmetries. See reference (*24*) for a compilation of theory references.

NuSTAR observations have set an upper limit on the Doppler broadening of <4100 km s^{-1} FWHM, consistent with the widths of ~3000 km s^{-1}

[1]Space Sciences Laboratory, University of California, Berkeley, CA 94720, USA. [2]Cahill Center for Astronomy and Astrophysics, California Institute of Technology, Pasadena, CA 91125, USA. [3]CCS-2, Los Alamos National Laboratory, Los Alamos, NM 87545, USA. [4]Physics Department, NC State University, Raleigh, NC 27695, USA. [5]Department of Physics, Durham University, Durham DH1 3LE, UK. [6]Department of Physics, McGill University, Rutherford Physics Building, Montreal, Quebec H3A 2T8, Canada. [7]Université de Toulouse, UPS-OMP, IRAP, Toulouse, France. [8]CNRS, Institut de Recherche en Astrophysique et Planétologie, 9 Av. colonel Roche, BP 44346, F-31028 Toulouse Cedex 4, France. [9]DTU Space, National Space Institute, Technical University of Denmark, Elektrovej 327, DK-2800 Lyngby, Denmark. [10]Lawrence Livermore National Laboratory, Livermore, CA 94550, USA. [11]Agenzia Spaziale Italiana (ASI) Science Data Center, Via del Politecnico snc I-00133, Roma, Italy. [12]Columbia Astrophysics Laboratory, Columbia University, New York, NY 10027, USA. [13]RIKEN Nishina Center, 2-1 Hirosawa, Wako, Saitama, 351-0198, Japan. [14]Kavli Institute for Particle Astrophysics and Cosmology, SLAC National Accelerator Laboratory, Menlo Park, CA 94025, USA. [15]INAF – Osservatorio Astronomico di Roma, via di Frascati 33, I-00040 Monteporzio, Italy. [16]Jet Propulsion Laboratory, California Institute of Technology, Pasadena, CA 91109, USA. [17]NASA Goddard Space Flight Center, Greenbelt, MD 20771, USA.
*Corresponding author. E-mail: boggs@berkeley.edu

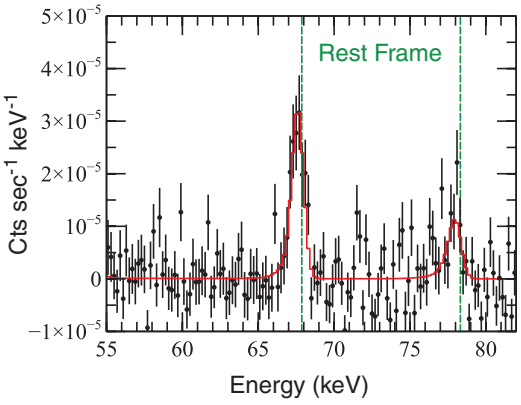

Fig. 1. SN1987A 55- to 80-keV background-subtracted spectrum measured with NuSTAR. Data from both telescopes are combined (for presentation only) and shown with 1σ error bars. Both of the ^{44}Ti lines are clearly measured. The vertical green lines are the rest-frame energies of the ^{44}Ti lines (67.87 and 78.32 keV). The redshift is evident in both lines, indicating the asymmetry of the explosion. Also shown is the best-fit model, convolved through the NuSTAR instrument response, for case (1), where the fitting parameters for the two lines are tied together (supplementary materials).

originally measured for the ^{56}Co lines (*9*, *10*). Although the limit on broadening itself is not surprising, the measured redshift is both statistically significant and large compared to the upper limit on Doppler broadening, indicative of an asymmetric ejection of ^{44}Ti in the initial explosion. The ^{56}Co gamma-ray lines also showed redshifts (~500 km s^{-1}), but the significance was marginal. The ^{56}Co detection also stands contrary to predictions of spherically symmetric explosion models that would produce blue-shifted gamma-ray lines due to increased absorption of the receding redshifted emission. The redshifted ^{56}Co lines suggest large-scale asymmetry in the explosion.

There has been growing evidence for asymmetries in supernovae explosions over the past decades (*25*). In SN1987A itself, asymmetry was initially supported by extensive evidence for mixing and polarized optical emission as reviewed in (*26*, *27*), and later by spatially resolved images of the ejecta (*27*, *28*). NuSTAR observations of the spatial distribution of ^{44}Ti in the Cas A supernova remnant shows direct evidence of asymmetry (*29*). Our results here suggest an even higher level of asymmetry for SN1987A. For comparison, NuSTAR measured a redshift for the integrated Cas A spectrum of (2100 ± 900) km s^{-1} and a line broadening corresponding to a fastest ejection velocity of ~5000 km s^{-1}. Given that ejection velocity and the age of the remnant (340 years), the estimated "look-back" redshift velocity for Cas A is ~1400 km s^{-1}, consistent with the measured redshift. From the spatially integrated ^{44}Ti spectrum alone, Cas A would not appear to have a statistically significant asymmetry: The spatial brightness distribution in Cas A revealed the asymmetries.

In the ^{44}Ti-powered phase, the dominant energy input to the ejecta comes through the subsequent positron emission of ^{44}Sc, when most of the gamma rays escape the ejecta without interacting. These positrons are produced deep in the ejecta, and both simple estimates and detailed models suggest that they are locally absorbed and instantaneously thermalized (*20*, *22*). The implication is that the UVOIR emission of SN1987A during the ^{44}Ti-powered phase should be dominated by the ejecta spatially coincident with the ^{44}Ti ejecta. In principle, UVOIR spectral imaging in the ^{44}Ti-powered phase can yield direct evidence for asymmetries. Hubble Space Telescope (HST) obtained resolved spectral images of the SN1987A ejecta (*28*) from June 2000 (4857 days after explosion), near the end of the phase when the UVOIR emission was truly dominated by ^{44}Ti decay (*21*). They reveal a bipolar structure elongated along the north-south direction. There is a clear gradient in velocity across ejecta, with the northern component showing a redshift of about 500 km s^{-1} in the [Ca II] λ7300 emission line, whereas the southern component showed a larger redshift of about 1700 km s^{-1}. The ejecta exhibit an overall redshift of ~1000 km s^{-1}. At the time, this asymmetry and overall redshift were noted but not emphasized, as they could be the result of blending of the [Ca II] λ7300 line with a [O II] λ7320 line. This shifted velocity distribution is consistent with our measured redshift of the ^{44}Ti lines. On the basis of our ^{44}Ti line profile, we might naïvely imagine the picture of a bright, redshifted clump or jet of ^{44}Ti, with the UVOIR emission tracing the spatial and velocity distribution of this clump. However, the spatial distribution of the ejecta in this HST observation does not immediately reveal such a large spatial asymmetry.

A single-lobe (i.e., very asymmetric) explosion model for SN1987A (*30*) could explain the observed evidence that ^{56}Ni was mixed to speeds exceeding 3000 km s^{-1} and redshifted, as evidenced by both the gamma-ray emission and the infrared forbidden line profiles of [Fe II] (mainly produced through ^{56}Ni decay) around 400 days after the explosion (*31*, *32*). In this model, the single lobe is oriented at an angle pointing away from us, producing the redshifted lines (*30*). The NuSTAR observations appear consistent with these single-lobe models. One consequence of such a highly asymmetric explosion is that the compact object produced by SN1987A would, presumably, receive a kick velocity opposite the direction of the ejecta (*33*).

REFERENCES AND NOTES

1. K. Hirata *et al.*, *Phys. Rev. Lett.* **58**, 1490–1493 (1987).
2. R. M. Bionta *et al.*, *Phys. Rev. Lett.* **58**, 1494–1496 (1987).
3. S. M. Matz *et al.*, *Nature* **331**, 416–418 (1988).
4. M. D. Leising, G. H. Share, *Astrophys. J.* **357**, 638 (1990).
5. J. D. Kurfess *et al.*, *Astrophys. J.* **399**, L137 (1992).
6. P. Bouchet *et al.*, *Astron. Astrophys.* **245**, 490 (1991).
7. C. Fransson, C. Kozma, *Astrophys. J.* **408**, L25 (1993).
8. W. D. Arnett, J. N. Bahcall, R. P. Kirshner, S. E. Woosley, *Annu. Rev. Astron. Astrophys.* **27**, 629–700 (1989).
9. J. Tueller *et al.*, *Astrophys. J.* **351**, L41 (1990).
10. B. J. Teegarden, *Adv. Space Res.* **11**, 217–227 (1991).
11. S. Park *et al.*, *Adv. Space Res.* **33**, 386–391 (2004).
12. E. A. Helder *et al.*, *Astrophys. J.* **764**, 11 (2013).
13. F. A. Harrison *et al.*, *Astrophys. J.* **770**, 103 (2013).
14. S. E. Woosley, T. A. Weaver, *Astrophys. J.* **101** (suppl.), 181 (1995).
15. G. Magkotsios *et al.*, *Astrophys. J.* **191** (suppl.), 66–95 (2010).
16. I. Ahmad *et al.*, *Phys. Rev. C Nucl. Phys.* **74**, 065803 (2006).
17. Materials and methods are available as supplementary materials on *Science* Online.
18. S. A. Grebenev, A. A. Lutovinov, S. S. Tsygankov, C. Winkler, *Nature* **490**, 373–375 (2012).
19. M. D. Leising, *Astrophys. J.* **651**, 1019–1022 (2006).
20. N. N. Chugai, R. A. Chevalier, R. P. Kirshner, P. M. Challis, *Astrophys. J.* **483**, 925–940 (1997).
21. J. Larsson *et al.*, *Nature* **474**, 484–486 (2011).
22. A. Jerkstrand, C. Fransson, C. Kozma, *Astron. Astrophys.* **530**, A45 (2011).
23. Y. Motizuki, S. Kumagai, *New Astron. Rev.* **48**, 69–73 (2004).
24. I. R. Seitenzahl, F. X. Timmes, G. Magkotsios, *Astrophys. J.* **792**, 10 (2014).
25. A. L. Hungerford, C. L. Fryer, M. S. Warren, *Astrophys. J.* **594**, 390–403 (2003).
26. L. Wang, J. C. Wheeler, *Annu. Rev. Astron. Astrophys.* **46**, 433–474 (2008).
27. K. Kjaer, B. Leibundgut, C. Fransson, A. Jerkstrand, J. Spyromilio, *Astron. Astrophys.* **517**, A51 (2010).
28. L. Wang *et al.*, *Astrophys. J.* **579**, 671–677 (2002).
29. B. W. Grefenstette *et al.*, *Nature* **506**, 339–342 (2014).
30. A. L. Hungerford, C. L. Fryer, G. Rockefeller, *Astrophys. J.* **635**, 487–501 (2005).
31. R. Haas *et al.*, *Astrophys. J.* **360**, 257 (1990).
32. J. Spyromilio, W. P. S. Meikle, D. A. Allen, *Mon. Not. R. Astron. Soc.* **242**, 669–673 (1990).
33. C. L. Fryer, A. Burrows, W. Benz, *Astrophys. J.* **496**, 333–351 (1998).

ACKNOWLEDGMENTS

This work was supported under NASA Contract no. NNG08FD60C and made use of data from the NuSTAR mission, a project led by the California Institute of Technology, managed by the Jet Propulsion Laboratory, and funded by the National Aeronautics and Space Administration. We thank the NuSTAR Operations, Software, and Calibration teams for support with the execution and analysis of these observations. This research has made use of the NuSTAR Data Analysis Software (NuSTARDAS) jointly developed by the ASI Science Data Center (ASDC, Italy) and the California Institute of Technology (USA). D.B. acknowledges funding from the French Space Agency (CNES). T.K. was supported by Japan Society for the Promotion of Science Grant-in-Aid for Young Scientists (B) (no. 24740185). N.J.W. acknowledges funding from the Technical University of Denmark. NuSTAR data are accessible from NASA's High Energy Astrophysics Science Archive Research Center (HEASARC, http://heasarc.gsfc.nasa.gov/).

SUPPLEMENTARY MATERIALS

www.sciencemag.org/content/348/6235/670/suppl/DC1
Materials and Methods
Figs. S1 to S3
Tables S1 and S2
References (*34*–*36*)

3 November 2014; accepted 8 April 2015
10.1126/science.aaa2259

PHYSICS

Creating and probing electron whispering-gallery modes in graphene

Yue Zhao,[1,2]* Jonathan Wyrick,[1]* Fabian D. Natterer,[1]* Joaquin F. Rodriguez-Nieva,[3]* Cyprian Lewandowski,[4] Kenji Watanabe,[5] Takashi Taniguchi,[5] Leonid S. Levitov,[3] Nikolai B. Zhitenev,[1]† Joseph A. Stroscio[1]†

The design of high-finesse resonant cavities for electronic waves faces challenges due to short electron coherence lengths in solids. Complementing previous approaches to confine electronic waves by carefully positioned adatoms at clean metallic surfaces, we demonstrate an approach inspired by the peculiar acoustic phenomena in whispering galleries. Taking advantage of graphene's gate-tunable light-like carriers, we create whispering-gallery mode (WGM) resonators defined by circular pn junctions, induced by a scanning tunneling probe. We can tune the resonator size and the carrier concentration under the probe in a back-gated graphene device over a wide range. The WGM-type confinement and associated resonances are a new addition to the quantum electron-optics toolbox, paving the way to develop electronic lenses and resonators.

Charge carriers in graphene exhibit light-like dispersion resembling that of electromagnetic waves. Similar to photons, electrons in graphene nanostructures propagate ballistically over micrometer distances, with the ballistic regime persisting up to room temperatures (*1*). This makes graphene an appealing platform for developing quantum electron optics, which aims at controlling electron waves in a fully coherent fashion. In particular, gate-tunable heterojunctions in graphene can be exploited to manipulate electron refraction and transmission in the same way that optical interfaces in mirrors and lenses are used to manipulate light (*2*). These properties have stimulated ideas in optics-inspired graphene electronics. First came Fabry-Pérot interferometers (*3*), which have been fabricated in planar npn heterostructures in single-layer graphene (*4*) and subsequently in bilayer (*5*) and trilayer graphene (*6*). The sharpness of the pn junctions achievable in graphene can enable precise focusing of electronic rays across the junction, allowing for electronic lensing and hyperlensing (*7*–*9*).

We report on electron whispering-gallery mode (WGM) resonators, an addition to the electron-optics toolbox. The WGM resonances are familiar for classical wave fields confined in an enclosed geometry—as happens, famously, in the whispering gallery of St. Paul's Cathedral. The WGM resonators for electromagnetic fields are widely used in a vast array of applications requiring high-finesse optical cavities (*10*–*12*). Optical WGM resonators do not depend on movable mirrors and thus lend themselves well to designs with a high quality factor. This can render the WGM design advantageous over the Fabry-Pérot design, despite challenges in achieving tunability due to their monolithic (single-piece) character [see (*12*) for a mechanically tunable optical WGM resonator]. Our system is free from these limitations, representing a fully tunable WGM resonator in which the cavity radius can be varied over a wide range by adjusting gate potentials. In contrast, the best electronic resonators known to date—the nanometer-sized quantum corrals designed by carefully positioning adatoms atop a clean metallic surface (*13*)—are not easily reconfigurable.

[1]Center for Nanoscale Science and Technology, National Institute of Standards and Technology, Gaithersburg, MD 20899, USA. [2]Maryland NanoCenter, University of Maryland, College Park, MD 20742, USA. [3]Department of Physics, Massachusetts Institute of Technology, Cambridge, MA 02139, USA. [4]Department of Physics, Imperial College London, London SW7 2AZ, UK. [5]National Institute for Materials Science, Tsukuba, Ibaraki 305-0044, Japan. *These authors contributed equally to this work. †Corresponding author. E-mail: nikolai.zhitenev@nist.gov (N.B.Z.); joseph.stroscio@nist.gov (J.A.S.)

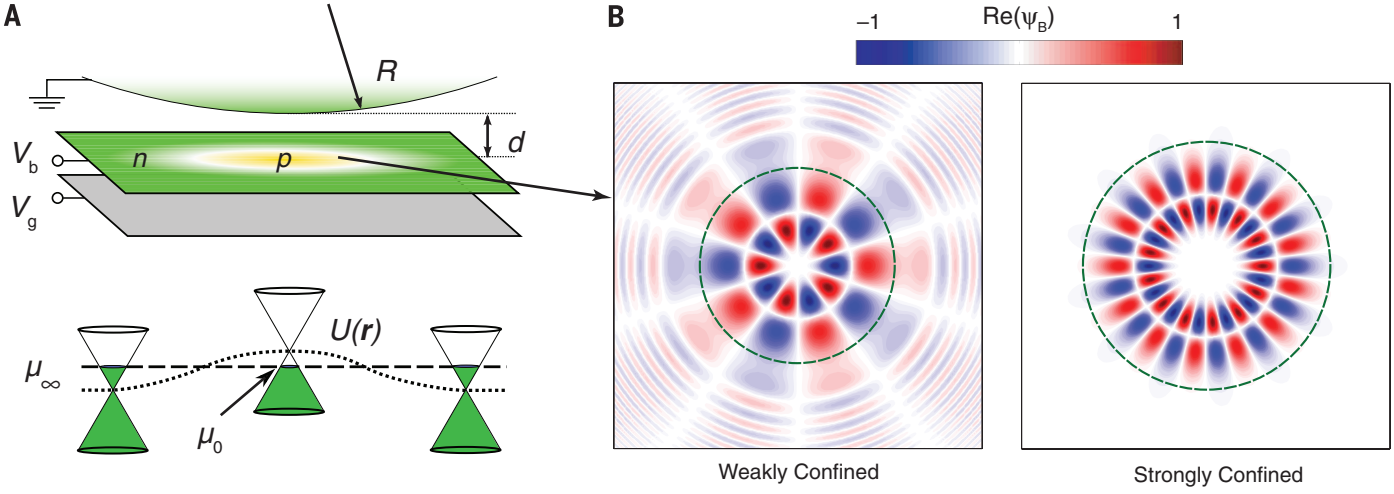

Fig. 1. Confined electronic states in microscopic electron cavities defined by pn junction rings in graphene. (**A**) The rings are induced by the STM tip voltage bias (V_b) and back-gate voltage (V_g), adjusted so as to reverse the carrier polarity beneath the tip relative to the ambient polarity. The pn junctions act as sharp boundaries giving rise to Klein scattering of electronic waves, producing mode confinement via the whispering-gallery mechanism. The cavity radius and the local carrier density are independently tunable by the voltages V_b and V_g. Electron resonances are mapped out by the STM spectroscopy measurements (see Fig. 2). Shown are the STM tip potential $U(\mathbf{r})$ and the quantities discussed in the text: the STM tip radius (R), its distance from graphene (d), and the local (μ_0) and ambient (μ_∞) Fermi levels with respect to the Dirac point. n and p label the electron and hole regions. (**B**) Spatial profile of WGM resonances. Confinement results from interference of the incident and reflected waves at the pn rings (dashed lines). The confinement is stronger for the larger angular momentum m values, corresponding to more oblique wave incidence angles. This is illustrated for $m = 5$ (weak confinement) and $m = 13$ (strong confinement). Plotted is the quantity Re(ψ_B), the real part of the second spinor component in Eq. 1.

Further, although WGM resonators are ubiquitous in optics and acoustics (*10*–*12*, *14*), only a few realizations of such resonators were obtained in nonoptical and nonacoustic systems. These include WGM for neutrons (*15*), as well as for electrons in organic molecules (*16*). In our measurements a circular electron cavity is created beneath the tip of a scanning tunneling microscope (STM), and we directly observe the WGM-type confinement of electronic modes. The cavity is defined by a tip-induced circular pn junction ring, at which the reflection and refraction of electron waves are governed by Klein scattering (Fig. 1). Klein scattering originates from graphene's linear energy dispersion and opposite group velocities for conduction and valence band carriers; Klein scattering at a pn junction features a strong angular dependence with a 100% probability for transmission at normal incidence, as well as focusing properties resembling negative refractive index metamaterials (*2*, *7*). Although Klein scattering is characterized by perfect transmission and no reflection for normal incidence, it gives rise to nearly perfect reflection for oblique incidence occurring in the WGM regime (*2*). As illustrated in Fig. 1B, this yields excellent confinement and high-finesse WGM resonances for modes with high angular momentum m and a less perfect confinement for non-WGM modes with lower m values.

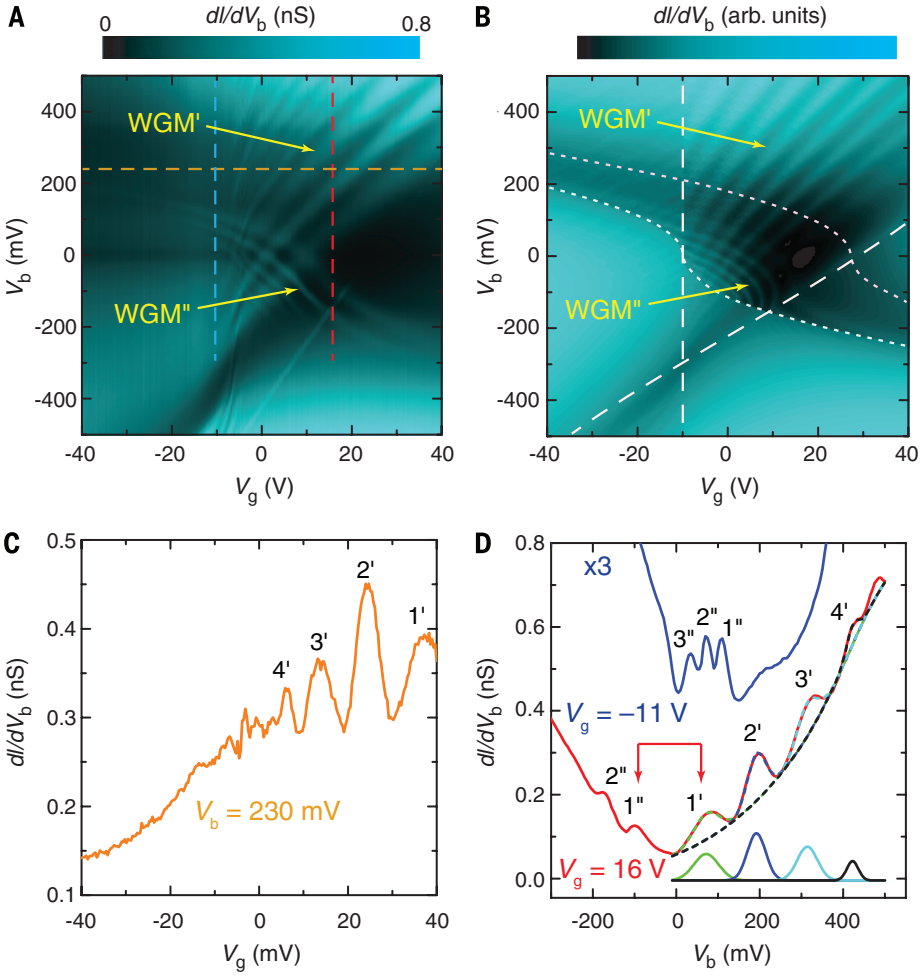

Fig. 2. Confined electronic states probed by STM measurements. (**A**) Differential tunneling conductance (dI/dV_b) for a single-layer graphene device, as a function of sample bias (V_b) and back-gate voltage (V_g). The gate map was obtained after increasing the probe-tip work function by exposure to deuterium to shift the interference fringes vertically downward (fig. S5) (*17*). The two fans of interference features, marked WGM′ and WGM″, originate from WGM resonances in the DOS (see text). (**B**) Interference features in dI/dV_b, calculated from the relativistic Dirac model. The features WGM′ and WGM″ in the (V_g,V_b) map originate, respectively, from the conditions $\varepsilon = \mu_0$ and $\varepsilon = \mu_0 + eV_b$ (see text). The boundaries of the WGM′ (and WGM″) regions are marked by dashed (and dotted) white lines, respectively. arb. units, arbitrary units. (**C**) dI/dV_b spectra taken along the horizontal line in (A) at V_b = 230 mV. (**D**) dI/dV_b spectra taken along the two vertical lines in the map in (A) at V_g = 16 V (red line) and V_g = –11 V (blue line, scaled ×3 and offset for clarity) (see text for discussion). The four peaks at positive bias at V_g = 16 V are fit to Gaussian functions, with the fits shown in the lower right of the figure. The peaks labeled 1″,2″,3″... correspond to WGM resonances probed at the energy $\varepsilon = \mu_0 + eV_b$, whereas the peaks labeled 1′,2′,3′..., are the same WGM resonances probed at the Fermi level $\varepsilon = \mu_0$, giving rise to the WGM″ and WGM′ fringes in the gate maps, respectively. The resonance spacing of order 40 mV translates into a cavity radius of 50 nm, using the relation $\Delta\varepsilon = \pi\hbar v_F/r$ (see text).

Electron optical effects in graphene have so far been explored using transport techniques, which lack spatial and angular resolution that would be indispensable for studying confined electronic states and/or electron lensing. Our scanning probe technique allows us to achieve nanometer-scale spatial resolution. The STM probe has a dual purpose: (i) creating a local pn junction ring, which serves as a confining potential for electronic states, and (ii) probing by electron tunneling the resonance states localized in this potential. The planar back gate and the STM tip, acting as a circular micrometer-sized top gate, can change both the overall background carrier density and the local carrier density under the tip. As such, pn and np circular junctions centered under the probe tip (Fig. 1A) can be tuned by means of the tip-sample bias V_b and the back-gate voltage V_g [see fig. S4 (*17*)]. For the purpose of creating resonant electronic modes inside the junction, this configuration gives us in situ, independent control over the carrier concentration beneath the STM tip and the pn ring radius. The tunneling spectral maps from such a device show a series of interference fringes as a function of the knobs (V_b,V_g) (Fig. 2). These fringes originate from resonant quasi-bound states inside the pn ring.

The measured spacing between fringes ($\Delta\varepsilon$) can be used to infer the cavity radius (r). Using the formula $\Delta\varepsilon = \pi\hbar v_F/r$ ($\hbar$, Planck's constant $\hbar$ divided by 2π; $v_F \approx 10^6$ m/s) and an estimate from Fig. 2A ($\Delta\varepsilon \approx 40$ meV), we obtain $r \approx 50$ nm, a value considerably smaller than the STM tip radius ($R \approx 1$ μm). This behavior can be understood from a simple electrostatic model of a charged sphere proximal to the ground plane. When the sphere-to-plane distance d is small compared with the sphere radius R, the induced image charge density cloud $\rho(r)$ behaves as $\rho(r) \propto 1/(d + r^2/2R)$, predicting a length scale $\sqrt{2Rd} \ll R$. This crude estimate is upheld, within an order of magnitude, by a more refined electrostatic modeling (*17*), which also gives a length scale much smaller than R.

The experimental results were obtained on a device consisting of a graphene layer on top of hexagonal boron nitride, stacked on SiO_2 with a doped Si back gate [see supplementary materials for details (*17*)]. Figure 2A shows a tunneling conductance map as a function of back-gate voltage (V_g) on the horizontal axis and sample bias (V_b) on the vertical axis. A series of interference-like fringes forming a curved fan (labeled WGM′) can be seen in the upper right of Fig. 2A. The center of the fan defines the charge neutrality point. This point can be off (0,0) in the (V_g,V_b) plane due to impurity doping of graphene (shift along V_g) and the contact potential difference between the probe tip and graphene (shift in V_b). As illustrated in fig. S5 (*17*), we are able to shift

the center point of the fan to lower V_b values by changing the tip work function, for example, with D_2 adsorption (*18*). Another interesting feature in such conductance maps is a (somewhat less visible) second fan of fringes (labeled WGM″), which is crossing the primary WGM′ fan. The fringes in the WGM″ fan follow the typical graphene dispersion with respect to the Fermi energy, which varies with doping as $\propto\sqrt{|V_g|}$ from higher sample bias to lower as a function of V_g. Examining the primary (WGM′) and secondary (WGM″) fringes more closely confirms that they originate from the same family of WGM resonances.

Figure 2C shows nine oscillations in a line cut across the WGM′ fan along the V_g axis. To understand the origin of these oscillations, we examine the two spectral line cuts along the V_b axis in Fig. 2D. The first spectrum in Fig. 2D at V_g = −11 V (blue curve) contains a group of resonances (labeled 1″ to 3″) near the Fermi level (V_b = 0) with a spacing of 37.6 ± 1.2 mV (*19*). In the map in Fig. 2A, these resonances can be seen to move to lower energies approximately following the typical Dirac point dispersion $\propto\sqrt{|V_g|}$. Taking a vertical cut at a higher back-gate voltage of V_g = 16 V (red curve) shows resonances 1″ and 2″ shifted down in energy in Fig. 2D. Focusing now at slightly higher energies, the WGM′ resonances appear at positive energies in Fig. 2D and are labeled 1′ to 4′ for V_g = 16 V. These four resonances are fit to Gaussian functions and shown deconvolved from the background conductance in the bottom right of the figure. The average spacing of these resonances is 116.9 ± 7.5 mV (*19*). A close examination of Fig. 2A indicates the one-to-one correspondence between the WGM″ resonances 1″, 2″,... and the WGM′ resonances 1′, 2′..., suggesting their common origin. We therefore conclude that the WGM″ resonances correspond to tunneling into the pn junction modes at energy $\varepsilon = \mu_0 + eV_b$ [μ_0, local Fermi level (see Fig. 1A)], whereas the WGM′ resonances reflect the action of the STM tip as a top gate, allowing tunneling into the same resonance mode at $\varepsilon = \mu_0$ [see fig. S3 (*17*)]. For example, resonance 1″ seen at $V_b \approx -100$ mV is now accessible at the Fermi level by the tip-graphene potential difference, as shown in fig. S3D (*17*), when tunneling into the WGM′ resonance 1′ at V_b = 82 mV in Fig. 2A.

To clarify the WGM character of these resonances, we analyze graphene's Dirac carriers in the presence of a potential induced by the STM tip described by the Hamiltonian $H = H_0 + U(\boldsymbol{r})$, where H_0 is the kinetic energy term and $U(\boldsymbol{r})$ describes the STM tip potential seen by charge carriers. Because relevant length scales—the electron's Fermi wavelength and the pn ring radius–are much greater than the atomic spacing, we focus on the low-energy states. We linearize the graphene electron spectrum near the K and K' points, bringing H_0 to the massless Dirac form: $\varepsilon\psi(\boldsymbol{r}) = [v_F\sigma\cdot\boldsymbol{p} + U(\boldsymbol{r})]\psi(\boldsymbol{r})$, where $\boldsymbol{p} = -i\hbar\nabla_r$ and $\sigma = (\sigma_x, \sigma_y)$ are pseudospin Pauli matrices. We take the tip potential to be radially symmetric, reflecting the STM tip geometry. Furthermore, the distance from the tip to graphene (d) is considerably smaller than the electron's Fermi wavelength and the pn ring radius, both of which are smaller than the STM tip radius. We can therefore use a parabola to approximate the tip potential, $U(r) = \kappa r^2$ (r, off-center displacement). The curvature κ, which affects the energy spectrum of WGM resonances, can be tuned with the bias and gate potentials, as discussed in the supplementary materials (*17*).

The WGM states with different angular momentum can be described by the polar decomposition ansatz

$$\psi_m(r,\phi) = \frac{1}{\sqrt{r}}\begin{pmatrix} u_A(r)e^{i(m-1)\phi} \\ u_B(r)e^{im\phi}\end{pmatrix} \quad (1)$$

where m is an integer angular momentum quantum number, ϕ is the polar angle, and A, B label the two graphene sublattices. We nondimensionalize the Schrödinger equation using the characteristic length and energy scales ($r_* = \sqrt{Rd}$, $\varepsilon_* = \hbar v_F/\sqrt{Rd}$) to obtain the radial eigenvalue equation of the two-component spinor $u(r)$ with components $u_A(r)$ and $u_B(r)$

$$\varepsilon u(r) = \left(-i\sigma_x\partial_r + \frac{m+1/2}{r}\sigma_y + \kappa r^2\right)u(r) \quad (2)$$

Here r is in units of r_*, ε is in units of ε_*, and κ is in units of $\kappa_* = \varepsilon_*/r_*^2$. This equation is solved using a finite difference method [see supplementary material (*17*)]. We can use this

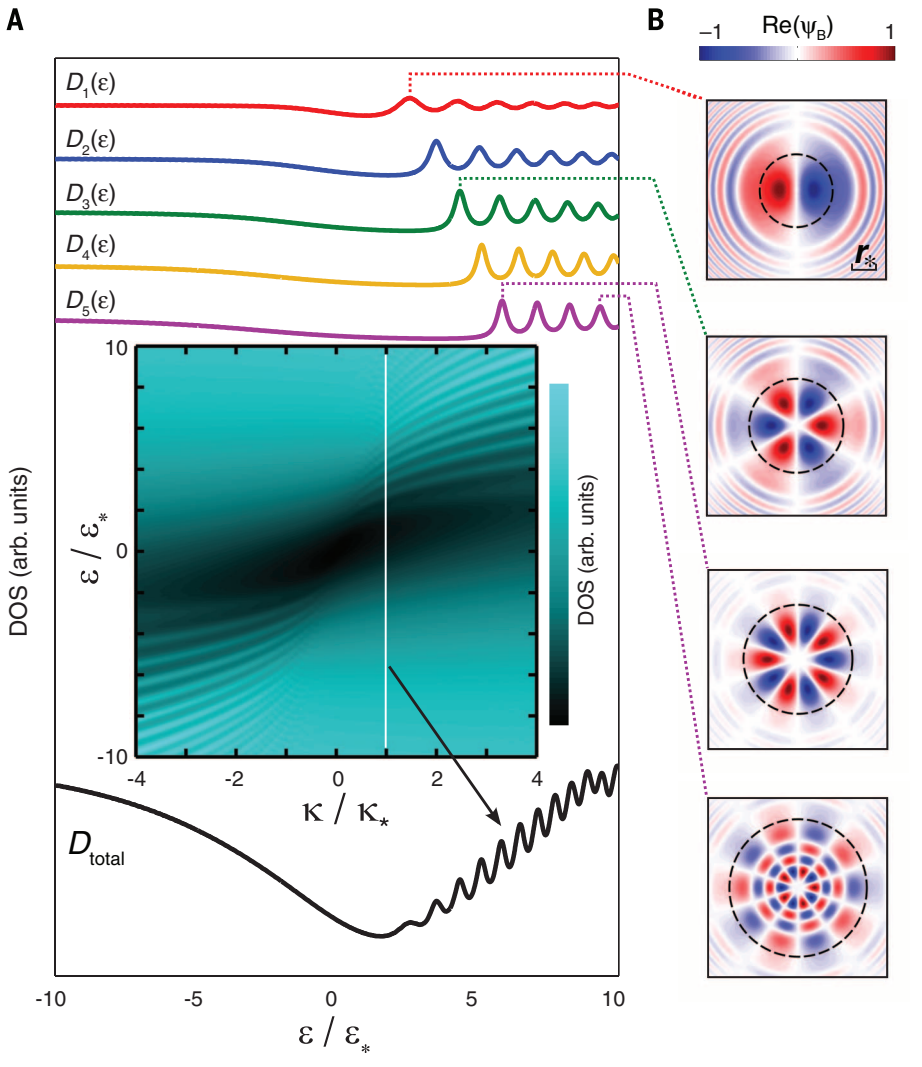

Fig. 3. Contributions of the WGM resonances with different *m* to the DOS for the relativistic Dirac model. (**A**) Colored curves represent partial-m contributions from angular momentum values m = 1,2,3,4,5 (see Eq. 3), evaluated for a confining potential $U(\boldsymbol{r}) = \kappa\boldsymbol{r}^2$ with curvature value $\kappa = \kappa_* = \varepsilon_*/Rd$. Different curves show the partial DOS contributions defined in Eq. 3, which are offset vertically for clarity. The inset shows the total DOS versus particle energy ε and the curvature κ (see text). The black curve shows the total DOS trace along the white line. (**B**) The Dirac wavefunction for different WGM states (see Eq. 1). Spatial structure is shown for several resonances in the partial DOS (black dashed circles mark the pn junction rings). The quantity plotted, $\mathrm{Re}(\psi_B)$, is the same as in Fig. 1B. The length scale $r_* = \sqrt{Rd}$ (the same in all panels) is marked. Note the confinement strength increasing with m.

microscopic framework to predict the measured spectral features. The tunneling current, expressed through the local density of states (DOS), is modeled as

$$I = \int_{\mu_0}^{\mu_0 + eV_b} d\varepsilon T(\varepsilon, V_b) \sum_m D_m(\varepsilon),$$
$$D_m(\varepsilon) = \sum_{r,\nu} e^{-\lambda r^2/2} |u_\nu(r)|^2 \delta(\varepsilon - \varepsilon_\nu) \quad (3)$$

which is valid for modest V_b values (*20*). Here μ_0 is the Fermi energy under the tip, which in general is different from ambient Fermi energy μ_∞ as a result of gating by the tip (see below). The transmission function $T(\varepsilon,V_b)$, which depends on the tip geometry, work function, and DOS, will be taken as energy-independent. The quantity $D(\varepsilon) = \sum_m D_m(e)$ represents the sum of partial-m contributions to the total DOS beneath the tip, with ν labeling eigenstates of Eq. 2 with fixed m. The weighting factor $e^{-\lambda r^2/2}$ is introduced to account for the finite size of the region where tunneling occurs, with the Gaussian halfwidth $\lambda^{-1/2} \sim r_*$ [see supplementary materials (*17*)].

The WGM resonances for different partial-m contributions $D_m(\varepsilon)$, which combine into the total DOS (Fig. 3), reveal that individual WGM states exhibit very different behavior depending on the m value [see Figs. 1B and 3B]. Klein scattering at the circular pn junction produces confinement creating the WGMs, and the confinement is stronger for the large-m modes and weaker for small-m modes. The Klein reflection probability is strongly dependent on the angle of incidence θ at the pn interface, growing as $R(\theta) \sim 1 - \exp[-\xi \sin^2(\theta)]$, where ξ is a characteristic dimensionless parameter (*21*). The value of θ grows with m as $\tan\theta \propto m$. As a result, larger values of m must translate into larger reflectivity and stronger confinement. This trend is clearly demonstrated in Figs. 1B and 3B. Also, as m increases, mode wavefunctions are being pushed away from the origin, becoming more localized near the pn ring, in full accord with the WGM physics.

To understand how one family of WGM resonances gives rise to two distinct fans of interference features seen in the data, we must account carefully for the gating effect of the STM tip. We start with recalling that conventional STM spectroscopy probes features at energies $\varepsilon_n = \mu_0 + eV_b$, where ε_n are system energy levels. This corresponds to the family WGM″ in our measurements. However, as discussed above, the tip bias variation causes the Fermi level beneath the tip to move through system energy levels ε_n, producing an additional family of interference features (WGM′) described by $\varepsilon_n = \mu_0$ [see fig. S3 and accompanying discussion (*17*)]. To model this effect, we evaluate the differential conductance $G = dI/dV_b$ from Eq. 3, taking into account the dependence μ_0 versus V_b. This gives

$$G \propto (1 - \eta) D(\mu_0 + eV_b) + \eta D(\mu_0) \quad (4)$$

with $\eta = -\partial\mu_0/\partial(eV_b)$. The two contributions in Eq. 4 describe the WGM′ and WGM″ families. We note that the second family originates from the small electron compressibility in graphene, resulting in a finite η and would not show up in a system with a vanishingly small η (e.g., in a metal). We use Eq. 4 with a value $\eta = 1/2$ to generate Fig. 2B. In doing so, we use electrostatic modeling [described in (*17*)] to relate the parameters (ε,κ) in the Hamiltonian, Eq. 2, and the experimental knobs (V_b, V_g). This procedure yields a very good agreement with the measured dI/dV_b (Fig. 2, A and B).

In addition to explaining how the two sets of fringes, WGM′ and WGM″, originate from the same family of WGM resonances, our model accounts for other key features in the data. In particular, it explains the large difference in the WGM′ and WGM″ periodicities noted above. It also correctly predicts the regions where fringes occur (Fig. 2B). The bipolar regime in which pn junction rings and resonances in the DOS occur (see fig. S6 and S7) takes place for the probed energies ε of the same sign as the potential curvature. In the case of a parabola $U(\boldsymbol{r}) = \kappa \boldsymbol{r}^2$, this gives the condition $\varepsilon\kappa > 0$, corresponding to the upper-right and lower-left quadrants in Fig. 3A, inset. However, under experimental conditions, the potential is bounded by $U(|\boldsymbol{r}| \to \infty) = \mu_0 - \mu_\infty$ (see Fig. 1A), which constraints the regions in which WGMs are observed (*17*). Accounting for the finite value $U(|\boldsymbol{r}| \to \infty)$ yields the condition $|\varepsilon| \le |\mu_0 - \mu_\infty|$, with $\mathrm{sgn}(\varepsilon) = \mathrm{sgn}(\kappa) = \mathrm{sgn}(\mu_0 - \mu_\infty)$. This gives the WGM′ and WGM″ regions in Fig. 2B bounded by white dashed and white dotted lines, respectively, and matching accurately the WGM′ and WGM″ location in our measurements.

The range of m values that our measurement can probe depends on the specifics of the tunneling region at the STM tip. We believe that a wide range of m values can be accessed; however, we are currently unable to distinguish different partial-m contributions, because the corresponding resonances are well aligned (Fig. 3). Different m states may contribute if the tunneling center is not the same as the geometric center of the tip, which is highly likely. As shown in (*13*), higher m states can be accessed by going off center by as little as 1 nm, which is likely in our real experiment due to a residual asymmetry of the STM tip [we model this effect by a Gaussian factor in Eq. 3]. We note in this regard that different angular momentum m values translate into different orbital magnetic moment values, opening an opportunity to probe states with different m by applying a magnetic field.

The explanation of the observed resonances in terms of the whispering-gallery effect in circular pn rings acting as tunable electronic WGM resonators has other notable ramifications. First, it can shed light on puzzling observations of resonances in previous STM measurements (*22*–*24*), which hitherto remained unaddressed. Second, our highly tunable setup in which the electron wavelength and cavity radius are controlled independently lends itself well to directly probing other fundamental electron-optical phenomena, such as negative refractive index for electron waves, Veselago lensing (*7*), and Klein tunneling (*2*). Further, we envision probing more exotic phenomena such as the development of caustics, where an incident plane wave is focused at a cusp (*25*–*27*), and special bound states for integrable classes of dynamics, where the electron path never approaches the confining boundary at perpendicular incidence (*28*). These advances will be enabled by the distinct characteristics of graphene that allow for electronic states to be manipulated at the microscale with unprecedented precision and tunability, thus opening a wide vista of graphene-based quantum electron-optics.

REFERENCES AND NOTES

1. A. S. Mayorov *et al*., *Nano Lett.* **11**, 2396–2399 (2011).
2. M. I. Katsnelson, K. S. Novoselov, A. K. Geim, *Nat. Phys.* **2**, 620–625 (2006).
3. A. V. Shytov, M. S. Rudner, L. S. Levitov, *Phys. Rev. Lett.* **101**, 156804 (2008).
4. A. F. Young, P. Kim, *Nat. Phys.* **5**, 222–226 (2009).
5. A. Varlet *et al*., *Phys. Rev. Lett.* **113**, 116601 (2014).
6. L. C. Campos *et al*., *Nat. Commun.* **3**, 1239 (2012).
7. V. V. Cheianov, V. Fal'ko, B. L. Altshuler, *Science* **315**, 1252–1255 (2007).
8. C.-H. Park, Y.-W. Son, L. Yang, M. L. Cohen, S. G. Louie, *Nano Lett.* **8**, 2920–2924 (2008).
9. J. R. Williams, T. Low, M. S. Lundstrom, C. M. Marcus, *Nat. Nanotechnol.* **6**, 222–225 (2011).
10. K. J. Vahala, *Nature* **424**, 839–846 (2003).
11. A. B. Matsko, V. S. Ilchenko, *IEEE J. Sel. Top. Quantum Electron.* **12**, 3–14 (2006).
12. M. Pöllinger, D. O'Shea, F. Warken, A. Rauschenbeutel, *Phys. Rev. Lett.* **103**, 053901 (2009).
13. M. F. Crommie, C. P. Lutz, D. M. Eigler, *Science* **262**, 218–220 (1993).
14. L. Rayleigh, *Philos. Mag. Ser. 6* **20**, 1001–1004 (1910).
15. V. V. Nesvizhevsky, A. Y. Voronin, R. Cubitt, K. V. Protasov, *Nat. Phys.* **6**, 114–117 (2010).
16. G. Reecht *et al*., *Phys. Rev. Lett.* **110**, 056802 (2013).
17. Additional supplementary text and data are available on *Science* Online.
18. K. Christmann, *Surf. Sci. Rep.* **9**, 1–163 (1988).
19. All uncertainties reported represent 1 SD from multiple measurements.
20. J. Tersoff, N. D. Lang, in *Scanning Tunneling Microscopy*, J. A. Stroscio, W. J. Kaiser, Eds. (Academic Press, San Diego, CA, 1993), chap. 1.
21. V. V. Cheianov, V. I. Fal'ko, *Phys. Rev. B* **74**, 041403 (2006).
22. G. M. Rutter *et al*., *Science* **317**, 219–222 (2007).
23. S. Jung *et al*., *Nat. Phys.* **7**, 245–251 (2011).
24. J. Chae *et al*., *Phys. Rev. Lett.* **109**, 116802 (2012).
25. J. Cserti, A. Pályi, C. Péterfalvi, *Phys. Rev. Lett.* **99**, 246801 (2007).
26. R. L. Heinisch, F. X. Bronold, H. Fehske, *Phys. Rev. B* **87**, 155409 (2013).
27. N. Agrawal (Garg), S. Ghosh, M. Sharma, *J. Phys. Condens. Matter* **26**, 155301 (2014).
28. J. Bardarson, M. Titov, P. Brouwer, *Phys. Rev. Lett.* **102**, 226803 (2009).

ACKNOWLEDGMENTS

Y.Z. acknowledges support under the Cooperative Research Agreement between the University of Maryland and the National Institute of Standards and Technology Center for Nanoscale Science and Technology, grant 70NANB10H193, through the University of Maryland. J.W. acknowledges support from the Nation Research Council Fellowship. F.D.N. greatly appreciates support from the Swiss National Science Foundation under project numbers 148891 and 158468. L.S.L. acknowledges support from STC CIQM/NSF-1231319. We thank S. Blankenship and A. Band for their contributions to this project and M. Stiles and P. First for valuable discussions.

SUPPLEMENTARY MATERIALS

www.sciencemag.org/content/348/6235/672/suppl/DC1
Supplementary Text
Figs. S1 to S7
References (*29*–*33*)

22 January 2015; accepted 31 March 2015
10.1126/science.aaa7469

GEOPHYSICS

Migrating tremor off southern Kyushu as evidence for slow slip of a shallow subduction interface

Y. Yamashita,[1]*† H. Yakiwara,[2] Y. Asano,[3] H. Shimizu,[1] K. Uchida,[1] S. Hirano,[2] K. Umakoshi,[4] H. Miyamachi,[2] M. Nakamoto,[1] M. Fukui,[1] M. Kamizono,[1] H. Kanehara,[5] T. Yamada,[6] M. Shinohara,[6] K. Obara[6]

Detection of shallow slow earthquakes offers insight into the near-trench part of the subduction interface, an important region in the development of great earthquake ruptures and tsunami generation. Ocean-bottom monitoring of offshore seismicity off southern Kyushu, Japan, recorded a complete episode of low-frequency tremor, lasting for 1 month, that was associated with very-low-frequency earthquake (VLFE) activity in the shallow plate interface. The shallow tremor episode exhibited two migration modes reminiscent of deep tremor down-dip of the seismogenic zone in some other subduction zones: a large-scale slower propagation mode and a rapid reversal mode. These similarities in migration properties and the association with VLFEs strongly suggest that both the shallow and deep tremor and VLFE may be triggered by the migration of episodic slow slip events.

Slow earthquakes are a range of seismic phenomena with longer durations than ordinary earthquakes. They are considered key to understanding the generation of megathrust earthquakes because their activity affects stress accumulation on the locked zone. Slow earthquakes are well documented in the deep transition zone between the seismogenic zone and stable sliding zone. Episodic tremor and slip (ETS) is the coupled phenomena of nonvolcanic deep low-frequency tremor (*1*) and slow slip events (SSEs) (*2*) with a specific recurrence interval. Observations of ETS have been documented in Cascadia (*3*) and southwestern Japan (*4*). ETS events also coincide with deep very-low-frequency earthquake (VLFE) activity (*5*). These events share a common mechanism as shear slip on the plate interface (*6*). Because the spatiotemporal evolution of deep tremor and VLFEs reflects the rupture process of SSEs (*7*), tremor activity is useful for assessing interplate aseismic slip in the deep transition zone. Many observations of deep tremor suggest that SSEs are common on the deep side of the seismogenic zone.

The shallow subducting plate interface near the trench was thought to be a conditionally stable zone (*8*). Understanding the slip potential of this region is important for evaluating the development of great earthquake ruptures, such as the 2011 Tohoku-Oki earthquake, and the associated potential for tsunami generation. Therefore, the nature of slow earthquakes (particularly SSEs, which account for the greatest moment release of slow earthquakes) has critical implications for the interplate slip and moment budget of the

[1]Institute of Seismology and Volcanology (SEVO), Faculty of Sciences, Kyushu University, 2-5643-29 Shin'yama, Shimabara 855-0843, Japan. [2]Nansei-Toko Observatory for Earthquakes and Volcanoes, Graduate School of Science and Engineering, Kagoshima University, 10861 Yoshino-cho, Kagoshima 892-0871, Japan. [3]National Research Institute for Earth Science and Disaster Prevention, 3-1 Tennodai, Tsukuba 305-0006, Japan. [4]Graduate School of Fisheries Science and Environmental Studies, Nagasaki University, 1-14 Bunkyo-machi, Nagasaki 852-8521, Japan. [5]Faculty of Fisheries, Nagasaki University, 1-14 Bunkyo-machi, Nagasaki 852-8521, Japan. [6]Earthquake Research Institute (ERI), The University of Tokyo, 1-1-1 Yayoi, Bunkyo-ku, Tokyo 113-0032, Japan.
***Corresponding author. E-mail: yamac@eri.u-tokyo.ac.jp**
†Present address: ERI, The University of Tokyo, 1-1-1 Yayoi, Bunkyo-ku, Tokyo 113-0032, Japan.

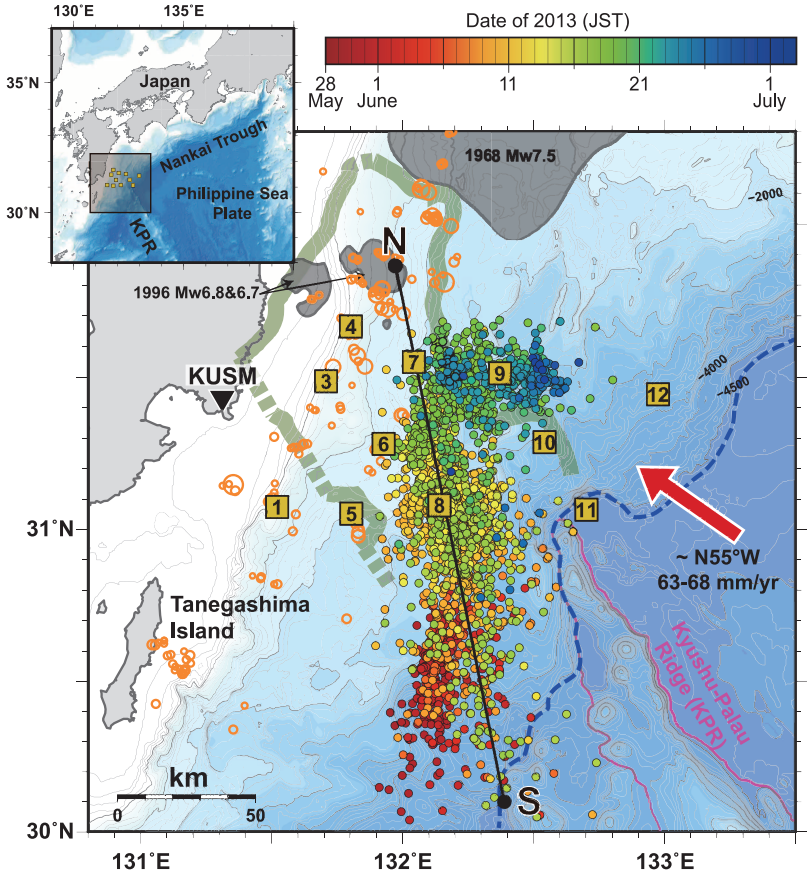

Fig. 1. Shallow low-frequency tremor distribution and tectonic setting. Location map (**inset**) and bathymetry of the study area, showing spatiotemporal distribution of shallow tremor (colored circles) [time zone is Japan standard time (JST), or universal time coordinated + 09:00], locations and numbers of OBS stations (yellow squares), epicenters of small repeating earthquakes (orange circles) (*16*), the coseismic slip area of M7-class interplate earthquakes (dark gray) (*26*, *27*), and the outer edge of the subducted KPR (dark green bold) (*24*). The convergence direction of the Philippine Sea Plate (*30*) is denoted by the red arrow, the trench axis is indicated by the dashed blue line, and bathymetric contours are shown at 100-m intervals. KUSM is a land-based seismic station, which used in Fig. 2A.

shallow plate interface. Shallow VLFE activity has been observed in Japan (*9*–*11*) and Costa Rica (*12*), but low-frequency tremor observations near the trench are scarce (*13*). The previous studies have not indicated spatiotemporal variation of activities for shallow tremor and VLFEs. Although SSEs have recently been detected at both deep and shallow plate interface in southwest Japan by Global Navigation Satellite System (GNSS) analysis (*14*), the spatiotemporal relationship with seismic shallow slow events is still unclear.

The region east off the east coast of southern Kyushu (the western part of Nankai Trough) is one of the most active areas of ordinary earthquake seismicity (fig. S1) and shallow VLFE seismicity in southwestern Japan (*9*, *10*). Estimation of interplate coupling from long-term ground deformation using GNSS data (*15*) and the existence of small repeating earthquakes (*16*) suggest that the subduction megathrust of this area is creeping (low interplate coupling) while producing small and moderate-sized interplate earthquakes. The locked Nankai subduction zone to the northeast provides a sharp contrast to this region. We expected a phenomenon like ETS to occur in the shallow plate interface because shallow VLFE seismicity is seen repeatedly (fig. S2), although no tremor has been previously reported in the area. We deployed 12 short-period ocean bottom seismometers (OBSs) for ~80 days to investigate shallow tremor activity of this area (Fig. 1) (*17*).

Fortuitously, the first major episode of shallow VLFE activity in 3 years started just after we deployed the OBSs. This VLFE episode occurred in the same area as previous activity, according to array analysis of data from land-based broadband seismic stations (*10*) (fig. S2). The episode lasted for 1 month and included three active stages (Fig. 2C). During the same time period, our OBS network recorded a complete, month-long episode of shallow tremor activity. The dominant frequency of the tremor waveforms, ranging from 0.5 to 8 Hz, was lower than that of ordinary earthquakes (Fig. 3) (*17*). Each peak of tremor in the OBS observations almost corresponded to each wave train recorded by land-based broadband seismographs, after allowing for the difference of ~1 min in travel time between the two sets of stations (Fig. 2, A and B).

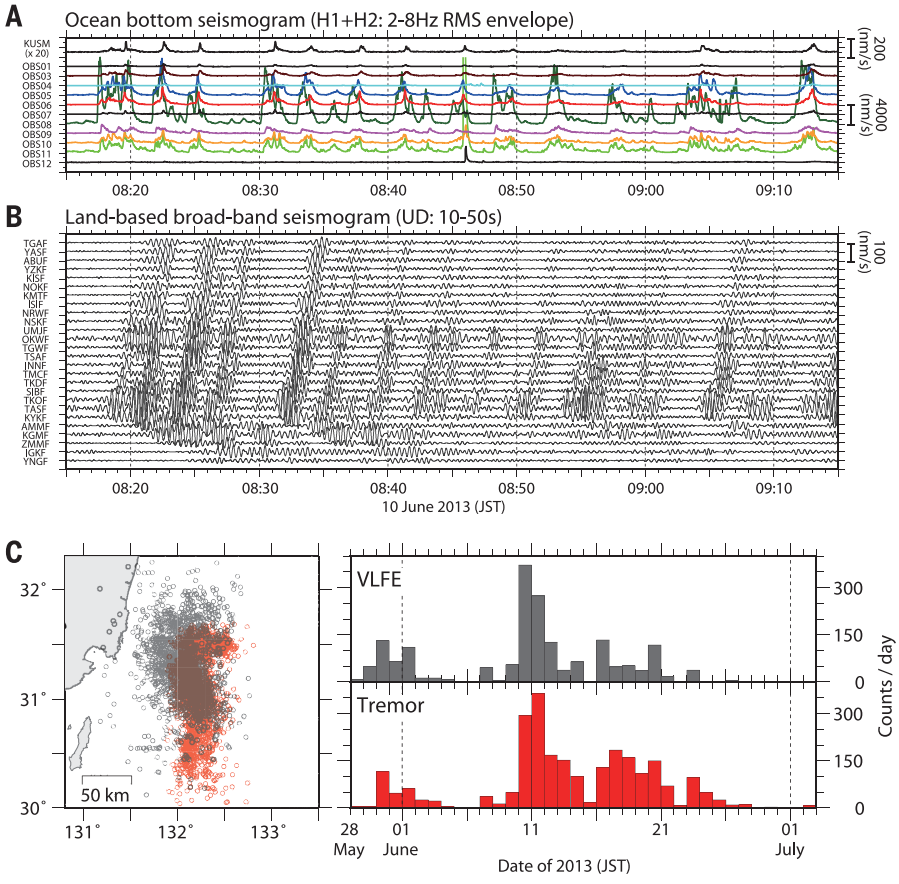

Fig. 2. Comparison with shallow tremor and VLFE activity. (**A**) Example of shallow tremor in 1-hour continuous root mean square (RMS) envelopes from the OBS network and land-based station KUSM (locations in Fig. 1). Envelope traces were processed with a 2- to 8-Hz band-pass filter and smoothed with a 5-s moving window. Note that the gain of the trace from KUSM is 20 times as high as that of the OBS stations. The event at 08:46 is an ordinary small earthquake near OBS station 11. (**B**) Example of shallow VLFE in 1-hour continuous waveforms from F-net land-based broadband stations operated by the National Research Institute for Earth Science and Disaster Prevention. Waveform traces were processed with a 10- to 50-s band-pass filter. UD, up-down (vertical) component. (**C**) Comparison of spatial (left) and temporal (right) distribution of shallow tremor (red) and shallow VLFEs (gray). Note that the shallow tremor and VLFEs were detected every 1 min and 15 s, respectively.

The shallow tremor episode started on 28 May 2013, had major activity on 10 to 14 June and 16 to 21 June, and was essentially finished on 27 June 2013 (Fig. 2C). The time sequence of the tremor episode is similar to that of VLFEs. The source locations of the shallow tremor were estimated using the envelope correlation method (*1*), assuming an *S*-wave velocity of 3.5 km/s (*17*). The envelope functions are from combining the horizontal channels, and the tremor locations come from 2-min windows. Horizontal locations were constrained to less than ±5 km within the OBS network (fig. S5), and they roughly overlapped the VLFE focal area (Fig. 2) (*17*). Although this method has poor depth resolution, well-constrained shallow tremors were concentrated at an estimated depth of ~15 km (fig. S6), consistent with the depth of the plate interface in this region. The shallow tremor was distributed in a narrow belt parallel to the trench (Fig. 1), matching the up-dip limit of interplate small repeating earthquakes in this region (*16*), which reflects the up-dip limit of the zone where the ordinary interplate earthquakes occur. Background seismicity is also nonactive in the focal region of shallow tremor (fig. S1). Thus, the shallow tremor and ordinary interplate earthquakes appear to be spatially distinct.

We detected two distinct sequences of migrating tremor events, separated by an aseismic period lasting a few days. In the first sequence, events began off the east coast of Tanegashima Island in early June 2013. They then migrated generally northward with a slight change to the north-northwest around OBS station 8, reaching the area of OBS stations 6 and 7 on 12 to 14 June (fig. S7). In the second sequence, events resumed south of OBS station 8 on 16 June. They migrated north-northwestward to the vicinity of OBS station 7, then turned sharply east to the area around OBS station 9 (fig. S8). Compared with the location of subducted Kyushu-Palau Ridge (KPR), the first migration stopped within the ridge but the second migration overrode and reached the outside of the ridge's edge.

In the first and second sequences, tremor migrated over a length of 90 km in 3 days and 1.5 days, respectively (Fig. 4). The tremor generally propagated along strike (before turning up-dip on June 18) at speeds of approximately 30 to 60 km/day, similar to or somewhat higher than the deep tremor at Nankai and Cascadia (*18*, *19*). The migration front of first sequence typically shows a piecewise linear pattern, as in the deep ETS event (*20*). In addition, the very short duration in which tremor migrated in the reverse direction at speeds of 100 to 200 km/day occurred during the later part and after the propagation of first migration sequence (Fig. 4). This fast and backward migration is, to some extent, similar to the rapid tremor reversal (RTR) observed in deep ETS activity (*18*, *19*).

The migration property of shallow tremor and its activity associated with VLFEs basically resembles the pattern of deep tremor during ETS events. Some theoretical studies have explained this tremor migration as the successive failure of small fault patches within the brittle-ductile transition

zone, as SSEs propagating on the plate interface increase the stress around zones of high slip rate (*21*, *22*). Therefore, the migration of shallow tremor may typify episodic SSEs in the near-trench shallow plate interface, analogous to the coupled phenomena of deep tremor, VLFEs, and episodic SSEs at the down-dip side of the locked zone (*7*). Although this study did not detect shallow SSEs associated with tremor and/or VLFE activity through geodetic evidence, the migration of shallow tremor is consistent with the migrating rupture front of SSE. These findings suggest that the both deeper and shallower sides of a subduction plate interface have similar frictional properties. The coupled phenomena of tremor, VLFEs, and SSEs probably occur in both plate interfaces.

The shallow tremor that we documented has some features in common with deep tremors, which suggests that there is a common generation process between shallow and deep tremors, as expected from processes like dehydration (*1*). The undulating surface structure of the KPR may play an important role in effective transportation of the clay minerals and fluid at depth and may thus be the key to the generation of shallow tremor in this area. On the other hand, there are some differences between both tremors in the details. The migration fronts of the two sequences of shallow tremor moved slightly faster than deep tremor sequences, which migrate at speeds ranging from a few to a few tens of kilometers per day (*18*, *19*). The shallow tremor migrated over almost the same area after a very short interval (2 days), and the second migration was faster than the first migration (fig. S9). We lack reports of large-scale and along-strike multiple migrations during a deep tremor episode, although RTR and very fast tremor streaks that migrate along the dip direction at 30 to 200 km/hour (*23*) are known to occur repeatedly, even within an episode. Therefore, the properties of large-scale and along-strike migration of shallow tremor are similar but not identical to those of deep tremor. The rapid reverse propagation is also not the same as the deep RTR reported for the Cascadia deep tremor that occurs during the linear propagation of the overall tremor front (*19*). Rheological differences between shallow and deep tremor zones may explain the difference in the behavior between both tremors.

The subducted KPR is thought to be a segment boundary of coseismic slip (*24*). Meanwhile, the migration episodes of tremor propagated obliquely across the KPR, which suggests that this ridge did not work as a strong segment boundary for the slow rupture. This behavior is consistent with the argument that subducted seamounts provide favorable conditions for aseismic creep and small earthquakes but unfavorable conditions for generation and propagation of large ruptures (*25*).

Shallow tremor stopped migrating further in the northward direction and turned sharply eastward around OBS station 7. This area is located in the up-dip side where large [moment magnitude (M_w) 6.5 to 7.5] megathrust events occur (*26*, *27*). Therefore, the locking or creeping state of deeper megathrust changed along-strike, and the migration to the northward direction was blocked by the locked zone. In addition, the migration did not finally reach to the up-dip side of the rupture area of the M_w 7.5 megathrust event. These observations suggest that the migration of shallow tremor occurred in a plate interface, which is the shallower extension of the creeping megathrust. In other words, the shallow tremor migration may be a response to the creeping of the deeper megathrust. Whether it can also occur up-dip of a locked megathrust such as at Nankai and Cascadia awaits future observations.

As the occurrence of the megathrust event approaches, the state of interplate coupling will become progressively weakened from the surrounding area, even despite the locked megathrust. As a result, a change of spatiotemporal activity of shallow slow earthquakes is expected in the up-dip side of the locked zone, similar to the case for deep slow earthquakes, as predicted by some computer simulation studies (*28*).

The worst-case scenario is for shallow slow earthquakes to precede a large seismic rupture,

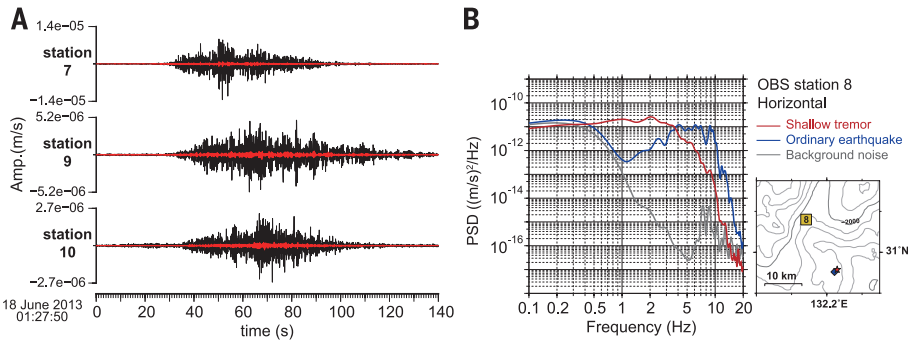

Fig. 3. Characteristics of shallow tremor in time and frequency domain. (**A**) Example waveforms of shallow tremor recorded at OBS stations. A vertical component waveform (red) is superimposed on a horizontal component (black). Each trace is normalized by the maximum amplitude (Amp.) of a horizontal component. More example waveforms are shown in fig. S3. (**B**) Example of power spectra of shallow tremor, ordinary earthquake, and background noise observed at OBS station 8. The ordinary earthquake spectrum is calculated from the *S*-wave record and its coda using a horizontal channel. The selected event occurred within several kilometers of the tremor and had approximately the same amplitude. The time-window length is 10.24 s, starting 2 s before the *S*-wave arrival. The tremor spectrum and background noise are stacked and from the same horizontal channel, using a 10.24-s window over a 102.4-s time period. The instrument response was corrected. An example of deep tremor and background noise spectra from west Shikoku, Japan, is shown recorded at the land-based seismic station also shown in fig. S4. PSD, power spectral density.

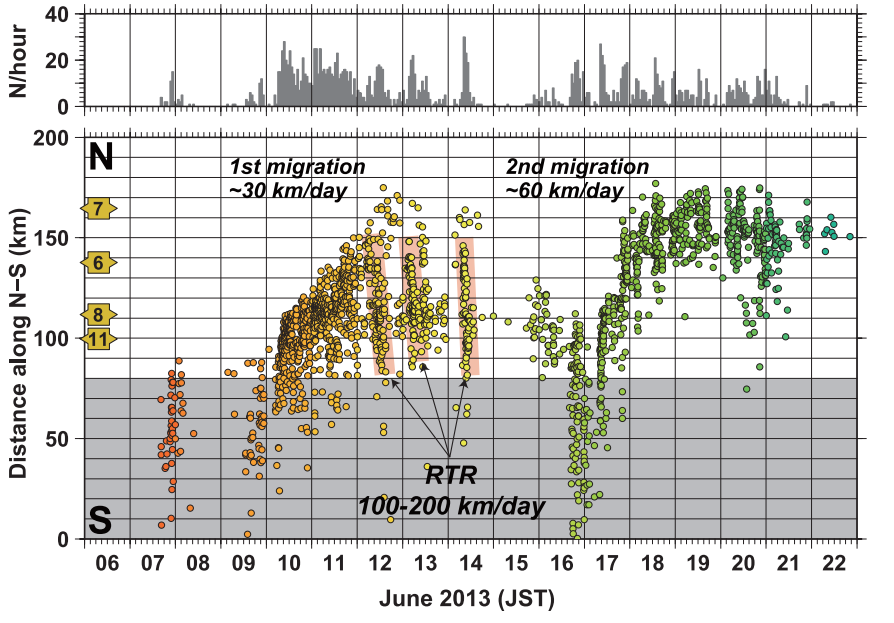

Fig. 4. Spatiotemporal change of shallow tremor activity. (**Top**) Hourly event counts (N, number of events) and (**bottom**) space-time plot of shallow tremor along line N–S in Fig. 1. Yellow polygons show the location and number of OBS stations. The gray shaded area indicates lower precision for the area outside the OBS network. The first and second migrations propagated north-northwestward at 30 to 60 km/day, and three RTR events (red shading) propagated in the reverse direction at 100 to 200 km/day.

such as the slow slip observed just before the Tohoku-Oki earthquake (*29*). Therefore, monitoring the spatiotemporal changes of shallow slow earthquakes is important for evaluating the slip of the shallow plate interface offshore. This aids assessment of the potential hazard of tsunamigenic earthquakes. Long-term ocean-bottom observations of many subduction zones and geodetic observations to confirm the suspected shallow SSEs for this region will further clarify the relationship between shallow slow earthquakes and the frictional behavior of megathrusts.

REFERENCES AND NOTES

1. K. Obara, *Science* **296**, 1679–1681 (2002).
2. G. Dragert, K. Wang, T. S. James, *Science* **292**, 1525–1528 (2001).
3. G. Rogers, H. Dragert, *Science* **300**, 1942–1943 (2003).
4. K. Obara, H. Hirose, F. Yamamizu, K. Kasahara, *Geophys. Res. Lett.* **31**, L23602 (2004).
5. Y. Ito, K. Obara, K. Shiomi, S. Sekine, H. Hirose, *Science* **315**, 503–506 (2007).
6. S. Ide, D. Shelly, G. Beroza, *Geophys. Res. Lett.* **34**, L03308 (2007).
7. K. Obara, T. Matsuzawa, S. Tanaka, T. Kimura, T. Maeda, *Geophys. Res. Lett.* **38**, L09311 (2011).
8. C. H. Scholz, J. Campos, *J. Geophys. Res.* **117**, B05310 (2012).
9. K. Obara, Y. Ito, *Earth Planets Space* **57**, 321–326 (2005).
10. Y. Asano, K. Obara, Y. Ito, *Earth Planets Space* **60**, 871–875 (2008).
11. H. Sugioka *et al.*, *Nat. Geosci.* **5**, 414–418 (2012).
12. J. I. Walter, S. Y. Schwartz, M. Protti, V. Gonzalez, *Geophys. Res. Lett.* **40**, 1517–1522 (2013).
13. K. Obana, S. Kodaira, *Earth Planet. Sci. Lett.* **287**, 168–174 (2009).
14. T. Nishimura, *Prog. Earth Planet. Sci.* **1**, 22 (2014).
15. L. M. Wallace *et al.*, *Geology* **37**, 143–146 (2009).
16. Y. Yamashita, H. Shimizu, K. Goto, *Geophys. Res. Lett.* **39**, L08304 (2012).
17. Materials and methods are available as supplementary materials on *Science* Online.
18. K. Obara, *J. Geophys. Res.* **115**, B00A25 (2010).
19. H. Houston, B. G. Delbridge, A. G. Wech, K. C. Creager, *Nat. Geosci.* **4**, 404–409 (2011).
20. H. Dragert, K. Wang, *J. Geophys. Res.* **116**, B12406 (2011).
21. R. Ando, R. Nakata, T. Hori, *Geophys. Res. Lett.* **37**, L10310 (2010).
22. N. M. Bartlow, S. Miyazaki, A. M. Bradley, P. Segall, *Geophys. Res. Lett.* **38**, L18309 (2011).
23. A. Ghosh *et al.*, *Geochem. Geophys. Geosyst.* **11**, Q12010 (2010).
24. Y. Yamamoto *et al.*, *Tectonophysics* **589**, 90–102 (2013).
25. K. Wang, S. L. Bilek, *Geology* **39**, 819–822 (2011).
26. Y. Yagi, M. Kikuchi, S. Yoshida, Y. Yamanaka, *J. Seismol. Soc. Jpn.* **2**, 139–148 (1998).
27. Y. Yagi, M. Kikuchi, S. Yoshida, T. Sagiya, *Geophys. Res. Lett.* **26**, 3161–3164 (1999).
28. T. Matsuzawa, H. Hirose, B. Shibazaki, K. Obara, *J. Geophys. Res.* **115**, B12301 (2010).
29. A. Kato *et al.*, *Science* **335**, 705–708 (2012).
30. S. Miyazaki, K. Heki, *J. Geophys. Res.* **106**, 4305–4326 (2001).

ACKNOWLEDGMENTS

We thank the crew of the *T/S Nagasaki-maru* (Faculty of Fisheries, Nagasaki University) for their skillful work and K. Creager, H. Houston, M. Vallee, K. Goto, Y. Yamanaka, K. Mochizuki, the members of SEVO of Kyushu University, and the ERI of The University of Tokyo for valuable discussions and comments. We also thank the anonymous reviewers for providing suggestions and comments that improved the manuscript. This study was supported by the Ministry of Education, Culture, Sports, Science and Technology (MEXT) of Japan under its Observation and Research Program for Prediction of Earthquakes and Volcanic Eruptions. Y.Y. received support as a Japan Society for the Promotion of Science research fellow (grant 24-3726). Shallow tremor catalog data are available in the supplementary materials.

SUPPLEMENTARY MATERIALS

www.sciencemag.org/content/348/6235/676/suppl/DC1
Materials and Methods
Figs. S1 to S9
References (*31*–*35*)
Data S1

8 December 2014; accepted 30 March 2015
10.1126/science.aaa4242

SURFACE SCIENCE

Adhesion and friction in mesoscopic graphite contacts

Elad Koren, Emanuel Lörtscher, Colin Rawlings, Armin W. Knoll, Urs Duerig*

The weak interlayer binding in two-dimensional layered materials such as graphite gives rise to poorly understood low-friction characteristics. Accurate measurements of the adhesion forces governing the overall mechanical stability have also remained elusive. We report on the direct mechanical measurement of line tension and friction forces acting in sheared mesoscale graphite structures. We show that the friction is fundamentally stochastic in nature and is attributable to the interaction between the incommensurate interface lattices. We also measured an adhesion energy of 0.227 ± 0.005 joules per square meter, in excellent agreement with theoretical models. In addition, bistable all-mechanical memory cell structures and rotational bearings have been realized by exploiting position locking, which is provided solely by the adhesion energy.

Adhesion and friction play a central role in mechanical systems because they are directly responsible for the energetics, dissipation, and wear (*1*). In particular, nanoscale systems are exceptionally susceptible to adhesion and friction as a consequence of a very large surface-to-volume ratio (*2*). Motivated by these issues, research has strongly focused on layered materials exhibiting weak layer-to-layer coupling, henceforth referred to as interlayer binding. Carbon-based materials are a particularly promising material class in this respect. A general phenomenon associated with layered materials is the strong suppression of sliding friction and stiction forces, termed superlubricity (*3*–*5*). Superlubricity arises from a structural mismatch between rotated atomically flat surfaces. As a result, shear displacements in mesoscale structures that are cut along a glide plane spontaneously revert to the initial equilibrium position, solely driven by interfacial adhesion forces, as soon as the externally applied displacement force is released (*6*, *7*).

In view of the high prospective impact of graphitic materials, many research groups have studied the interlayer binding energy theoretically. However, such calculations are challenging because of the substantial contribution from van der Waals interactions and the localized nature of the π-orbital bonding across the graphite planes (*8*–*12*). Current estimates for the interlayer binding energy range from 0.14 J m^{-2} (24 meV per atom) to 0.34 J m^{-2} (56 meV per atom). Experimental data for the adhesion energy of graphite are scarce, and measurements rely on indirect methods building on the exfoliation of multiwalled carbon nanotubes, $\sigma = 0.21 \pm 0.06$ J m^{-2} (*13*); the flexure mechanics of thin graphite sheets, $\sigma = 0.19 \pm 0.01$ J m^{-2} (*14*); or measurements of the desorption energy of aromatic molecules, $\sigma = 0.32 \pm 0.03$ J m^{-2} (*15*). We distinguish between the theoretically calculated binding energy (pertaining to the separation of two surfaces that initially are in perfect atomic registry) and the experimental adhesion energy (relating to the separation of two surfaces from an equilibrium contact position for which the lattices do not necessarily match).

Adhesion and friction in layered materials in general, and in graphite specifically, are not well understood. Here, we report on an experimental study of the interface adhesion and friction in mesoscopic structures made of highly oriented pyrolytic graphite (HOPG). We exploit the unique nanopositioning accuracy and force sensitivity of scanning probe microscopy to repeatedly shear individual nano-sized graphitic mesa structures and to measure the applied shear forces during their mechanical exfoliation along a single basal glide plane. The shear force is composed of a reversible displacement force and a smaller irreversible friction force characterized by a force hysteresis. This strategy allows us to investigate the fundamental mechanisms leading to friction and to relate the reversible displacement force to the adhesion interaction between the sliding surfaces. In addition, the displacement force characteristics can be engineered by the mesa design outline to yield multiple local energy minima at which the sheared structures can be arrested.

The studies were performed on an atomic force microscopy (AFM) setup under ambient conditions. Samples featuring cylindrical and more complex shaped mesa structures with a typical height of 50 nm were fabricated from high-quality HOPG substrates by means of reactive ion etching, using structured Pd-Au metal layers as self-aligned shadow masks (Fig. 1A) (*7*, *14*). For mechanical shearing, a Pt/Ir metal-coated AFM tip was brought into contact with the metal mask on top of the mesa (Fig. 1C). The tip apex was cold-welded to the metal by applying a force and electrical current pulse of 50 nN and 1 mA, respectively, for 1 s. As a result, a strong mechanical contact between the tip and the metal mask formed, which allowed us to apply lateral shear forces of up to 200 nN and to induce a shear glide along a single basal plane in the HOPG structure. After sliding, the exposed basal plane surface was free of observable defects,

IBM Research–Zürich, Säumerstasse 4, 8803 Rüschlikon, Switzerland.
*Corresponding author. E-mail: drg@zurich.ibm.com

as confirmed by AFM inspection of sheared mesas (Fig. 1E).

We measured the lateral shear force required to move the tip parallel to the mesa plane at zero applied normal force (Fig. 2). The observed force signal has several distinct features: (i) The lateral force changes sign when the tip passes from the left position through the center and then to the right position, reaching the same average plateau value of $F_P \approx 45$ nN. (ii) In the plateau regions, the lateral force is essentially independent of the scan direction and position. (iii) The measured force signal is highly reproducible throughout repeated lateral scans. From (i) and (ii), we conclude that the lateral shear force is dominantly conservative in nature; from (iii), we conclude that the sheared interface geometry is stable throughout the experiment and the manipulations are nondestructive.

Starting from the center position toward the right or left side, the lateral force builds up at a rate of ~10 nN nm^{-1} until it saturates at the plateau value F_P. In this initial phase, the upper section of the mesa, termed the mobile section, remains fixed until sufficient shear stress is built up in the mesa to trigger yielding at a glide plane. Sliding of the mobile section sets in at a tip displacement of ~5 nm, after which the tip displacement represents the actual sliding motion of the mobile section (Fig. 2B). The force trace and retrace signals exhibit substantial fluctuations and hysteresis (Fig. 2B, inset), similar to those observed in the sliding friction of carbon nanotubes (*16*) and in superlubricity sliding of nanoscale flakes (*4*) for a rotational mismatch of greater than 5° between the sliding surfaces.

Conservative displacement forces are strictly a function of the displacement x, whereas dissipative friction forces depend on the direction of motion. The overall energy dissipation for a closed path of length ℓ is given by

$$E_{\mathrm{diss}} = \int_0^{\ell} F_{\mathrm{fr}}\, dx \qquad (1)$$

where the friction force is given by the difference of the measured shear force at a position x between trace and retrace sliding, $F_{\mathrm{fr}}(x) = F_{\mathrm{S,trace}}(x) - F_{\mathrm{S,retrace}}(x)$. An apparent correlation appears as high or low friction force values persist over sliding distances of 10 to 50 nm (Fig. 3A). We also observed unusual behavior, such as short-lived amplitude spikes (up to 10 nN) and negative friction force over some sliding paths. The latter feature indicates energy recovery during such phases.

The values of the friction force are Gaussian-distributed, with a mean value of 1.6 nN and a variance of $\sigma_{\mathrm{fr}} = 2.45$ nN (Fig. 3C). From the central limit theorem, we conclude that the friction force arises from statistically independent events with finite correlation lengths. Therefore, we expect that the variance of the distribution of the friction force averaged over a sliding interval Δx should converge to a zero value, provided that enough independent events are probed in the sliding interval. On the other hand, correlation manifests itself as a persistence of the variance if the averaging interval Δx is smaller than the correlation length. As anticipated from the intuitive interpretation of the friction force data (Fig. 3A), the variance decays as expected for statistically independent events if the averaging interval is larger than ~20 nm (Fig. 3D). By averaging over a sliding distance of 90 nm, we obtain a robust number for the mean friction force of 1.6 nN (1σ uncertainty of 0.3 nN).

From the measured interface energy $\sigma \approx 0.227$ J m^{-2} (see below), we estimate the load force to be on the order of $P \approx (\sigma/c)(\pi r^2) \approx 24$ μN for a cylindrical mesa with a radius of $r = 100$ nm and assuming an interaction length $c \approx 0.3$ nm, on the order of the c-axis lattice spacing. From this estimated load, we obtain an effective friction coefficient of $\mu \approx 7 \times 10^{-5}$, which is more than three orders of magnitude lower than the typical friction coefficient $\mu \approx 0.1$ to 0.3 observed in dry sliding contacts.

Theoretical arguments and simulations predict that the friction force does not scale with the contact area A (*17*, *18*). The effect originates from a cancellation of forces acting on the interface atoms except at the periphery. The exponent γ in the scaling equation $F_{\mathrm{fr}} \propto A^{\gamma}$ can assume values in the range from 0 to 0.5, depending on the type of lattice mismatch and the shape of the sliding object (*18*, *19*). Recently, fractional scaling has been confirmed in an experiment that measured the sliding friction forces of amorphous antimony and single-crystal gold islands on a graphite surface (*20*). For the amorphous islands, an exponent of $\gamma = 0.5$ was measured, as predicted by theory for a random interface. For the single-crystal Au islands, an exponent of $\gamma = 0.33 \pm 0.15$ was obtained. We find $\gamma = 0.35 \pm 0.05$, in agreement with this latter value (Fig. 3B).

The friction force can also be written as $F_{\mathrm{fr}} = F_0 N^{\gamma}$, where F_0 is the mean force acting on an

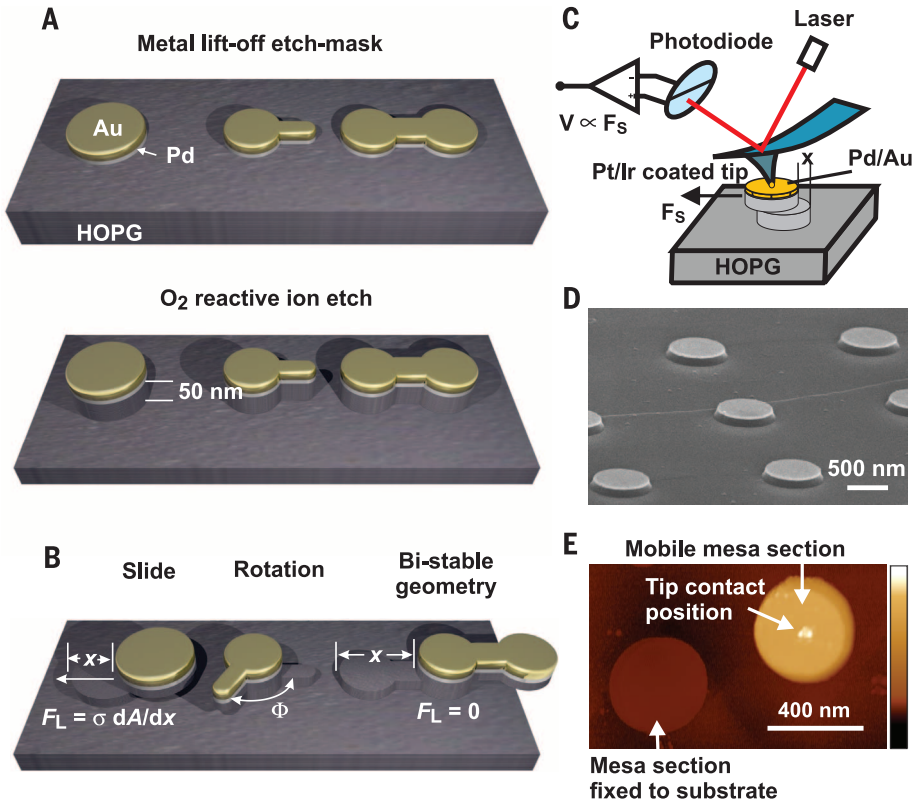

Fig. 1. Experimental procedures. (**A**) Metal masks consisting of Pd (10 nm) and Au (15 nm) are fabricated on the freshly cleaved surface of a HOPG sample by electron beam lithography and liftoff techniques. The mesa structures emerge during a dry oxygen plasma etch, which selectively thins down only the unprotected HOPG surface by 50 nm. The mesa structures are sheared along a basal glide plane by applying a corresponding force to the top metal surface. (**B**) The adhesion energy is determined by measuring the line tension force F_L acting on sheared cylindrical mesas. Stabilization of a rotation axis is possible, allowing the rotation of the mesa around the cylinder axis, while a dumbbell structure provides multiple stable equilibria whenever cylindrical sections overlap. (**C**) Schematic of the AFM experiment. A Pt/Ir tip is cold-welded to the metal mask on top of the mesas. Force is applied by a shear motion, and the shear force is measured via the induced cantilever torsion. (**D**) Scanning electron microscopy image of cylindrical mesa structures with a radius of 200 nm and etch depth of 50 nm. (**E**) AFM image of a completely sheared cylindrical mesa (100 nm height range mapped to nonlinear color scale). The mesa was sheared at a basal plane 10 nm above the substrate surface, and the top section was put down on the substrate surface to the right of the original mesa. The tip contact point close to the center is visible as a small hillock on the Au top surface.

individual atom and N is the number of interface atoms. We find $F_0 = 14^{+15}_{-8}$ pN (*21*) (Fig. 3B), in good agreement with the value of $F_0 \approx \sigma/(cn) \approx$ 20 pN estimated from the measured adhesion energy with an atomic density at the interface (n) of 38.2 nm^{-2}. The results suggest that the friction force originates from a genuine interaction between the rotationally misaligned graphite lattices at the sliding interface. This is remarkable because it is a well-known empirical fact (*20*), also predicted theoretically (*17*, *22*), that fractional scaling is an extremely fragile interface property that can only occur if the lattice interaction is not perturbed by defects or contaminations.

Numerical simulations of adhesion interaction between two circular graphene sheets with radii of 4 to 15 nm show that a moiré superstructure, attributable to the lattice misorientation in the rotated sheets, is the root cause for the fluctuating shear forces (*21*). The superstructure is isomorphic to the graphene lattice and consists of domains of approximate AB and AA stacking corresponding to atomic and hollow sites in the graphene lattice, respectively. The lattice period of the superstructure is given by

$$L = \frac{a}{\sqrt{2 - 2\cos\Phi}} \qquad (2)$$

where a = 0.142 nm denotes the in-plane lattice constant of graphite and Φ is the rotation angle. The moiré pattern is shifted roughly perpendicular to the slide direction by one lattice constant L for a lateral displacement of the graphene sheets by one lattice unit a. As a result, the shear force exhibits a multitude of periodic maxima and minima, with periods on the order of 0.2 to 0.4 nm, whenever stacking domains enter or leave the overlap area at the boundary (fig. S3A). According to the Tomlinson mechanism, such short-period force fluctuations are responsible for energy dissipation and friction in the system. The amplitude of the force fluctuations scales with the overlap area approximately to the power of 0.35, similar to the friction force scaling observed in the experiment, and scales with the rotation angle to the power of –1.5 (fig. S4). From the simulations we conclude that the mean rotational misalignment between the sliding surfaces in the experiment must be between 5° and 10°, which gives the correct order of magnitude of fluctuations of the shear force in relation to the experimental friction force values (fig. S4B).

In a real experiment, sliding is performed using a compliant actuator, and hence neither the rotation angle Φ nor the off-axis y position are strictly constant, which profoundly affects the sliding friction (*23*, *24*). Allowing the top sliding surface to follow a path in the x-y-Φ space that locally minimizes the interface energy leads to a hidden pseudo–random walk trajectory in the y-Φ space and corresponding correlations. In the model simulation, we also included thermal activation by allowing the system to choose among all path energy options, with probabilities proportional to the corresponding Boltzmann factors. The surprising result of the simulation is that the character of the force fluctuations changes from a periodic pattern (fig. S3A) to a highly random spiky pattern (fig. S6A). This pattern is strikingly similar to the measured friction force (Fig. 3A). Rotational degrees of freedom have been proposed as a mechanism leading to irregular sharp peaks in the friction signal due to the restoration of a high-friction state when the sliding surfaces reorient into a commensurate state (*23*). In our case, however, the force spikes are not signaling a commensurate state between the sliding lattices, but rather a randomly occurring high energy barrier in the potential landscape of rotated sliding interface.

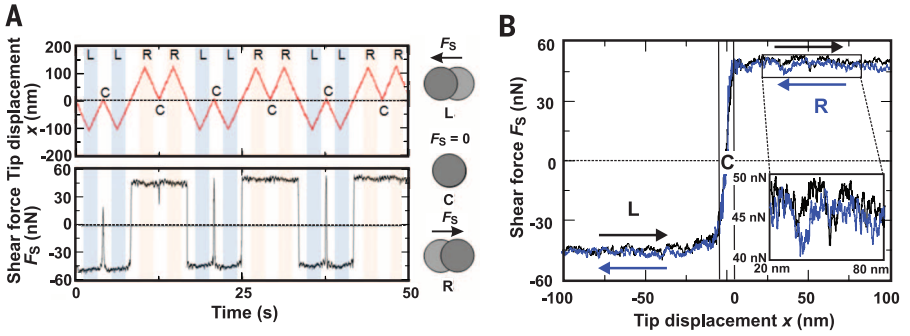

Fig. 2. Shear force measurements. (**A**) Time traces of the tip displacement x with respect to the center position (C) and the measured shear force F_S acting on the top surface of a cylindrical mesa with a radius of 100 nm. The shear force changes sign in accordance with a displacement to the right (R) or to the left (L) with respect to the center position, but not in accordance with the scan direction. (**B**) Measured shear force versus tip displacement. Black and blue curves denote the scan direction from left to right and from right to left, respectively, as indicated by the arrows. Inset: Enlarged view of the shear force for a trace and retrace scan showing the nonreversible friction contribution.

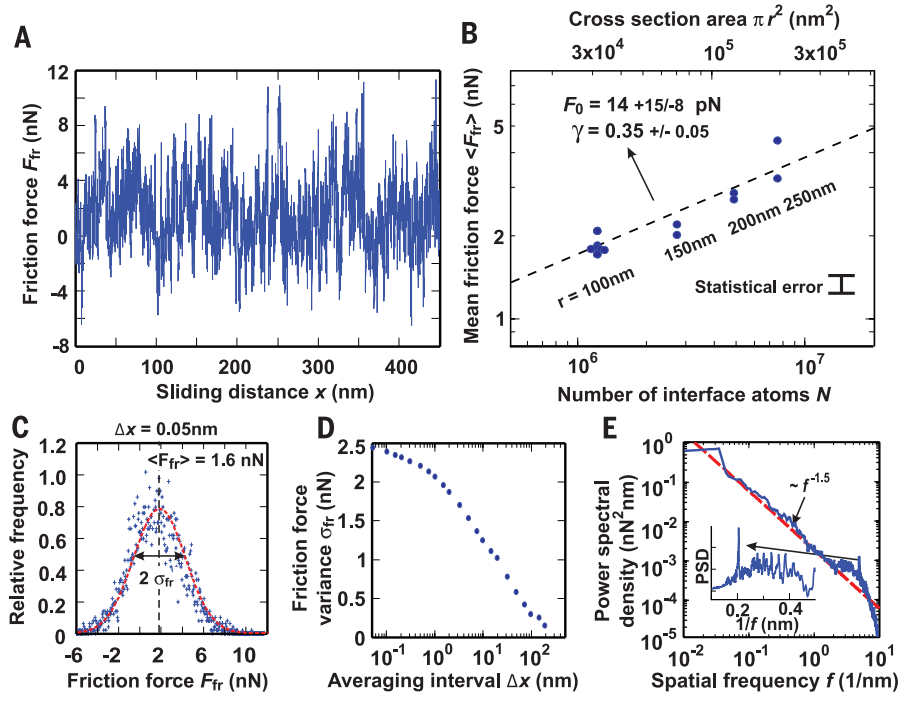

Fig. 3. Dissipative friction forces. (**A**) The friction force is defined as the difference of the shear force at a position x between trace and retrace sliding. The data represent a concatenation of five different friction force curves recorded over a sliding distance of 90 nm for mesa structures with a radius of 100 nm. (**B**) Mean value of the friction force versus cross-sectional area πr^2 or number of interface atoms N = 38.2 nm^{-2} × πr^2 determined from 90-nm trace-retrace curves of circular mesa structures with a radius r from 100 to 250 nm. Dashed line is a least-squares fit to the data with $\langle F_{fr}\rangle = F_0 N^{\gamma}$, with F_0 = 14 pN and γ = 0.35. Error bar indicates the variance $\sigma_{fr} \approx$ 0.3 nN of the data determined from (D) for Δx = 90 nm. (**C**) Histogram of the distribution of the friction force recorded at a sampling interval of Δx = 0.05 nm and a Gaussian fit (dashed line) with a mean value of $\langle F_{fr}\rangle$ = 1.6 nN and variance of σ_{fr} = 2.45 nN. (**D**) Variance σ_{fr} of the friction force distribution as a function of the averaging interval Δx. (**E**) Power spectral density (PSD) determined from the experimental friction force data shown (A). The data reveal a $f^{-1.5}$ scaling (dashed line). The inset shows the PSD as a function of period in the range from 0.1 to 0.5 nm.

The correlations arising from the pseudo–random walk in the y-Φ space are reflected in a non-integer power law scaling with an exponent of –1.5 of the power spectral density determined from the experimental (Fig. 3E) and simulated data (fig. S6). Interestingly, the lattice structure still shows up in the power spectrum at spatial periods in the range from 0.2 to 0.5 nm with a prominent peak at 0.2 nm, corresponding to the periods obtained for a rigid slide—that is, $\Delta y = 0$ and $\Delta\Phi = 0$. The fact that we experimentally observe spectral features that can be traced back to the lattice interaction provides additional evidence that the measured friction force is genuinely due to a moiré interaction between rotated surfaces at the interface. It is also clear from the pseudo–random walk mechanism that forward and backward slides will never follow exactly the same path; this explains the huge spread of the observed local friction force, which can even assume negative values over some slide intervals.

The dominant conservative part of the lateral force is due to the interface energy at the glide planes, which gives rise to a line tension force opposing the creation of new surface area. The component of the line tension force in the slide direction is

$$F_L = \sigma \frac{dA}{dx} \tag{3}$$

where the interface tension σ denotes the mean adhesion energy per unit area, A is the overlap area of the mesa sections, and x is the displacement of the mobile section with respect to the initial position. For a mesa with a circular cross section of radius r, we find

$$A(x) = 2r^2\left[\cos^{-1}\left(\frac{x/2}{r}\right) - \frac{x/2}{r}\sqrt{1-\left(\frac{x/2}{r}\right)^2}\right] \tag{4}$$

and

$$F_L(x) = -2\sigma r\sqrt{1-\frac{(x/2)^2}{r^2}} \tag{5}$$

The maximum force $F_{S0} = 2\sigma r$ that has to be applied to initiate sliding must be equal to the line tension force at zero displacement x. Therefore, F_{S0} scales linearly with r, as is confirmed by the experimental data (Fig. 4A). We obtain an interface tension of $\sigma = 0.227 \pm 0.005$ J m^{-2} (*21*), which is ~15% larger than previously reported experimental values measured for the interaction between graphite sheets in contact (*13*, *14*). The value is in excellent agreement with the mean interface energy calculated from the model of Kolmogorov *et al.* (*9*, *21*).

To validate the interface energy picture, we measured the force characteristics for a complete slide from perfect overlap at $x = 0$ nm to zero overlap at $x = 2r$ (Fig. 4B). The measured force curves for the cylindrical mesas are perfectly predicted by Eq. 5 using our experimental value of σ. Also shown is the force curve measured for a compound mesa structure consisting of a cylindrical section with a radius of 200 nm connected to a rectangular beam section pointing along the slide direction (Fig. 4B). The first part of the force curve is identical to that of a circular structure, and for $x > 400$ nm the force is constant because of the linear decrease of the overlap area on the rectangular beam section. The slight deviation from the predicted characteristics at the crossover is due to the tapered profile in the actual device.

We observed a gradual asymptotic approach to the line tension force curves characterizing mesa sliding. This shows that the process leading to superlubricity is a continuous one, which in some cases can extend over a distance of up to 50 nm, as seen in the force trace of the large compound mesa structure (Fig. 4B). On the other hand, assuming that the graphite stack is in perfect lattice registry, we would expect that a huge breakoff force is required in order to overcome the lattice barrier. The binding energies for regular AB stacking are on the order of $E_{AB} = 0.14$ to 0.34 J m^{-2}, yielding a breakoff force on the order of $A \times (E_{AB}/c) \approx A \times (0.5$ to 1.1 nN nm$^{-2})$. For our mesa structures, this is in the range from 1 to 100 μN, which we never observed. The details of the breakoff mechanism are not clear. Initiation of the glide plane could, for example, be tied to stacking fault planes (*25*) or could involve the propagation of local stacking boundary defects (*26*). Because we see no breakoff force, we conclude that the shear strength Y_S for basal plane sliding in graphite mesostructures is solely governed by line tension forces, $Y_S = F_L/A = \sigma(d \log A/dx)$, and therefore it depends on the structure's geometry rather than being a generic material constant.

To assure the feasibility of surface force-driven actuation, we must require that the friction forces are negligible with respect to the line tension forces; that is, max $F_{fr} < F_L$. The friction forces scale as the radius r of the structure to the power of 2γ. A safe bound for the maximum of the friction force in accounting for the substantial fluctuations is provided by a $6\sigma_{fr}$ criterion, yielding an estimated maximum friction force of max $F_{fr} \approx 6\sigma_{fr}(r_0)[(r/r_0)^{2\gamma}]$, where r_0 denotes the radius of a characterized reference structure. With F_L from Eq. 5, we obtain a lower cutoff radius of

$$r > \left(\frac{6\sigma_{fr}(r_0)}{r_0^{2\gamma}}\frac{1}{2\sigma}\right)^{\frac{1}{1-2\gamma}} \tag{6}$$

Substituting the measured values from the experiment, $r_0 = 100$ nm, $\sigma_{fr}(r_0) = 2.45$ nN, $\gamma = 0.35$, and $\sigma = 0.227$ J m^{-2}, we conclude that line tension forces dominate friction forces down to structure sizes with a radius of ~2 nm. This result is encouraging in view of the technical feasibility of graphene-based nanomechanical devices. However, structures with dimensions on the order of tens of nanometers would still be required in order to guarantee low-energy dissipation actuation in line with the low value of the mean friction force.

Determining the underlying theory to calculate intrinsic adhesion energy and forces allows us to engineer the structure geometry with respect

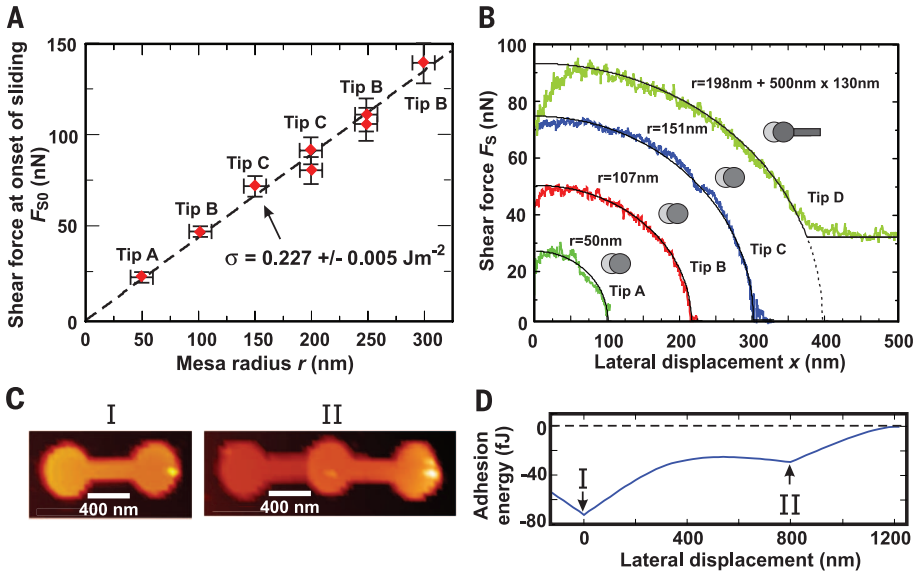

Fig. 4. Conservative forces due to adhesion energy. (**A**) Shear force at onset of mesa sliding F_{S0} as a function of the radius of cylindrical mesas. Standard deviation indicated by error crosses (*21*). Three different cantilevers (tips A, B, and C) were used. Dashed line corresponds to a weighted least-squares fit to the data, yielding $\sigma = 0.227$ J m^{-2} with a variance of 0.005 J m^{-2}. (**B**) Measured shear force F_S as a function of the lateral displacement x of the mobile top mesa section for different mesa structures and different cantilevers. Solid lines show the calculated shear force according to Eq. 5. The dotted line in the graph of the compound structure shows the extrapolation of the shear force for the cylindrical part only. (**C**) Dumbbell mesa structure with a height of 80 nm before and after sliding to a stable equilibrium position where the circular sections overlap. The glide plane is at a height of 70 nm above the substrate surface. (**D**) Calculated adhesion energy for the dumbbell mesa structure.

to a targeted energy and corresponding displacement force profile. For example, structures featuring multiple local energy minima displacement profiles act as metastable geometric traps. Switching between the trap states involves only minimal frictional resistance and virtually zero wear. The mechanical transition between local minima can be realized by different means such as mechanical, electrostatic, and magnetic actuation or by a thermal gradient mechanism (*27*). Multiple energy minima positions are obtained, for example, in a dumbbell structure (Fig. 4, C and D). The AFM tip is used to first induce a glide plane defect and then direct the mobile upper part from the initial energy minimum position (Fig. 4C, left inset) to the other local energy minimum position where the cylindrical sections overlap (Fig. 4C, right inset). After actuation, the tip is released from the metal surface by applying a negative load of >200 nN, and the actuated mesa is imaged in the tapping mode. Note that the glide plane surface of the fixed bottom mesa is clearly visible in the AFM image. Adhesion guiding combined with ultralow-friction properties can also be exploited for stabilizing rotational structures (fig. S1) and thus provides a versatile engineering platform for nanoscale devices in general.

REFERENCES AND NOTES

1. A. Vanossi, N. Manini, M. Urbakh, S. Zapperi, E. Tosatti, *Rev. Mod. Phys.* **85**, 529–552 (2013).
2. B. Bhushan, J. N. Israelachvili, U. Landman, *Nature* **374**, 607–616 (1995).
3. J.-M. Martin, C. Donnet, T. Le Mogne, T. Epicier, *Phys. Rev. B* **48**, 10583–10586 (1993).
4. M. Dienwiebel *et al.*, *Phys. Rev. Lett.* **92**, 126101 (2004).
5. X. Feng, S. Kwon, J. Y. Park, M. Salmeron, *ACS Nano* **7**, 1718–1724 (2013).
6. J. Cumings, A. Zettl, *Science* **289**, 602–604 (2000).
7. Z. Liu *et al.*, *Phys. Rev. Lett.* **108**, 205503 (2012).
8. M. Dion, H. Rydberg, E. Schröder, D. C. Langreth, B. I. Lundqvist, *Phys. Rev. Lett.* **92**, 246401 (2004).
9. A. N. Kolmogorov, V. H. Crespi, *Phys. Rev. B* **71**, 235415 (2005).
10. S. Lebègue *et al.*, *Phys. Rev. Lett.* **105**, 196401 (2010).
11. L. Spanu, S. Sorella, G. Galli, *Phys. Rev. Lett.* **103**, 196401 (2009).
12. X. Chen, F. Tian, C. Persson, W. Duan, N.-X. Chen, *Sci. Rep.* **3**, 3046 (2013).
13. L. X. Benedict *et al.*, *Chem. Phys. Lett.* **286**, 490–496 (1998).
14. Z. Liu *et al.*, *Phys. Rev. B* **85**, 205418 (2012).
15. R. Zacharia, H. Ulbricht, T. Hertel, *Phys. Rev. B* **69**, 155406 (2004).
16. A. Kis, K. Jensen, S. Aloni, W. Mickelson, A. Zettl, *Phys. Rev. Lett.* **97**, 025501 (2006).
17. M. H. Müser, L. Wenning, M. O. Robbins, *Phys. Rev. Lett.* **86**, 1295–1298 (2001).
18. A. S. de Wijn, *Phys. Rev. B* **86**, 085429 (2012).
19. E. Gnecco, E. Meyer, *Fundamentals of Friction and Wear* (Springer, New York, 2007).
20. D. Dietzel, M. Feldmann, U. D. Schwarz, H. Fuchs, A. Schirmeisen, *Phys. Rev. Lett.* **111**, 235502 (2013).
21. See supplementary materials on *Science* Online.
22. U. Tartaglino, V. N. Samoilov, B. N. Persson, *J. Phys. Condens. Matter* **18**, 4143–4160 (2006).
23. A. E. Filippov, M. Dienwiebel, J. W. M. Frenken, J. Klafter, M. Urbakh, *Phys. Rev. Lett.* **100**, 046102 (2008).
24. A. S. de Wijn, C. Fusco, A. Fasolino, *Phys. Rev. E* **81**, 046105 (2010).
25. E. Koren, A. Knoll, E. Lörtscher, U. Duerig, *Nat. Commun.* **5**, 5837 (2014).
26. P. San-Jose, R. V. Gorbachev, A. K. Geim, K. S. Novoselov, F. Guinea, *Nano Lett.* **14**, 2052–2057 (2014).
27. A. Barreiro *et al.*, *Science* **320**, 775–778 (2008).

ACKNOWLEDGMENTS

We thank U. Drechsler and M. Tschudy for invaluable technical support and M. Despont, D. Grogg, O. Hod, and R. Allenspach for stimulating discussions. Supported by the FP7 Marie Curie Actions of the European Commission and ITN fellowship cQOM (Project ID 290161) (E.K.). Data are available in the supplementary materials or upon request.

SUPPLEMENTARY MATERIALS

www.sciencemag.org/content/348/6235/679/suppl/DC1
Materials and Methods
Supplementary Text
Figs. S1 to S11
Tables S1 to S3
References (*28*–*41*)

3 December 2014; accepted 2 April 2015
10.1126/science.aaa4157

SOLAR CELLS

Impact of microstructure on local carrier lifetime in perovskite solar cells

Dane W. deQuilettes,[1] Sarah M. Vorpahl,[1] Samuel D. Stranks,[2]* Hirokazu Nagaoka,[1] Giles E. Eperon,[2] Mark E. Ziffer,[1] Henry J. Snaith,[2] David S. Ginger[1]†

The remarkable performance of hybrid perovskite photovoltaics is attributed to their long carrier lifetimes and high photoluminescence (PL) efficiencies. High-quality films are associated with slower PL decays, and it has been claimed that grain boundaries have a negligible impact on performance. We used confocal fluorescence microscopy correlated with scanning electron microscopy to spatially resolve the PL decay dynamics from films of nonstoichiometric organic-inorganic perovskites, $CH_3NH_3PbI_3(Cl)$. The PL intensities and lifetimes varied between different grains in the same film, even for films that exhibited long bulk lifetimes. The grain boundaries were dimmer and exhibited faster nonradiative decay. Energy-dispersive x-ray spectroscopy showed a positive correlation between chlorine concentration and regions of brighter PL, whereas PL imaging revealed that chemical treatment with pyridine could activate previously dark grains.

As active layers in solar cells, organic-inorganic perovskites (*1*, *2*) combine the promise of solution processing (*3*, *4*) with the ability to tailor the band gap through chemical substitution (*5*–*7*), yielding solar cell power conversion efficiencies as high as 20.1% (*8*). Concomitant with their photovoltaic performance, perovskites also exhibit high fractions of radiative recombination, with apparent carrier lifetimes of 250 ns or longer (*9*, *10*), and are challenging the dogma that solution-processed semiconductors inevitably possess high densities of performance-limiting defects. Ensuring that all recombination is radiative is critical for approaching the thermodynamic efficiency limits for solar cells and other optoelectronic devices (*11*).

Carrier recombination lifetimes measured by photoluminescence (PL) are commonly taken as a hallmark of perovskite film quality, with longer decay lifetimes used as indicators of better-performing materials (*9*, *10*, *12*–*14*). Carrier recombination kinetics have been described as a combination of trap-assisted, monomolecular (first-order), and bimolecular (second-order) recombination (*15*). Although most studies agree that radiative bimolecular recombination dominates at high initial carrier densities ($n_0 > 10^{17}$ cm^{-3}) (*15*–*18*), reports of kinetics at lower excitation densities (and relevant to solar cell operation) (*19*) range from single-exponential (*12*, *20*), to biexponential (*13*, *14*), to stretched-exponential (*6*, *9*) functions with varying levels of fidelity. These distributions have in turn been explained in terms of unintentional doping (*21*) or charge trapping (*22*). The perovskite growth conditions (*3*, *4*, *10*) and post-deposition treatments (*12*, *23*) can greatly alter film morphology, carrier lifetime, and device performance, yet the underlying relations between these parameters are important open questions. For instance, perovskite films grown from nonstoichiometric mixed halide (Cl/I) precursor solutions have exhibited lifetimes of hundreds of nanoseconds, but PL lifetimes in films grown from chloride-free precursors are generally much shorter (*9*, *20*).

Correlated confocal PL and scanning electron microscopy (SEM) have been a powerful tool to reveal structure/function relationships in biology (*24*). We applied similar techniques to study structure/function relationships in perovskite films. We found substantial local PL heterogeneity even for $CH_3NH_3PbI_3(Cl)$ films with average lifetimes of ~1 μs (comparable to the longest lifetimes reported) (*9*, *10*), which suggests that considerable

[1]Department of Chemistry, University of Washington, Box 351700, Seattle, WA 98195-1700, USA. [2]Clarendon Laboratory, University of Oxford, Parks Road, Oxford OX1 3PU, UK.
*Present address: Research Laboratory of Electronics, Massachusetts Institute of Technology, Cambridge, MA 02139, USA. †Corresponding author. E-mail: ginger@chem.washington.edu

scope remains for reducing nonradiative recombination in these films. In addition to observing entire grains that appear dark, we also observed that grain boundaries are associated with PL quenching, indicating that they are not as benign as has been suggested previously (*25*, *26*). We further used PL microscopy to show that post-deposition chemical treatments can activate previously dark regions in the film, and we correlated local energy-dispersive x-ray spectroscopy (EDS) with confocal fluorescence maps, finding that brighter grains with longer lifetimes were associated with local spikes in Cl concentration.

We studied $CH_3NH_3PbI_3(Cl)$ films prepared on glass slides by spin-coating a nonstoichiometric mixed halide precursor solution composed of CH_3NH_3I and $PbCl_2$ (3:1) in *N,N*-dimethylformamide (*19*, *27*). Films prepared under identical conditions and incorporated into standard solar cell device architectures (fig. S1) (*19*) exhibit power conversion efficiencies (η) up to 14.5% (Fig. 1A), which is comparable to efficiencies in other reports using this architecture (*2*, *28*). Figure 1B shows that our PL lifetimes are as long as those reported for films used in the best devices to date (*10*). These films exhibited average carrier lifetimes >1000 ns when excited at low intensity (30 nJ/cm^2, n_0 ~ 10^{15} cm^{-3}). At short times (Fig. 1B, inset), the PL decay could appear nearly single-exponential, but at longer times, the decay deviated from a single-exponential decay (*6*, *9*, *15*). We fit the decay in Fig. 1B with a stretched-exponential function of characteristic lifetime τ_c = 431 ns and distribution parameter β = 0.57, which we interpret as arising from a superposition of exponential relaxation functions (see below) with an average lifetime of $\langle\tau\rangle$ = 1005 ns (*19*, *29*).

Green and co-workers recently examined microscopic PL quenching of discontinuous perovskite islands with n- and p-type capping layers (*30*). Here, we used fluorescence microscopy to probe the inherent decay properties of neat semiconducting films. Figure 1 shows a correlated SEM micrograph (Fig. 1C), confocal PL image (Fig. 1D), and an overlaid SEM/PL microscopy image (Fig. 1E) of a high-performing perovskite film on a glass substrate. Although this film appears contiguous (Fig. 1C) and exhibits $\langle\tau\rangle$ = 1005 ns, Fig. 1D shows a large distribution in local PL intensity across the film. We observed these large distributions in films prepared in different research labs (fig. S2D) (*19*), and we exclude variations in film thickness (fig. S2) (*19*) and photodegradation during imaging (fig. S3) (*19*) as primary causes. The PL intensity not only varied from grain to grain, with roughly 30% of grains imaged in Fig. 1C consisting of dark grains (*19*), but we also observed ~65% lower PL intensity at grain boundaries (fig. S4, A to C) (*19*), after deconvolution of the microscope point-spread function (fig. S5) (*19*). These results are surprising because, through considerations of detailed balance (*11*, *31*), one expects high-performance films to have minimal nonradiative decay.

Instead, the spatial variations in PL intensity in the polycrystalline perovskite films are suggestive of variations in local nonradiative decay

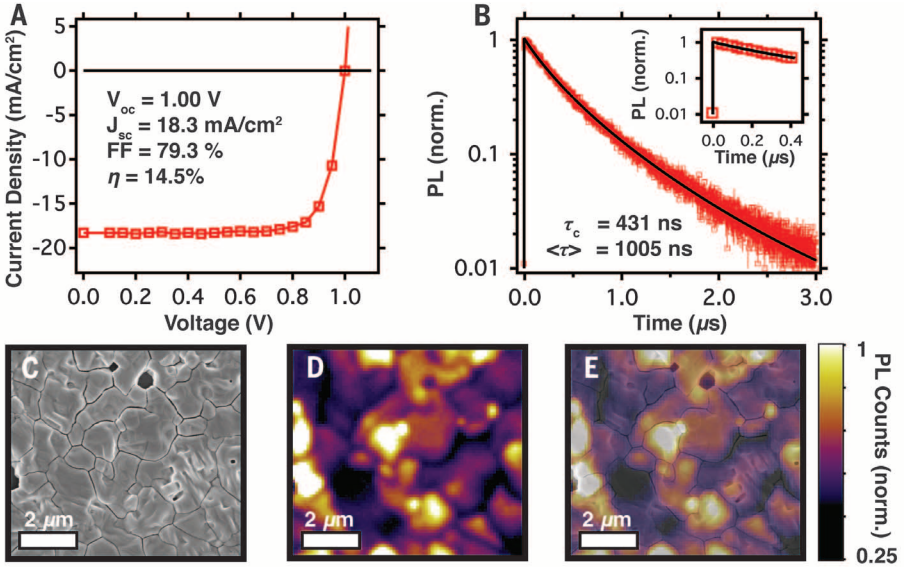

Fig. 1. Solar cell device measurement, bulk PL lifetime measurement, and correlated images from (SEM) and fluorescence microscopy experiments. (**A**) Light current-voltage (*J-V*) characteristics of a high-performing mixed halide perovskite solar cell. (**B**) Bulk time-resolved PL decay trace of $CH_3NH_3PbI_3(Cl)$ perovskite film on glass after excitation at 470 nm, 125 kHz, 30 nJ/cm^2 (n_0~10^{15}cm^{-3}) and fitted to a stretched-exponential function with $\langle\tau\rangle$ = 1005 ns, (τ_c = 431 ns, β = 0.57), with nearly single-exponential dynamics at short times (inset). (**C**) Correlated SEM micrograph, (**D**) fluorescence image, and (**E**) composite image showing significant variations in PL intensity across different grains and grain boundaries.

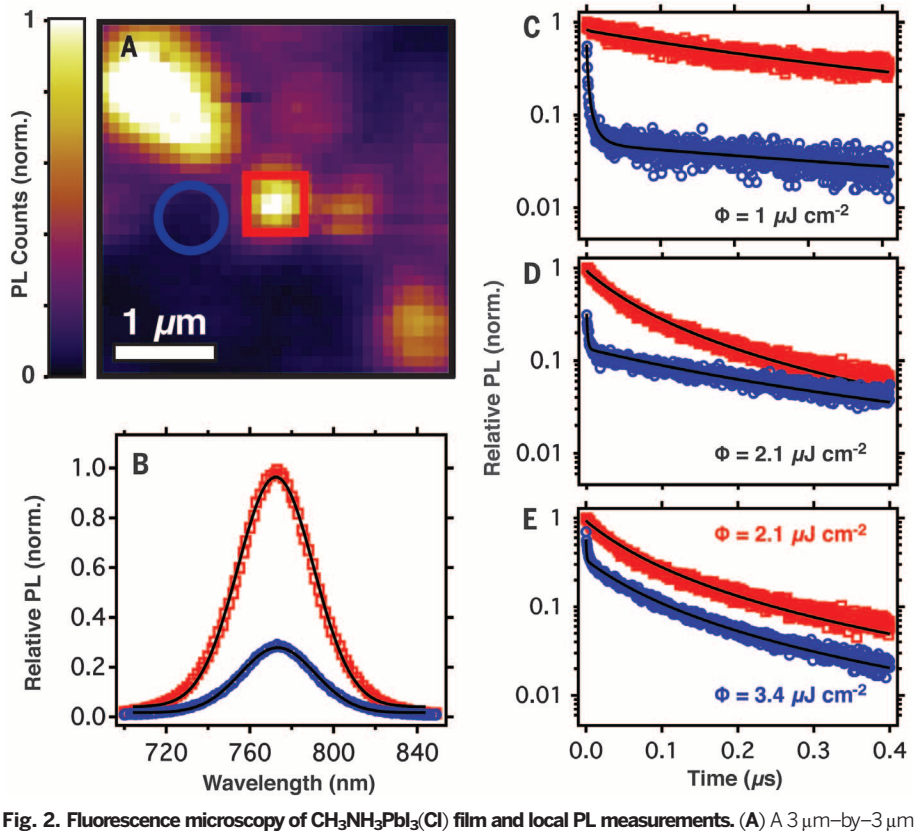

Fig. 2. Fluorescence microscopy of $CH_3NH_3PbI_3(Cl)$ film and local PL measurements. (**A**) A 3 μm–by–3 μm fluorescence image of the perovskite film with bulk lifetime $\langle\tau\rangle$ = 1010 ns (τ_c = 433 ns, β = 0.57). (**B**) Relative steady state PL spectra of bright (red square) and dark (blue circle) regions. (**C**) Time-resolved PL decay curves of bright (red square) and dark (blue circle) regions after excitation at 470 nm, 125 kHz, φ = 1 μJ/cm^2 (n_0 ~ 5 × 10^{16} cm^{-3}), (**D**) φ = 2.1 μJ/cm^2 (n_0 ~ 1 × 10^{17}cm^{-3}), and (**E**) bright region measured at φ = 2.1 μJ/cm^2 versus dark region measured at φ = 3.4 μJ/cm^2 (n_0 ~ 1.6 × 10^{17}cm^{-3}), showing that dark regions require higher initial carrier densities to exhibit kinetics dominated by bimolecular recombination. Black traces are simulations to the data (*19*).

rates. By taking local steady-state and time-resolved PL data, we confirmed that darker regions have greater nonradiative loss. Figure 2 shows a confocal PL image (Fig. 2A) along with local PL spectra (Fig. 2B) and lifetime data (Fig. 2, C to E) from a film with a long average bulk lifetime ($<\tau>$ = 1010 ns). Figure 2B shows the steady-state spectra of a bright (red square) and dark (blue circle) region. The PL spectrum collected at the dark region is both red-shifted (~2 nm) and slightly broader than the bright region (fig. S6) (*19*). These trends suggest a less sharp band edge (*32*), probably caused by the presence of defect states or shallow trapping levels in the darker regions. In Fig. 2, C to E, we show local PL decays of the indicated dark and bright regions at low (1 $\mu J/cm^2$), medium (2.1 $\mu J/cm^2$), and high (3.4 $\mu J/cm^2$) excitation fluences. Several studies have reported a transition from trap-assisted monomolecular recombination to free-carrier bimolecular recombination over this fluence range (*15*, *18*). Consistent with the picture that bright regions have fewer nonradiative pathways, bright regions show a slower decay, a transition to bimolecular recombination–dominated kinetics at a lower excitation fluence, and more efficient PL quenching when contacted by fullerene (fig. S7) (*19*) in comparison to dim regions. We modeled the PL dynamics (black lines in Fig. 2, C to E) as a combination of trapping, monomolecular, and bimolecular recombination (*19*). We report a higher deep trap-state density in the dark region (4×10^{16} cm^{-3}) as compared to the bright region ($<1 \times 10^{15}$ cm^{-3}). In addition, we extracted the trapping, monomolecular, and bimolecular decay rates in both regions to be 1×10^{-8} cm^3 s^{-1}, 1×10^{6} s^{-1}, and 2.3×10^{-11} cm^3 s^{-1} to 7.8×10^{-11} cm^3 s^{-1}, respectively. We also report consistent ratios of PL intensity measured across the steady state and integrated time-resolved PL measurements (fig. S8) for bright and dark regions (*19*).

The local PL lifetimes are also shorter at grain boundaries (fig. S4E) (*19*). Grain boundaries frequently serve as nonradiative recombination centers in polycrystalline semiconductor films (*33*). Studies have suggested that grain boundaries in perovskites are less detrimental than in other semiconductors (*25*, *26*), or even beneficial (*34*). Other results suggest that single-crystal perovskites exhibit even higher performance (*35*–*37*), and some describe improvements in carrier lifetime and device performance from post-growth treatments, such as exposure of the film to pyridine (C_5H_5N), in the context of surface passivation (*12*, *23*).

In this context, we next show that pyridine vapor exposure can brighten dark domains. In Fig. 3, A and B, we show the PL from a $CH_3NH_3PbI_3(Cl)$ film before and after exposure to pyridine vapor. The entire film was both brighter (~8× integrated over the entire image) and more uniform after pyridine exposure (no enhancement without pyridine, fig. S9) (*19*). For instance, the relative increase of a dark domain (squares in Fig. 3, A and B), was 180% larger than the relative increase of a bright domain (circles). The PL emission also blue-shifted (by ~3 nm) and narrowed slightly (Fig. 3C) after pyridine exposure, which could be caused by a reduction in shallow trap density. Finally, Fig. 3D shows that the grain boundary brightness, relative to the surrounding grains, increased by 11% and the width decreased by 25% after pyridine exposure (see fig. S10 for other examples) (*19*). Both trends are consistent with passivation, albeit incomplete, of defects at grain boundaries. Although pyridine treatment can also result in some restructuring of film morphology (fig. S10) (*19*), these data suggest that pyridine was indeed remediating nonradiative defects in the perovskite film.

Finally, we explored the role of Cl in perovskite films by comparing SEM/EDS elemental composition traces with local PL intensity traces. Figure 4A shows an overlaid SEM/PL microscopy image of a $CH_3NH_3PbI_3(Cl)$ film on glass. We tracked the changes in PL intensity with Cl content (Fig. 4B) and showed that bright regions correlate with areas of higher relative Cl content (Cl/Cl+I) (trace Cl in $CH_3NH_3PbI_3$ control films, fig. S11) (*19*). Although films prepared from Cl/I mixed halide precursors stoichiometrically resemble triiodides (*38*), there is evidence for residual Cl at levels of ~2 weight % or less (*13*, *39*). The lifetime enhancement in the presence of Cl is consistent with recent findings that Cl-rich nucleation sites lead to better crystal coalescence (*40*, *41*) and helps explain why films grown in the presence of Cl have slower recombination rates (*9*, *17*). We hypothesize that Cl could be present at the surface or within the crystals, interstitially or substitutionally, or simply at the substrate surface as a residual but unincorporated component left over from the seeding of low-defect crystallites. We performed

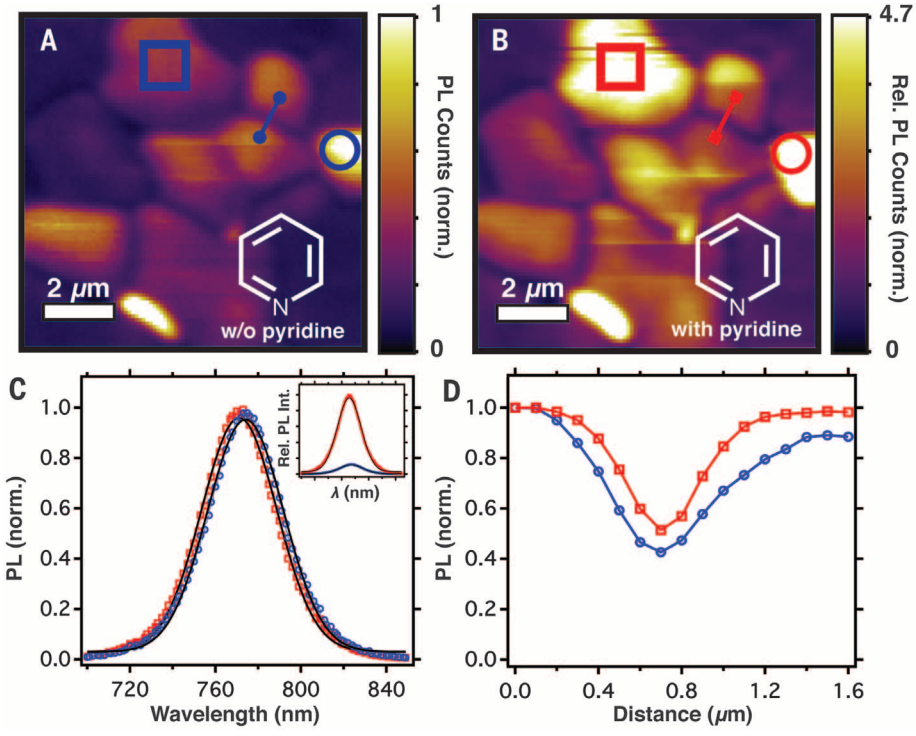

Fig. 3. Fluorescence microscopy of $CH_3NH_3PbI_3(Cl)$ film with pyridine vapor treatment. (**A**) Fluorescence image before and (**B**) after treatment showing activation of the $CH_3NH_3PbI_3(Cl)$ film. (**C**) Bulk steady-state PL spectra showing the relative PL intensities before (blue circle) and after (red square) treatment (inset) and normalized spectra showing a slight blue shift and narrowing of full width at half maximum after treatment. (**D**) Grain boundary PL line scan before [blue line in (A)] and after [red line in (B)] treatment, showing slight relative reduction in PL quenching across the grain boundary after treatment.

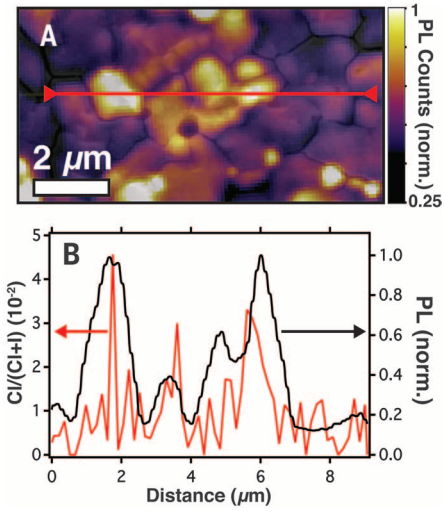

Fig. 4. Correlated images and line scans of $CH_3NH_3PbI_3(Cl)$ film using fluorescence microscopy, SEM, and EDS. (**A**) SEM micrograph overlaid on fluorescence image and (**B**) EDS line scan showing that the local elemental weight ratio of Cl/(Cl+I) tracks areas of higher integrated PL intensity, indicating that Cl is associated with better-performing grains.

time-of-flight secondary ion mass spectrometry (ToF-SIMS) (fig. S11F) (*19*) and found higher Cl content in $CH_3NH_3PbI_3(Cl)$ films than in $CH_3NH_3PbI_3$ films without Cl. This technique probes the top 2 nm of the film.

Although perovskite solar cells have better radiative efficiencies than many other types, such as dye-sensitized, organic, or even cadmium telluride solar cells, they still suffer from greater nonradiative losses than inorganic materials such as gallium arsenide and are only at present approaching the radiative efficiencies of copper indium gallium selenide (CIGS) (*31*). Our results identify a subpopulation of dark grains and grain boundaries as specific targets for perovskite growth and passivation studies, and show that local fluorescence lifetime imaging provides a route by which changes in film processing can be evaluated to assess their influence on carrier recombination in films. By removing these nonradiative pathways to obtain uniform brightness with high emissivity across all grains, it is likely that we will see the performance of perovskite devices approach the thermodynamic limits for solar cells and other light-emitting devices.

REFERENCES AND NOTES

1. T. C. Sum, N. Mathews, *Energ. Environ. Sci.* **7**, 2518–2534 (2014).
2. M. A. Green, A. Ho-Baillie, H. J. Snaith, *Nat. Photonics* **8**, 506–514 (2014).
3. J. Burschka *et al.*, *Nature* **499**, 316–319 (2013).
4. G. E. Eperon, V. M. Burlakov, P. Docampo, A. Goriely, H. J. Snaith, *Adv. Funct. Mater.* **24**, 151–157 (2014).
5. G. Xing *et al.*, *Nat. Mater.* **13**, 476–480 (2014).
6. G. E. Eperon *et al.*, *Energ. Environ. Sci.* **7**, 982–988 (2014).
7. J. H. Noh, S. H. Im, J. H. Heo, T. N. Mandal, S. I. Seok, *Nano Lett.* **13**, 1764–1769 (2013).
8. National Center for Photovoltaics at the National Renewable Energy Laboratory, Research cell efficiency records, www.nrel.gov/ncpv/ (accessed 11 April 2015).
9. S. D. Stranks *et al.*, *Science* **342**, 341–344 (2013).
10. H. Zhou *et al.*, *Science* **345**, 542–546 (2014).
11. O. D. Miller, E. Yablonovitch, S. R. Kurtz, *IEEE J. Photovolt.* **2**, 303–311 (2012).
12. N. K. Noel *et al.*, *ACS Nano* **8**, 9815–9821 (2014).
13. J. You *et al.*, *ACS Nano* **8**, 1674–1680 (2014).
14. P. W. Liang *et al.*, *Adv. Mater.* **26**, 3748–3754 (2014).
15. S. D. Stranks *et al.*, *Phys. Rev. Appl.* **2**, 034007 (2014).
16. F. Deschler *et al.*, *J. Phys. Chem. Lett.* **5**, 1421–1426 (2014).
17. C. Wehrenfennig, M. Liu, H. J. Snaith, M. B. Johnston, L. M. Herz, *Energ. Environ. Sci.* **7**, 2269–2275 (2014).
18. J. S. Manser, P. V. Kamat, *Nat. Photonics* **8**, 737–743 (2014).
19. See the supplementary materials on *Science* Online.
20. G. Xing *et al.*, *Science* **342**, 344–347 (2013).
21. Y. Yamada, T. Nakamura, M. Endo, A. Wakamiya, Y. Kanemitsu, *J. Am. Chem. Soc.* **136**, 11610–11613 (2014).
22. M. Saba *et al.*, *Nat. Commun.* **5**, 5049 (2014).
23. A. Abate *et al.*, *Nano Lett.* **14**, 3247–3254 (2014).
24. S. Watanabe *et al.*, *Nat. Methods* **8**, 80–84 (2011).
25. E. Edri *et al.*, *Nano Lett.* **14**, 1000–1004 (2014).
26. W. J. Yin, T. Shi, Y. Yan, *Adv. Mater.* **26**, 4653–4658 (2014).
27. M. M. Lee, J. Teuscher, T. Miyasaka, T. N. Murakami, H. J. Snaith, *Science* **338**, 643–647 (2012).
28. P. Gao, M. Grätzel, M. K. Nazeeruddin, *Energ. Environ. Sci.* **7**, 2448–2463 (2014).
29. K. Munechika *et al.*, *Nano Lett.* **11**, 2725–2730 (2011).
30. X. Wen *et al.*, *J. Phys. Chem. Lett.* **5**, 3849–3853 (2014).
31. K. Tvingstedt *et al.*, *Sci. Rep.* **4**, 6071 (2014).
32. S. De Wolf *et al.*, *J. Phys. Chem. Lett.* **5**, 1035–1039 (2014).
33. C. H. Seager, *Annu. Rev. Mater. Sci.* **15**, 271–302 (1985).
34. J. S. Yun *et al.*, *J. Phys. Chem. Lett.* **6**, 875–880 (2015).
35. Q. Dong *et al.*, *Science* **347**, 967–970 (2015).
36. W. Nie *et al.*, *Science* **347**, 522–525 (2015).
37. D. Shi *et al.*, *Science* **347**, 519–522 (2015).
38. M. Grätzel, *Nat. Mater.* **13**, 838–842 (2014).
39. G. Grancini *et al.*, *J. Phys. Chem. Lett.* **5**, 3836–3842 (2014).
40. Y. Tidhar *et al.*, *J. Am. Chem. Soc.* **136**, 13249–13256 (2014).
41. S. T. Williams *et al.*, *ACS Nano* **8**, 10640–10654 (2014).

ACKNOWLEDGMENTS

This material is based in part on work supported by the State of Washington through the University of Washington Clean Energy Institute. D.W.D. acknowledges support from an NSF Graduate Research Fellowship (DGE-1256082). S.M.V. acknowledges support from a National Defense Science and Engineering Graduate Fellowship. The research leading to these results has received funding from the European Union Seventh Framework Program (FP7/2007-2013) under Grant Agreement No. 604032 of the MESO project. G.E.E. is supported by the Engineering and Physical Sciences Research Council and Oxford Photovoltaics through a Nanotechnology Knowledge Transfer Network Collaborative Award in Science and Engineering. The authors gratefully acknowledge funding from the National Institute for Biomedical Imaging and Bioengineering (NIH grant EB-002027) supporting the National ESCA and Surface Analysis Center for Biomedical Problems and ToF-SIMS instrumentation. D.W.D. thanks I. Braly, S. Braswell, D. Moerman, and B. Miller for valuable assistance. S.M.V. gratefully acknowledges D. Graham for assistance with ToF-SIMS. Additional data, including materials, methods, and key controls, are available online as supplementary materials (*19*).

SUPPLEMENTARY MATERIALS

www.sciencemag.org/content/348/6235/683/suppl/DC1
Materials and Methods
Supplementary Text
Figs. S1 to S11

19 December 2014; accepted 14 April 2015
10.1126/science.aaa5333

CATALYSIS

Identification of molybdenum oxide nanostructures on zeolites for natural gas conversion

Jie Gao,[1] Yiteng Zheng,[1] Jih-Mirn Jehng,[2,3] Yadan Tang,[2] Israel E. Wachs,[2]* Simon G. Podkolzin[1]*

Direct methane conversion into aromatic hydrocarbons over catalysts with molybdenum (Mo) nanostructures supported on shape-selective zeolites is a promising technology for natural gas liquefaction. We determined the identity and anchoring sites of the initial Mo structures in such catalysts as isolated oxide species with a single Mo atom on aluminum sites in the zeolite framework and on silicon sites on the zeolite external surface. During the reaction, the initial isolated Mo oxide species agglomerate and convert into carbided Mo nanoparticles. This process is reversible, and the initial isolated Mo oxide species can be restored by a treatment with gas-phase oxygen. Furthermore, the distribution of the Mo nanostructures can be controlled and catalytic performance can be fully restored, even enhanced, by adjusting the oxygen treatment.

Methane (CH_4), the main component of natural gas, has the highest H-to-C ratio of all hydrocarbons; therefore, it is more environmentally friendly in terms of CO_2 emissions than oil or coal-derived fuels. However, 30 to 60% of natural gas reserves are classified as "stranded" because shipping gas is not economical, and the costs of liquefaction or building a pipeline are usually prohibitively high (*1*–*5*). The problem of natural gas utilization is exacerbated by burning and venting of the associated gas produced in the course of crude oil production at remote locations. Conversion of methane into shippable liquids can solve these problems but remains scientifically challenging (*1*–*3*, *6*–*8*).

[1]Department of Chemical Engineering and Materials Science, Stevens Institute of Technology, Hoboken, NJ 07030, USA. [2]Operando Molecular Spectroscopy and Catalysis Laboratory, Department of Chemical Engineering, Lehigh University, Bethlehem, PA 18015, USA. [3]Department of Chemical Engineering, National Chung Hsing University, Taichung, Taiwan, Republic of China.
*Corresponding author. E-mail: iew0@lehigh.edu (I.E.W.); simon.podkolzin@stevens.edu (S.G.P.)

One of the technologies under development is direct methane conversion into liquid aromatic hydrocarbons in a single step (dehydroaromatization with the main reaction $6CH_4 \rightarrow C_6H_6 + 9H_2$) using catalysts with Mo nanostructures supported on shape-selective zeolites (*2*, *8*–*16*). This technology offers two advantages over other methane activation chemistries: Complete oxidation, as well as explosive combustion, is not possible because of the absence of O_2 or other oxidizing reagents, and processing can be performed at remote locations because no reagents are needed. The biggest issues in commercialization are rapid catalyst deactivation and comparatively low single-pass conversion levels of ~10% (*2*, *8*, *13*–*16*). Development of improved catalysts has been hindered by a lack of molecular-level understanding of the identity of the zeolite-supported Mo nanostructures and their structural transformations.

We studied Mo nanostructures supported on ZSM-5 zeolites by combining quantum chemical calculations using density functional theory (DFT) with multiple spectroscopic techniques, including in situ ultraviolet-visible diffuse reflectance

spectroscopy (UV-vis DRS), in situ infrared (IR) spectroscopy, and operando Raman spectroscopy at elevated reaction temperatures with simultaneous online mass spectrometry of reaction products. We determined the identity and anchoring sites of the initial Mo oxide nanostructures and established structure-activity relationships. The catalytic activity can be fully restored by regenerating initial Mo oxide nanostructures with a gas-phase O_2 treatment. Furthermore, the activity can even be enhanced by controlling the distribution of Mo oxide nanostructures by adjusting conditions of such an O_2 regeneration treatment.

Molybdenum nanostructures supported on zeolites were initially present in an oxide form after Mo deposition and an oxygen treatment at elevated temperatures (our samples were calcined at 773 K) (*17*). The number of MoO_x units in an average individual nanostructure was evaluated using the edge energy (E_g) of the in situ UV-vis DRS spectra. The E_g values for the following well-defined Mo oxide reference compounds are presented in Fig. 1A: (i) MoO_6-coordinated Mo_7-Mo_{12} clusters, (ii) linear chains of alternating MoO_4 and MoO_6 units, (iii) infinite layered sheets of MoO_5 units, (iv) Mo_2O_7 dimer as MoO_3-O-MoO_3, (v) isolated MoO_4 and MoO_6 monomers, and (vi) aqueous molybdate anions as a function of the solution pH (*18*). The E_g values in Fig. 1A exhibit a linear correlation with the number of bridging Mo-O-Mo covalent bonds around the central Mo cation and, correspondingly, with the number of MoO_x units in a nanostructure. The E_g value for a representative catalyst sample with 2 weight percent (wt %) Mo supported on a ZSM-5 (Si/Al = 15) zeolite, which is the most common zeolite evaluated for methane dehydroaromatization, was 4.8 eV, which falls in the range of isolated MoO_x nanostructures with a single Mo atom.

The nature of the Mo oxide nanostructures was further examined with in situ Raman spectroscopy by varying the concentration of Mo from 0.7 to 3.3 wt % on a ZSM-5 zeolite support with a constant Si/Al ratio of 15 (Fig. 1B) and by varying the Si/Al ratio from 15 to 140 at a constant Mo concentration of 1.3 wt % (Fig. 1C). The spectrum for 1.3 wt % Mo on ZSM-5 with Si/Al = 15 is shown in both sets in Fig. 1, B and C, and a similar spectrum is shown in operando Raman measurements with methane flow in fig. S1 (*17*). The absence of sharp Raman bands from crystalline MoO_3 nanoparticles (NPs) at 996, 815, and 666 cm^{-1} (*19*) or crystalline $Al_2(MoO_4)_3$ at ~1004 and 1045 cm^{-1} (*18*, *20*) indicates, in agreement with the UV-vis results in Fig. 1A, that Mo oxide was completely dispersed; any amorphous Mo oxide species would crystallize at the elevated pretreatment temperature of 773 K. Some spectra exhibited weak shoulder features at 950 cm^{-1} from Mo oxide species in zeolite framework vacancy defects and at 1026 cm^{-1} from Mo oxide species on extra-framework alumina NPs (*17*).

For the ZSM-5 (Si/Al = 15) zeolite in Fig. 1B, a single Raman band at 993 cm^{-1} was observed in the Mo-O stretching region for all Mo concentrations. However, at higher Si/Al ratios in Fig. 1C, a new band at 975 cm^{-1} was observed, and an additional band appeared at 984 cm^{-1} at the highest Si/Al = 140 (Fig. 1C). These three bands cannot be attributed to a single Mo oxide nanostructure because their relative intensities change with the Si/Al ratio. To determine the identity and anchoring sites of these Mo oxide structures in the ZSM-5 zeolite framework, various monomeric Mo oxide species were evaluated with DFT calculations, and the calculated normal vibrational modes were compared with the experimental Raman spectra.

After calcination at 773 K, Mo was present in its highest oxidation state of +6, as evidenced by the absence of d-d transitions for reduced Mo in the in situ UV-vis spectra. Our DFT calculations show that neutral MoO_3 species on framework Si sites are unstable and that framework Al sites are required for anchoring (*17*). This result is in agreement with changes in the in situ IR spectra for surface OH groups as a function of the Mo loading in fig. S2 (*17*) that showed preferential elimination of Brønsted acid sites (H^+ on $[AlO_4]^-$) after Mo deposition. On a site with two adjacent framework Al atoms, the stoichiometry of the Mo oxide species should be $Mo(=O)_2^{2+}$ as dioxo species to counterbalance the 2– charge of $2[AlO_4]^-$ and maintain Mo in the +6 oxidation state. The size of isolated Mo dioxo species serves as a geometric restriction, which determines the acceptable range of separation distances between the two anchoring framework Al-atom sites. Because ZSM-5 is a Si-rich zeolite, Lowenstein's rule prohibits one Al atom to be the first neighbor of another Al atom in the framework as Al-O-Al. An arrangement of Al-O-Si-O-Al with two Al atoms as second neighbors was not found experimentally, based on ^{27}Al nuclear magnetic resonance (NMR) and additional characterization for ZSM-5 samples with Si/Al > 8 (*21*, *22*). Finally, an arrangement of Al-O-$(Si\text{-}O)_2$-Al with two Al atoms as third neighbors must be the only possible double Al-atom anchoring sites for Mo dioxo species. Our DFT results confirm that two Al atoms as fourth neighbors in Al-O-$(Si\text{-}O)_3$-Al can serve only as two individual single anchoring sites (*17*).

Although the exact distribution of Al atoms among different framework sites in ZSM-5 zeolites is currently not well understood, it can be varied by adjusting the zeolite synthesis procedure. For example, the number of Al atoms as double anchoring sites in the arrangement Al-O-$(Si\text{-}O)_2$-Al can be varied from 4 to 46% for ZSM-5 samples with Si/Al = ~20, based on characterization with hydrated Co cations (*22*). The fraction of Al atoms as double anchoring sites typically decreases, but not proportionally, with the increasing Si/Al ratio for the same synthesis procedure (*22*). Our evaluation of Al-O-$(Si\text{-}O)_2$-Al arrangements in ZSM-5 shows that these sites can serve as double Al-atom anchoring sites if they are located in the same channel, but not in the same plane. Additional classification of double Al-atom anchoring sites is provided in fig. S4 (*17*). A representative $Mo(=O)_2^{2+}$ dioxo structure on

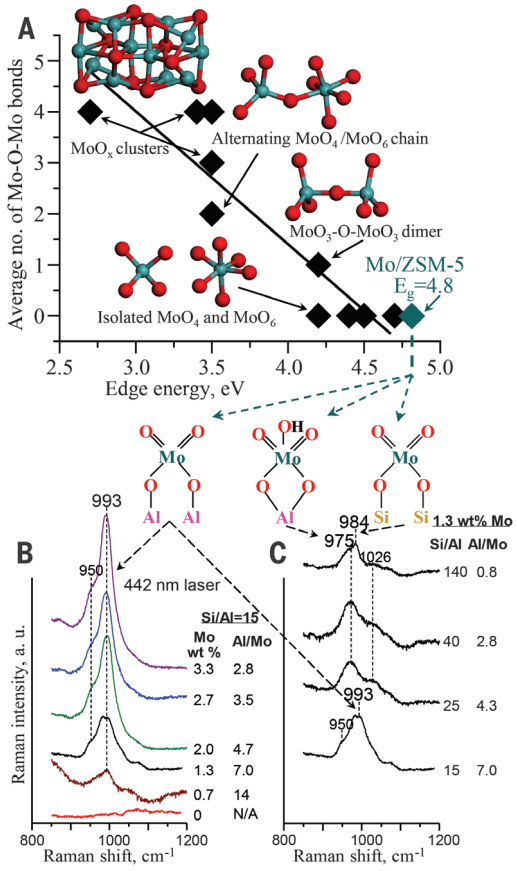

Fig. 1. Spectroscopic measurements. (**A**) Electronic edge values based on in situ UV-vis spectra of reference Mo oxide compounds exhibit a linear correlation with the number of bridging Mo-O-Mo covalent bonds around the central Mo cation. The value of 4.8 eV for 2 wt % Mo/ZSM-5 (Si/Al = 15) corresponds to Mo oxide species with a single Mo atom. (**B** and **C**) In situ Raman spectra of Mo/ZSM-5 catalysts under oxygen flow at 773 K as a function of (B) Mo loading for constant Si/Al = 15 and (C) Si/Al ratio for constant 1.3 wt % Mo loading with band assignments to Mo oxide species based on DFT calculations. a. u., arbitrary units.

an anchoring site with a pair of Al atoms in T8 and T12 framework positions is shown in Fig. 2. In this nanostructure, the Mo atom is bridge-bonded to two framework Al atoms through two neighboring framework oxygen atoms and terminated with two additional oxygen atoms. The normal vibrational modes obtained with DFT calculations for these terminal oxygen atoms in $Mo(=O)_2^{2+}$ are summarized in Table 1. The symmetric stretch (ν_s) is calculated to be at 992 cm^{-1}. The calculated geometries and normal vibrational modes for the $Mo(=O)_2^{2+}$ nanostructure on other double Al-atom anchoring sites with two bridging framework O atoms are similar (table S2 and fig. S6) (*17*). On a site with a single framework Al atom, the stoichiometry of Mo oxide species should be $Mo(=O)_2(OH)^+$ to counterbalance the 1– charge of $[AlO_4]^-$ and maintain Mo in the +6 oxidation state. The vibrational mode for the symmetric stretch of the terminal oxygen atoms in these Mo species is predicted to be at 975 cm^{-1}, based on evaluation of geometries and vibrational modes of the $Mo(=O)_2(OH)^+$ nanostructure anchored on single Al-atom sites in T8 (Table 1) and other ZSM-5 framework positions (table S1 and fig. S5) (*17*).

Raman spectroscopy gives rise to strong bands of symmetric stretches (ν_s) and weaker bands of asymmetric stretches (ν_{as}), with the latter sometimes being undetectable. In our previous studies of MoO_3/SiO_2 (*19*, *20*), ν_{as} for $Mo(=O)_2$ was not observed for Mo loadings below 4 wt %. Therefore, only ν_s is expected to be observed for lower Mo loadings. A comparison of the dominant Raman bands at 975 and 993 cm^{-1} in Fig. 1 with the calculated symmetric stretch values (ν_s) in Table 1 (975 and 992 cm^{-1}) allowed us to assign these bands to two distinct isolated Mo dioxo species anchored on, respectively, single and double Al-atom framework sites.

The identification of the isolated Mo oxide structures provided insight as to how they were affected by the main catalyst formulation parameters: the Mo loading and Si/Al ratio. At a low Si/Al = 15, Mo oxide species preferentially anchored on sites with two Al atoms (band at 993 cm^{-1} in Fig. 1B). Even at the highest Mo loading of 3.3 wt %, the Al/Mo atomic ratio is 2.8, which allowed all Mo atoms to be anchored on double Al-atom sites. However, when the Si/Al ratio increased, the number of Al atoms per unit volume of the zeolite decreased, and the number of sites with two Al atoms should have decreased more rapidly than the overall number of Al atoms. As a result, at higher Si/Al ratios of 25 and 40 in Fig. 1C, the dominant band was at 975 cm^{-1}, arising from $Mo(=O)_2OH$ species anchored on sites with one Al atom. The identification of single and double Al-atom anchoring sites is in agreement with previous findings that each Mo atom displaces one H^+ from framework $[AlO_4]^-$ sites in ZSM-5 with Si/Al = 40 and two H^+ in ZSM-5 with Si/Al = 15 (*23*). At the highest Si/Al = 140 shown in Fig. 1C, when the corresponding Al/Mo ratio fell below unity to 0.8, there were not even enough single Al-atom sites for stabilizing all Mo atoms. For this catalyst formulation, Mo oxide species were forced to be stabilized, not in the zeolite pores but on the least preferable Si sites on the external surface of the zeolite. A new band at 984 cm^{-1} for Si/Al = 140 in Fig. 1C is consistent with our previous Raman spectra for Mo oxide species supported on amorphous SiO_2 (*19*, *20*). Our DFT calculations confirmed that Mo dioxo species did not stabilize in zeolite pores in the absence of Al sites and that the structure of isolated $Mo(=O)_2$ dioxo species as $(Si\text{-}O\text{-})_2Mo(=O)_2$ on the external surface of the zeolite (Fig. 1; full details in fig. S8 and table S4) (*17*) is similar to that on SiO_2. These findings are also supported by the in situ IR spectra of the surface OH region for ZSM-5 (Si/Al = 15) as a function of the Mo loading in fig. S2 (*17*). The intensity of the peak at 3608 cm^{-1} for OH groups on framework Al sites (*24*) decreased through replacement by Mo oxide species at low Mo loadings, followed by a decrease in the intensity of the peak at 3745 cm^{-1} for OH groups on the external surface Si sites (*24*) at higher Mo loadings. The isolated Mo oxide structures preferentially anchored on double Al-atom framework sites, then single Al-atom framework sites, and finally Si sites on the external surface of the zeolite. The isolated Mo oxide nanostructures anchored on these three types of zeolite sites are shown schematically in Fig. 1 and with 3D animation in movie S1.

Dynamic changes of Mo nanostructures under reaction and regeneration conditions were evaluated by simultaneously collecting operando Raman spectroscopy and online mass spectrometry measurements, first with CH_4 flow at 953 to 1053 K (fig. S1) (*17*) and then under regeneration conditions with gas-phase O_2 flow at 773 K (figs. S10 and S11) (*17*). Upon CH_4 introduction, CO_2 was the only initial carbon-containing product, and the Raman band at 993 cm^{-1} for the isolated Mo oxide structures gradually disappeared. Because CH_4 was the only reactant, Mo oxide nanostructures reduced to oxycarbide or carbide species. Several studies with different techniques, such as x-ray absorption fine structure, Mo L_{III} edge x-ray absorption near-edge structure, and ^{95}Mo NMR, provide direct evidence that the reduced Mo phase is a carbide with the stoichiometry of MoC_x or MoC_xO_y and that the initial oxide species agglomerate into particles with a size of ~0.6 nm (*25*–*28*). After the induction period, CO_2 formation stopped, the Raman band at 993 cm^{-1} for the initial Mo oxide species was no longer observed (Fig. 2B and fig. S1) (*17*), and the catalyst performed CH_4 dehydroaromatization with C_6H_6 as the main hydrocarbon product.

Our results demonstrate that an O_2 treatment can reverse both the carbide formation and the agglomeration of Mo nanostructures. The Raman spectra at 753 K for the initial catalyst with isolated Mo oxide structures and for the regenerated catalyst after reaction in Fig. 2 are similar, with a single band at 993 cm^{-1} and a shoulder feature at 950 cm^{-1}. The similarity in the Raman band positions and intensities before reaction and after regeneration indicates that the regeneration converts carbided Mo NPs into an oxide phase, redisperses this phase into isolated oxide nanostructures with a single Mo atom, and allows these Mo oxide species to diffuse and then stabilize on substantially the same zeolite anchoring sites as in the initial catalyst before the reaction.

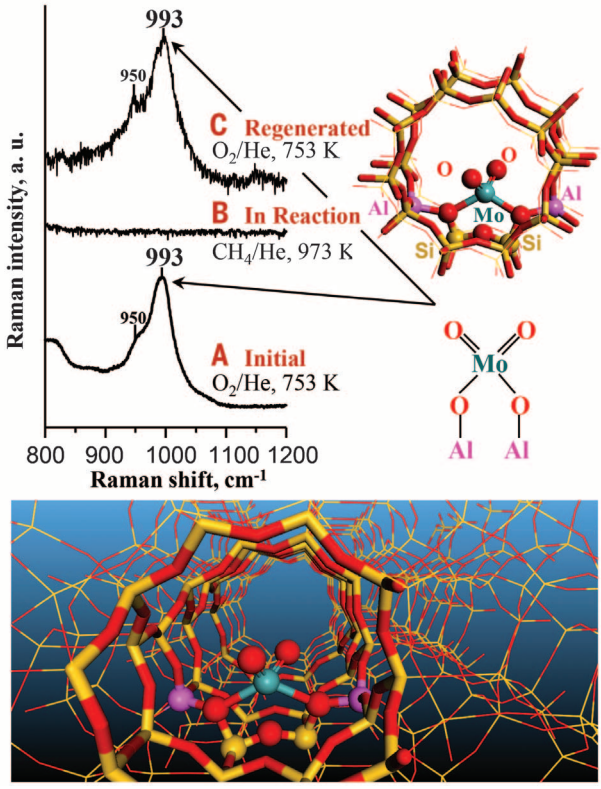

Fig. 2. Operando Raman spectra of 2 wt % Mo/ZSM-5 (Si/Al = 15). Spectra (**A**) after initial pretreatment with gas-phase oxygen, (**B**) during reaction with methane, and (**C**) after regeneration with gas-phase oxygen are shown. The spectra demonstrate that the initial $Mo(=O)_2^{2+}$ nanostructures anchored on double Al-atom framework sites (shown schematically on the right and in a zeolite pore below) with a vibrational mode at 993 cm^{-1} are recovered after regeneration.

Effects of regeneration time with O_2 on the identity of Mo nanostructures and on catalytic performance with CH_4 after regeneration were evaluated by combining additional Raman spectroscopic measurements with reaction testing. Raman spectra were collected in O_2 flow at 773 K for two 1.3 wt % Mo/ZSM-5 (Si/Al = 15 and 25) catalysts after their deactivation in reaction with CH_4. The evolution of Raman spectra as a function of regeneration time in figs. S10A and S11A (*17*) shows that isolated Mo oxide nanostructures were regenerated sequentially. Isolated $Mo(=O)_2$ species anchored on double Al-atom framework sites were regenerated first, as evidenced by a single initial Raman band at 993 cm^{-1}. With increased regeneration time, a second Raman band at 975 cm^{-1} caused by $Mo(=O)_2OH$ species anchored on single Al-atom sites appeared and grew in intensity. Finally, a third Raman band at 984 cm^{-1} due to $Mo(=O)_2$ species anchored on Si sites on the external surface of the zeolite appeared and grew in intensity for the catalyst with a lower Al concentration in the zeolite (Si/Al = 25 instead of 15). These direct spectroscopic observations demonstrate that exposure to gas-phase O_2 first regenerates isolated Mo oxide nanostructures anchored on sites with two Al atoms, then forces these species to migrate to sites with one Al atom and, eventually, to Si sites on the external surface of the zeolite.

A comparison of C_6H_6 formation rates in CH_4 conversion as a function of time on stream for a fresh 1.3 wt % Mo/ZSM-5 catalyst (Si/Al = 25) versus the same catalyst after deactivation in the reaction with CH_4 and subsequent regeneration for 120 min (Fig. 3A) demonstrates that the catalytic performance can be fully restored. The C_6H_6 formation rates after regeneration matched those for the fresh catalyst. Additional reaction results for C_6H_6 and H_2 formation rates for two 1.3 wt % Mo/ZSM-5 (Si/Al = 15 and 25) catalysts as a function of regeneration time (figs. S10 and S11) (*17*) show that both the overall activity and selectivity to C_6H_6 fully recovered after regeneration. Thus, rapid catalyst deactivation can be successfully addressed by regeneration with gas-phase O_2, and the catalyst lifetime can be extended by repeated regeneration cycles.

Correlations between the structure of the initial Mo oxide species and catalytic performance can be established by comparing the evolution of the Raman spectra with changes in reaction rates as a function of regeneration time in figs. S10 and S11 (*17*). The catalytic activity was restored once Mo oxide nanostructures on double Al-atom framework sites were regenerated (after ~20 min). With increased regeneration time, these isolated Mo oxide species migrated from double to single Al-atom zeolite framework sites, and the catalytic performance with CH_4 remained unchanged. Furthermore, the catalytic performance of a regenerated catalyst can be optimized and may exceed that of a fresh catalyst if the regeneration treatment is stopped before Mo oxide nanostructures are forced to migrate to Si anchoring sites on the external surface of the zeolite. Specifically for the 1.3 wt % Mo/ZSM-5 (Si/Al = 25) catalyst, Mo oxide nanostructures were regenerated and moved from double to single Al-atom zeolite framework sites for regeneration times between 20 and 100 min (fig. S11A) (*17*). Notably, Mo nanostructures remained anchored on zeolite framework Al sites when the regeneration was limited to this duration, and the rates of C_6H_6 formation for such regenerated catalyst samples actually exceeded those for the fresh catalyst. The C_6H_6 formation rates for a catalyst regenerated for 100 min in Fig. 3A exceeded those for the same catalyst before deactivation during the initial time on stream period. In contrast, when the regeneration time was extended beyond 100 min, Mo oxide nanostructures were forced to migrate from Al framework sites to Si anchoring sites on the external surface of the zeolite. This change in the anchoring sites caused the catalytic activity to decrease to the level of the fresh catalyst, and the C_6H_6 formation rates for the catalyst regenerated for 120 min (Fig. 3A) matched those for the fresh catalyst. With time on stream with CH_4, the catalytic activity declined likely because of migration, growth, and coking of Mo NPs, and the performance for all regenerated catalysts eventually became indistinguishable. However, in the first 60 min of time on stream, the benzene formation rates in Fig. 3A and fig. S11C (*17*) were dependent on the identity of the initial Mo oxide nanostructures.

For understanding these initial activity differences, transition-state DFT calculations were used for comparing CH_4 activation over catalytic Mo carbide nanostructures anchored on the identified three types of anchoring sites: double and single Al-atom zeolite framework sites and Si sites on the external surface of the zeolite. The calculations compared the first step (breaking of the CH_3-H bond in methane), which is likely the rate-determining step, over the Mo carbide nanostructure with a stoichiometry of Mo_4C_2 on the three zeolite anchoring sites (*29*). The CH_4 activation mechanism is similar for all anchoring sites, as illustrated in Fig. 3, which compares reaction pathways for a double Al-atom anchoring site inside a zeolite framework pore (Fig. 3, B, E, and F) and a Si site on the external surface of the

Table 1. DFT-calculated vibrational modes for isolated Mo oxide species supported on ZSM-5 (cm^{-1}): symmetric stretch (ν_s), asymmetric stretch (ν_{as}), and bend (δ).

Mo species	ν_s O=Mo=O	ν_{as} O=Mo=O	δ O=Mo=O
$Mo(=O)_2$ on a double Al-atom site	992	972	388
$Mo(=O)_2OH$ on a single Al-atom site	975	962	356

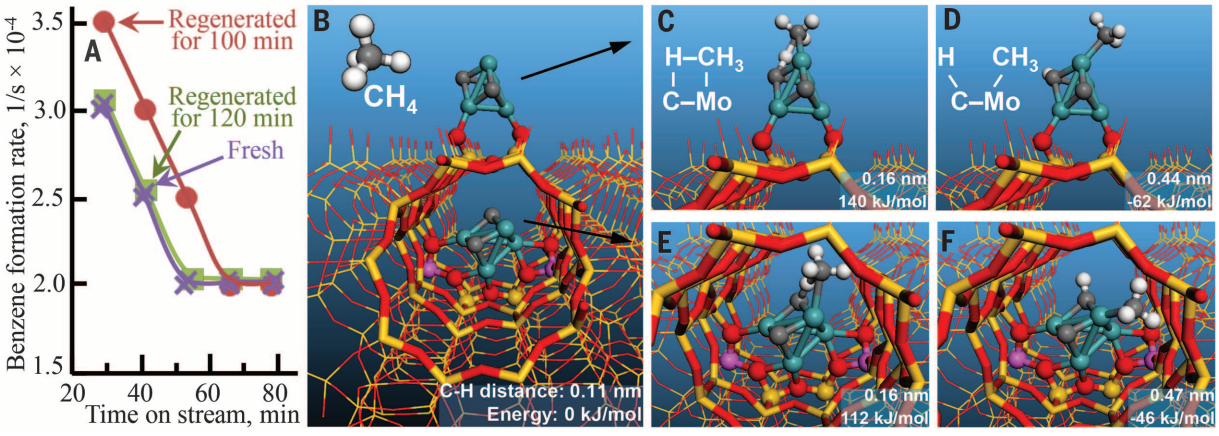

Fig. 3. Catalytic activity of Mo nanostructures. (**A**) Benzene formation rates in methane conversion over a 1.3 wt % Mo/ZSM-5 (Si/Al = 25) catalyst. The catalytic activity declines with time on stream but is fully restored after 120 min of gas-phase oxygen regeneration. Initial activity is enhanced by controlling the distribution of Mo nanostructures: Activity is higher after 100 min of regeneration when Mo oxide nanostructures are anchored mostly on framework Al sites and not forced to migrate to Si sites on the external surface of the zeolite. (**B** to **F**) Reaction mechanism calculations show that the energy barrier for methane activation with the formation of CH_3 and H species on the surface of the catalyst is lower when a Mo nanostructure is anchored on a framework Al site [(B), (E), and (F)] versus on a Si site on the external surface [(B) to (D)].

zeolite (Fig. 3, B to D). The CH_4 initially approaches an exposed Mo atom, an atom that is not directly bonded to the zeolite. In the transition state (Fig. 3, C and E), CH_4 forms a Mo-CH_3-H-C cycle in which the C atom of CH_4 binds to the exposed Mo atom and, simultaneously, one of the H atoms of CH_4 binds to a C atom in the carbide. Thus, a Mo-C pair of atoms in the Mo carbide nanostructure serves as a single catalytic active site. This dual Mo-C site activates CH_4 in a scissoring motion that produces a CH_3 group bonded to Mo and an H atom bonded to C of the carbide (Fig. 3, D and F). Although the mechanism of CH_4 activation is similar, differences in geometries and electronic properties of Mo carbide nanostructures anchored on Al and Si sites lead to differences in their catalytic properties. The CH_4 activation energy over the Mo carbide anchored on the double Al-atom site of 112 kJ/mol in Fig. 3E is lower than 140 kJ/mol for the Si site in Fig. 3C. The transition state for the single Al-atom anchoring site is analogous to that for the double Al-atom site in Fig. 3E, with a comparable activation energy of 117 kJ/mol (table S6) (*17*). The CH_4 reaction is therefore predicted to be dominated by the activity of Mo nanostructures anchored on framework Al sites. This computational result is consistent with known experimental observations that the catalytic activity of Mo nanostructures depends strongly on the Si/Al ratio of the supporting zeolite and declines substantially when Al framework sites are lost through dealumination (*2*, *8*, *13*–*15*, *30*).

The obtained information on the identity of Mo structures, their regeneration, and their influence on catalytic activity opens new opportunities for rational design of improved catalyst formulations and for optimizing reaction conditions for direct conversion of natural gas into liquid transportation fuels and valuable feedstocks for the chemical industry. It is important to control the distribution of Mo oxide species and limit their anchoring to framework Al sites because initial Mo oxide nanostructures anchored on Al sites of the zeolite framework are converting into carbided Mo NPs with higher catalytic activity than those produced by initial Mo oxide species anchored on Si sites. The number and distribution of single and double Al-atom anchoring sites can be optimized by adjusting a zeolite synthesis procedure. The number of Si anchoring sites on the external surface of the zeolite can be reduced, or these Si sites can be eliminated completely by adjusting the Mo deposition procedure. Furthermore, the catalytic performance of Mo species and their periodic regeneration can be optimized by adjusting catalyst formulations (for example, with promoter metals) and changing the temperatures of the reaction and regeneration, flow rates, and other reaction conditions.

REFERENCES AND NOTES

1. E. McFarland, *Science* **338**, 340–342 (2012).
2. J. H. Lunsford, *Catal. Today* **63**, 165–174 (2000).
3. S. G. Podkolzin, E. E. Stangland, M. E. Jones, E. Peringer, J. A. Lercher, *J. Am. Chem. Soc.* **129**, 2569–2576 (2007).
4. R. Khalilpour, I. A. Karimi, *Energy* **40**, 317–328 (2012).
5. International Energy Agency, "Golden rules for a golden age of gas - World Energy Outlook special report on unconventional gas," (International Energy Agency, Paris, France, 2012); www.worldenergyoutlook.org/goldenrules/.
6. J. A. Labinger, J. E. Bercaw, *Nature* **417**, 507–514 (2002).
7. X. Guo *et al*., *Science* **344**, 616–619 (2014).
8. A. Holmen, *Catal. Today* **142**, 2–8 (2009).
9. L. Wang *et al*., *Catal. Lett.* **21**, 35–41 (1993).
10. L. Y. Chen, L. W. Lin, Z. S. Xu, X. S. Li, T. Zhang, *J. Catal.* **157**, 190–200 (1995).
11. F. Solymosi, A. Erdőhelyi, A. Szöke, *Catal. Lett.* **32**, 43–53 (1995).
12. J. Z. Zhang, M. A. Long, R. F. Howe, *Catal. Today* **44**, 293–300 (1998).
13. Y. Xu, X. Bao, L. Lin, *J. Catal.* **216**, 386–395 (2003).
14. Z. R. Ismagilov, E. V. Matus, L. T. Tsikoza, *Energy Environ. Sci* **1**, 526–541 (2008).
15. T. V. Choudhary, E. Aksoylu, D. W. Goodman, *Catal. Rev. Sci. Eng.* **45**, 151–203 (2003).
16. J. J. Spivey, G. Hutchings, *Chem. Soc. Rev.* **43**, 792–803 (2014).
17. Supplementary materials are available on *Science* Online.
18. H. Tian, C. A. Roberts, I. E. Wachs, *J. Phys. Chem. C* **114**, 14110–14120 (2010).
19. E. L. Lee, I. E. Wachs, *J. Phys. Chem. C* **111**, 14410–14425 (2007).
20. E. L. Lee, I. E. Wachs, *J. Phys. Chem. C* **112**, 20418–20428 (2008).
21. S. Sklenak *et al*., *Phys. Chem. Chem. Phys.* **11**, 1237–1247 (2009).
22. J. Dědeček, Z. Sobalík, B. Wichterlová, *Catal. Rev. Sci. Eng.* **54**, 135–223 (2012).
23. J.-P. Tessonnier *et al*., *J. Phys. Chem. B* **110**, 10390–10395 (2006).
24. P. Hoffmann, J. A. Lobo, *Microporous Mesoporous Mater.* **106**, 122–128 (2007).
25. H. S. Lacheen, E. Iglesia, *J. Catal.* **230**, 173–185 (2005).
26. H. Aritani, H. Shibasaki, H. Orihara, A. Nakahira, *J. Environ. Sci. (China)* **21**, 736–740 (2009).
27. S. Liu, L. Wang, R. Ohnishi, M. Ichikawa, *J. Catal.* **181**, 175–188 (1999).
28. H. Zheng *et al*., *J. Am. Chem. Soc.* **130**, 3722–3723 (2008).
29. J. Gao *et al*., *J. Phys. Chem. C* **118**, 4670–4679 (2014).
30. J. P. Tessonnier, B. Louis, S. Rigolet, M. J. Ledoux, C. Pham-Huu, *Appl. Catal. A* **336**, 79–88 (2008).

ACKNOWLEDGMENTS

The work in S.G.P.'s group at Stevens Institute of Technology was supported by the NSF under grant CBET-1133987. The work in I.E.W.'s group at Lehigh University was supported by the NSF under grant CBET-1134012. The Materials Studio software was used under a collaborative research license from BIOVIA Corp. in San Diego, California. Author contributions: J.G. and Y.Z. obtained the computational and reaction-testing results and discussed the overall results; J.-M.J. and Y.T. obtained the experimental spectroscopic data and discussed the overall results; I.E.W. conceived and supervised the spectroscopic experiments and interpreted the results; and S.G.P. conceived and supervised the calculations and reaction testing, interpreted the results, and prepared the initial manuscript.

SUPPLEMENTARY MATERIALS

www.sciencemag.org/content/348/6235/686/suppl/DC1
Materials and Methods
Figs. S1 to S12
Tables S1 to S6
References
Movie S1

16 January 2015; accepted 26 March 2015
Published online 9 April 2015;
10.1126/science.aaa7048

INORGANIC CHEMISTRY

A synthetic Mn_4Ca-cluster mimicking the oxygen-evolving center of photosynthesis

Chunxi Zhang,[1]* Changhui Chen,[2] Hongxing Dong,[2]* Jian-Ren Shen,[3] Holger Dau,[4]* Jingquan Zhao[1]

Photosynthetic splitting of water into oxygen by plants, algae, and cyanobacteria is catalyzed by the oxygen-evolving center (OEC). Synthetic mimics of the OEC, which is composed of an asymmetric manganese-calcium-oxygen cluster bound to protein groups, may promote insight into the structural and chemical determinants of biological water oxidation and lead to development of superior catalysts for artificial photosynthesis. We synthesized a Mn_4Ca-cluster similar to the native OEC in both the metal-oxygen core and the binding protein groups. Like the native OEC, the synthetic cluster can undergo four redox transitions and shows two magnetic resonance signals assignable to redox and structural isomerism. Comparison with previously synthesized Mn_3CaO_4-cubane clusters suggests that the fourth Mn ion determines redox potentials and magnetic properties of the native OEC.

The oxygen-evolving center (OEC) in photosystem II (PSII) of plants, algae, and cyanobacteria facilitates splitting of water into O_2, protons, and electrons (*1*–*4*). Crystallographic structures (*5*–*8*) reveal that the core of the OEC consists of a Mn_3CaO_4 cubane motif and a "dangler" Mn linked via two bridging oxides, forming a distinct asymmetric Mn_4Ca-cluster (Fig. 1A). This cluster is coordinated to four water molecules, one imidazole, and six carboxylate groups of the amino acid residues of the PSII polypeptides (Fig. 1C). The structure of the OEC as well as the oxidation states of the four manganese ions undergo changes during the water-oxidation reaction cycle, or S-state cycle (*4*, *9*, *10*). Spectroscopic results and computational chemistry have provided insight in reaction intermediates and mechanisms (*4*, *9*–*16*). The lability of

the protein-bound OEC prevents electrochemical characterization and controlled modification of its structure and constituents. Only molecular mimics can facilitate direct measurement and major chemical variation of redox potentials or proton binding energies (pK_a values); alternative mechanistic pathways can be explored, and spectroscopic signatures of the native OEC and computational approaches can be "calibrated."

Numerous multi-manganese complexes have been synthesized as possible mimics of the OEC (*17*–*22*), some of which contained a Mn_3CaO_4 cluster resembling closely the cubane part of the native OEC (*19*–*21*). Investigation of chemical variants proved useful for unravelling determinants of Mn oxidation potentials. Replacement of the calcium of the Mn_3CaO_4 cubane increased the redox potential of the $Mn^{IV}{}_3/Mn^{IV}{}_2Mn^{III}$ couple by more than 1 V ($Ca^{2+} \approx Sr^{2+} < Zn^{2+} < Y^{3+} < Sc^{3+} < Mn^{3+}$) (*22*). Calcium (*20*) or silver ions (*21*) were incorporated in the Mn4 dangling position, but mimicking the natural paragon by proper coordination of a fourth Mn ion was never attained.

We synthesized complex **I**, $[Mn_4CaO_4(Bu^tCO_2)_8(Bu^tCO_2H)_2(py)]$ (Bu^t, tert-butyl; py, pyridine), at a high yield (~50%) and starting from inexpensive commercial chemicals. Briefly, a precursor of **I** was synthesized by a reaction of $Bu^n{}_4NMnO_4$ (Bu^n, n-butyl), $Mn(CH_3CO_2)_2{\cdot}(H_2O)_4$, and $Ca(CH_3CO_2)_2{\cdot}H_2O$ (molar ratio of 4: 1: 1) in boiling acetonitrile in the presence of an excess of pivalic acid. Complex **I** was obtained after recrystallization of the precursor in the presence of 2% pyridine in ethyl acetate (Fig. 1E). Crystallographic characterization (Fig. 1, B and D) reveals one Mn_3CaO_4 cubane linked to a dangler Mn via O5, which is bridging between four metal ions (thus denoted as μ_4-O). This is in line with the influential first OEC model deduced from crystallographic data at 3.5 Å resolution (*6*) and related mechanistic proposals (*23*). The asymmetric Mn_4CaO_4-cluster of **I** is similar to the native OEC regarding both structure of the Mn_4Ca-oxo core and the ligating carboxylate groups (table S5). The integration of the Ca ion into the Mn_3CaO_4 cubane as well as its anchoring by three carboxylates bridging to Mn1, Mn2, and Mn4 is identical, as is a Mn-carboxylate chain topology (Mn1–OCO–Mn2–OCO–Mn3–OCO–Mn4). In the synthetic complex, all metal ions that are pairwise connected by a bridging oxygen are also connected by a bridging carboxylate. The same design principle applies to the biological complex, with the notable exception of the Mn1–Mn4 connectivity. There are further differences: The μ_2-O4 atom of the native OEC is replaced by a bridging carboxylate group, and the terminally coordinated water molecules are replaced by more complex groups.

[1]Laboratory of Photochemistry, Institute of Chemistry, Chinese Academy of Sciences, Beijing, 100190, China. [2]College of Materials Science and Chemical Engineering, Harbin Engineering University, Harbin 150001, China. [3]Photosynthesis Research Center, Graduate School of Natural Science and Technology, Okayama University, Okayama 700-8530, Japan. [4]Department of Physics, Free University Berlin, Arnimallee 14, 14195 Berlin, Germany.
***Corresponding author. E-mail: chunxizhang@iccas.ac.cn (C.Z.); dhongxing@hrbeu.edu.cn (H.D.); holger.dau@fu-berlin.de (H.D.)**

Bond-valence sum (BVS) analysis of **I** suggests oxidation states of $Mn1^{3+}$, $Mn2^{4+}$, $Mn3^{4+}$, and $Mn4^{3+}$ (Fig. 1B and table S2), in complete analogy to the OEC in its S_1 state (Fig. 1A) (*8*, *10*). The Mn–Mn distances of ~2.75 Å (table S3) match x-ray absorption fine-structure (XAFS) (*4*, *10*) and recent x-ray free electron laser (XFEL) (*8*) results on the S_1-state OEC. Because of its close structural similarity, our synthetic model supports that the generally shorter interatomic distances found in the recent XFEL study (*8*) [shorter than in (*7*)] are chemically reasonable for a $CaMn^{III}{}_2Mn^{IV}{}_2O_{21}N_1$ complex (21 first-sphere O-ligands in the native OEC, including O-Glu_{189}, versus 22 in **I**).

One informative difference between **I** and the native OEC is the coordination of O5, the μ_4-O atom bridging between three Mn and a single Ca ion, likely playing a decisive role in photosynthetic water oxidation (*7*, *8*, *12*, *14*, *15*, *24*, *25*). The Mn3/4–O5 bond lengths (1.85/1.85 Å) are shorter in **I** than in the native OEC (2.2/2.3 Å). Even more remarkable, in the native OEC the Mn1–O5 distance is so long (2.7 Å) that Mn1 becomes effectively five-coordinated, with an open coordination site that may be essential for coordination of a "substrate" water molecule upon oxidation of Mn4 from the +3 to the +4 state (*8*, *14*, *15*). Comparison of **I** and the OEC clarifies the origin of this prominent structural difference: In the synthetic complex, Mn1 and Mn4 are clamped together by a single bridging carboxylate, whereas in the OEC, they are spaced by ligation of two neighboring protein residues, His^{332} and Glu^{333}, to Mn1, Mn3 and Mn4. Only the His^{332}-Glu^{333} dyad breaks the rule that each pair of μ-oxo–bridged metal ions also is μ-carboxylato–bridged. We therefore propose that in the protein, the absence of μ-carboxylato–bridging between Mn1 and Mn4, possibly supported by a spacing effect of the His^{332}-Glu^{333} dyad, allows for formation of the functionally crucial open coordination site at the Mn1 ion.

The cyclic voltammogram (CV) of **I** dissolved in 1,2-dichloroethane (Fig. 2) shows that five redox states are accessible. Thus, the synthetic

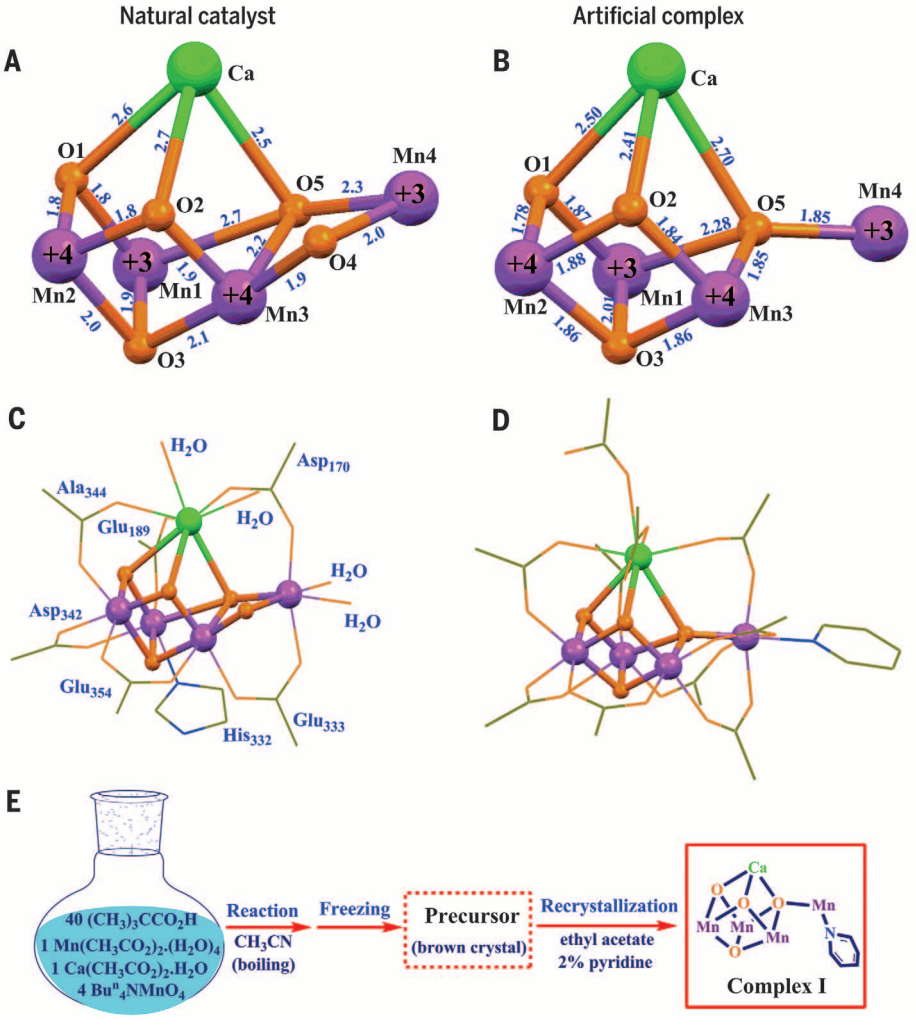

Fig. 1. Crystal structures of the native OEC and the synthetic Mn_4Ca complex I. (**A**) Mn_4CaO_5 core of the native OEC (*8*). (**B**) Mn_4CaO_4 core of **I**. (**C**) Structure of the native OEC, including ligating protein side-chains and water molecules. (**D**) Structure of **I**, including all ligand groups. (**E**) Synthesis of **I**. Distances are given in angstroms; Mn, Ca, O, N, and C are shown in purple, green, orange, blue, and yellow, respectively. For clarity, all H atoms and pivalic CH_3 groups are omitted.

complex can accumulate oxidation equivalents in close analogy to the native OEC (*4*, *9*, *10*). Although the native OEC is embedded in a protein environment that is closely mimicked in complex **I**, there are also water molecules close to the native metal-oxo core, which might render direct comparison of redox potentials problematic. Yet, the voltammograms of **I** in 1,2-dichloroethane and acetonitrile are similar (fig. S8), suggesting that the redox potentials do not depend strongly on solvent polarity. Addition of trace amounts of water (≤ 1%) to **I** in acetonitrile could modify the complex through ligand exchange (fig. S12) and results in obscured CV oxidation and reduction waves, possibly relating to a superimposed catalytic wave (figs. S9 and S10).

The as-synthesized complex is in the S_1-state. The $S_1 \rightarrow S_2$ transition of **I** is detected at a redox potential [~0.8 V versus normal hydrogen electrode (NHE)], which is close to the estimated potential of the corresponding OEC redox transition (≥ 0.9 V) (*3*, *26*) but is remarkably different from that of the previously Mn_3CaO_4 complex without a dangling Mn ion, indicating that the fourth Mn ion could play a crucial role in tuning the redox potential of the Mn_4Ca-cluster (*19*–*21*). Before and after dissolution in organic solvent, complex **I** exhibits a broad parallel-mode electron paramagnetic resonance (EPR) signal (fig. S3), which resembles the *g* value and width of the S_1-state signal of the native OEC.

To trap the S_2 state of **I**, we used $[Fe(phen)_3](PF_6)_3$ (phen, 1,10-phenanthroline) as a chemical oxidant with a redox potential of +1.1 V versus NHE. Two S_2-state signals are observed in the perpendicular-mode EPR spectrum (Fig. 3): (i) a multiline EPR signal centered at *g* value of 2.0, with a width of ~1600 G and more than 20 hyperfine peaks, and (ii) a signal centered at a *g* value greater than 4, with a width of ~500 G and without resolved hyperfine structure. The two EPR signals observed are similar to the well-known $g = 2.0$ and $g \geq 4.1$ EPR signals, both observed in the S_2-state of the native OEC (*9*, *27*, *28*). Both EPR signals of **I** exhibit a linear Curie-plot behavior (fig. S6), suggesting that both are ground-state signals, in full analogy to the native OEC, in which the two EPR signals and their respective spin states ($g = 2$ signal, $S = 1/2$; $g = 4.1/4.9$ signals, $S \geq 3/2$) have been proposed to arise from two OEC conformers differing in the localization of the Mn^{3+} ion in the S_2-state ($Mn1^{3+}Mn4^{4+}$ versus $Mn1^{4+}Mn4^{3+}$) (*28*).

The possibility of structural conformers potentially affecting the exchange coupling between Mn ions is suggested by subtle structural difference between the two monomers resolved in the crystallographic unit cell of **I**. Specifically, the nonidentical Mn1-Mn4 and Ca-O5 distances (table S4) may be of relevance. These differences were determined for the crystallographically characterized S_1-state cluster. At present, it is still open whether and how these differences are amplified for the dissolved complex or through Mn oxidation in the $S_1 \rightarrow S_2$ transition. A similarly close analogy of the magnetic properties has never been observed for cubane-type Mn_3CaO_4 complexes

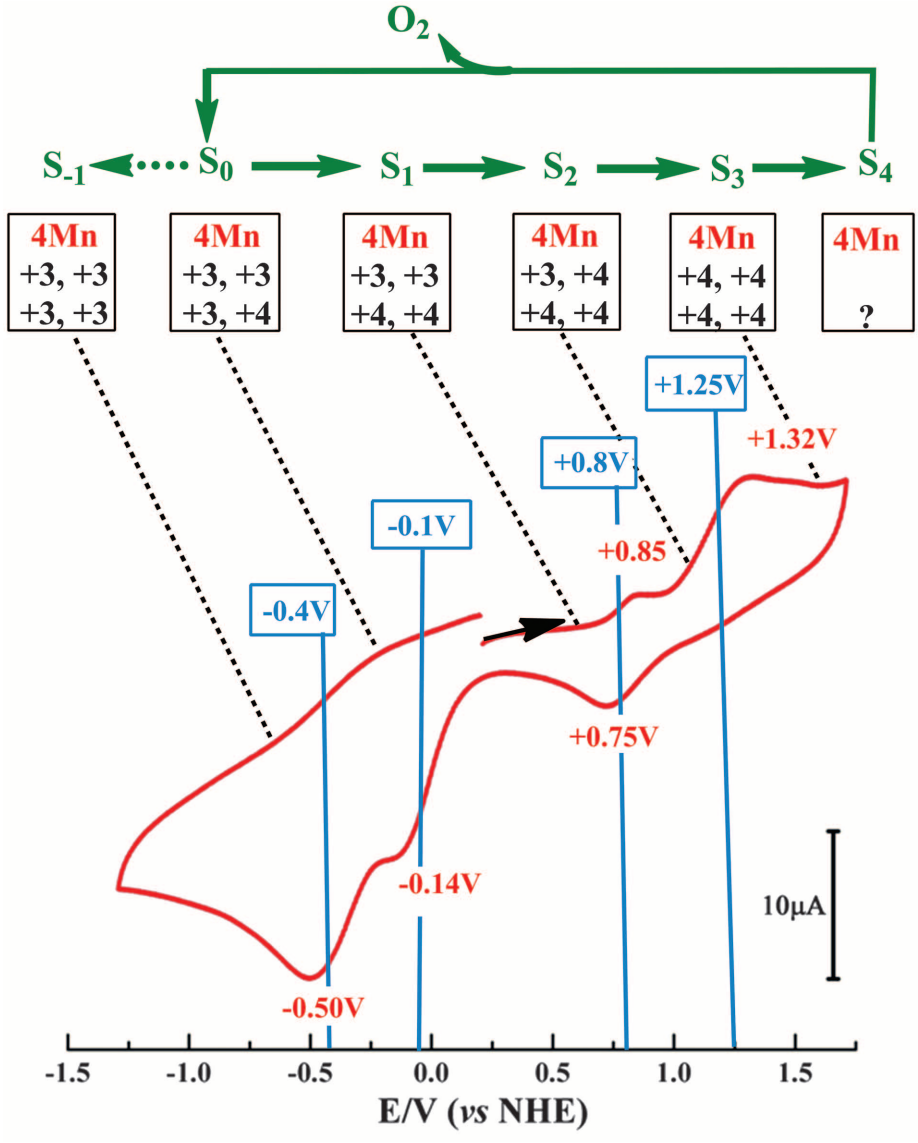

Fig. 2. S-state cycle of the native OEC and CV of I. Potentials versus NHE; scan rate of 100 mV/s. Native OEC is in green, peak positions of CV waves are in red, and estimated midpoint potentials are in blue. The likely oxidation states of the four Mn ions in various S-states of the native OEC and plausible oxidation states of **I** are indicated with black numbers. A CV of **I** in acetonitrile and further details are provided in fig. S8.

(*19*–*21*) nor for any other multinuclear Mn complex. The observation of a low-spin multiline signal in **I** contrasts the high-spin state of Mn_3CaO_4 cubane complexes (*20*, *29*), supporting that the fourth Mn ion is crucial regarding the magnetic properties of the heterobimetallic complexes. Complex **I** and future variants could become valuable model systems in experimental and theoretical investigations aiming at insight in the magnetic properties of the biological complex, in which the spin localization has been suggested to be of relevance in the O-O bond formation chemistry (*14*).

Each of the four redox transition of **I** increases the potential for the subsequent oxidation step—for example, from 0.8 V ($S_1 \rightarrow S_2$) to 1.25 V ($S_2 \rightarrow S_3$) (Fig. 2). In the native OEC, the $S_1 \rightarrow S_2$ transition is not coupled to a charge-compensating proton release (*11*), and its redox potential increases (*10*) to an unknown level. On the basis of the general similarity of the $S_1 \rightarrow S_2$ transition in **I** and the native OEC, we propose that in both, a potential increase of similar magnitude may occur. This potential increase in the $S_1 \rightarrow S_2$ transition can explain why in PSII, a charge-compensating and redox-potential–lowering deprotonation of the OEC—likely coupled to further chemical changes—precedes Mn oxidation in the $S_2 \rightarrow S_3$ (*13*) and $S_3 \rightarrow S_4$ transition (*30*). In the native OEC, redox leveling through deprotonation reduces the overpotential need for accumulation of oxidizing equivalents (*1*, *10*). In the absence of efficient redox leveling, the overpotential need would be prohibitively high, as shown by the behavior of **I** in organic solvents (Fig. 2 and fig. S8).

Although **I** is similar in many ways to native OEC, it still deviates in several functionally crucial aspects, including the water-binding sites at Mn4 and the Ca ion. We consider the synthesis of **I** as a first step for synthesis of further variants that mimic native OEC even closer. The synthetic flexibility is illustrated by related complexes **II** and **III** (Fig. 4), which have terminal ligands at the Ca ion or at Mn4 that are exchanged by alternative neutral ligands. In the native OEC, these terminal ligand sites are occupied by water molecules. The binding sites of the readily exchangeable neutral ligands on Ca and the dangler Mn in the described synthetic complexes may serve as potential positions to create water binding sites that resemble closely the respective sites of the native OEC. Last, the complexes described here can serve as references for calculation of vibrational spectra (fig. S13) and absolute OEC redox potentials; the latter is pressingly needed for verification of computational models (*12*, *14*).

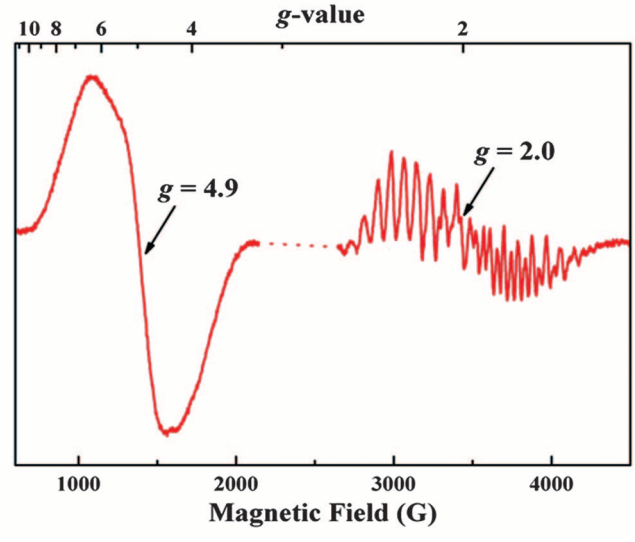

Fig. 3. EPR spectrum of I in its $Mn^{IV}_3Mn^{III}$ state (S_2-state) at 7K. The broad multiline signal (>20 lines) centered close to $g = 2$ as well as EPR signals at higher g values ($g > 4$) are assignable to the Mn complex in different spin states. For clarity, the signal at $g = \sim 3$ range from $[Fe(phen)_3]^{3+}$ (figs. S4 and S7) was replaced with a dashed line.

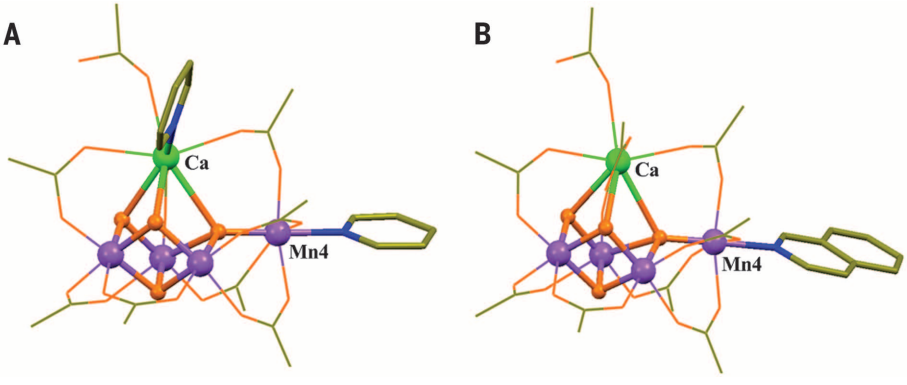

Fig. 4. Structures of complexes with exchanged terminal ligands. The complexes differ from **I** by ligand exchange either on (**A**) Ca (**II**) or (**B**) Mn4 (**III**).

REFERENCES AND NOTES

1. J. P. McEvoy, G. W. Brudvig, *Chem. Rev.* **106**, 4455–4483 (2006).
2. J. Barber, *Chem. Soc. Rev.* **38**, 185–196 (2009).
3. H. Dau, I. Zaharieva, *Acc. Chem. Res.* **42**, 1861–1870 (2009).
4. J. Yano, V. Yachandra, *Chem. Rev.* **114**, 4175–4205 (2014).
5. A. Zouni *et al.*, *Nature* **409**, 739–743 (2001).
6. K. N. Ferreira, T. M. Iverson, K. Maghlaoui, J. Barber, S. Iwata, *Science* **303**, 1831–1838 (2004).
7. Y. Umena, K. Kawakami, J. R. Shen, N. Kamiya, *Nature* **473**, 55–60 (2011).
8. M. Suga *et al.*, *Nature* **517**, 99–103 (2015).
9. J. M. Peloquin, R. D. Britt, *Biochim. Biophys. Acta* **1503**, 96–111 (2001).
10. H. Dau, M. Haumann, *Coord. Chem. Rev.* **252**, 273–295 (2008).
11. W. Junge, M. Haumann, R. Ahlbrink, A. Mulkidjanian, J. Clausen, *Phil. Trans. R. Soc. Lond. B.* **357**, 1407–1418 (2002).
12. H. Isobe *et al.*, *Dalton Trans.* **41**, 13727–13740 (2012).
13. A. Klauss, M. Haumann, H. Dau, *Proc. Natl. Acad. Sci. U.S.A.* **109**, 16035–16040 (2012).
14. P. E. M. Siegbahn, *Biochim. Biophys. Acta* **1827**, 1003–1019 (2013).
15. N. Cox *et al.*, *Science* **345**, 804–808 (2014).
16. H. Nilsson, F. Rappaport, A. Boussac, J. Messinger, *Nat. Commun.* **5**, 4305 (2014).
17. C. S. Mullins, V. L. Pecoraro, *Coord. Chem. Rev.* **252**, 416–443 (2008).
18. G. C. Dismukes *et al.*, *Acc. Chem. Res.* **42**, 1935–1943 (2009).
19. J. S. Kanady, E. Y. Tsui, M. W. Day, T. Agapie, *Science* **333**, 733–736 (2011).
20. S. Mukherjee *et al.*, *Proc. Natl. Acad. Sci. U.S.A.* **109**, 2257–2262 (2012).
21. J. S. Kanady *et al.*, *J. Am. Chem. Soc.* **136**, 14373–14376 (2014).
22. E. Y. Tsui, T. Agapie, *Proc. Natl. Acad. Sci. U.S.A.* **110**, 10084–10088 (2013).
23. E. M. Sproviero, J. A. Gascón, J. P. McEvoy, G. W. Brudvig, V. S. Batista, *J. Am. Chem. Soc.* **130**, 3428–3442 (2008).
24. L. Rapatskiy *et al.*, *J. Am. Chem. Soc.* **134**, 16619–16634 (2012).
25. M. Pérez Navarro *et al.*, *Proc. Natl. Acad. Sci. U.S.A.* **110**, 15561–15566 (2013).
26. I. Vass, S. Styring, *Biochemistry* **30**, 830–839 (1991).
27. A. Boussac, A. W. Rutherford, *Biochim. Biophys. Acta* **1457**, 145–156 (2000).
28. D. A. Pantazis, W. Ames, N. Cox, W. Lubitz, F. Neese, *Angew. Chem. Int. Ed.* **51**, 9935–9940 (2012).
29. V. Krewald, F. Neese, D. A. Pantazis, *J. Am. Chem. Soc.* **135**, 5726–5739 (2013).
30. M. Haumann *et al.*, *Science* **310**, 1019–1021 (2005).

ACKNOWLEDGMENTS

This work was supported by the National Natural Science Foundation of China (nos. 20973186, 31070216, 21076049, and 91427303), Chinese Academy of Sciences (KJCX2-YW-W25), Japan Society for the Promotion of Science (no. 24000018/Shen), and by the Deutsche Forschungsgemeinschaft (CRC 1078, A4/Dau). We thank A. Zouni and W. Junge for their suggestions. Crystallographic data have been deposited at the Cambridge Crystallographic Database Centre, and the deposition numbers are 1042697(**I**), 1042515 (**II**), and 1042514 (**III**).

SUPPLEMENTARY MATERIALS

www.sciencemag.org/content/348/6235/690/suppl/DC1
Materials and Methods
Figs. S1 to S13
Tables S1 to S8
References (*31*–*35*)

9 January 2015; accepted 2 April 2015
10.1126/science.aaa6550

VACCINES

Long-term measles-induced immunomodulation increases overall childhood infectious disease mortality

Michael J. Mina,[1,2]* C. Jessica E. Metcalf,[1,3] Rik L. de Swart,[4] A. D. M. E. Osterhaus,[4] Bryan T. Grenfell[1,3]

Immunosuppression after measles is known to predispose people to opportunistic infections for a period of several weeks to months. Using population-level data, we show that measles has a more prolonged effect on host resistance, extending over 2 to 3 years. We find that nonmeasles infectious disease mortality in high-income countries is tightly coupled to measles incidence at this lag, in both the pre- and post-vaccine eras. We conclude that long-term immunologic sequelae of measles drive interannual fluctuations in nonmeasles deaths. This is consistent with recent experimental work that attributes the immunosuppressive effects of measles to depletion of B and T lymphocytes. Our data provide an explanation for the long-term benefits of measles vaccination in preventing all-cause infectious disease. By preventing measles-associated immune memory loss, vaccination protects polymicrobial herd immunity.

Measles vaccines were introduced 50 years ago and were followed by striking reductions in child morbidity and mortality (*1*, *2*). Measles control is now recognized as one of the most successful public health interventions ever undertaken (*3*). Despite this, in many countries vaccination targets remain unmet, and measles continues to take hundreds of thousands of lives each year (*3*). Even where control has been successful, vaccine hesitancy threatens the gains that have been made (*1*, *4*). The introduction of mass measles vaccination has reduced childhood mortality by 30 to 50% in resource-poor countries (*5*–*8*) and by up to 90% in the most impoverished populations (*9*, *10*). The observed benefits cannot be explained by the prevention of primary measles virus (MV) infections alone (*11*, *12*), and they remain a central mystery (*13*).

MV infection is typified by a profound, but generally assumed to be transient, immunosuppression that renders hosts more susceptible to other pathogens (*14*–*17*). Thus, contemporaneous reductions in nonmeasles mortality after vaccination are expected. However, reductions in infectious disease mortality after measles vaccination can last throughout the first 5 years of life (*5*–*10*), which is much longer than anticipated by transient immunosuppression, which is generally considered to last for weeks to months (*16*, *17*).

Proposed mechanisms for a nonspecific beneficial effect of measles vaccination range from suggestions that live vaccines may directly stimulate cross-reactive T cell responses or that they may train innate immunity to take on memory-like phenotypes (*13*, *18*–*21*). Although well described by Aaby (*11*, *12*) and others (*22*) in observational studies, primarily in low-resource settings, these effects may not fully explain the long-term benefits observed with measles vaccination and cannot explain the pre-vaccination associations of measles and infectious disease mortality we describe below. The World Health Organization (WHO) recently addressed this issue (*22*) and concluded that measles vaccination is associated with large reductions in all-cause childhood mortality but that there is no firm evidence to explain an immunological mechanism for the nonspecific vaccine benefits.

Recent work (*17*, *23*) invoked a different hypothesis that a loss of immune memory cells after MV infection resets previously acquired immunity, and vaccination prevents this effect. de Vries *et al.* (*17*) reproduced transient measles immune suppression in macaques, characterized by systemic depletion of lymphocytes and reduced innate immune cell proliferation (*24*). Although peripheral blood lymphocyte counts were restored within weeks as expected (*25*), the authors hypothesized that rapid expansions of predominantly measles-specific B and T lymphocytes masked an ablated memory-cell population (*17*). In other words, MV infection replaced the previous memory cell repertoire with MV-specific lymphocytes, resulting in "immune amnesia" (*17*) to nonmeasles pathogens. Previous investigations of virus-induced memory-cell depletion suggest that recovery requires restimulation, either directly or via cross-reactive antigens (*26*–*29*).

We propose that, if loss of acquired immunological memory after measles exists, the resulting impaired host resistance should be detectable in the epidemiological data collected during periods when measles was common and [in contrast to previous investigations that focus on low-resource settings (*5*–*12*)] should be apparent in high-resource settings where mortality from opportunistic infections during acute measles immune suppression was low. Relatively few countries report the necessary parallel measles and mortality time series to test this hypothesis. National-level data from England, Wales, the United States, and Denmark [Fig. 1, A to C; see supplementary materials (SM) 1 for details], spanning the decades surrounding the introduction of mass measles vaccination campaigns, meet our data criteria.

To assess the underlying immunological hypothesis (Fig. 1D) using population-level data, we required that first, nonmeasles mortality should be correlated with measles incidence data, especially because the onset of vaccination reduces the latter. Second, an immune memory loss mechanism should present as a strengthening of this association when measles incidence data are transformed to reflect an accumulation of previous measles cases (a measles "shadow"). For example, if immune memory loss (or more broadly, immunomodulation) lasts 3 years, the total number of immunomodulated individuals (S) in the nth quarter can be calculated as the sum of the measles cases (M) over the previous (and current) 12 quarters: $S_n = M_{n-11} + M_{n-10} + \ldots + M_{n-1} + M_n$. In practice, we weighted the quarters using a gamma function. Dividing S by the total population of interest thus provides the prevalence of immunomodulation (see SM 2, and 3; fig. S1, A to C; and movie S1 for detailed methods). Third, the strength of this association should be greatest when the mean duration over which the cases are accumulated matches the mean duration required to restore immunological memory after MV infection. Fourth, the estimated duration should be consistent both with the available evidence of increased risk of mortality after MV, compared with uninfected children, and with the time required to build a protective immune repertoire in early life (Fig. 1D, fig. S2, and SM 5 and 6).

To explicitly address whether the observed nonspecific benefits of vaccination can be attributed to the prevention of MV immunomodulation, evidence for the four hypotheses must be present separately within the pre-vaccine eras.

Reductions in nonmeasles infectious disease mortality (SM 1) are shown in Fig. 1, for children aged 1 to 9 years in Europe and aged 1 to 14 years in the United States, shortly after the onset of mass vaccination in each country. The fall in mortality was later in Denmark, corresponding to the introduction of measles vaccination in the 1980s, as compared to the late 1960s for the United Kingdom and United States. In all locations, measles incidence showed significant ($P < 0.001$) associations with mortality (Fig. 1, E to G). However, effect sizes varied (fig. S3A), reflecting low reporting in the United States [fig. S3B and (*30*)] and changes in health care practice between eras. Adjusting for year as a covariate (SM 4) had little effect on the point estimates (fig. S3C). These associations could reflect transient measles immune suppression. Thus, to address our second hypothesis that MV immunomodulation can explain

[1]Department of Ecology and Evolutionary Biology, Princeton University, Princeton, NJ, USA. [2]Medical Scientist Training Program, School of Medicine, Emory University, Atlanta, GA, USA. [3]Fogarty International Center, National Institutes of Health, Bethesda, MD, USA. [4]Department of Viroscience, Erasmus University Medical Center, Rotterdam, Netherlands.
*Corresponding author. E-mail: michael.j.mina@gmail.com

long-term increased mortality and, consequently, improved survival after vaccination, we transformed measles incidence into population prevalence of MV immunomodulation, with the duration of the immunomodulation (the time required to rebuild sufficiently protective immune memory) defined by a gamma distribution to weight the previous time points summed together, as discussed above and in SM 2 and movie S1.

When the gamma-distributed transformation was applied to the England and Wales measles data, the best-fit duration of MV immunomodulation, as determined by the linear fit of the corresponding prevalence of MV immunomodulation to the mortality data (SM 3), centered at a 28.3-month duration of measles-induced immunomodulation. This corresponded to a strong and significantly improved association between measles and all-cause infectious disease mortality [coefficient of determination (R^2) = 0.92 versus 0.37; $P < 0.00001$; Fig. 2, A to C]. Simpler additive transformations (SM 2 and movie S1) return the same qualitative pattern (Fig. 2D), and adjusting for year in the model had no effect (fig. S4). Figure 2, E and F, shows the time series for the actual and predicted mortalities (calculated from the linear fits), together with the prevalence of

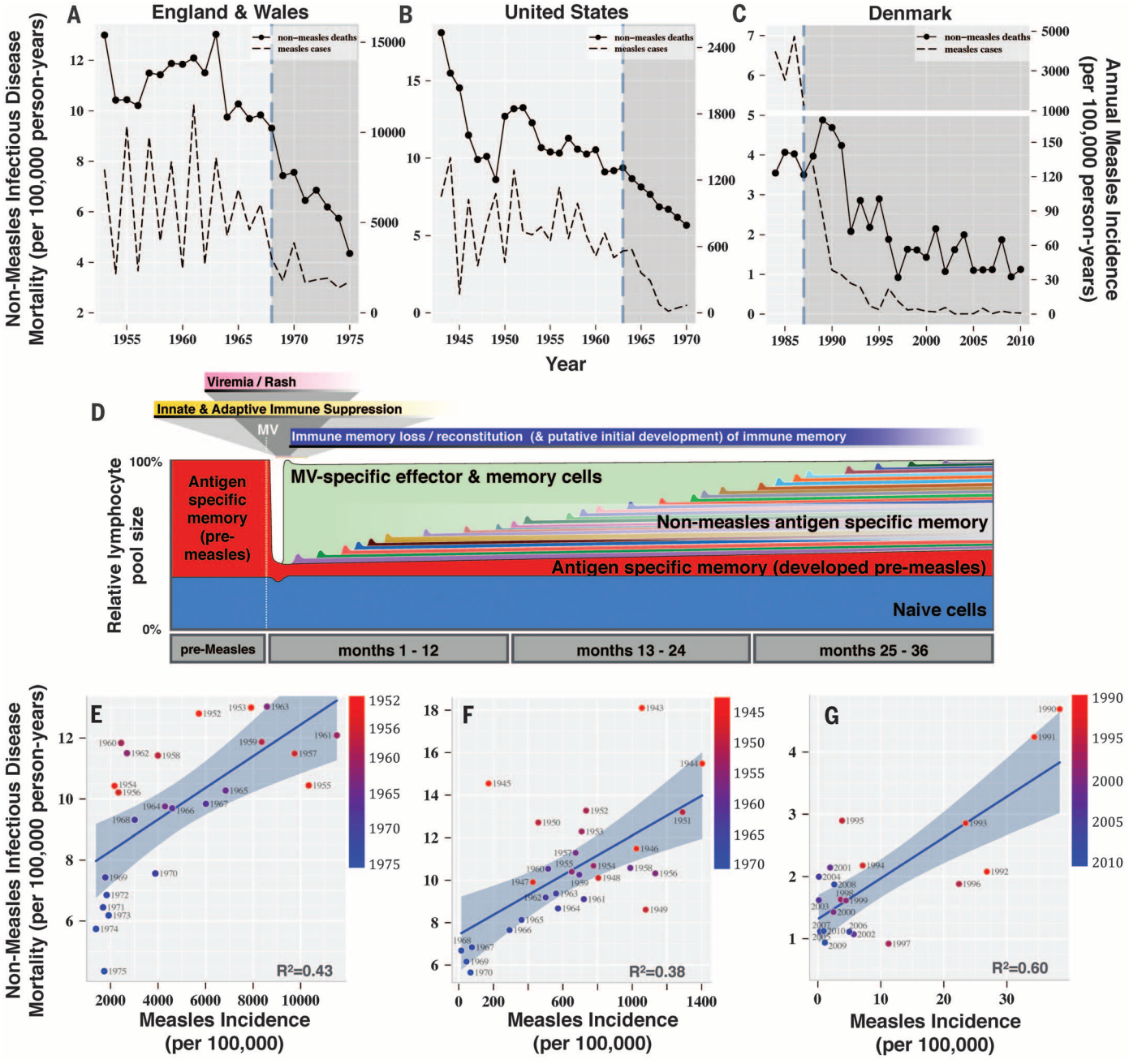

Fig. 1. Measles incidence, nonmeasles infectious disease mortality, and measles-induced immunomodulation. Nonmeasles infectious disease mortality and measles incidence time series (**A** to **C**) and regressions (**E** to **G**) are shown for England and Wales, the United States, and Denmark. The vertical dashed lines in (A) to (C) indicate the year of introduction of the measles vaccine. (**D**) Measles-induced lymphopenia and subsequent measles-specific lymphocyte expansion in the weeks after MV infection, as described in (*17*, *23*), are shown, and time is extended to depict hypothesized long-term immunomodulatory effects of MV infection and reconstitution of the immune response through individual exposures. Scatter plots and best-fit regression curves (plotted with 95% confidence bands) are shown for nonmeasles infectious disease mortality versus measles incidence for England and Wales (E), the United States (F), and Denmark (G).

MV immunomodulation (see movie S2 for the full paths of these transformations). Overall, a simple weighted integral of measles incidence captures the nonmeasles mortality data remarkably well and more closely than the raw incidence.

To evaluate our fourth hypothesis, we compared the best-fit gamma distribution (indicating average time to return of full immunity) to (i) the previously observed (*31*) duration of elevated relative risk (RR) of all-cause mortality after intensive measles exposure (albeit in children exposed before 6 months of age) and (ii) to the global age distribution (fig. S2) of bacterial invasive disease in children under 5 years of age [an estimate for the time required to build protective immunity (*32*)]. Both the elevated RR of mortality after measles exposure and declines from peak rates of bacterial disease, indicating the development of sufficiently protective immunity, fell precisely along the gamma curve (R^2 =0.97 and 0.99, respectively; Fig. 2G).

We tested these results for nonspecific effects of vaccination (*11*) by applying the same procedures to the pre-vaccination data alone. Before vaccination, the best-fit duration of MV immunomodulation was no different (centered at 28.0 versus 28.3 months; Fig. 2, B to D, and fig. S5A) and closely matched the duration identified in the post-vaccine era as well (29.2 months; fig. S5A). Moreover, the coefficients describing the slope of mortality rate versus prevalence of immunomodulation were nearly identical (Fig. 2, B and I, and fig. S5B). This effect held regardless of which era's respective best-fit gamma transform was used (fig. S5, B to D), because optimizing the transformation using only the pre-vaccine data permitted accurate prediction of the post-vaccine era data that was not used to fit the model (known as out-of-sample prediction). The results

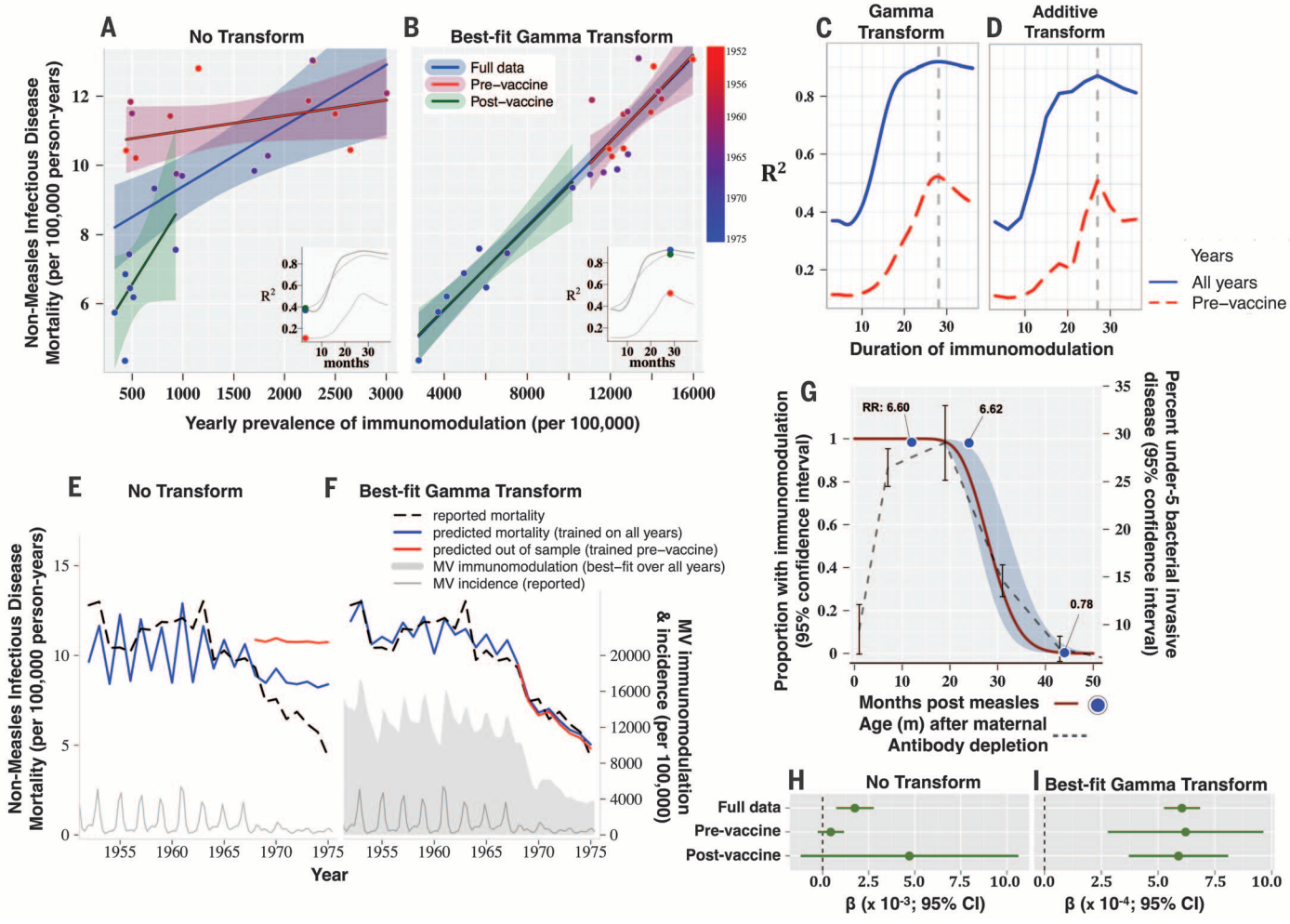

Fig. 2. England and Wales: Measles-induced immunomodulation and nonmeasles infectious disease mortality (1952–1975). Annual incidence of nonmeasles infectious disease mortality regressed against the prevalence of MV immunomodulation, given (**A**) no transform or (**B**) the best-fit gamma transform (that provides the best linear fit, R^2, to the data). Individual regression lines and 95% confidence intervals are plotted for regressions over the full data set (blue), the pre-vaccine era data only (green), and the post-vaccine era data only (red). R^2 is plotted against the mean duration of MV immunomodulation for the (**C**) gamma or (**D**) additive transformation for the full data set (blue lines) or the pre-vaccine data only (red lines). Inset graphs in (A) and (B) are the same as (C), and the location of the dots (color coded as per the regression lines) represent the duration of immunomodulation and the R^2 values associated with the scatter plot shown. In (**E** and **F**), the measured nonmeasles infectious disease mortality is plotted (broken line) along with the predicted annual mortalities (solid blue and red lines), predicted using the regression coefficients from the (**H**) untransformed or (**I**) best-fit transformed data. Predictions in (E) and (F) are either in sample and based on the full data set (blue line), or out of sample and based on the pre-vaccine data only (red line). In (F), for example, the in-sample mortality prediction is made from the regression coefficients (I) from the best-fit transformed data for the full data set (blue line), and mortality is also predicted entirely out of sample for the post-vaccine era by optimizing the gamma transformation and calculating regression coefficients using only data from the pre-vaccine era (red line; fig. S5C). (**G**) The best-fit gamma distribution (optimized against the full data set) is shown (dark red line), along with the distribution of under-5 bacterial invasive disease versus age after the depletion of maternal antibodies (broken gray line), and the relative risk of non-MV mortality after MV infection, described in (*31*), is also shown plotted against time since MV infection (blue points). (H) and (I) The regression coefficients for the best-fit lines shown in (A) and (B) are plotted with 95% confidence intervals in (H) and (I), respectively.

are robust to the chosen focal age groups (1 to 4 and 5 to 9 years old age groups shown in fig. S6) and are sensitive to the specific order and magnitude of the measles epidemics, because randomizing the time series by year erased the above effects (fig. S7).

Furthermore, results were robust to individual disease classes (table S1), with best-fit durations of immunomodulation predisposing to individual classes of infectious disease mortality lasting between 18 and 30 months (mean, 27 months; median, 24 months). Exceptions were rubella [although rubella was not included in the primary analysis (SM 1)] and septicemia, which had best-fit durations of immune memory loss of approximately 12 and 3 months, respectively.

Many previous investigations described stronger nonspecific benefits of MV vaccination in females than males (*7*, *11*, *13*); thus, as an additional test of our hypotheses, we also compared genders. In agreement, we found consistently stronger associations among females (fig. S8). To test the England and Wales findings, we applied the full analysis to data from the United States (Fig. 3 and movie S3). Here, the optimized gamma transformation centered at 30.9 months (versus 28.3 for the United Kingdom) again greatly improved the fit of the data (R^2 = 0.88 versus 0.42; Fig. 3, A to F), showed very strong agreement with previously observed durations of mortality risk after intensive measles exposure (R^2 = 0.999, Fig. 3G), and was predicted by the age distribution of invasive bacterial infections in children under 5 (R^2 = 0.921; Fig. 3G).

We tested whether declines in mortality after vaccination were caused by nonspecific benefits of vaccination. Transformation of the data from the pre-vaccine era increased the strength of the association markedly (R^2 = 0.87 versus 0.07). As in the United Kingdom, very similar best-fit gamma transformations were obtained before (and after) vaccination (centered at 30.3 and 29.2 months; Fig. 3C and fig. S9A); the coefficients of association (with mortality) across vaccine eras were again consistent (Fig. 3, B and I, and fig. S9); the results were robust across age groups (fig. S10); the strengths of association were stronger in females (fig. S11); and adjusting for year had no effect (fig. S12).

The data from Denmark (SM 1) were recorded at yearly rather than quarterly intervals and limited the scope of analyses. Furthermore, because measles vaccine introduction in Denmark in 1987 occurred as data became available and was so successful that within its first year, measles incidence was reduced by an order of magnitude (Fig. 1C), we were compelled to focus on the two decades that followed the logarithmic reduction of cases (1990–2010). Despite these limitations, transformation of the yearly data (using eqs. 3 and 8 in SM 2) led to steep peaks in model fit at 30 months duration of MV immunomodulation that predicted mortality (R^2 = 0.77; Fig. 4A). When we inferred quarterly incidence data from the annualized data [using monthly measles incidence data from a large population sample in Denmark (*33*) to estimate proportions of annual cases occurring each quarter; SM 1], the best fit indicated a 26.4-month duration of MV immunomodulation (Fig. 4, B and E), agreeing with the durations defined for England and Wales and the United States above, as well as the previously observed risk of mortality after measles (Fig. 4C).

These results provide population evidence for a generalized prolonged (roughly 2- to 3-year) impact of measles infection on subsequent mortality from other infectious diseases. Fluctuations

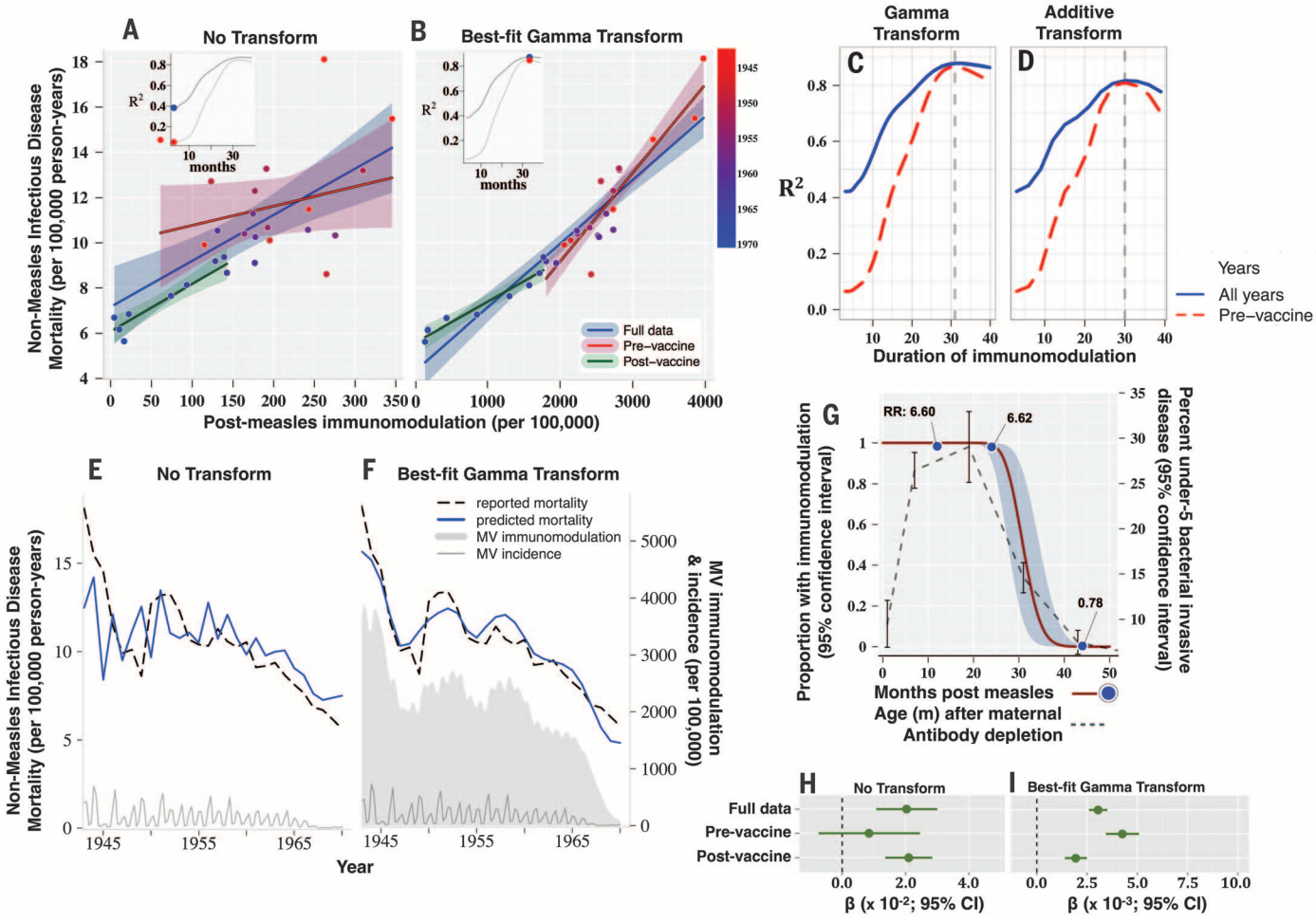

Fig. 3. USA: Measles-induced immunomodulation and nonmeasles infectious disease mortality (1943–1970). (**A** to **I**) Plots are as described for England and Wales in Fig. 2.

in childhood mortality in the United Kingdom, the United States, and Denmark are explained by a simple weighted integral that describes the prevalence of measles immune memory loss and thus captures the impact of measles infection and immune depletion. We anticipate that morbidity data might show stronger effects.

As a further test of the immunosuppressive impact of measles, we carried out a similar analysis on pertussis. Pertussis is a vaccine-preventable disease that is not known to be immunosuppressive and for which high-quality weekly data (*34*) are available for England and Wales that were collected during the pre–measles vaccine years described above. We found no correlation (fig. S13) between pertussis incidence and nonpertussis infectious disease mortality. No correlation was observed even when the pertussis data were transformed to reflect the sum of previous pertussis cases (a pertussis "shadow") extending over 48 months (fig. S13).

Our results show that when measles was common, MV infections could have been implicated in as many as half of all childhood deaths from infectious disease, thus accounting for nearly all of the interannual fluctuations in childhood infectious disease deaths. The reduction of MV infections was the main factor in reducing overall childhood infectious disease mortality after the introduction of vaccination.

Consistency in the best-fit duration of MV immunomodulation (the time required to restore protective immune memory) in all three countries, the close fit to observed durations of increased mortality after intensive MV exposure, and its correspondence to the early development of immunity (before 5 years of age) through exposure all provide strong evidence for a measles immune effect. The similarity in results obtained for both pre- and post-vaccine eras, the qualitative consistency across ages, and the stronger associations in females (*7*) provide further support for an underlying immunomodulatory mechanism. Finally, these results are consistent with multiple immuno-epidemiologic and case-controlled studies that show reduced or absent antigen-specific cellular responses lasting 3 years after measles (*35*, *36*) and reduced atopy even 15 years after infection (*37*).

The correspondence between our results and previous epidemiological data by Aaby *et al.* (*31*) should be viewed with the caveat that the increased relative risk of mortality after intensive measles exposure was measured in children exposed before 6 months of age, not all of whom developed features of clinical measles infections. Other studies (*12, 38, 39*) have failed to detect long-term immunologic sequelae of measles. These previous cohort studies have focused on low-income countries, primarily in West Africa, where very high rates of death from opportunistic infections during acute measles immune suppression drive mortality dynamics and mask the pernicious long-term immunological effects of measles infection. For example, approximately 50% of all childhood deaths recorded over 5 years of follow-up occurred within only 2 months of measles infection, precluding the detection of long-term sequelae in those children.

MV infection and vaccination produce strong and durable herd immunity against subsequent epidemics (*40*). Our results thus suggest an extra dynamical twist: MV infections could also reduce population immunity against other infections in which MV immunomodulation could be envisioned as a measles-induced immune amnesia (*17*); hence, measles vaccination might also be preserving herd protection against nonmeasles infections.

Measles vaccination is one of the most cost-effective interventions for global health, and our results imply further immunological dividends:

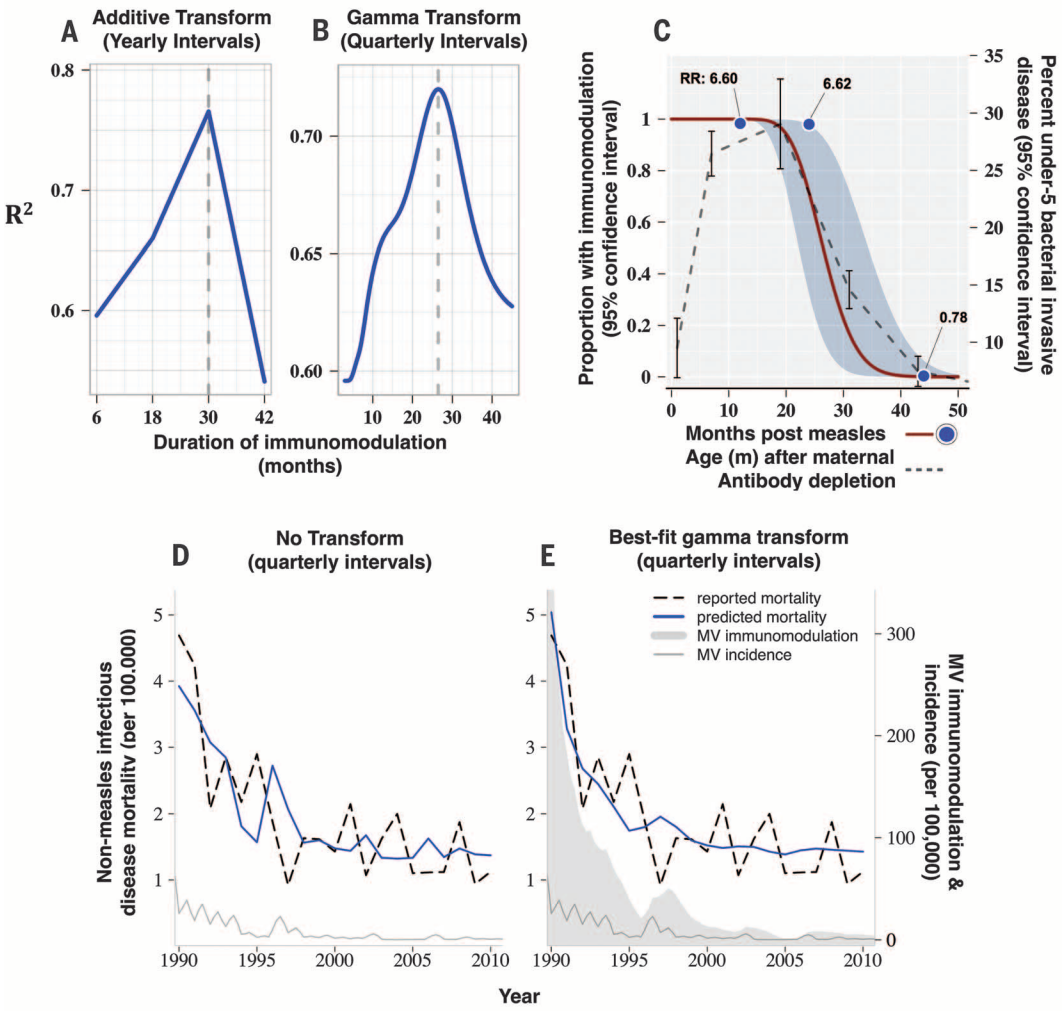

Fig. 4. Denmark: Measles-induced immunomodulation and non-MV infectious disease mortality (1990–2010). R^2 versus duration of measles-induced immunomodulation when measles data are transformed using (**A**) the additive transformation with yearly intervals or (**B**) the gamma transform with quarterly intervals, where yearly measles incidence was converted to quarterly incidence based on (*33*). The best-fit gamma transform (**C**), as well as the predicted nonmeasles mortality, predicted from the untransformed (**D**) or the best-fit gamma transform (**E**) MV immunomodulation data, are shown and are described for the respective figures in Figs. 2 and 3.

mortality (and probably morbidity) reductions linked to measles vaccination might be much greater than previously considered. This is of particular importance today where, especially in wealthy nations, reduced opportunistic infections during acute measles immunosuppression, added to the comparative rarity of infection, has led to a public view of measles as a benign childhood disease. Our findings help dispel the mystery surrounding the disproportionately large reductions in mortality seen after the introduction of measles vaccinations and reinforce the importance of measles vaccination in a global context.

REFERENCES AND NOTES

1. W. J. Moss, D. E. Griffin, *Lancet* **379**, 153–164 (2012).
2. E. Simons *et al.*, *Lancet* **379**, 2173–2178 (2012).
3. R. T. Perry *et al.*, *MMWR Morb. Mortal. Wkly. Rep.* **63**, 103–107 (2014).
4. S. B. Omer, D. A. Salmon, W. A. Orenstein, M. P. deHart, N. Halsey, *N. Engl. J. Med.* **360**, 1981–1988 (2009).
5. J. D. Clemens *et al.*, *Am. J. Epidemiol.* **128**, 1330–1339 (1988).
6. M. A. Koenig *et al.*, *Bull. World Health Organ.* **68**, 441–447 (1990).
7. A. Desgrées du Loû, G. Pison, P. Aaby, *Am. J. Epidemiol.* **142**, 643–652 (1995).
8. P. Aaby, J. Bukh, I. M. Lisse, A. J. Smits, *J. Infect.* **8**, 13–21 (1984).
9. E. A. Holt, R. Boulos, N. A. Halsey, L. M. Boulos, C. Boulos, *Pediatrics* **85**, 188–194 (1990).
10. Z. Kabir, J. Long, V. P. Reddaiah, J. Kevany, S. K. Kapoor, *Bull. World Health Organ.* **81**, 244–250 (2003).
11. P. Aaby, T. R. Kollmann, C. S. Benn, *Nat. Immunol.* **15**, 895–899 (2014).
12. P. Aaby *et al.*, *Int. J. Epidemiol.* **32**, 106–115 (2003).
13. K. L. Flanagan *et al.*, *Clin. Infect. Dis.* **57**, 283–289 (2013).
14. C. L. Karp *et al.*, *Science* **273**, 228–231 (1996).
15. B. Hahm, *Curr. Top. Microbiol. Immunol.* **330**, 271–287 (2009).
16. S. Schneider-Schaulies, J. Schneider-Schaulies, *Curr. Top. Microbiol. Immunol.* **330**, 243–269 (2009).
17. R. D. de Vries *et al.*, *PLOS Pathog.* **8**, e1002885 (2012).
18. J. Kleinnijenhuis *et al.*, *Proc. Natl. Acad. Sci. U.S.A.* **109**, 17537–17542 (2012).
19. G. R. Lee, S. T. Kim, C. G. Spilianakis, P. E. Fields, R. A. Flavell, *Immunity* **24**, 369–379 (2006).
20. M. G. Netea, J. Quintin, J. W. van der Meer, *Cell Host Microbe* **9**, 355–361 (2011).
21. S. Saeed *et al.*, *Science* **345**, 1251086 (2014).
22. WHO, Meeting of the Strategic Advisory Group of Experts on immunization, March 2014, *Systematic Review of the Non-specific Effects of BCG, DTP and Measles Containing Vaccines*, http://www.who.int/immunization/sage/meetings/2014/april/3_NSE_Epidemiology_review_Report_to_SAGE_14_Mar_FINAL.pdf.
23. R. D. de Vries, R. L. de Swart, *PLOS Pathog.* **10**, e1004482 (2014).
24. W. H. Lin, R. D. Kouyos, R. J. Adams, B. T. Grenfell, D. E. Griffin, *Proc. Natl. Acad. Sci. U.S.A.* **109**, 14989–14994 (2012).
25. R. T. Perry, N. A. Halsey, *J. Infect. Dis.* **189**, S4–S16 (2004).
26. L. K. Selin, K. Vergilis, R. M. Welsh, S. R. Nahill, *J. Exp. Med.* **183**, 2489–2499 (1996).
27. S. K. Kim, M. A. Brehm, R. M. Welsh, L. K. Selin, *J. Immunol.* **169**, 90–98 (2002).
28. S. K. Kim, R. M. Welsh, *J. Immunol.* **172**, 3139–3150 (2004).
29. C. D. Peacock, S. K. Kim, R. M. Welsh, *J. Immunol.* **171**, 655–663 (2003).
30. A. R. Hinman, W. A. Orenstein, M. J. Papania, *J. Infect. Dis.* **189**, S17–S22 (2004).
31. P. Aaby, J. Bukh, D. Kronborg, I. M. Lisse, M. C. da Silva, *Am. J. Epidemiol.* **132**, 211–219 (1990).
32. WHO, *Global Review of the Distribution of Pneumococcal Invasive Disease by Age and Region* (2011); www.who.int/immunization/sage/6_Russel_review_age_specific_epidemiology_PCV_schedules_session_nov11.pdf.
33. O. Horwitz, K. Grünfeld, B. Lysgaard-Hansen, K. Kjeldsen, *Am. J. Epidemiol.* **100**, 136–149 (1974).
34. J. A. Clarkson, P. E. M. Fine, *Int. J. Epidemiol.* **14**, 153–168 (1985).
35. A. Kipps, L. Stern, E. Vaughan, *S. Afr. Med. J.* **86**, 104–108 (1996).
36. S. O. Shaheen *et al.*, *BMJ* **313**, 969–974 (1996).
37. S. O. Shaheen *et al.*, *Lancet* **347**, 1792–1796 (1996).
38. P. Aaby, B. Samb, M. Andersen, F. Simondon, *Am. J. Epidemiol.* **143**, 1035–1041 (1996).
39. P. Aaby, I. M. Lisse, K. Mølbak, K. Knudsen, H. Whittle, *Pediatr. Infect. Dis. J.* **15**, 39–44 (1996).
40. D. J. Earn, P. Rohani, B. M. Bolker, B. T. Grenfell, *Science* **287**, 667–670 (2000).

ACKNOWLEDGMENTS

Data for analyses regarding England and Wales were retrieved from the Office of Population Censuses and Surveys and the Office for National Statistics (www.ons.gov.uk). We thank P. Rohani for supplying us with historical data on pertussis, as originally described in (*34*). Data for U.S. analyses were retrieved from the U.S. Centers for Disease Control and Prevention, National Center for Health Statistics (www.cdc.gov/nchs). Data for Denmark was retrieved from Statistics Denmark (www.statbank.dk) and WHO (www.apps.who.int). This work is funded by the Bill and Melinda Gates Foundation, the Science and Technology Directorate of the Department of Homeland Security [contract HSHQDC-12-C-00058 (B.T.G. and C.J.E.M.)], and the RAPIDD program of the Science and Technology Directorate of the Department of Homeland Security and the Fogarty International Center, National Institutes of Health (C.J.E.M. and B.T.G).

SUPPLEMENTARY MATERIALS

www.sciencemag.org/content/348/6235/694/suppl/DC1
Materials and Methods
Supplementary Text
Figs. S1 to S13
Table S1
References (*41*–*43*)
Movies S1 to S3

24 November 2014; accepted 1 April 2015
10.1126/science.aaa3662

CHROMOSOMES

CENP-C reshapes and stabilizes CENP-A nucleosomes at the centromere

Samantha J. Falk,[1,2]* Lucie Y. Guo,[1,3]* Nikolina Sekulic,[1]* Evan M. Smoak,[1,3,4]* Tomoyasu Mani,[1,3] Glennis A. Logsdon,[1,3] Kushol Gupta,[1] Lars E. T. Jansen,[5] Gregory D. Van Duyne,[1,3] Sergei A. Vinogradov,[1,3] Michael A. Lampson,[2,3,4] Ben E. Black[1,2,3]†

Inheritance of each chromosome depends upon its centromere. A histone H3 variant, centromere protein A (CENP-A), is essential for epigenetically marking centromere location. We find that CENP-A is quantitatively retained at the centromere upon which it is initially assembled. CENP-C binds to CENP-A nucleosomes and is a prime candidate to stabilize centromeric chromatin. Using purified components, we find that CENP-C reshapes the octameric histone core of CENP-A nucleosomes, rigidifies both surface and internal nucleosome structure, and modulates terminal DNA to match the loose wrap that is found on native CENP-A nucleosomes at functional human centromeres. Thus, CENP-C affects nucleosome shape and dynamics in a manner analogous to allosteric regulation of enzymes. CENP-C depletion leads to rapid removal of CENP-A from centromeres, indicating their collaboration in maintaining centromere identity.

Centromeres direct chromosome inheritance at cell division, and nucleosomes containing a histone H3 variant, centromere protein A (CENP-A), are central to current models of an epigenetic program for specifying centromere location (*1*). The centromere inheritance model in metazoans suggests that the high local concentration of preexisting CENP-A nucleosomes at the centromere guides the assembly of nascent CENP-A, which occurs once per cell cycle after mitotic exit. This model predicts that after initial assembly into centromeric chromatin, CENP-A must be stably retained at that centromere; otherwise, centromere identity would be lost before the next opportunity for new loading in the next cell cycle. Here, we use biochemical reconstitution to measure the shape and physical properties of CENP-A nucleosomes with and without its close binding partner, CENP-C, and combine these studies with functional tests that reveal the mechanisms underlying the high stability of centromeric chromatin.

CENP-C recognizes CENP-A nucleosomes via a region termed its central domain (amino acids 426 to 537; CENP-C^{CD}) (*2*, *3*). We first considered how CENP-C^{CD} may affect the overall shape of the CENP-A–containing nucleosome using an intranucleosomal fluorescence resonance energy transfer (FRET)–based approach. We designed an experiment to measure FRET efficiency, Φ_{FRET},

[1]Department of Biochemistry and Biophysics, Perelman School of Medicine, University of Pennsylvania, Philadelphia, PA 19104, USA. [2]Graduate Program in Cell and Molecular Biology, Perelman School of Medicine, University of Pennsylvania, Philadelphia, PA 19104, USA. [3]Graduate Program in Biochemistry and Molecular Biophysics, Perelman School of Medicine, University of Pennsylvania, Philadelphia, PA 19104, USA. [4]Department of Biology, University of Pennsylvania, Philadelphia, PA 19104, USA. [5]Instituto Gulbenkian de Ciência, 2780-156 Oeiras, Portugal.
*These authors contributed equally to this work. **†Corresponding author. E-mail: blackbe@mail.med.upenn.edu**

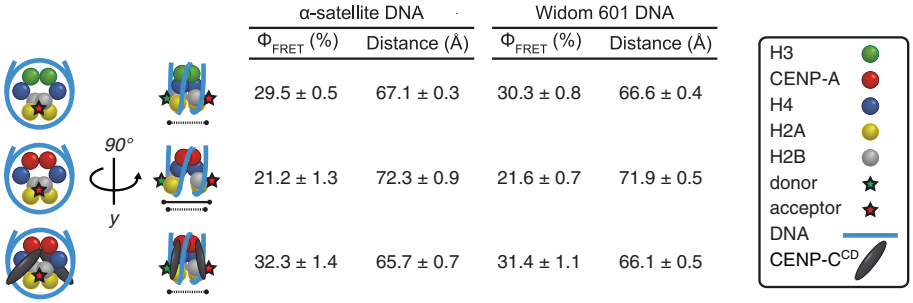

	α-satellite DNA		Widom 601 DNA	
	Φ_{FRET} (%)	Distance (Å)	Φ_{FRET} (%)	Distance (Å)
	29.5 ± 0.5	67.1 ± 0.3	30.3 ± 0.8	66.6 ± 0.4
	21.2 ± 1.3	72.3 ± 0.9	21.6 ± 0.7	71.9 ± 0.5
	32.3 ± 1.4	65.7 ± 0.7	31.4 ± 1.1	66.1 ± 0.5

Fig. 1. CENP-A nucleosomes have a conventional shape only upon CENP-C^{CD} binding. Calculated FRET efficiencies (Φ_{FRET}) and distances between donor and acceptor fluorophores on H2B S123C for the indicated nucleosomes on either α-satellite or Widom 601 DNA. Data are shown as the mean ± SEM of three independent nucleosome reconstitutions.

between two fluorophores on defined positions on the H2B subunits of CENP-A nucleosomes in the absence or presence of CENP-C^{CD} and then used these measurements to calculate intranucleosomal distances (Fig. 1 and fig. S1). The H2B distances for CENP-A nucleosomes in the absence of CENP-C^{CD} are ~5 Å farther apart than expected from their crystal structure (PDB ID 3AN2) (*4*), indicating that CENP-A–containing nucleosomes in solution prefer a histone octamer configuration not captured in the crystal structure. It is likely that CENP-A nucleosomes sample both conformations in solution, with crystal contacts stabilizing the form that was reported (*4*). In contrast to CENP-A nucleosomes, conventional

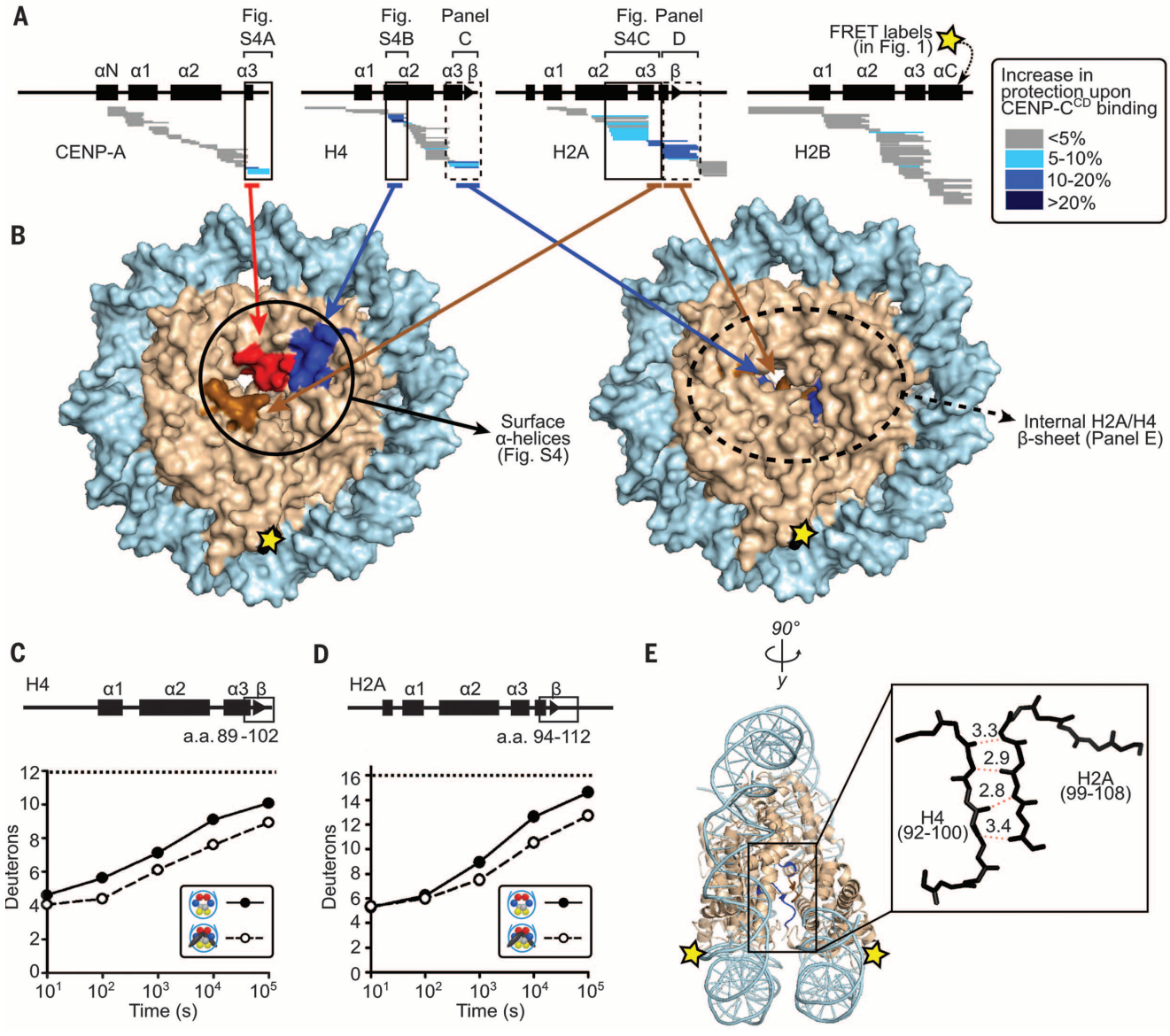

Fig. 2. CENP-C^{CD} rigidifies CENP-A nucleosomes. (**A**) HXMS of all histone subunits of the CENP-A nucleosome from a single time point (10^4 s; see all time points in fig. S3). Each horizontal bar represents an individual peptide, and peptides are placed beneath schematics of secondary structural elements. (**B**) Regions showing substantial protection from HX mapped onto the structure of the CENP-A nucleosome (PDB ID 3AN2). (**C** and **D**) Comparison of representative peptides spanning the β-sheet region in histone H4 and histone H2A over the time course. The maximum number of deuterons possible to measure by HXMS for each peptide is shown by the dotted line. (**E**) The internal H4/H2A interface mapped (see fig. S5) onto the canonical nucleosome crystal structure (PDB ID 1KX5).

nucleosomes have smaller H2B distances in solution (Fig. 1) that are consistent with their crystal structure (*5*). Separation of H2A/H2B dimers from each other is consistent with a nucleosome model based on rotation of the CENP-A/CENP-A′ interface in $(CENP\text{-}A/H4)_2$ heterotetramers (*6*). Upon binding of CENP-C^{CD}, with the known stoichiometry of two CENP-C^{CD} molecules per nucleosome (*3*), the H2A/H2B distances shorten to ones that are nearly identical to those in conventional nucleosomes (Fig. 1). The differences we observed between H3 nucleosomes, CENP-A nucleosomes, and CENP-A nucleosomes in a complex with CENP-C^{CD} are found using either the human α-satellite DNA sequence that corresponds to the most heavily occupied site at centromeres (*7*) or the completely synthetic "601" nucleosome positioning sequence (*8*) (Fig. 1).

The shape change that we measure within the nucleosome upon CENP-C^{CD} binding most likely occurs through rotation at the four-helix bundles between histone dimer pairs within the octameric core, with interhistone contacts being stabilized or destabilized depending on the preference for rotational state. We tested this prediction using hydrogen/deuterium exchange-mass spectrometry (HXMS). Strong protection of CENP-A nucleosomes (Fig. 2A and figs. S3D and S4) is conferred by CENP-C^{CD} binding on peptides spanning helices that are predicted (*3*) to contact it (i.e., the α3 helix and C-terminal residues of CENP-A, the α2 helices of both H4 and H2A, and regions of H2A encompassing its acidic patch residues). In addition to the surface changes induced by CENP-C^{CD}, there are internal changes to the nucleosome that we measure by HX (Fig. 2, A and B, and movie S1) that are consistent with the change in nucleosome shape that we observed by FRET (Fig. 1). The separation of H2A/H2B dimers in CENP-A nucleosomes lacking CENP-C^{CD} (Fig. 1) is predicted to weaken an internal, intermolecular β sheet that serves as the physical connection between the H2A subunit on one face of the nucleosome and the H4 subunit on the opposite face. When CENP-C^{CD} binds to the CENP-A nucleosome, peptides spanning the corresponding β-sheet residues of both H2A and H4 exhibit extra protection from HX by 1 to 2 deuterons, where the same level of HX takes 5 to 10 times

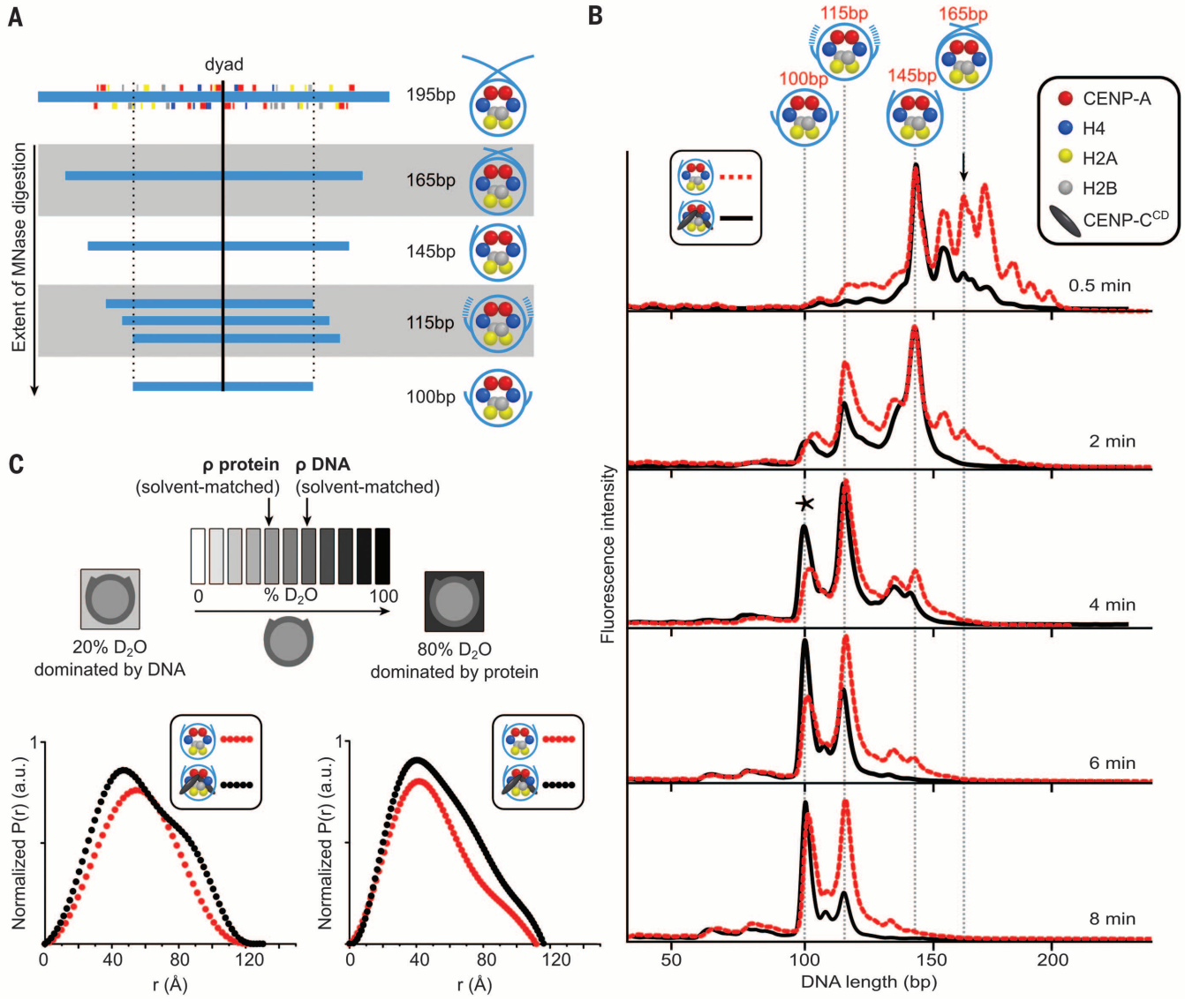

Fig. 3. Alterations in the nucleosome terminal DNA upon CENP-C^{CD} binding. (**A**) Major micrococcal nuclease (MNase)–digested DNA fragments observed for CENP-A nucleosomes assembled on its native centromere sequence. (**B**) MNase digestion profiles of CENP-A nucleosomes in the absence (red) and presence (black) of CENP-C^{CD}. The black arrow (0.5 min) points to the 165-bp peak (DNA crossed at the dyad). The asterisk (4 min) denotes the final 100-bp peak. (**C**) Scheme of SANS contrast variation experiment together with paired distance distribution curves for CENP-A nucleosomes alone (red) and bound by CENP-C^{CD} (black) in the indicated SANS contrast variation conditions.

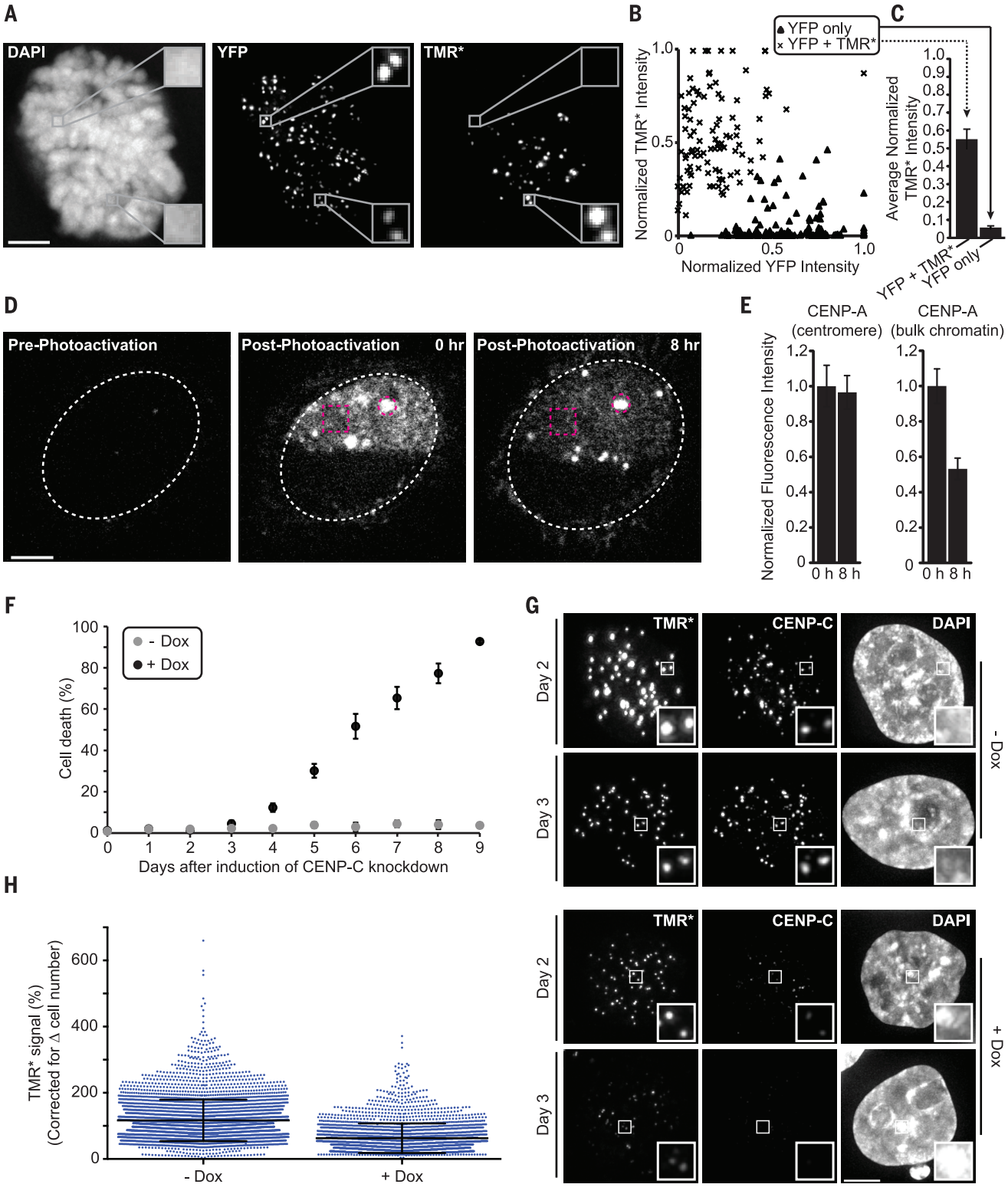

Fig. 4. Depletion of CENP-C reduces the high stability of CENP-A at centromeres. (**A** to **C**) Cells expressing SNAP-tagged CENP-A were pulse-labeled with TMR*, then fused with cells expressing YFP-tagged CENP-A. Representative images (A) show a cell in the second mitosis after fusion; insets show 3x magnification. X-means clustering was used to classify YFP only (triangles) or YFP and TMR* ("x" marks) centromeres (B), and mean (± SEM) TMR* intensity was calculated for each group (C). (**D** and **E**) Cells expressing high levels of CENP-A-PAGFP were photoactivated in bulk (box) and centromeric (circle) chromatin. Representative images (D) show a subset of centromeres in a single *z* section. Fluorescence intensity was quantified at 0 and 8 hours after photoactivation [(E), mean ± SEM]. (**F**) CENP-C knockdown begins causing cell death 4 days post-induction (mean ± SD). (**G** and **H**) Cells with (+ Dox) and without (– Dox) CENP-C depletion were pulse-labeled with TMR* (day 2), and the relative CENP-A-SNAP signals were analyzed (day 3). Quantification shows CENP-A-SNAP signal retained at day 3 (>2500 centromeres plotted with mean ± SD). Scale bars, 5 μm.

as long to occur than in CENP-A nucleosomes lacking CENP-C^{CD} (Fig. 2 and figs. S5 and S6).

Because CENP-C might also affect the extent that DNA wraps the nucleosomes, we reconstituted CENP-A nucleosomes using a 195–base pair (bp) DNA sequence from α-satellite DNA (*9*) that contains a contiguous sequence spanning the major binding site it occupies on human centromeres (*7*) (Fig. 3A). We first overdigested CENP-A nucleosomes and found very strong protection of 100 bp (fig. S9). Using a subsequent restriction digest of the 100-bp digestion product, we found that they were uniquely positioned, with their dyad precisely where the same-sized fragment previously mapped with native centromeric particles (*7*) (fig. S9). CENP-A–containing nucleosomes have many discrete intermediate digestion products before the strongly protected 100-bp fragment is generated (Fig. 3, A and B, and fig. S10). When CENP-C^{CD} is bound, digestion products larger than a nucleosome core particle [e.g., >145 bp, where DNA strands could cross at ~165 bp for conventional nucleosomes (*10*)] are missing at early time points (Fig. 3B). This suggests that when CENP-C^{CD} binds to the nucleosome, the DNA above the dyad rarely crosses, as it would normally cross for conventional nucleosomes. Second, digestion to the 100-bp final fragment proceeds more quickly (Fig. 3B). Thus, transient unwrapping of two helical turns (i.e., ~20 bp) from each terminus of the nucleosome is enhanced when CENP-C^{CD} is bound.

To determine whether CENP-C^{CD} binding leads to a steady-state structural change of nucleosomal DNA, we used small-angle neutron scattering (SANS) with contrast variation. When CENP-C^{CD} binds to CENP-A nucleosome core particles, the distance distribution profiles reflecting the shape in solution substantially redistribute for both the protein- and DNA-dominated measurements (Fig. 3C, fig. S11, and table S3). The increase in larger interatomic vectors for the protein component is expected to accompany an additional component (CENP-C^{CD}). The pronounced redistribution of vectors to both smaller and larger distances in DNA-dominated scattering when CENP-C^{CD} is bound is attributed to compaction of the nucleosome core (smaller vectors) and opening of the nucleosome terminal DNA when CENP-C^{CD} is bound (larger vectors).

We took two complementary approaches in cells to determine whether CENP-A is stably retained at the centromere upon which it is initially deposited (see the legend for fig. S12 that describes the motivation for these experiments). First, we used cell cycle–synchronized fluorescence pulse labeling of CENP-A in "donor" cells and subsequent cell fusion with an "acceptor" cell line. The donor cells express SNAP-tagged CENP-A that has been pulse labeled with tetramethylrhodamine-Star (TMR*) to irreversibly label CENP-A (*11*) before cell fusion. The acceptor cells express yellow fluorescent protein (YFP)–tagged CENP-A that is loaded at all centromeres, continuing even after fusion. At time points through the subsequent cell cycle (fig. S12) until the second mitosis (Fig. 4A), we observed no detectable exchange of the TMR*-labeled donor CENP-A to the acceptor centromeres in a shared nucleoplasm. Quantitation of the fluorescence at each centromere in these heterokaryons yields a bimodal distribution. The donor centromere group with high TMR* and low YFP (Fig. 4B, "x" symbols) has an average TMR* signal of 0.538 ± 0.005 (normalized arbitrary units where the maximal measured TMR* signal in each heterokaryon equals 1) (Fig. 4C), whereas the acceptor centromere group with high YFP and low TMR* (Fig. 4B, triangle symbols) has an average TMR* signal of 0.055 ± 0.005 (Fig. 4C). These data indicate that once assembled at a centromere, an individual CENP-A molecule is stably maintained at that particular centromere.

As a complementary approach to test CENP-A stability at individual centromeres, we used a photoactivatable version of CENP-A (CENP-A-PAGFP). We induced expression of CENP-A to the extent that it is present at locations throughout the nucleus, but with clear enrichment at centromeres, and then activated a defined region of each cell nucleus (Fig. 4D, 0 hours postphotoactivation). CENP-A-PAGFP signal is quantitatively retained at the activated centromeres and does not accumulate at unactivated centromeres (Fig. 4, D and E), indicating that there is negligible exchange between centromeres, consistent with our cell fusion results. In contrast, CENP-A-PAGFP signal in bulk chromatin decays, with about half of the protein removed by 8 hours after photoactivation.

To investigate whether CENP-C stabilizes CENP-A at centromeres, we combined SNAP labeling of CENP-A with CENP-C depletion (Fig. 4), for which we generated a cell line with a chromosomally integrated, doxycycline-inducible CENP-C short hairpin RNA cassette. In our SNAP system, CENP-C depletion leads to a dramatic decrease in the retention over 24 hours of the existing pool of CENP-A at centromeres (Fig. 4, G and H). Without CENP-C depletion, the average retention of CENP-A is slightly >100% (112% ± 63% SD), an increase that is explained by having a small pool of prenucleosomal CENP-A in the cell population that is labeled by the TMR* pulse and subsequently incorporated into centromeres. Nascent CENP-A deposition is also decreased when CENP-C is depleted (fig. S16C)—consistent with its proposed role in the CENP-A assembly reaction (*12*, *13*)—but this would only affect incorporation of the small prenucleosomal pool in the CENP-A retention measurements (Fig. 4, G and H). Thus, our findings implicate CENP-C in stabilizing CENP-A nucleosomes at centromeres. We cannot rule out the possibility that removal of CENP-C in turn removes another centromere component that stabilizes CENP-A nucleosomes, but we favor the idea that CENP-C is the key molecule for stabilizing CENP-A nucleosomes based on its direct binding to it.

CENP-A nucleosomes are highly stable at the centromeres upon which they are initially assembled. This stability is possible through collaboration with CENP-C. Along with the intranucleosomal rigidity of CENP-A and histone H4, where the key interfacial amino acids are important for accumulation at centromeres (*6*, *14*, *15*), the physical changes imposed by CENP-C combine to make CENP-A nucleosomes at centromeres very long-lived (fig. S21). Our data support a model of a steady-state octameric histone core where H2A/H2B dimers can exchange from either terminus of the CENP-A nucleosome. At the center, there is an essentially immobile $(CENP\text{-}A/H4)_2$ heterotetramer (*16*) (Fig. 4 and figs. S12 to S14). Thus, the physical properties related to CENP-A nucleosome stability at centromeres are tied to the intrinsic properties of the $(CENP\text{-}A/H4)_2$ heterotetramer (*6*, *14*, *15*) and the extrinsic properties imposed by CENP-C (Figs. 1 to 3 and fig. S21).

REFERENCES AND NOTES

1. B. E. Black, D. W. Cleveland, *Cell* **144**, 471–479 (2011).
2. C. W. Carroll, K. J. Milks, A. F. Straight, *J. Cell Biol.* **189**, 1143–1155 (2010).
3. H. Kato *et al.*, *Science* **340**, 1110–1113 (2013).
4. H. Tachiwana *et al.*, *Nature* **476**, 232–235 (2011).
5. K. Luger, A. W. Mäder, R. K. Richmond, D. F. Sargent, T. J. Richmond, *Nature* **389**, 251–260 (1997).
6. N. Sekulic, E. A. Bassett, D. J. Rogers, B. E. Black, *Nature* **467**, 347–351 (2010).
7. D. Hasson *et al.*, *Nat. Struct. Mol. Biol.* **20**, 687–695 (2013).
8. P. T. Lowary, J. Widom, *J. Mol. Biol.* **276**, 19–42 (1998).
9. J. M. Harp *et al.*, *Acta Crystallogr. D Biol. Crystallogr.* **52**, 283–288 (1996).
10. R. D. Kornberg, *Annu. Rev. Biochem.* **46**, 931–954 (1977).
11. L. E. T. Jansen, B. E. Black, D. R. Foltz, D. W. Cleveland, *J. Cell Biol.* **176**, 795–805 (2007).
12. S. Erhardt *et al.*, *J. Cell Biol.* **183**, 805–818 (2008).
13. B. Moree, C. B. Meyer, C. J. Fuller, A. F. Straight, *J. Cell Biol.* **194**, 855–871 (2011).
14. E. A. Bassett *et al.*, *Dev. Cell* **22**, 749–762 (2012).
15. B. E. Black *et al.*, *Nature* **430**, 578–582 (2004).
16. D. L. Bodor, L. P. Valente, J. F. Mata, B. E. Black, L. E. T. Jansen, *Mol. Biol. Cell* **24**, 923–932 (2013).

ACKNOWLEDGMENTS

We thank our University of Pennsylvania colleagues (J. Bell, C. Bialas, J. DeNizio, Y. Goldman, W. Hu, L. Lippert, L. Mayne, T. Panchenko, B. Türegün, and Z. Zhao) and S. Krueger and K. Sarachan [National Institute of Standards and Technology (NIST)] for assistance and advice with experiments; A. Straight (Stanford) for reagents and advice; and D. Cleveland (University of California, San Diego), J. Lippincott-Schwartz (NIH), K. Luger (Colorado State University), and E. Makeyev (Nanyang Technical University) for reagents. This work was supported by NIH grant GM082989 (B.E.B.), European Research Council grant ERC-2013-CoG-615638 (L.E.T.J.), predoctoral fellowships from the American Heart Association (E.M.S.) and NIH (CA186430, L.Y.G.), and a postdoctoral fellowship from the American Cancer Society (N.S.). We acknowledge support from NIH grants GM008275 (UPenn Structural Biology Training Grant, L.Y.G. and E.M.S), GM008216 (UPenn Genetics Training Grant, S.J.F.), and GM007229 (UPenn Cell and Molecular Biology Training Grant, G.A.L.). This work used facilities supported in part by NSF (agreement DMR-0944772). We acknowledge the support of NIST in providing the neutron research facilities used in this work.

SUPPLEMENTARY MATERIALS

www.sciencemag.org/content/348/6235/699/suppl/DC1
Materials and Methods
Figs. S1 to S21
Tables S1 to S3
Movie S1
References (*17*–*56*)

28 July 2014; accepted 7 April 2015
10.1126/science.1259308

STRUCTURAL VIROLOGY

Near-atomic cryo-EM structure of the helical measles virus nucleocapsid

Irina Gutsche,[1,2]* Ambroise Desfosses,[3]† Grégory Effantin,[1,2] Wai Li Ling,[4,5,6] Melina Haupt,[7] Rob W. H. Ruigrok,[1,2] Carsten Sachse,[3] Guy Schoehn[1,2,4,5,6]

Measles is a highly contagious human disease. We used cryo–electron microscopy and single particle–based helical image analysis to determine the structure of the helical nucleocapsid formed by the folded domain of the measles virus nucleoprotein encapsidating an RNA at a resolution of 4.3 angstroms. The resulting pseudoatomic model of the measles virus nucleocapsid offers important insights into the mechanism of the helical polymerization of nucleocapsids of negative-strand RNA viruses, in particular via the exchange subdomains of the nucleoprotein. The structure reveals the mode of the nucleoprotein-RNA interaction and explains why each nucleoprotein of measles virus binds six nucleotides, whereas the respiratory syncytial virus nucleoprotein binds seven. It provides a rational basis for further analysis of measles virus replication and transcription, and reveals potential targets for drug design.

Nonsegmented negative-strand RNA viruses (nsNSVs, or *Mononegavirales*) cause epidemics of serious respiratory tract illnesses [e.g., measles virus (MeV) and respiratory syncytial virus (RSV)] and outbreaks of lethal zoonotic diseases [e.g., Ebola virus and Nipah virus (NiV)]. Although preventable by vaccination, measles still remains one of the leading sources of death among young children worldwide (*1*). MeV belongs to the *Paramyxoviridae* family of *Mononegavirales*, which is further divided in two subfamilies: *Paramyxovirinae* (containing MeV and NiV) and *Pneumovirinae* (e.g., RSV).

The genome of negative-strand RNA viruses (NSVs) is enwrapped with the viral nucleoprotein N. The resulting ribonucleoprotein complex, called the nucleocapsid, protects the viral genetic information while providing a flexible helical template for viral transcription and replication by the viral RNA polymerase L, which, in the *Paramyxoviridae* and *Rhabdoviridae* families of *Mononegavirales*, is associated with the modular phosphoprotein cofactor P (*2*). As a unique structure in nucleic acid biology, the NSV nucleocapsid constitutes an attractive potential target for antiviral drugs without harmful side effects. Like all *Mononegavirales* nucleoproteins, MeV N is composed of two globular domains, the N- and C-terminal domains (NTD and CTD), which together form a stable peanut-shaped nucleoprotein core (N_{core}, residues 1 to 391 in MeV N) holding the RNA molecule in the interdomain cleft. In addition, like other *Paramyxovirinae*, MeV N features a long, intrinsically disordered tail domain (N_{tail}, residues 392 to 525) (Fig. 1A) that confers to the nucleocapsids a structural plasticity hampering their analysis at better than ~2 nm resolution (*3*, *4*).

Removal of the N_{tail} tightens the MeV nucleocapsid helix, decreasing both its diameter and pitch (*3*–*5*). Our previous cryo–electron microscopy (cryo-EM) map of the resulting N_{core}-RNA helix at 12 Å resolution (*5*) provided precise helical parameters and the domain organization of the MeV N_{core}, and a number of low- and medium-resolution EM reconstructions of other *Mononegavirales* nucleocapsids are available (*6*–*9*). However, the only atomic-resolution structural information about *Mononegavirales* nucleocapsids comes from x-ray crystallography of N-RNA rings obtained upon nonspecific encapsidation of short cellular RNAs by recombinant nucleoproteins of RSV (*7*) and of two rhabdoviruses (*10*, *11*), whereas such rings could not yet be observed for *Paramyxovirinae*. In addition, the crystal structure of the RNA-free NiV N_{core} (N^0_{core}) bound to a short N-terminal region of P (N^0_{core}-P_{50}) (*12*), has been solved recently. We therefore focused on the helical state of the MeV N_{core}-RNA nucleocapsid, so as to (i) obtain a high-resolution three-dimensional (3D) structure of the N_{core} monomer, (ii) identify the molecular determinants of helical nucleocapsid polymerization, and (iii) directly visualize the RNA inside the nucleoprotein and understand why each MeV nucleoprotein binds exactly six ribonucleotides, whereas the RSV N binds seven. Here, we report the 3D structure of recombinant MeV N_{core}-RNA nucleocapsids at 4.3 Å resolution, determined by single particle–based helical image analysis (*13*, *14*) (fig. S1). This cryo-EM map reveals the detailed domain architecture of the N_{core}, its secondary structure elements and many bulky side chains, the rationale of the nucleoprotein packing into a helix, and the mode of nucleoprotein-RNA interaction. Combined with the atomic structures of the RSV N and NiV N^0_{core}, this 3D reconstruction allows us to build a reliable pseudoatomic model of the MeV N_{core}-RNA helix.

The left-handed MeV N_{core}-RNA helix is composed of 12.34 nucleoprotein subunits per turn, with a pitch of 49.54 Å and an outer diameter of 190 Å, in good agreement with previous studies (*3*–*5*) (table S1). The RNA thread winds around the nucleoprotein bobbin, accommodated inside the cleft between the outward-pointing NTD and the inward-oriented CTD, and shielded from above by the N subunits from the successive helical turn (Fig. 1B). As in the nsNSV N-RNA rings, MeV N_{core} oligomerization is mainly mediated via the exchange subdomains called the NTD arm (residues 1 to 36) and the CTD arm (residues 373 to 391). Our 3D reconstruction shows how the NTD arm of the N_i protomer inserts into a groove in the CTD of the N_{i+1} subunit, whereas the CTD arm lies on top of the N_{CTD} of the N_{i-1} subunit, generating a repeated helical structure (Fig. 1, C to F). Unlike in the model of the RSV nucleocapsid (*15*), the N_{i-1} and N_{i+1} subunits in the MeV N_{core}-RNA helix do not interact directly.

The domain organization of the MeV N_{core} (Fig. 1D) corroborates the assumption that all nsNSV nucleoproteins share the same global fold (*2*, *16*) (fig. S2A). In particular, the CTD fold appears conserved among the *Paramyxoviridae* (MeV, NiV, RSV) (*7*, *12*). The major difference between the pneumovirus RSV and the *Paramyxovirinae* MeV and NiV is located, as predicted (*7*, *12*), at the distal tip of the NTD (residues 91 to 159 in MeV N). The local resolution of the cryo-EM map in this solvent-exposed region, known as an antigenic site of MeV N (residues 122 to 150) (*17*), seems to be the lowest, probably indicating mobility with respect to the nucleocapsid core (fig. S1D). In NiV N^0_{core}-P_{50} crystals, the RNA-free nucleoprotein is observed in an open state (*12*). The present structure of the MeV N_{core}-RNA monomer enables accurate modeling of the hinge motion between NTD and CTD, which has been proposed to be associated with the open-closed transition accompanying nucleocapsid formation (fig. S2, B and C) (*12*).

On the basis of the NiV N^0_{core}-P_{50} structure, the N-terminal domain of *Paramyxovirinae* P was assigned two simultaneous roles (*12*): (i) trapping the nucleoprotein in an open RNA-free conformation by rigidifying the CTD, and (ii) preventing its polymerization by interfering with the binding of the exchange subdomains. Indeed, although crystallization of NiV N^0_{core}-P_{50} required deletion of both the NTD and CTD arms, the first and second α helices of the helix-kink-helix peptide of P (Pα1 and Pα2) were shown to overlay with the NTD and CTD arm loops of RSV N, respectively (*12*). In MeV, the NTD arm begins with an α helix (residues 2 to 14) (Fig. 1D and fig. S2A) that fits into a hydrophobic groove formed by three conserved CTD α helices of the N_{i+1} subunit (Fig. 2A) (*12*). Specifically, four aromatic residues (Phe^{11}, Phe^{269}, Tyr^{303}, and Phe^{324}) that are conserved in *Paramyxovirinae* (*12*) seem to stack together, thereby fixing the NTD arm α helix and rigidifying the helix bundle around it (Fig. 2B). Furthermore, the NTD arm α helix of MeV N_{i-1} perfectly superimposes with Pα1 from the NiV N^0_{core}-P_{50} structure, although the latter

[1]CNRS, Unit for Virus Host-Cell Interactions, 38042 Grenoble, France. [2]Université Grenoble Alpes, Unit for Virus Host-Cell Interactions, 38042 Grenoble, France. [3]Structural and Computational Biology Unit, European Molecular Biology Laboratory, 69917 Heidelberg, Germany. [4]Université Grenoble Alpes, IBS, 38044 Grenoble, France. [5]CNRS, IBS, 38044 Grenoble, France. [6]CEA, IBS, 38044 Grenoble, France. [7]Institut Laue-Langevin, 38000 Grenoble, France.
*Corresponding author. E-mail: gutsche@embl.fr †Present address: School of Biological Sciences, University of Auckland, Auckland 1010, New Zealand.

is actually positioned upside down, and the CTD arm loop of the MeV N_{i+1} overlaps with Pα2 (Fig. 2C). Therefore, Pα1 may indeed compete with the NTD arm of the N_{i-1} protomer, and Pα2 with the CTD arm of the N_{i+1} protomer (*12*). The first α helix of P and the NTD arm α helix of MeV N appear to play similar roles: They lock the CTD and the NTD-CTD junction into a stable conformation, either open or closed depending on the presence of RNA in the interdomain cleft.

The MeV N_{core}-RNA structure explains biochemical observations (*18*, *19*) and demonstrates how and why each MeV N binds six ribonucleotides [three stacked bases facing the protein (i.e., "3-bases-in") and three stacked bases pointing

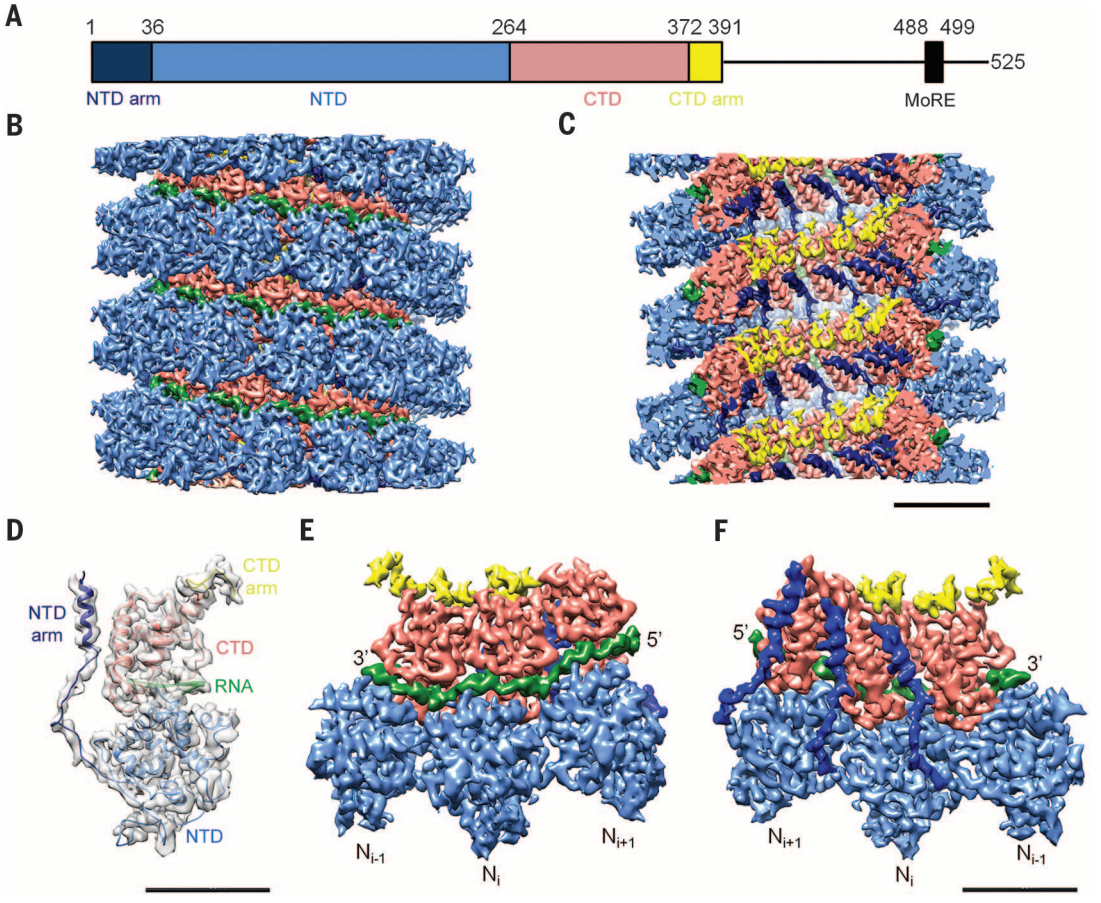

Fig. 1. Cryo-EM structure of the MeV N_{core}-RNA nucleocapsid at near-atomic resolution. (**A**) Schematic of MeV N (navy blue, NTD arm; blue, NTD; salmon, CTD; yellow, CTD arm). The same color code (with RNA in green) is used for the rest of the figure. (**B** and **C**) Isosurface representation of the cryo-EM 3D reconstruction of the helical nucleocapsid: (B) front view, (C) cutaway view. (**D**) Ribbon representation of one N_{core} monomer, with the corresponding segmented cryo-EM density shown in transparent gray. (**E** and **F**) Close-up of three consecutive protomers from the exterior (E) and from the interior (F) of the helix. Scale bars, 50 Å [(B) and (C)], 30 Å [(D) to (F)].

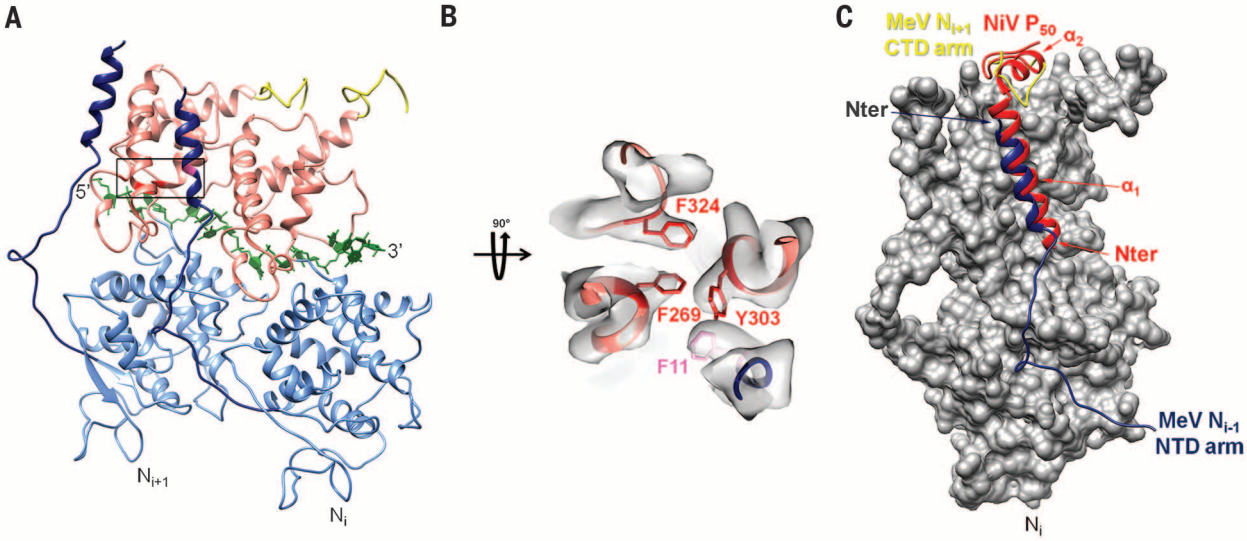

Fig. 2. Exchange domains and N_{core} oligomerization. (**A**) Ribbon representation of two consecutive protomers (colors as in Fig. 1). (**B**) Close-up of the stack of aromatics fixing the N_i subunit NTD arm on the CTD of the N_{i+1} subunit and rigidifying the CTD helix bundle. Pink, Phe^{11} of the N_i subunit; red, Phe^{269}, Tyr^{303}, and Phe^{324} of the N_{i+1} subunit; transparent gray, cryo-EM density. (**C**) The P_{50} peptide (red) of NiV superposes with the NTD arm of the MeV N_{i-1} subunit (navy blue) and the CTD arm of the N_{i+1} subunit (yellow) of MeV. The gray molecular surface represents the MeV N_i subunit. The N termini of N and P_{50} and the first and second α helices of P_{50} are indicated.

toward the solvent (i.e., "3-bases-out")], whereas RSV N binds seven ribonucleotides ("3-bases-in" and "4-bases-out") (Fig. 3, A and B, and figs. S3 and S4). In both viruses, the "3-bases-in" of the N_i subunit are 2-3-4, while base 1 stacks onto the last base of the N_{i-1} to form an outward-oriented stack of three (5-6-1) or four (5-6-7-1) bases which crosses the N_{i-1}-N_i interface, thereby probably contributing to the stability of the nucleocapsid helix. Switch 1 (between bases 1 and 2) constrains the RNA to turn inward, and switch 2 (between bases 4 and 5) orients the RNA outward again (Fig. 3, C to F, and fig. S3). Thus, the RNA topology in MeV and RSV is similar (fig. S4). In MeV nucleocapsid, the outwards-facing groove is however shorter, in particular because long conserved residues R194, K198, Q201, Q202 and Y260 (Fig. 3G) point into it from the 5′ end, sterically hindering packing of a fourth base (Fig. 3, D to F, and figs. S3 and S4). Importantly, Y260, strictly conserved in *Paramyxovirinae* and featuring a well defined side-chain cryo-EM density, does not flip away from the RNA-binding cleft upon RNA encapsidation as proposed (*12*), but stacks with base 2, orienting bases 2-3-4 "in" and therefore contributing to the switch 1 (Fig. 3, E and F). The mechanism of the switch 2 (assured by Lys^{180}, Asp^{186}, and Asn^{351} in MeV N-RNA) also differs between the two viruses (Fig. 3C and fig. S3). Finally, as in RSV, in MeV the N-RNA contacts seem to be rather RNA backbone–specific than base-specific. In particular, three positively charged residues, Lys^{180}, Arg^{194}, and Arg^{354}, show a clear side-chain density and make hydrogen bonds to the RNA backbone (Fig. 3C), and Arg^{195} (Fig. 3D) and Lys^{198} (Fig. 3E) may contribute as well. All these basic residues are conserved among *Paramyxovirinae* (Fig. 3G) and are present in equivalent positions in RSV N (*12*).

Both the nucleoprotein protomer and the entire helical nucleocapsid are dynamic entities that must rearrange during the viral replication cycle. Our findings show how the exchange subdomains of N invade the adjacent subunits in the helix, resulting in a stable and yet flexible nucleocapsid assembly. The NTD arm α helix of MeV N_i inserts into the N_{i+1} to ensure the major stabilizing interaction, whereas the CTD arm not only tethers to the N_{i-1} but also permits the intrinsically unfolded N_{tail} to escape outside between two helical turns, leading to the increased flexibility of the native MeV N-RNA (*4*, *20*). The N_{tail} appears to emerge out of the nucleocapsid core in close proximity to the RNA belt surrounding it, so as to dock the P-L complex into its functional environment on the viral genome (*21*–*23*). Thus, our structure provides a framework for understanding nucleocapsid architecture and remodeling during viral transcription and replication. It

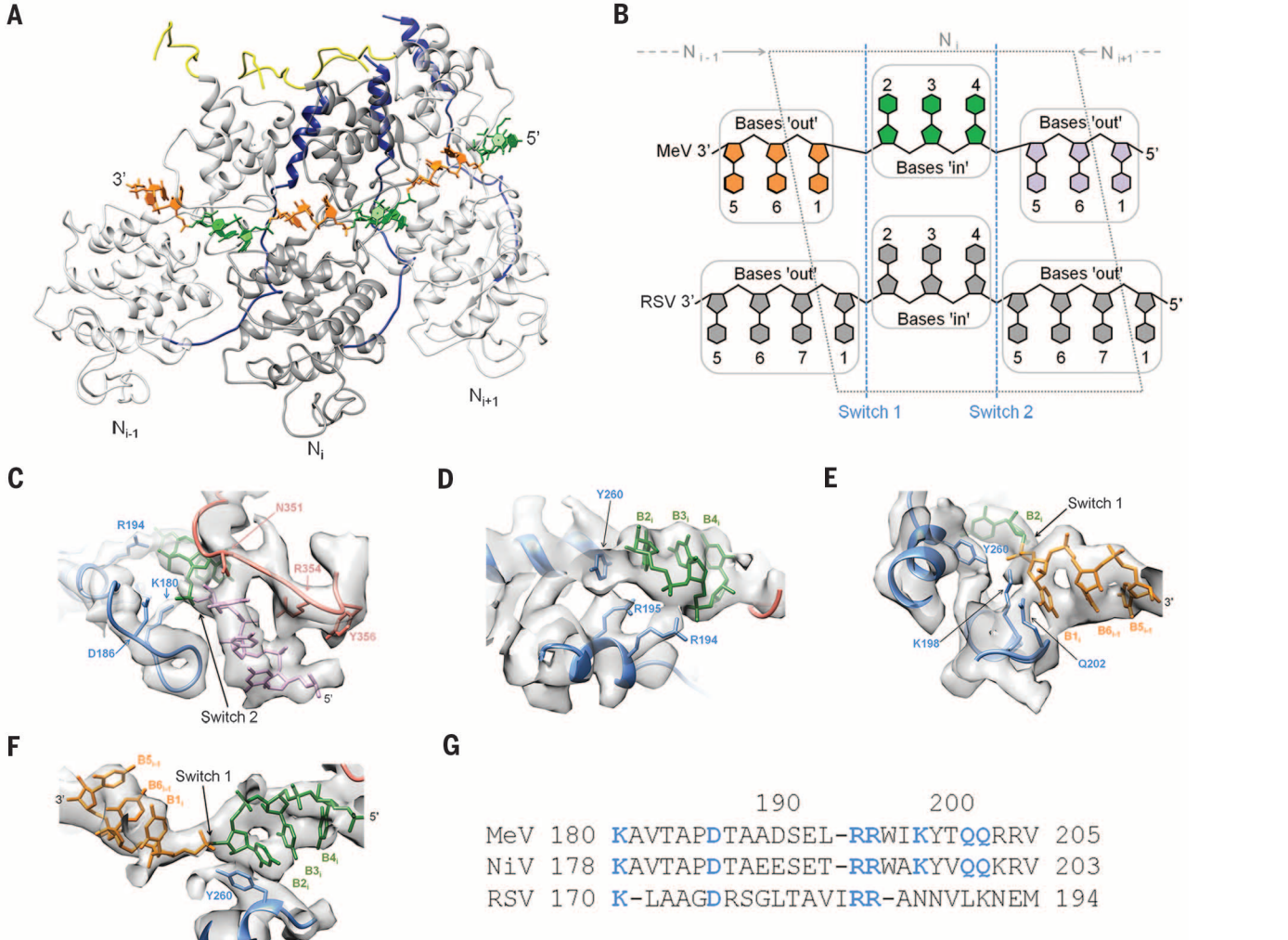

Fig. 3. Nucleoprotein-RNA interaction. (**A**) Ribbon representation of three consecutive protomers [navy blue, NTD arm; yellow, CTD arm; green, RNA (bases "in"); orange (bases "out"]. (**B**) Schematics of the RNA topology for MeV and RSV. For MeV, bases "in" are in green, bases "out" in orange and pink; RSV RNA in gray. Positions and boundaries of successive nucleoprotein subunits on the RNA are indicated; switches in RNA conformation are shown as blue dotted lines. (**C** to **F**) Close-up of protein-RNA interaction (scale bar, 10 Å). Protein colors are as in Figs. 1 and 2; RNA colors are the same as in (A) and (B). Numbers of relevant residues and bases are indicated, as are switches in RNA backbone. (**G**) Sequence alignment of the RNA-binding motif of MeV, NiV, and RSV N. Amino acid abbreviations: A, Ala; D, Asp; E, Glu; G, Gly; I, Ile; K, Lys; L, Leu; M, Met; N, Asn; P, Pro; Q, Gln; R, Arg; S, Ser; T, Thr; V, Val; W, Trp; Y, Tyr.

may also stimulate the design of new antiviral drugs, because it reveals key regions interfering with nucleoprotein oligomerization and/or genome encapsidation. Finally, because MeV shares many common features with other *Paramyxoviridae* and with nsNSVs in general, this near-atomic structure of the helical MeV N_{core}-RNA nucleocapsid may be valuable for the whole *Mononegavirales* field.

REFERENCES AND NOTES

1. www.who.int/mediacentre/factsheets/fs286/en/.
2. R. W. H. Ruigrok, T. Crépin, D. Kolakofsky, *Curr. Opin. Microbiol.* **14**, 504–510 (2011).
3. D. Bhella, A. Ralph, R. P. Yeo, *J. Mol. Biol.* **340**, 319–331 (2004).
4. A. Desfosses, G. Goret, L. Farias Estrozi, R. W. H. Ruigrok, I. Gutsche, *J. Virol.* **85**, 1391–1395 (2011).
5. G. Schoehn *et al.*, *J. Mol. Biol.* **339**, 301–312 (2004).
6. E. H. Egelman, S. S. Wu, M. Amrein, A. Portner, G. Murti, *J. Virol.* **63**, 2233–2243 (1989).
7. R. G. Tawar *et al.*, *Science* **326**, 1279–1283 (2009).
8. P. Ge *et al.*, *Science* **327**, 689–693 (2010).
9. R. Cox *et al.*, *Proc. Natl. Acad. Sci. U.S.A.* **111**, 15208–15213 (2014).
10. A. A. V. Albertini *et al.*, *Science* **313**, 360–363 (2006).
11. T. J. Green, X. Zhang, G. W. Wertz, M. Luo, *Science* **313**, 357–360 (2006).
12. F. Yabukarski *et al.*, *Nat. Struct. Mol. Biol.* **21**, 754–759 (2014).
13. A. Desfosses, R. Ciuffa, I. Gutsche, C. Sachse, *J. Struct. Biol.* **185**, 15–26 (2014).
14. See supplementary materials on *Science* Online.
15. S. E. Bakker *et al.*, *J. Gen. Virol.* **94**, 1734–1738 (2013).
16. T. J. Green *et al.*, *J. Virol.* **88**, 3766–3775 (2014).
17. R. Buckland, P. Giraudon, F. Wild, *J. Gen. Virol.* **70**, 435–441 (1989).
18. P. Calain, L. Roux, *J. Virol.* **67**, 4822–4830 (1993).
19. F. Iseni *et al.*, *RNA* **8**, 1056–1067 (2002).
20. M. R. Jensen *et al.*, *Proc. Natl. Acad. Sci. U.S.A.* **108**, 9839–9844 (2011).
21. R. L. Kingston, W. A. Baase, L. S. Gay, *J. Virol.* **78**, 8630–8640 (2004).
22. S. Longhi *et al.*, *J. Biol. Chem.* **278**, 18638–18648 (2003).
23. S. A. Krumm, M. Takeda, R. K. Plemper, *J. Biol. Chem.* **288**, 29943–29953 (2013).

ACKNOWLEDGMENTS

We thank A. Jakobi for assistance in real-space coordinate refinement using PHENIX, and M. Jamin for discussions and comments on the manuscript. This work used the platforms of the Grenoble Instruct Center (ISBG: UMS 3518 CNRS-CEA-UJF-EMBL) with support from FRISBI (ANR-10-INSB-05-02) and GRAL (ANR-10-LABX-49-01) within the Grenoble Partnership for Structural Biology (PSB); the electron microscope facility is supported by the Rhône-Alpes Region and by the Fondation pour la Recherche Medicale. A.D. received support from EMBL Interdisciplinary Postdoc (EIPOD) fellowships under Marie Curie Actions (PCOFUND-GA-2008-229597). The data reported in this manuscript are tabulated in the main paper and in the supplementary materials. The cryo-EM map of the helical MeV N_{core}-RNA nucleocapsid and the atomic model are deposited in the Electron Microscopy Data Bank and in the Protein Data Bank with accession codes EMDB-2867 and 4uft. The authors declare no competing financial interests. I.G., R.W.H.R., and G.S. designed the study; M.H. purified biological material; I.G., A.D., W.L.L., C.S., and G.S. performed research and analyzed data; R.W.H.R. and G.E. contributed to data interpretation; and I.G. wrote the paper with input from G.E.

SUPPLEMENTARY MATERIALS

www.sciencemag.org/content/348/6235/704/suppl/DC1
Materials and Methods
Figs. S1 to S4
Table S1
References (*24*–*35*)

23 December 2014; accepted 6 April 2015
Published online 16 April 2015;
10.1126/science.aaa5137

OPTOGENETICS

Engineering of a light-gated potassium channel

Cristian Cosentino,[1]* Laura Alberio,[1] Sabrina Gazzarrini,[1] Marco Aquila,[1] Edoardo Romano,[1] Solei Cermenati,[1] Paolo Zuccolini,[1] Jan Petersen,[2] Monica Beltrame,[1] James L. Van Etten,[3] John M. Christie,[2] Gerhard Thiel,[4] Anna Moroni[1]†

The present palette of opsin-based optogenetic tools lacks a light-gated potassium (K^+) channel desirable for silencing of excitable cells. Here, we describe the construction of a blue-light–induced K^+ channel 1 (BLINK1) engineered by fusing the plant LOV2-Jα photosensory module to the small viral K^+ channel Kcv. BLINK1 exhibits biophysical features of Kcv, including K^+ selectivity and high single-channel conductance, but reversibly photoactivates in blue light. Opening of BLINK1 channels hyperpolarizes the cell to the K^+ equilibrium potential. Ectopic expression of BLINK1 reversibly inhibits the escape response in light-exposed zebrafish larvae. BLINK1 therefore provides a single-component optogenetic tool that can establish prolonged, physiological hyperpolarization of cells at low light intensities.

Potassium ion (K^+) channels have a modular structure with sensor domains connected to a central ion-conducting pore (*1*). The pore integrates signals coming from the sensors and translates them into opening or closing the channel (*2*). This allows K^+ channels to alter the membrane potential of cells in response to a variety of physiological stimuli. Extending the range of signal inputs recognized by K^+ channels can be achieved by grafting exogenous sensor domains onto the pore module (*3*, *4*). With this modular interplay between sensor and pore, it is possible to engineer synthetic channels that respond to any signal by *ex novo* coupling of sensors to pores. This strategy provides new tools for the investigation and manipulation of biological functions (*5*). An attractive synthetic channel in this context is a light-gated K^+ channel, which is important because of the ability of K^+ to terminate excitatory currents within cells. This device would allow remote manipulation of the membrane potential with high temporal and spatial resolution and would represent an efficient control mechanism for many cellular processes, including neuronal firing and hormone release.

Several attempts have been made to create synthetic light-gated K^+ channels (*6*–*9*); however, these systems suffer from several shortcomings in that they require the addition of cofactors (*6*, *7*), are irreversible (*8*), or rely on multiple components (*9*). To overcome these obstacles, we engineered a single-component light-gated K^+ channel by fusing the LOV2-Jα photosensory region of a plant blue-light receptor (*10*) to the miniature K^+ channel pore Kcv (*11*). Rational design and directed evolution were employed to ultimately generate a blue-light–inducible K^+ channel that functions reversibly to drive cell membrane potentials to K^+ equilibrium in the absence of exogenous cofactors. The LOV2-Jα photoswitch from *Avena sativa* phototropin 1 (hereafter LOV) can be used to control protein activity by light-induced conformational changes (*12*). We therefore adopted this strategy to place Kcv under light control. LOV was fused to various regions of Kcv known to be mechanically important for channel gating (fig. S1A and constructs 3 to 12 in table S1).

A functional complementation approach based on the growth rescue of Δ*trk1* Δ*trk2* potassium transport–deficient yeast (strain SGY1528) (*13*) was adapted to screen for light-gated channel activity after replica plating (fig. S1B). One Kcv variant with LOV fused at the N terminus (LK) showed light-induced growth on selective agar (4 mM K^+) and liquid culture (fig. S1, B and C). LK was expressed in *Xenopus* oocytes and tested by a two-electrode voltage clamp. LK currents showed modest but reproducible increases in conductance after transfer from darkness to blue light (455 nm, 80 $\mu W/mm^2$) (fig. S2A). However, photostimulation of LK currents required tens of minutes to develop and appeared to be irreversible. In an attempt to enhance coupling of LOV to Kcv, the soluble photosensory region of LK was tethered to the plasma membrane. Introducing a putative myristoylation/palmitoylation sequence (MGCTVSAE) (*14*) at the N terminus of LK resulted in improved, but unexpected, properties. The new variant myLK (Fig. 1A and fig. S2B) showed an enhanced response to light compared with LK, but, in this case, light was found to inhibit rather than activate the channel conductance (fig. S2B). Moreover, the effect of light was reversible and it did not decrease after repetitive exposures. The light sensitivity of the channel was wavelength-specific, elicited by blue but not by red light (fig. S2B). The dynamic range of the light effect (DR), i.e., the ratio between light and dark current, was approximately 1.3. To improve the performance of myLK, three point

[1]Department of Biosciences, University of Milano, Italy. [2]Institute of Molecular, Cell and Systems Biology, University of Glasgow, UK. [3]Department of Plant Pathology and Nebraska Center for Virology, University of Nebraska-Lincoln, Lincoln, NE 68583-0900, USA. [4]Membrane Biophysics, Technical University of Darmstadt, Darmstadt, Germany.
*Present address: Illumina Italy, Via Senigallia 18/2, Milano 20161, Italy. †Corresponding author. E-mail: anna.moroni@unimi.it

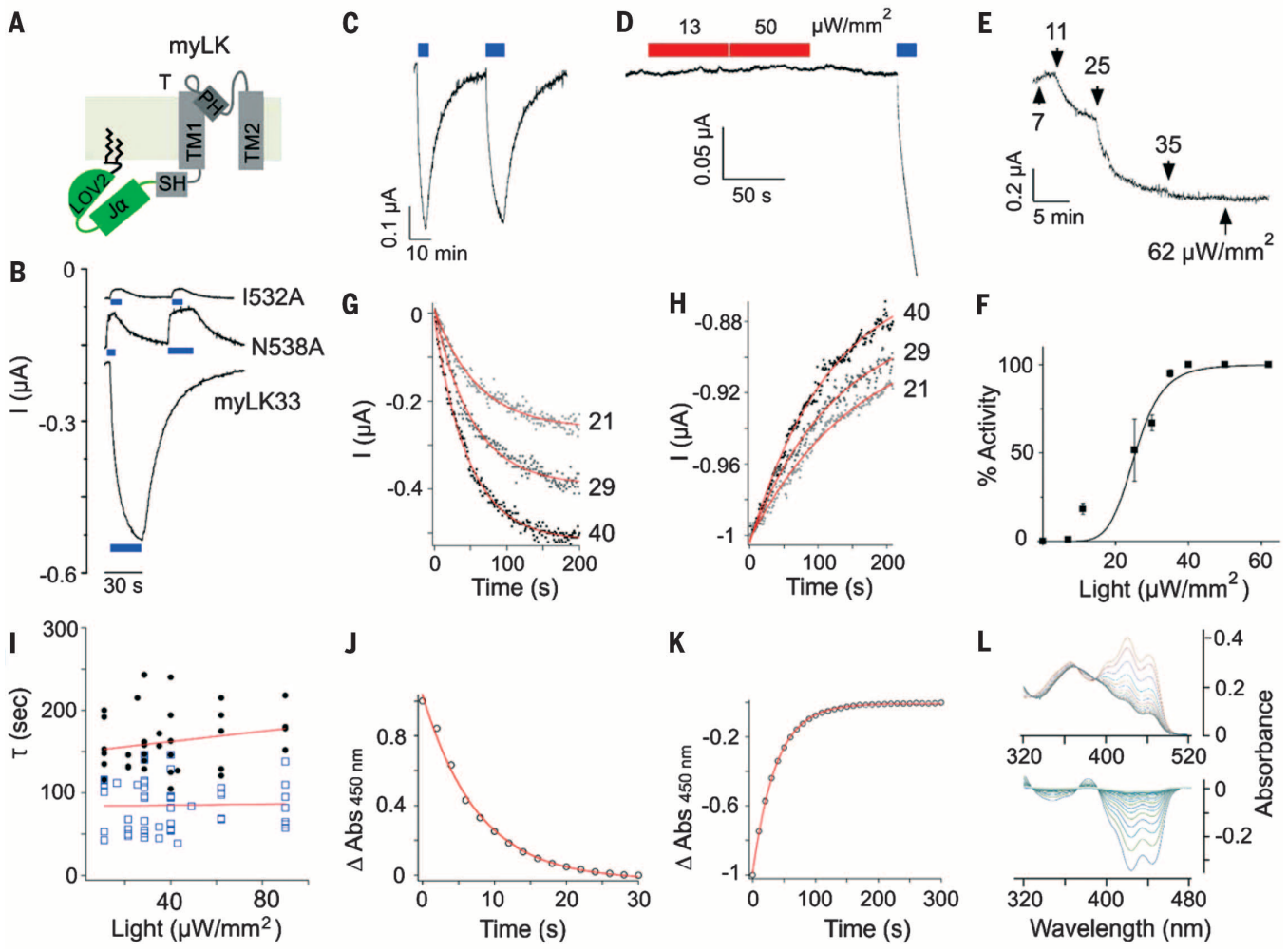

Fig. 1. Engineering and functional characterization of light-gated myLK channels. (**A**) Cartoon representation of myLK engineered by fusing LOV to Kcv with an additional N terminal myristoylation/palmitoylation sequence; myLK is shown as a monomer in the membrane. Kcv comprises slide helix (SH), pore-helix (PH), turret (T), and transmembrane domains (TM1 and TM2) (*23*). The LOV domain includes LOV2 and Jα (*10*). Jagged lines indicate lipid anchoring to the membrane. (**B**) Currents recorded at −60 mV in 100 mM $[K^+]_{out}$, from oocytes expressing myLK mutants: I532A, N538A, and myLK33. Note that myLK I532A and N538A conductances are inhibited by blue light (blue bars, 455 nm), whereas that of myLK33 is activated. (**C**) Repetitive photoactivation of myLK33 shows the reproducibility of the effect. (**D**) Red light (red bars, 617 nm) at two light intensities, 13 and 50 μW/mm^2, does not activate myLK33 current, whereas blue light does. (**E**) Current response of myLK33 to increasing light intensities recorded at −80 mV showing threshold (>7 μW/mm^2) and saturating (35 μW/mm^2) values of light intensity. (**F**) Dose-response curve obtained from $n = 4$ oocytes. Line indicates data fitting by a Hill-type equation, yielding a dissociation constant $k = 25$ μW/mm^2 and a Hill coefficient $n = 6$. (**G**) Kinetics of myLK33 activation by different intensities of blue light and (**H**) subsequent inactivation in the dark. An oocyte expressing myLK33 was exposed to a repetitive light/dark regime with increasing light intensities ranging from low (21 μW/mm^2) to medium (29 μW/mm^2) to saturating (40 μW/mm^2) intensities. The current responses to the three light treatments are normalized to common starting values $I = 0$ for the onset of channel activation and $I = -1$ for the start of current decay in the dark; numbers on current traces indicate the light intensities in μW/mm^2. Fitting of data with single exponential equation (red lines) yields similar τ_{on} values for low (21 μW/mm^2, $\tau = 49$ s), medium (29 μW/mm^2, $\tau = 52$ s), and high (40 μW/mm^2, $\tau = 59$ s) light intensity. Currents decay in the dark with the same velocity, irrespective of pretreatment with a high ($\tau = 148$ s), medium ($\tau = 137$ s), or low ($\tau = 158$ s) light. (**I**) τ_{on} (blue symbols) and τ_{off} (black symbols) from a large number of independent experiments plotted as a function of light intensity. (**J**) Photoadduct formation kinetics for myL (construct 13, table S1) expressed and purified from *Escherichia coli*. Light-induced absorption changes were recorded at 450 nm ($\Delta Abs_{450\ nm}$) in response to blue-light irradiation (455 nm, 90 μW/mm^2) and show exponential kinetics ($\tau_{on} = 7.6$ s). (**K**) Dark recovery of $Abs_{450\ nm}$ after light excitation shows exponential kinetics ($\tau_{off} = 38$ s). (**L**) Representative light-induced absorption spectra of myL recorded at 2-s intervals (upper panel) and light-minus-dark difference spectra recorded every 10 s (lower panel).

mutations (G528A, I532A, and N538A) known to augment LOV-effector protein interactions (*15*) were introduced into the construct, singly or in combination (constructs 15 to 21, table S1). Several of these variants exhibited robust differential growth over a range of selective conditions (fig. S3). Notably, two mutants, myLKI532A and myLKN538A, had increased DR values, 1.5 and 1.9, respectively (Fig. 1B), confirming that myLK architecture enables rational protein design.

To screen for additional DR improvements, random mutagenesis was performed using myLKN538A to generate a library of myLK-encoding sequences. Potassium transport–deficient yeasts, transformed with this mutant library, were grown initially on nonselective agar plates and then replica-plated onto selective medium before exposure to darkness or light. Yeast expressing the parental myLKN538A channel did not grow on media with $[K^+]_{out}$ below 4 mM. Thus, variants growing below this concentration were selected for further characterization. Thirty-five variants were obtained showing strong differential growth in the light (either

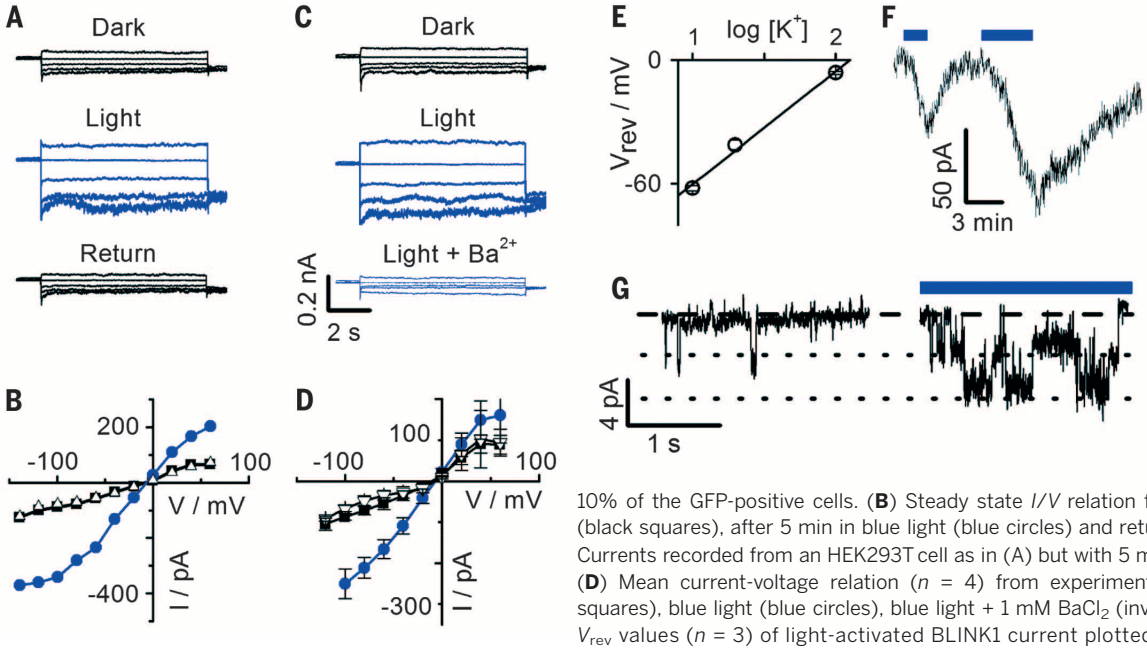

Fig. 2. Properties of BLINK1 in HEK293T cells. (**A**) Whole-cell currents recorded in HEK293T cells expressing myLJSK (BLINK1), in dark, blue light (455 nm, 40 μW/mm^2) and after returning to the dark. Voltage steps from +60 to –120 mV, tails at –80 mV (selected traces are shown every 40 mV). A measurable current, above the background, was found in about 8 to 10% of the GFP-positive cells. (**B**) Steady state *I/V* relation from currents in (A): dark (black squares), after 5 min in blue light (blue circles) and return in dark (triangles). (**C**) Currents recorded from an HEK293T cell as in (A) but with 5 mM of $BaCl_2$ added in light. (**D**) Mean current-voltage relation (n = 4) from experiments as in (B): dark (black squares), blue light (blue circles), blue light + 1 mM $BaCl_2$ (inverted triangles). (**E**) Mean V_{rev} values (n = 3) of light-activated BLINK1 current plotted as a function of $[K^+]_{out}$; slope = 58 mV/log $[K^+]$. Pipette solution contained 130 mM K^+. (**F**) Repetitive activation/deactivation of BLINK1 current at –70 mV by blue light/dark transitions. (**G**) Single-channel fluctuations recorded at –70 mV from the same BLINK1-expressing cell in dark (left) and in blue light (right). Dashed line indicates zero current level; dotted lines indicate apparent single-channel opening levels. Calculated single-channel conductance is 70 pS.

activation or inhibition), 13 of which survived a second round of selection (to eliminate false positives) and were sequenced. The recovered mutations mapped throughout the randomized portion of myLK, but a subset clustered around proline 13 of Kcv (fig. S4), a residue known to affect channel gating (*16*). Notably, one particular variant, myLK33 (construct 33, fig. S4), harboring a mutation in P13 (P13L) and in the myristoylation/palmitoylation sequence (A7T), was activated rather than inhibited by light, with a relatively large DR value (DR = 3) (Fig. 1B). MyLK33 was therefore chosen for extensive functional characterization.

The channel could be repeatedly activated by light when expressed in oocytes without undergoing apparent inactivation (Fig. 1C). Activation was blue-light specific because red light had no perceivable effect on channel activity (Fig. 1D). By exposing the oocyte to increasing light intensities (Fig. 1E), we obtained a sigmoidal current response with a distinct activation threshold (Fig. 1F). The mean dose-response curve was best fitted with a Hill function yielding a value for half-activation, k = 25 μW/mm^2, and a Hill coefficient n = 6. This operational light sensitivity of the cell is less by a factor of about 500 than that of cells expressing light-sensitive pumps such as NpHR (*17*).

To obtain information on the kinetics of channel activation/deactivation in light/dark, cells were irradiated with different intensities of blue light and transferred back into darkness. Activation and deactivation kinetics could be fitted with a single exponential function (Fig. 1, G and H). The time constants did not change over a wide range of light intensities, from suboptimal to saturating (Fig. 1I). Activation (τ_{on}, 87 ± 28 s, n = 52) was about twice as fast as deactivation (τ_{off} 168 ± 31 s, n = 43). To further examine the relationship between channel gating and the photocycle of the sensor, we performed spectroscopic measurements on the sensor portion of the protein (myL), which was used to construct the channel. Global photoadduct formation at saturating light intensity (90 μW/mm^2) and its recovery in the dark (Fig. 1, J to L) show exponential kinetics with values of 7.6 s for τ_{on} and 38 s for τ_{off}. Hence, myL activates, under the same light conditions, about 10 times as fast as the channel, whereas photoadduct decay is about 4.5 times as fast as channel deactivation in the dark. Thus, the primary light sensing by the photosensor seems to be only loosely correlated with channel gating. This agrees with the observation that other constructs harboring the same photoswitch as myLK33 (see, for example, I532A and N538A) responded to light with a different kinetics (Fig. 1B). Together, these findings suggest that light-regulated channel activity is mostly dominated by slow conformational changes that follow LOV2-Jα photo activation.

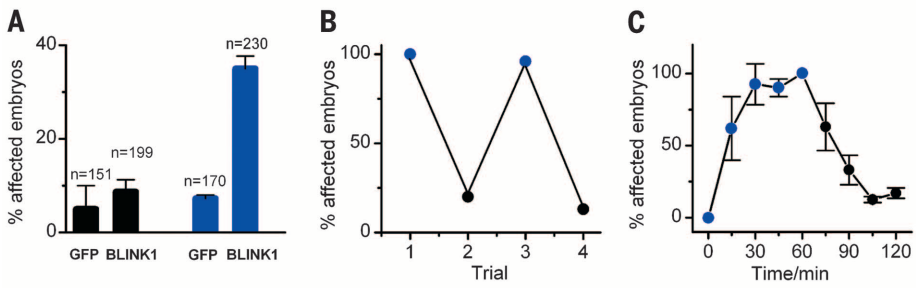

Fig. 3. Light controls the behavior of zebrafish expressing BLINK1. (**A**) Altered escape response in 2-day-old zebrafish, expressing BLINK1 or GFP. The embryos were injected at t_0, kept 24 hours in the dark, and then either exposed to blue light (80 μW/mm^2) (blue) or kept in the dark (black). The escape response was tested by gentle mechanical stimulation with a pipette tip (see movie S1). Number of embryos (n) is indicated. (**B**) Reversibility of the effect of blue light on the escape response. Each data point represents the response of a batch of 2-day-old BLINK1-injected embryos, preselected for positive light response (n = 15). The embryos were repetitively exposed to blue light (blue circles) and dark (black circles) treatments (30 to 45 min each). (**C**) Kinetics of the light effect on the escape response of 2-day-old embryos. At time zero, blue light was turned on and the response to mechanical stimulation was checked every 15 min. After 60 min, the effect reached the maximum and the light was turned off to monitor the deactivation kinetics. Data are from three experiments in which the n of responding embryos was 62 over a total number of 163 (38%). Data were normalized to the maximum number of responding embryos at plateau in each experiment (after 60 min of light).

Experimental evidence that myLK33 retains the pore properties of the parental K^+-selective channel Kcv is summarized in fig. S5. Barium, a known Kcv channel blocker, completely inhibited both dark- and light-induced currents of myLK33 (fig. S5A). The current-voltage (*I-V*) curve (fig. S5B) shows that light activation of myLK33 is voltage-independent. The reversal potentials (V_{rev}) of myLK33 photocurrent shifted according to the Nernst equation by 51 mV for a 10-fold increase in external K^+ concentration, a value similar to that of Kcv (*11*) (fig. S5C). Moreover, exchanging 100 mM external K^+ with Na^+ shifted V_{rev} to the left by 110 mV, indicating a very low Na^+ permeability (P_{Na}/P_K = 0.015 ± 0.001 (n = 4) (fig. S5D).

Despite these desirable features, in vivo application of myLK33 is hampered by its high dark activity. We have previously shown in other synthetic channels that the linker between the sensor and the effector module influences the coupling of the two (*4*). We therefore progressively reduced the linker region within myLK in an attempt to improve the control of the photosensor over the channel pore (constructs 23 to 37 in table S1 and fig. S6). Best results were obtained with myLJSK, which lacks the final nine amino acid residues within the Jα helix (fig. S7A). This variant showed stringent differential growth in the yeast complementation assay (fig. S7B) but was poorly expressed in oocytes. Immunolabeling showed that this channel is present on the membrane of human embryonic kidney 293T (HEK293T) cells, albeit at a moderate level, when compared with the parental channel Kcv (fig. S7C). Subsequent electrophysiological characterization in HEK293T cells demonstrated that myLJSK is activated by blue light (Fig. 2, A and B). Light activation is fully reversible in the dark (Fig. 2, A and B) and inhibited by Ba^{2+} (Fig. 2, C and D). Importantly, myLJSK lacks any channel activity in darkness, as evident from the comparison of the amount of current in the dark and in the presence of Ba^{2+} (fig. S7D). Channel opening moves the reversal potential of the cell with E_K, the K^+ equilibrium voltage (Fig. 2E). The light sensitivity of myLJSK occurs in the same range as that of myLK33, being saturated at ~60 $\mu W/mm^2$ (fig. S7E).

Light gating of myLJSK is best appreciated in gap-free recordings. Repetitive exposure to blue light caused rapid activation followed by deactivation in darkness (Fig. 2F). Data recorded from single-channel fluctuations (Fig. 2G) showed a light-induced increase in channel activity and indicated a unitary conductance of about 70 pS, consistent with the high conductance of Kcv and its synthetic variant Kv_{Synth1} (*4*). The high single-channel conductance and the relatively low macroscopic currents (≤400 pA at −100 mV) are consistent with the low number of channels, which were detectable by immunolocalization (fig. S7C). A low number of channel proteins with a large unitary conductance offers the advantage of an efficient control over the membrane voltage with minimal disturbance of the cell. These properties of myLJSK ultimately fulfilled our criteria for successful light gating of Kcv. Hence, we renamed this variant BLINK1, blue-light–induced K^+ channel 1. Expression of BLINK1 in Sf9 insect cells (fig. S8A) produced fluorescence properties that are characteristic for LOV-containing proteins (fig. S8, B and C). Photoadduct formation and decay for BLINK1 was therefore analyzed by fluorescence spectroscopy and showed kinetics similar to those obtained for myLOV in vitro (14.5 s for τ_{on} and 51s for τ_{off}) (fig. S8, D and E).

To determine the in vivo applicability of BLINK1 for optogenetics, we examined its ability to regulate the escape response of zebrafish embryos. Two-day old embryos respond to touch with a burst of swimming (*18*). We reasoned that BLINK1 photoactivation in zebrafish neurons (either somatosensory or motor) and/or in myocytes would prevent or drastically impair this behavior. Embryos injected with either BLINK1 or green fluorescent protein (GFP) RNA showed robust escape motions when kept in darkness [over 90% of embryos in both cases (BLINK1, n = 199; GFP, n = 151)]. By contrast, when embryos were exposed to blue light, 37% of BLINK1-expressing embryos exhibited a reduced escape response (n = 230) compared with just 9% in control larvae (n = 170) (Fig. 3A and movie S1). The blue-light effect was fully and repetitively reverted in darkness (Fig. 3B), as expected for a BLINK1-driven effect. The light-driven effect on embryonic escape motion developed with a half-time of 15 to 20 min and was reverted by dark with a similar kinetics (Fig. 3C).

Several additional observations underscored that BLINK1 was expressed in zebrafish and that altered behavior of the larvae was driven directly by its activation in blue light. First, the presence of the channel is detectable by Western blotting in BLINK1-injected embryos (fig. S9A). Second, the success of eliciting escape behavior was highly dependent on the wavelength of light with red light (617 nm) being ineffective at evoking altered behavior (fig. S9B). Third, in the dark, viability and morphology were similar in embryos expressing BLINK1 or GFP (wild-type embryos at 2dpf BLINK1 = 77%, n = 81; GFP = 69%, n = 59), confirming that BLINK1 is tightly closed in the absence of light. Taken together, these data demonstrate the ability of BLINK1 to modulate behavioral responses in vivo.

In conclusion, we have created a light-activated K^+ selective channel by combining a blue-light sensor and a simple K^+ channel pore. The resulting BLINK1 channel is fully genetically encoded and does not depend on external factors for its light regulation, as the flavin mononucleotide chromophore is ubiquitously present in cells. BLINK1 is therefore a promising tool in optogenetics and has several desirable properties relative to other light-gated pumps (*17*, *19*, *20*) and channels (*21*, *22*) used for inhibiting the functions of excitable cells. First, in contrast to light-gated pumps, which move H^+ or Cl^- ions, it moves K^+, a physiological ion, down its electrochemical equilibrium. Thus, BLINK1 does not expose the cell to unphysiological hyperpolarizations or ion gradients. Second, its large unitary conductance guarantees that a small number of channels can efficiently decrease the input resistance of cells and hyperpolarize the membrane. In addition, the channel does not inactivate in light, which allows long-term control of channel activity by light. The apparent sensitivity of BLINK1 to light, combined with its slow kinetics, makes it a powerful tool for long-term inhibition of cells at low light intensities. Our pilot experiments in zebrafish demonstrate that BLINK1 can be successfully used as an in vivo optogenetic tool. Besides an obvious application for inhibiting neuronal activity, this channel will also find applications in the control of cellular processes, which require long-term stabilization of the membrane voltage such as cell cycle regulation or the control of hormone secretion.

REFERENCES AND NOTES

1. S. B. Long, E. B. Campbell, R. Mackinnon, *Science* **309**, 897–903 (2005).
2. R. Latorre, F. J. Morera, C. Zaelzer, *J. Physiol.* **588**, 3141–3148 (2010).
3. U. M. Ohndorf, R. MacKinnon, *J. Mol. Biol.* **350**, 857–865 (2005).
4. C. Arrigoni *et al.*, *J. Gen. Physiol.* **141**, 389–395 (2013).
5. M. R. Banghart, M. Volgraf, D. Trauner, *Biochemistry* **45**, 15129–15141 (2006).
6. M. Banghart, K. Borges, E. Isacoff, D. Trauner, R. H. Kramer, *Nat. Neurosci.* **7**, 1381–1386 (2004).
7. H. Janovjak, S. Szobota, C. Wyart, D. Trauner, E. Y. Isacoff, *Nat. Neurosci.* **13**, 1027–1032 (2010).
8. J. Y. Kang *et al.*, *Neuron* **80**, 358–370 (2013).
9. D. Schmidt, P. W. Tillberg, F. Chen, E. S. Boyden, *Nat. Commun.* **5**, 3019 (2014).
10. J. M. Christie, *Annu. Rev. Plant Biol.* **58**, 21–45 (2007).
11. B. Plugge *et al.*, *Science* **287**, 1641–1644 (2000).
12. J. M. Christie, J. Gawthorne, G. Young, N. J. Fraser, A. J. Roe, *Mol. Plant* **5**, 533–544 (2012).
13. F. C. Chatelain *et al.*, *PLOS ONE* **4**, e7496 (2009).
14. C. Aicart-Ramos, R. A. Valero, I. Rodriguez-Crespo, *Biochim. Biophys. Acta* **1808**, 2981–2994 (2011).
15. D. Strickland *et al.*, *Nat. Methods* **7**, 623–626 (2010).
16. B. Hertel *et al.*, *Eur. Biophys. J.* **39**, 1057–1068 (2010).
17. J. Mattis *et al.*, *Nat. Methods* **9**, 159–172 (2011).
18. R. M. Colwill, R. Creton, *Rev. Neurosci.* **22**, 63–73 (2011).
19. F. Zhang *et al.*, *Nature* **446**, 633–639 (2007).
20. X. Han, E. S. Boyden, *PLOS ONE* **2**, e299 (2007).
21. A. Berndt, S. Y. Lee, C. Ramakrishnan, K. Deisseroth, *Science* **344**, 420–424 (2014).
22. J. Wietek *et al.*, *Science* **344**, 409–412 (2014).
23. S. Tayefeh *et al.*, *Biophys. J.* **96**, 485–498 (2009).

ACKNOWLEDGMENTS

We thank G. Romani for providing the antibody to Kcv; D. Minor for the *Saccharomyces cerevisiae* SGY1528 strain; U. P. Hansen, I. Schroeder, and A. Bertl for helpful discussion; and M. Ascagni for technical help with confocal microscopy. This work was supported by Fondazione Cariplo grant 2009-3519, PRIN (Programmi di Ricerca di Rilevante Interesse Nazionale) 2010CSJX4F, and MAE (Ministero Affari Esteri) 01467532013-06-27 to A.M.; by the UK Biotechnology and Biological Sciences Research Council (BB/J016047/1 and BB/M002128) to J.M.C.; and by the Landes-Offensive zur Entwicklung Wissenschaftlich-ökonomischer Exzellenz (LOEWE) initiative Soft Control to G.T.

SUPPLEMENTARY MATERIALS

www.sciencemag.org/content/348/6235/707/suppl/DC1
Materials and Methods
Figs. S1 to S9
Table S1
Movie S1
References (*24–31*)

11 November 2014; accepted 7 April 2015
10.1126/science.aaa2787

MALARIA

A forward genetic screen identifies erythrocyte CD55 as essential for *Plasmodium falciparum* invasion

Elizabeth S. Egan,[1,2] Rays H. Y. Jiang,[1,3] Mischka A. Moechtar,[1] Natasha S. Barteneva,[4] Michael P. Weekes,[5] Luis V. Nobre,[5] Steven P. Gygi,[6] Joao A. Paulo,[6] Charles Frantzreb,[1] Yoshihiko Tani,[7] Junko Takahashi,[7] Seishi Watanabe,[8] Jonathan Goldberg,[1] Aditya S. Paul,[1] Carlo Brugnara,[9] David E. Root,[10] Roger C. Wiegand,[10]* John G. Doench,[10] Manoj T. Duraisingh[1,10]†

Efforts to identify host determinants for malaria have been hindered by the absence of a nucleus in erythrocytes, which precludes genetic manipulation in the cell in which the parasite replicates. We used cultured red blood cells derived from hematopoietic stem cells to carry out a forward genetic screen for *Plasmodium falciparum* host determinants. We found that CD55 is an essential host factor for *P. falciparum* invasion. CD55-null erythrocytes were refractory to invasion by all isolates of *P. falciparum* because parasites failed to attach properly to the erythrocyte surface. Thus, CD55 is an attractive target for the development of malaria therapeutics. Hematopoietic stem cell–based forward genetic screens may be valuable for the identification of additional host determinants of malaria pathogenesis.

Severe malaria is caused by *Plasmodium falciparum* and is one of the leading causes of mortality among children globally (*1*). During infection, parasites invade and replicate within human erythrocytes (*2*). Host erythrocyte polymorphisms that confer resistance to severe malaria have been identified with epidemiologic approaches (*3*, *4*). Genome-wide association studies have searched for host determinants of malaria, but functional validation in the erythrocyte remains challenging owing to the absence of a nucleus (*5*–*7*). Recent advances in the ex vivo production of erythrocytes now enable generation of genetically altered cells that support *P. falciparum* infection (*8*–*11*). Here, we used ex vivo–cultured red blood cells (cRBCs) in a forward genetic screen in order to identify host determinants of malaria infection.

The human erythrocyte is a terminally differentiated minimal cell that lacks organelles and a nucleus and has a small proteome (*12*). To identify erythrocyte proteins that influence *P. falciparum* infection, we designed a screening strategy involving RNA interference (RNAi)–based knockdown of gene expression in hematopoietic progenitor cells, induction of ex vivo erythropoiesis, and last, infection of terminally differentiated erythroblasts with *P. falciparum*. Because gene knockdowns that affect erythroid development could have potent yet nonspecific effects on parasites in this approach, we first screened the erythrocyte proteome so as to identify genes that influence

[1]Department of Immunology and Infectious Diseases, Harvard T. H. Chan School of Public Health, Boston, MA, USA. [2]Division of Infectious Diseases, Boston Children's Hospital, Boston, MA, USA. [3]Department of Global Health and Center for Drug Discovery and Innovation, University of South Florida, Tampa, FL, USA. [4]Department of Pediatrics, Harvard Medical School and Program in Cellular and Molecular Medicine, Boston Children's Hospital, Boston, MA, USA. [5]Cambridge Institute for Medical Research, University of Cambridge, Cambridge, UK. [6]Department of Cell Biology, Harvard Medical School, Boston, MA, USA. [7]Japanese Red Cross Kinki Block Blood Center, Osaka, Japan. [8]Japanese Red Cross Kyushu Block Blood Center, Fukuoka, Japan. [9]Department of Laboratory Medicine, Boston Children's Hospital and Harvard Medical School, Boston, MA, USA. [10]The Broad Institute of Harvard and Massachussetts Insititute of Technology, Cambridge, MA, USAA.
*Present address: Preceres, Cambridge, MA, USA.
†Corresponding author. E-mail: mduraisi@hsph.harvard.edu

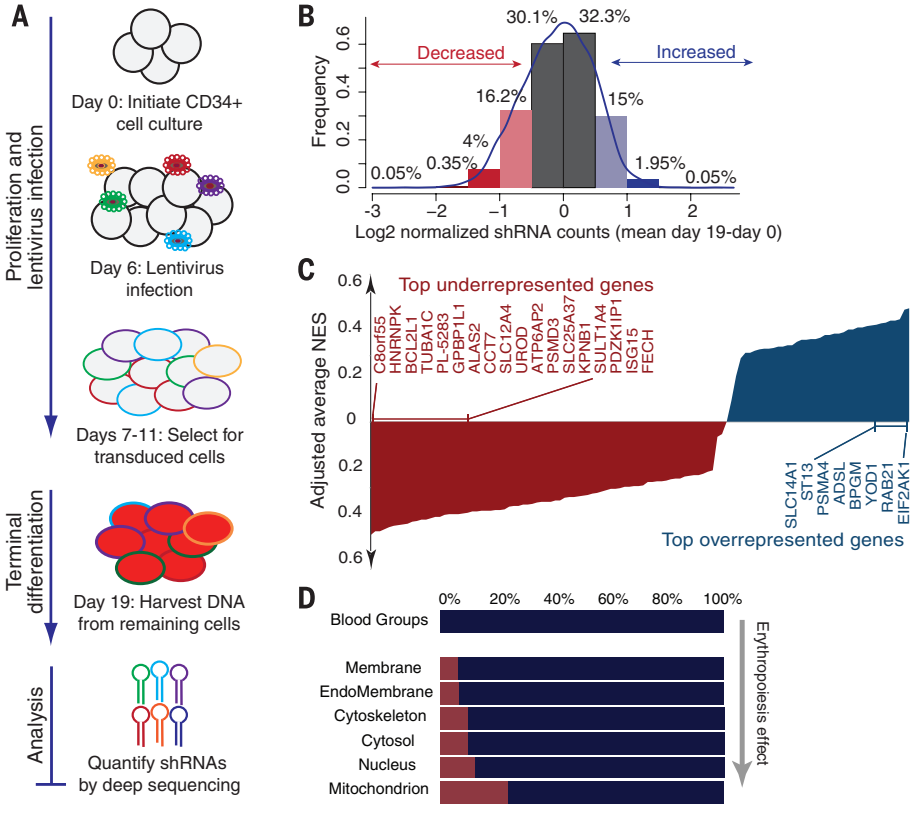

Fig. 1. Pooled shRNA screen for genes that regulate terminal erythroid differentiation. (**A**) Schematic of pooled shRNA screen. CD34$^+$ HSCs were induced toward erythroid development, transduced with shRNA library on Day 6, and selected with puromycin. On day 19, shRNA proviruses in orthochromatic erythroblasts were quantified by means of Illumina (San Diego, CA) sequencing. (**B**) Change in relative abundance of 5530 shRNAs in erythrocyte proteome library after 19 days of differentiation. (**C**) RNAi gene enrichment ranking (RIGER) analysis of 116 candidate genes based on magnitude of erythropoiesis phenotype. NES, normalized enrichment score. (**D**) Predicted localization of library components, with percent of genes that influence erythropoiesis in red.

terminal differentiation of erythrocytes (Fig. 1A, fig. S1A, and data set S1). CD34$^+$ hematopoietic stem cells (HSCs) were transduced with our pooled erythrocyte proteome short hairpin RNA (shRNA) library and induced to proliferate and differentiate to the orthochromatic erythroblast stage (when parasite infection can occur) (*13*). After 19 days, we quantified each shRNA in the surviving orthochromatic erythroblasts relative to the original library, with the prediction that shRNAs underrepresented in the differentiated erythroblasts would target genes important for erythropoiesis.

The erythropoiesis screen yielded sufficient cells for full coverage of the library (>1500 cells per shRNA) (fig. S1B) (*14*), and deep sequencing of shRNA proviruses isolated from the terminally differentiated erythroid cells revealed a normal distribution (fig. S1C). Of shRNAs, 4.4% were depleted more than 50% in day-19 cRBCs relative to the original library pool, whereas 2% were enriched (Fig. 1B), indicating that these shRNAs can influence erythropoiesis. We ranked genes according to the depletion or enrichment of multiple shRNAs (*15*) and identified 116 candidates that grouped into categories relevant to terminal erythroid differentiation, including heme metabolism, protein turnover, and apoptosis (Fig. 1C, figs. S1D and S2, and data sets S2 and S3). We validated four top hits (fig. S3 and data set S4). This functional analysis of erythropoiesis provides a framework with which to study host determinants of malaria infection.

To identify factors that influence host susceptibility to *P. falciparum* infection, we chose to focus on a small subset of the erythrocyte proteome: 42 genes encoding human blood groups. All known *P. falciparum* receptors fall within this group, and the shRNAs targeting these genes did not appear to affect erythroid development (Fig. 1D). Also, focusing on a small gene set increased the sensitivity to a level required for the inherently complex parasite screen (*16*).

We transduced hematopoietic progenitor cells (HPCs) with a pooled lentivirus shRNA library targeting the blood group genes (Fig. 2A). At the late orthochromatic erythroblast stage, we infected the knockdown cells with a green fluorescent protein (GFP)–expressing line of *P. falciparum* strain 3D7. We isolated the parasitized cells and quantified the relative abundance of each shRNA in the population by means of deep sequencing (fig. S4). In parallel, we quantified the abundance of each shRNA in a control population of knockdown cRBCs not exposed to parasites. Hairpins

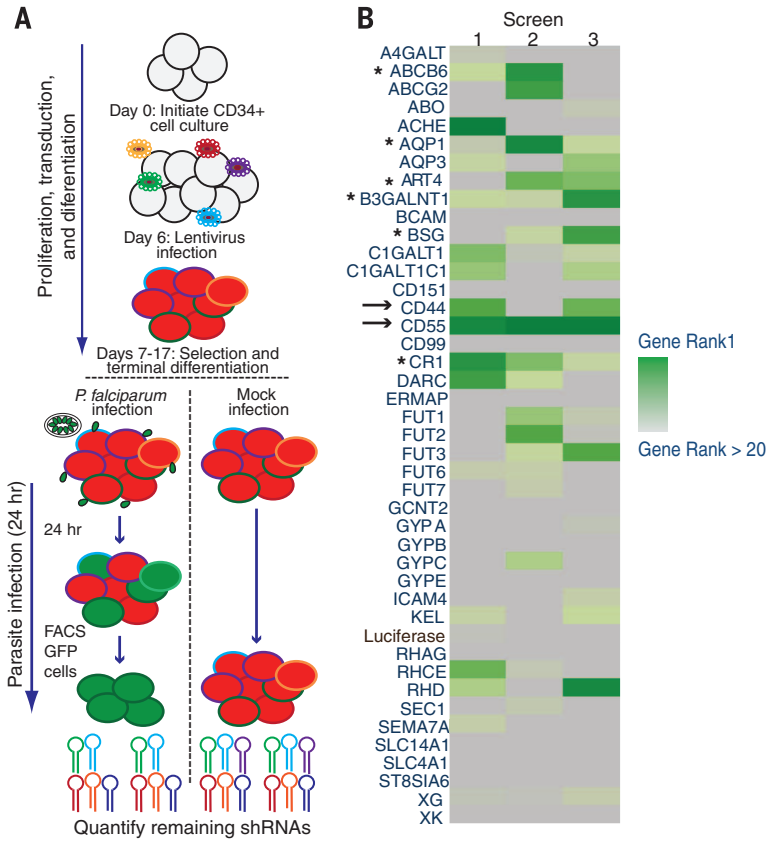

Fig. 2. Pooled shRNA screen to identify host determinants of *P. falciparum* infection. (**A**) Schematic of blood group shRNA screen. HPCs were transduced with pooled lentivirus library expressing 308 shRNAs targeting 42 blood group genes. Knockdown cRBCs infected with *P. falciparum* were sorted, and shRNAs were quantified by means of deep sequencing. (**B**) RIGER analysis ranking results for three independent experiments. Genes were ranked according to NES scores (green heat map). Arrows indicate top hits; asterisks indicate additional candidates.

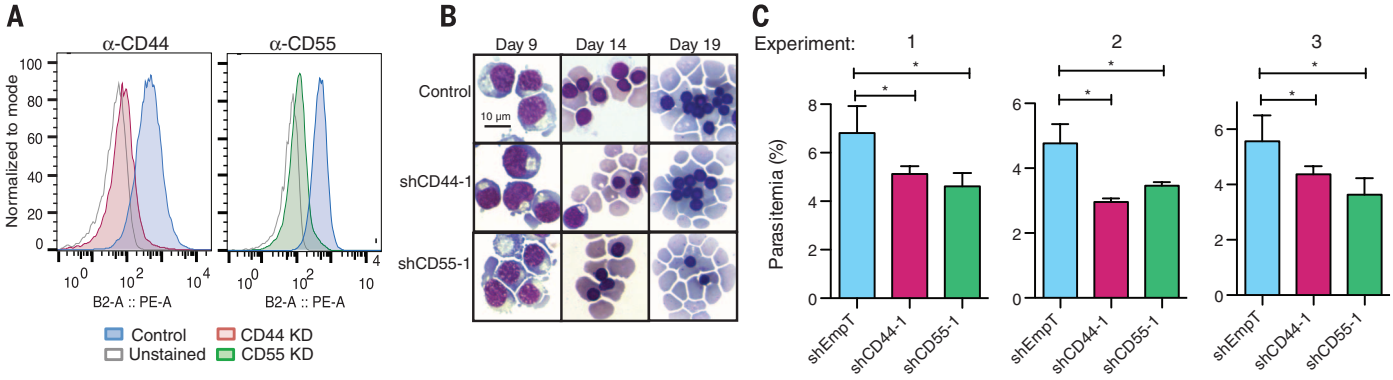

Fig. 3. Validation of CD44 and CD55 as host factors required for *P. falciparum* invasion. (**A**) CD44 and CD55 levels on day 19/20 cRBCs expressing CD44, CD55, or control shRNAs (EmpT). Detection was performed by means of antibody staining and flow cytometry. (**B**) Morphology of differentiating cRBCs depleted for CD44 and CD55, detected by means of May-Grünwald and Giemsa staining. (**C**) *P. falciparum* strain 3D7 invasion assays in control, CD44 knockdown, and CD55 knockdown cRBCs. Three independent biological replicates from two distinct bone marrow donors are shown. Mean ± SD, $n = 2$ or 3 assays. *$P < 0.05$, one-tailed t test.

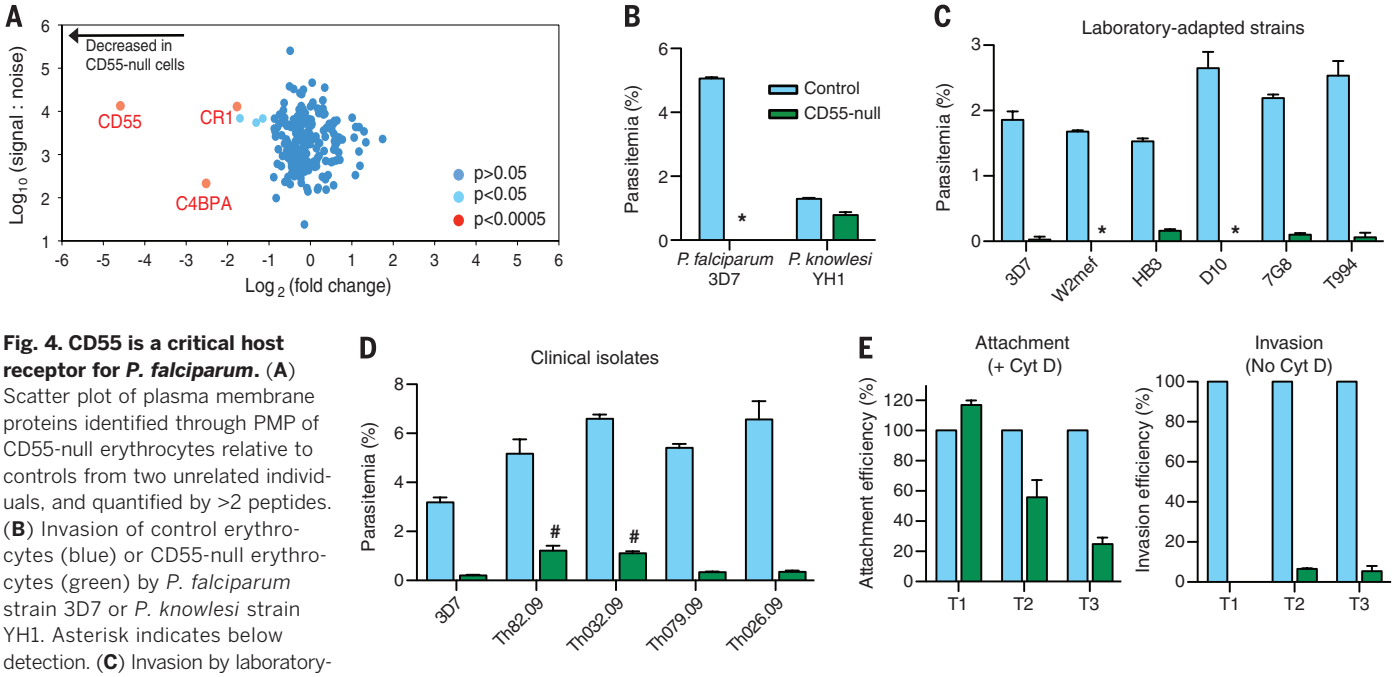

Fig. 4. CD55 is a critical host receptor for *P. falciparum*. (**A**) Scatter plot of plasma membrane proteins identified through PMP of CD55-null erythrocytes relative to controls from two unrelated individuals, and quantified by >2 peptides. (**B**) Invasion of control erythrocytes (blue) or CD55-null erythrocytes (green) by *P. falciparum* strain 3D7 or *P. knowlesi* strain YH1. Asterisk indicates below detection. (**C**) Invasion by laboratory-adapted *P. falciparum* strains. (**D**) Invasion by *P. falciparum* clinical isolates. Pound sign indicates thin smears showed 0.6 to 1% gametocytes. For (B) to (D), mean ± SD, $n = 3$ assays. 10,000 cells scored per well by means of flow cytometry. (**E**) Efficiency of *P. falciparum* 3D7 merozoite attachment to the surface of CD55-null (green) versus control (blue) RBCs by using cytochalasin D (Cyt D). Invasion was measured in the absence of Cyt D. T1, 30 min; T2, 60 min; and T3, 180 min after addition of schizonts (fig. S10). Attachment to controls at T1 was 3.6 to 5.3%. Mean ± SD, $n = 2$ biological replicates. 20,000 cells scored per well by means of flow cytometry.

underrepresented in infected cells compared with control cells were considered hits because they may target host genes required for efficient parasite infection.

We ranked candidates from three replicates (Fig. 2B and data set S5) (*15*). Among the highly ranked genes were basigin (BSG) and CR1, both of which have described roles in *P. falciparum* invasion (*17*–*19*). The top-ranked candidate was CD55, also known as decay-accelerating factor (DAF), which carries the Cromer blood group antigens. CD55 is a glycosylphosphatidylinositol-linked complement-regulatory protein that protects cells from lysis by complement (*20*). On epithelial cells, CD55 is a receptor for bacterial and viral pathogens (*21*–*23*). Another hit, CD44, defines the Indian blood group and facilitates keratinocyte invasion by group A *Streptococcus* (*24*, *25*).

For validation, we expressed individual shRNAs targeting CD44 and CD55 in HPCs so as to generate mature red blood cells deficient in CD44 or CD55 (Fig. 3A). Morphological development of the knockdown cells was indistinguishable from control cRBCs (Fig. 3B), as were levels of Band 3, CD49d, and CD71 (fig. S5) (*26*). To determine whether the amount of CD44 or CD55 on red blood cells influences *P. falciparum* infection, we assessed parasite invasion into the knockdown cRBCs compared with control cRBCs. We observed ~30% reduction in parasitemia in cells deficient for either CD44 or CD55 relative to control cRBCs (Fig. 3C). The same trend was observed by using alternative shRNAs for CD44 and CD55, suggesting that the results were not because of off-target effects of the shRNAs (fig. S6). Levels of known

Table 1. Geographic distribution of CD55* coding variants as percent of population, from the 1000 Genomes Project, phase I. CD55 isoform ENST00000367064 (DAF-2).

ΔAA*		R52L	L82R	Y133H	A227P	I231V	V333I	G354A	G372E
IΣBT†		CROM3	CROM8		CROM1				
Pops(1092)‡	Exp§								
Aggr(688)	low	0	0	0	00	0	0	0	0
TSI(98)	low	0	0	0	00	1.02	0	0	0
ASW(61)	high	4.92	0	1.64	01.64	0	0	0	0
CLM(60)	high	0	0	0	03.33	0	0	0	1.67
LWK(97)	high	0	0	0	14.43	0	0	1.03	0
YRI(88)	high	5.68	1.14	0	01.14	0	1.14	0	0
P value‖		3.56×10^{-5}	0.28	0.28	7.85×10^{-11}	1	0.28	0.28	0.28

*Amino acid change and location; reference single-nucleotide polymorphism numbers are given in (*13*). †International Society of Blood Transfusion type. ‡Populations: Aggr, aggregated populations with no variant in sample (CHS, Southern Han Chinese, China; MXL, Mexican Ancestry in Los Angeles, CA; PUR, Puerto Rican in Puerto Rico; CEU, Utah residents with North and West European ancestry; CHB, Han Chinese in Bejing; FIN, Finnish in Finland; GBR, British in UK; IBS, Iberian populations in Spain; JPT, Japanese in Tokyo); TSI, Toscani in Italy; ASW, African Ancestry in Southwest US; CLM, Colombian in Medellin, Colombia; LWK, Luhya in Webuye, Kenya; and YRI, Yoruba in Ibadan, Nigeria. The numbers of individuals sampled are shown in parentheses. §Exposure of current or ancestral population to malaria based on World Health Organization DALY (disability-adjusted life year per 100,000 population) malaria data: high, DALY ≥ 10; low, DALY < 10. ‖Fisher's exact test comparing populations with high and low exposure.

P. falciparum receptors were unchanged in CD44- and CD55-deficient cRBCs, which suggests that the observed effects on invasion were directly attributable to CD44 and CD55 (fig. S7).

Complete absence of Cromer blood group antigens is rare and has been described in nine individuals with the Inab phenotype, most of whom have stop codons in the CD55 coding sequence (*20*). Cells from Inab individuals have normal osmotic fragility, do not undergo hemolysis in vivo, and are not particularly susceptible to complement-mediated lysis (*27*, *28*). We used mature erythrocytes from a Japanese patient with the Inab phenotype (termed CD55-null cells) (*29*) to test whether CD55 has an essential role for *P. falciparum* invasion. To first characterize any inherent differences between the CD55-null and wild-type (WT) control samples, we adapted plasma membrane profiling (PMP) using tandem mass tag-based mass spectrometry for use in erythrocytes (*30*). CD55 was

absent from the Inab erythrocytes (Fig. 4A). Only two other notable differences were found between the CD55-null and WT cells: a 75% reduction in CR1, which is well within the range of natural variation (*19*), and a similar reduction in C4BPA, a serum protein that binds to complement regulatory proteins. Only a weak association has been observed between parasite invasion efficiency and natural variation in CR1 levels, and only when all sialylated proteins have been removed from the cell surface (*18*, *19*).

To determine the contribution of CD55 to *P. falciparum* infection in mature erythrocytes, we used the CD55-null cells in invasion assays. The CD55-null erythrocytes were refractory to invasion by *P. falciparum* strain 3D7, which suggests that host CD55 is essential for parasite infection (Fig. 4B). This finding suggests that the reduced but substantial parasitemia observed in the cells in which CD55 was knocked down depended on residual CD55. The CD55-null cells were similarly nonsusceptible to invasion by additional laboratory-adapted *P. falciparum* strains, including the CR1-independent W2mef line (Fig. 4C). Parasite invasion was also significantly impaired in erythrocytes from a second, unrelated Inab patient with a different genetic basis for the condition (fig. S8A) (*31*). Proliferation of parasites was also diminished in these Inab cells (fig. S8B), which suggests that CD55 would be required to support a productive malaria infection.

Besides laboratory-adapted strains, several clinical isolates of *P. falciparum* from Senegalese patients were also dependent on CD55 for invasion (Fig. 4D), providing additional evidence that CD55 is likely a critical host factor for all *P. falciparum* strains. In contrast to *P. falciparum*, the zoonotic human malaria parasite *P. knowlesi* invaded CD55-null and WT erythrocytes with similar efficiency (Fig. 4B). Thus, CD55 on human erythrocytes may interact with a parasite ligand specific to *P. falciparum* that is not expressed by other malaria parasites. Deletion of known invasion ligands (EBA140, EBA175, EBA181, RH1, RH2a, or RH2b) did not enable parasite invasion in the absence of CD55 (fig. S9).

To determine whether CD55 is involved in attachment of *P. falciparum* to the erythrocyte or at a later stage of the invasion process, we used cytochalasin D to enable isolation of cells with parasites adhered to the outer surface (*32*). Initially, attachment of *P. falciparum* merozoites was similar for the CD55-null and WT cells, but over time, parasites selectively detached from the cells lacking CD55, mirroring the invasion defect (Fig. 4E). Thus, CD55 may not be required for the primary interaction of merozoites with the RBC surface, but instead be critical for the stage of committed, irreversible attachment seen during formation of the tight junction (*33*).

Our results reveal an essential role for CD55 in *P. falciparum* invasion of human red blood cells. Levels of CD55 vary dynamically during clinical malaria and may influence the course of infection (*34*). Moreover, we identified two CD55 polymorphisms significantly enriched in persons with ancestral exposure to malaria (Table 1) (*35*), both of which have been previously described almost exclusively in individuals of African descent (*20*).

The existence of hematologically normal individuals completely lacking CD55 suggests that targeting CD55 on erythrocytes would not elicit substantial toxicity. In light of its critical role in parasite infection, CD55 could serve as an attractive target for the development of malaria therapeutics. Aside from CD55, the only other known strain-transcendent receptor for *P. falciparum*, basigin, binds to RH5, which is a leading malaria vaccine candidate (*17*, *36*, *37*). Our studies also establish the feasibility of forward genetic cellular screening by use of cultured erythrocytes derived from HSCs to identify critical host determinants of *P. falciparum* malaria biology and pathogenesis.

REFERENCES AND NOTES

1. C. J. Murray *et al.*, *Lancet* **379**, 413–431 (2012).
2. R. M. Fairhurst, T. E. Wellems, in *Mandell, Douglas, and Bennett's Principles and Practice of Infectious Diseases*, G. L. Mandell, J. E. Bennett, R. Dolin, Eds. (Churchill Livingstone Elsevier, Philadelphia, 2010), vol. 2, chap. 275, pp. 3437–3462.
3. A. C. Allison, *BMJ* **1**, 290–294 (1954).
4. S. M. Taylor, R. M. Fairhurst, *Curr. Opin. Hematol.* **21**, 193–200 (2014).
5. C. Timmann *et al.*, *Nature* **489**, 443–446 (2012).
6. M. Jallow *et al.*, *Nat. Genet.* **41**, 657–665 (2009).
7. K. A. Rockett *et al.*, *Nat. Genet.* **46**, 1197–1204 (2014).
8. M. C. Giarratana *et al.*, *Nat. Biotechnol.* **23**, 69–74 (2005).
9. M. C. Giarratana *et al.*, *Blood* **118**, 5071–5079 (2011).
10. P. A. Tamez, H. Liu, S. Fernandez-Pol, K. Haldar, A. Wickrema, *Blood* **114**, 3652–3655 (2009).
11. A. K. Bei, C. Brugnara, M. T. Duraisingh, *J. Infect. Dis.* **202**, 1722–1727 (2010).
12. E. M. Pasini *et al.*, *Blood* **108**, 791–801 (2006).
13. Materials and methods are available as supplementary materials on *Science* Online.
14. Ž. Strezoska *et al.*, *PLOS ONE* **7**, e42341 (2012).
15. B. Luo *et al.*, *Proc. Natl. Acad. Sci. U.S.A.* **105**, 20380–20385 (2008).
16. Supplementary text is provided as supplementary materials on *Science* Online.
17. C. Crosnier *et al.*, *Nature* **480**, 534–537 (2011).
18. W. H. Tham *et al.*, *Proc. Natl. Acad. Sci. U.S.A.* **107**, 17327–17332 (2010).
19. C. Spadafora *et al.*, *PLOS Pathog.* **6**, e1000968 (2010).
20. J. R. Storry, M. E. Reid, M. H. Yazer, *Immunohematology* **26**, 109–118 (2010).
21. C. B. Coyne, J. M. Bergelson, *Cell* **124**, 119–131 (2006).
22. B. Nowicki, L. Truong, J. Moulds, R. Hull, *Am. J. Pathol.* **133**, 1–4 (1988).
23. D. P. O'Brien *et al.*, *J. Biol. Chem.* **283**, 23922–23930 (2008).
24. H. M. Schrager, S. Albertí, C. Cywes, G. J. Dougherty, M. R. Wessels, *J. Clin. Invest.* **101**, 1708–1716 (1998).
25. C. Cywes, M. R. Wessels, *Nature* **414**, 648–652 (2001).
26. J. Hu *et al.*, *Blood* **121**, 3246–3253 (2013).
27. M. E. Reid *et al.*, *Blood* **78**, 3291–3297 (1991).
28. A. H. Merry, V. I. Rawlinson, M. Uchikawa, M. R. Daha, R. B. Sim, *Br. J. Haematol.* **73**, 248–253 (1989).
29. J. Takahashi, H. Nagumo, *Japan J. Transf. Cell Ther.* **54**, 359 (2008) (in Japanese).
30. M. P. Weekes *et al.*, *Science* **340**, 199–202 (2013).
31. K. Hue-Roye *et al.*, *Immunohematology* **21**, 53–55 (2005).
32. L. H. Miller, M. Aikawa, J. G. Johnson, T. Shiroishi, *J. Exp. Med.* **149**, 172–184 (1979).
33. A. F. Cowman, D. Berry, J. Baum, *J. Cell Biol.* **198**, 961–971 (2012).
34. M. Gwamaka, M. Fried, G. Domingo, P. E. Duffy, *Malar. J.* **10**, 386 (2011).
35. 1000 Genomes Project Consortium *et al.*, *Nature* **491**, 56–65 (2012).
36. K. E. Wright *et al.*, *Nature* **515**, 427–430 (2014).
37. G. E. Weiss *et al.*, *PLOS Pathog.* **11**, e1004670 (2015).

ACKNOWLEDGMENTS

We thank D. Wirth, M. Ganter, A. Nicholson-Weller, M. Waldor, S. Lux, R. Husson, B. Burleigh, and members of the Duraisingh Laboratory for helpful discussions and reading of the manuscript. We thank C. Westhoff and C. Lomas-Francis of the New York Blood Center for gift of the second Inab sample. We thank U. Kanjee for technical assistance and D. Ndiaye, S. Mboup, and S. Volkman for *P. falciparum* clinical isolates from Senegal. This work was supported by a Gates Foundation Grand Challenges Exploration Award OPP1035276 (M.T.D.), NIH grant R01AI091787 (M.T.D.), a Pediatric Scientist Development Program Fellowship from the Eunice Kennedy Shriver National Institute of Child Health and Human Development K12-HD000850 (E.S.E), NIH grant K08 1K08AI103034-01A1 (E.S.E.), Boston Children's Hospital Faculty Development Award (E.S.E.), NIH grant K01DK098285 (J.A.P.), and the Cambridge Biomedical Research Center, UK (M.P.W. and L.V.N.). Additional data can be found in the supplementary materials.

SUPPLEMENTARY MATERIALS

www.sciencemag.org/content/348/6235/711/suppl/DC1
Materials and Methods
Supplementary Text
Figs. S1 to S10
References (*38*–*42*)
Data sets S1 to S5

22 November 2014; accepted 9 April 2015
10.1126/science.aaa3526

Will you be published in *Science* this December?

(If you have a recent PhD you could be.)

To be published in *Science* is a special moment for any scientist. But to do so at the very start of your career is extremely exciting indeed. If you are a recent PhD graduate you could be published in *Science* this December, and receive a very special prize in Stockholm during the week of Nobel.

The journal *Science* & SciLifeLab have established The *Science* & SciLifeLab Prize for Young Scientists, to recognize and reward excellence in PhD research and support young scientists at the start of their careers. It's about bright minds, bright ideas and bright futures.

Four winners will be selected for this international award. They will have their essays published by the journal *Science* and share a new total of 60,000 USD in prize money. The winners will be awarded in Stockholm during the second week of December when the city is alive with excitement and celebrates the new Nobel Laureates at the annual Nobel Prize ceremony. They will take part in a truly unique week of events including meeting leading scientists in their fields.

"The last couple of days have been exhilarating. It has been an experience of a lifetime. Stockholm is a wonderful city and the Award winning ceremony exceeds my wildest dreams."
–Dr. Dan Dominissini, 2014 Prize Winner

Who knows, having your work published in the journal *Science* could be a major stepping stone in your career and and the *Science* & SciLifeLab Prize for Young Scientists makes this possible.

Science & SciLifeLab PRIZE FOR YOUNG SCIENTISTS

This prize is made possible with the kind support of the Knut and Alice Wallenberg Foundation. This Foundation grants funding in two main areas; research projects of high scientific potential and individual support of excellent scientists.

The 2015 Prize is now open. The deadline for submissions is August 1, 2015.
Enter today: www.sciencemag.org/scilifelabprize

The 2015 Prize categories are:

- Cell and Molecular Biology
- Ecology and Environment
- Genomics and Proteomics
- Translational Medicine

Knut och Alice Wallenbergs Stiftelse

Science AAAS

SciLifeLab

eppendorf

adVantage **New Promotion March 1 – June 30, 2015**

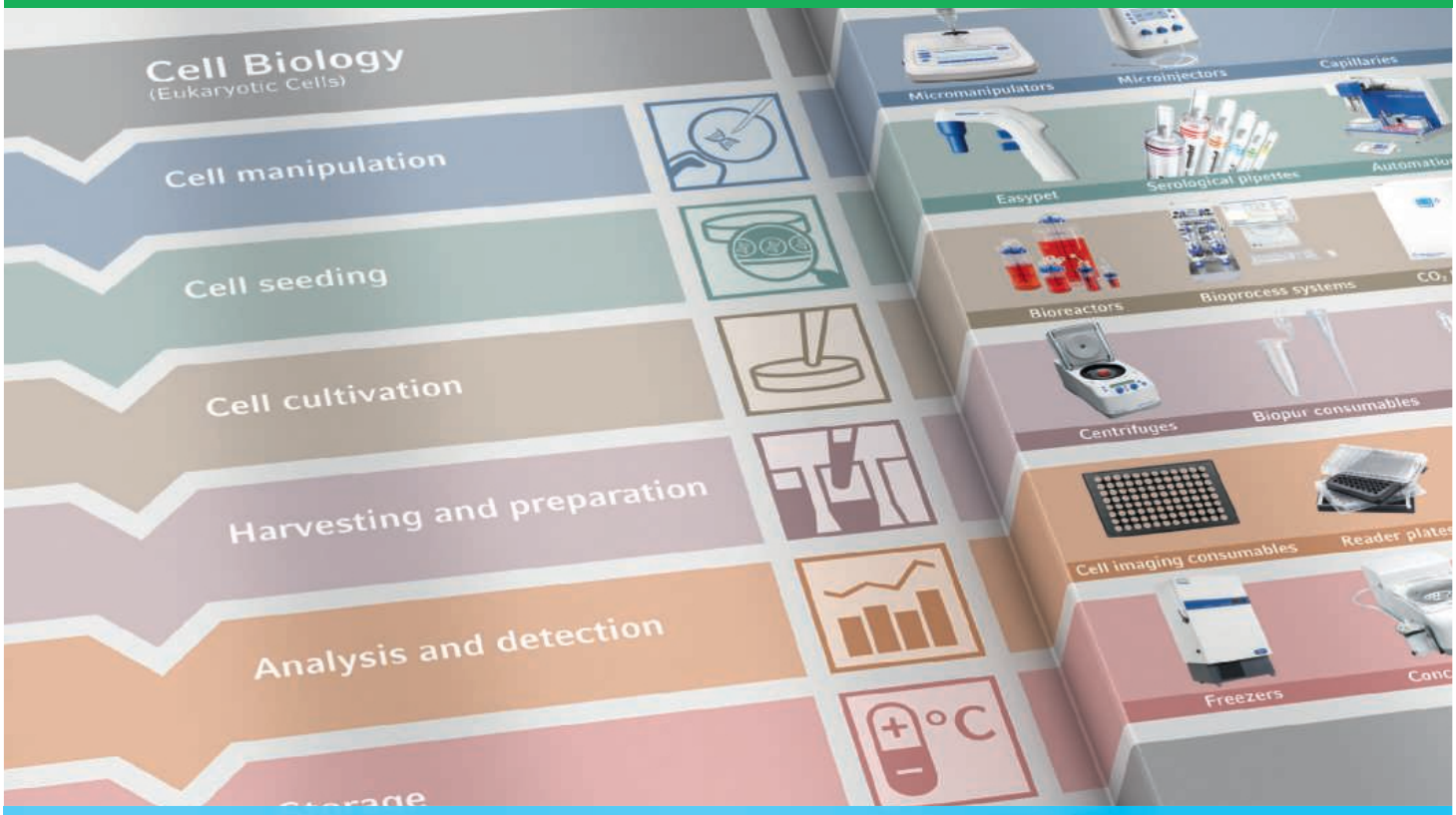

Take Good Care of Your Cells

Smart solutions for your cell biology processes—now with up to 21 % off

As a workflow-oriented provider of lab equipment, Eppendorf offers instruments, consumables, and accessories that perfectly fit your processes in the lab and thus your daily lab work. Our comprehensive solutions are engineered with smart innovations to simplify or even eliminate cumbersome lab work.

Benefit now from substantial savings on:

> Eppendorf Xplorer® electronic multi-channel pipettes
> Centrifuge 5702 R with rotor
> Eppendorf ThermoMixer® C
> Eppendorf BioSpectrometer® fluorescence with µCuvette G1.0
> Divisible twin.tec PCR Plates 96

www.eppendorf.com/advantage

Genotyping Arrays

The newest arrays, Axiom Porcine Genotyping Array and Axiom Equine Genotyping Array, each with more than 600,000 markers, will be available to the agriculture community under the Axiom Expert Design Program. These two high-density arrays add to the product portfolio that includes bovine, chicken, maize, salmon, and wheat. Affymetrix has recently launched arrays with the newest content for genomic breeding in soybean and cotton, and arrays for buffalo, rainbow trout, rose, and strawberry. Also new are enhanced wheat arrays that have come out of the U.K.-based Wheat Institute Strategic Programme (WISP). With Affymetrix's advanced bioinformatics and innovative design strategies, Axiom arrays routinely support genome-wide genotyping and accurately call the genotypes of both diploid and polyploid species.

Affymetrix
For info: 888-362-2447
www.affymetrix.com/agrigenomics

Microscopy Illumination

The new Lumen 1600-LED from Prior Scientific is the latest product in Prior's ever-expanding microscopy illumination product line. The Lumen 1600-LED offers individual control for 16 selectable wavelengths. With its unique 16 selectable LED wavelengths, the Lumen 1600-LED is compatible with all simple and multiband filter sets. For the user who wants ease of use, the Lumen 1600-LED has a "white light" mode with simple on/off and intensity buttons. Fitting directly to most microscopes the system enables for rapid switching between LED wavelengths to allow for capture of high speed events. The Lumen 1600-LED is controlled via a manual keypad controller, TTL, USB, analogue input for dynamic intensity control. Excitation filters can be fitted in the optical path for controlled switching with no moving parts. Providing 25,000+ hours of bulb life, the Lumen 1600-LED is an environmentally friendly illumination system that requires no special disposal regulations.

Prior Scientific
For info: 800-877-2234
www.prior.com

Trace Gas Analyzer

The new PTR-QiTOF and the PTR-TOF 1000 are now available, complementing the PTR-TOF trace gas analyzer series. Both instruments can be optionally equipped with the new fast GC add-on, combining Gas Chromatographic separation with real-time trace VOC analysis. Featuring a Quadrupole ion guide (Qi), the new PTR-QiTOF achieves a performance, no other commercial PTR-TOFMS system has ever been able to demonstrate before. Scientists can expect up to 25x more sensitivity, one order of magnitude lower detection limit and 20% higher mass resolution. This boost in sensitivity is especially beneficial for cutting-edge applications like eddy-covariance flux measurements, where ultralow VOC concentrations have to be quantified with more than 10 Hz. The high time-resolution and sensitivity of IONICON PTR-TOF instruments enable flux measurements of biogenic VOCs, providing new insights to our understanding of the atmospheric VOC budget by studying active atmosphere-ecosystem exchange of a vast number of BVOCs.

Ionicon
For info: +43-512-214-800
www.ionicon.com/ptr-qitof

Cathode Gauge

The Granville-Phillips Series 500 Cold Cathode Gauge sets a new accuracy standard (±10%) for wide pressure range CC gauges. The Series 500 features a longer lifetime than traditional CC gauges and fast, reliable starting. Its patent-pending method for determining pressure dosage over time provides for predictive maintenance, and USB connectivity assures ease of setup and pressure monitoring. The Series 500's unprecedented accuracy is based on innovative technology and time-tested calibration techniques. It offers a wide measurement range from 10^{-10} to 10^{-2} Torr, and includes electronic, digital, and analog interfaces. The USB interface and GP Connect software provides setup and diagnostics, including screens for setting up the gauge, graphing the pressure trend, and checking usage statistics. Applications include R&D, coating, semiconductor, analytical, high-energy physics, general vacuum, and other applications requiring long life and accuracy.

MKS Instruments
For info: 978-645-5500
www.mksinst.com

Ebola Antigens/Antibodies

Several products have been designed for the development of an enzyme-linked immunosorbent assay (ELISA) detection assay for the Ebola virus. The new products comprise three different monoclonal antibodies to the Ebola virus and two recombinant proteins (from the Sudan and Zaire strains) suitable for use in producing an optimized ELISA test kit for Ebola. An antigen-capture ELISA test for Ebola offers the possibility of diagnosis within the first few days after symptoms begin. Diagnosing Ebola can be a challenge because the early symptoms are nonspecific to Ebola infection and are often seen in patients with more commonly occurring diseases, such as malaria and typhoid fever. Accurate diagnostics are essential in controlling an outbreak. Ideally a test should be an easy-to-use and affordable solution that enables the rapid screening of suspected patients and people travelling out of an outbreak region.

AMS Biotechnology
For info: +44-(0)-1235-828200
www.amsbio.com

Electronically submit your new product description or product literature information! Go to www.sciencemag.org/products/newproducts.dtl for more information.

Newly offered instrumentation, apparatus, and laboratory materials of interest to researchers in all disciplines in academic, industrial, and governmental organizations are featured in this space. Emphasis is given to purpose, chief characteristics, and availability of products and materials. Endorsement by *Science* or AAAS of any products or materials mentioned is not implied. Additional information may be obtained from the manufacturer or supplier.

Join Keystone Symposia in Asia for our October Conferences on Nutrition and Diabetes

Human Nutrition, Health and Environment

October 14–18, 2015
China World Hotel | Beijing | China

Scientific Organizers: Martin Kussmann, Hannelore Daniel and Jacqueline Pontes Monteiro

Understanding interactions of nutrition and lifestyle with an individual's genetic makeup is vital for maintaining health and delaying disease onset. Toward that end, this meeting aims to: 1) Bring together researchers from traditionally separated disciplines: nutrition, (gen) omics, clinics, physiology, epidemiology, analytics, biomathematics; 2) Advance nutrition research as a quantitative, holistic and molecular science; 3) Review/challenge classical pre-clinical models and clinical study designs, incorporating improved translational in vitro and in vivo models, human intervention study designs, and innovative new tools/technologies for molecular phenotyping; and 4) Connect basic science to patient- and consumer-relevant outputs in terms of personalized dietary/nutritional counseling and monitoring/diagnostics.

Session Topics:

- The Interaction between Human Genome, Diet and Environment
- Translational Models for Human Nutrition and Health
- Human Nutritional and Lifestyle Interventions
- Capturing and Monitoring Human Individuality
- From Nutrigenomics to Systems Nutrition
- Nutrition 2.0 – Translation into Solutions for Human Health
- Global Nutrition and Sustainability

Global Health Travel Award Deadline (for investigators from developing countries): May 12, 2015;
Scholarship & Discounted Abstract Deadline: June 16, 2015; Abstract Deadline: July 14, 2015; Discounted Registration Deadline: August 13, 2015

For additional details, visit **www.keystonesymposia.org/15T1**.

Diabetes: New Insights into Molecular Mechanisms and Therapeutic Strategies

October 25–29, 2015
Westin Miyako Kyoto | Kyoto | Japan

Scientific Organizers: Takashi Kadowaki, Juleen R. Zierath, Nobuya Inagaki and Barbara B. Kahn

The prevalence of type 2 diabetes is rising to epidemic proportions worldwide. Type 2 diabetes is a complex disease caused by dysfunction of multiple organ systems, and disease susceptibility is profoundly influenced by both genetic and environmental factors. This meeting brings together leading professionals in the academic and pharmaceutical communities with various specialties in diabetes research to share new approaches and research paradigms. The meeting will present the latest discoveries in diabetes research, highlighting essential aspects of diabetes, as well as emerging themes that are likely to provide novel therapeutic approaches.

Session Topics:

- Islet Dysfunction in Diabetes
- Regenerative Medicine in Diabetes
- Gut Biology and Systemic Metabolism
- CNS Control of Metabolism
- Novel Insights into Adipocyte Biology
- Molecular Mechanisms Underlying Insulin Resistance
- Genetics and Epigenetics of Diabetes
- Diabetes and Healthy Lifespan

Scholarship & Discounted Abstract Deadline: June 25, 2015; Abstract Deadline: July 23, 2015; Discounted Registration Deadline: August 25, 2015

For additional details, visit **www.keystonesymposia.org/15T2**.

KEYSTONE SYMPOSIA™
on Molecular and Cellular Biology
Accelerating Life Science Discovery


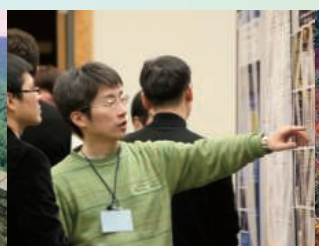


R&D SYSTEMS™
a bio-techne brand

Do You Suffer from **Panel Envy?**

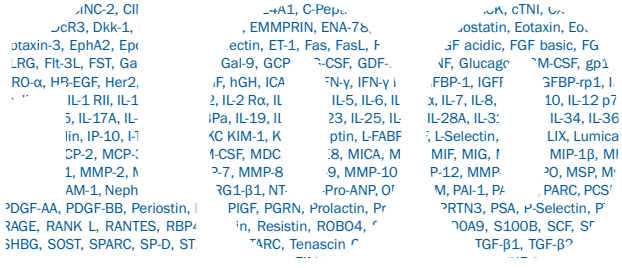

analytes in 1 Luminex® assay.

EXPLORE NOW
rndsystems.com/**100Plex**

#PanelEnvy #100Plex

Science Careers Advertising

For full advertising details, go to ScienceCareers.org and click For Employers, or call one of our representatives.

Tracy Holmes
Worldwide Associate Director
Science Careers
Phone: +44 (0) 1223 326525

THE AMERICAS

E-mail: advertise@sciencecareers.org
Fax: 202 289 6742

Tina Burks
Phone: 202 326 6577

Nancy Toema
Phone: 202 326 6578

Marci Gallun
Sales Administrator
Phone: 202 326 6582

Online Job Posting Questions
Phone: 202 312 6375

EUROPE / INDIA / AUSTRALIA / NEW ZEALAND / REST OF WORLD

E-mail: ads@science-int.co.uk
Fax: +44 (0) 1223 326532

Axel Gesatzki
Phone: +44 (0) 1223 326529

Sarah Lelarge
Phone: +44 (0) 1223 326527

Kelly Grace
Phone: +44 (0) 1223 326528

JAPAN

Katsuyoshi Fukamizu (Tokyo)
E-mail: kfukamizu@aaas.org
Phone: +81 3 3219 5777

Hiroyuki Mashiki (Kyoto)
E-mail: hmashiki@aaas.org
Phone: +81 75 823 1109

CHINA / KOREA / SINGAPORE / TAIWAN / THAILAND

Ruolei Wu
Phone: +86 186 0082 9345
E-mail: rwu@aaas.org

ScienceCareers
FROM THE JOURNAL SCIENCE AAAS

ScienceCcareers.org

Learn more and conduct your job search the easy way.

- Search thousands of job postings
- Create job alerts based on your criteria
- Get career advice from our Career Forum experts
- Download career advice articles and webinars
- Complete an individual development plan at "myIDP"

Target your job search using relevant resources on **ScienceCareers.org**.

ScienceCareers
FROM THE JOURNAL SCIENCE AAAS

63 north

KNOWLEDGE FOR A BETTER WORLD

Photo: Carl-Erik Eriksson

Trondheim is the ancient Viking capital of Norway. The Nidelva River flows through the city, and you can even fish for salmon during your lunch break. You'll find hiking, alpine and cross-country skiing, cycling and more within a 10-minute drive of the city centre.

Research adventure at 63 degrees north

Remote yet modern. Beautiful and peaceful. Quality and equality. All that combined with long-term government research funding and the UN's ranking as one of the best countries to live in. Welcome to Trondheim and NTNU. The best minds, world-class research, and just the right size city for a great life.

We welcome top scientists from all cultures and nations who want to contribute to our goal: Knowledge for a better world.

TOP RESEARCH DEMANDS BRILLIANT MINDS
– WE'RE ALWAYS LOOKING FOR THE BEST

Photo: Geir Mogen/Kavli Institute for Systems Neuroscience

NTNU neuroscientists May-Britt and Edvard Moser were awarded the Nobel Prize in Medicine or Physiology in December 2014.

NTNU – Trondheim
Norwegian University of
Science and Technology

www.ntnu.edu

南京工業大學
NANJING UNIVERSITY OF TECHNOLOGY

海外领军人才招聘

Overseas Talents Recruitment

Nanjing Tech University, with a history of more than one hundred years, is a multidisciplinary university with a particular strength in engineering.

Aiming at excellence and innovation, Nanjing Tech University is set to become a first-class research university with a global vision. We are now seeking outstanding academic and research leaders in the following and related fields: Basic disciplines from within the Physical Sciences; Cutting edge disciplines from within the Life Sciences; Applied disciplines from within the Information Sciences; Humanities represented by Management Science.

Applicants should have a Ph.D. with at least 3-years research experience from leading universities or institutes. Candidates should demonstrate an internationally recognized research record and outstanding achievements. Successful candidates are expected to develop vigorous research programs and lead an independent research team. Successful candidates will be provided with a competitive relocation fee and salary package, generous start-up funds and spacious laboratories.

Interested candidates should visit **http://rczyb.njtech.edu.cn** for application details.
Phone: **Ms. Wang +86-25-58139148.**
E-mail: **job@njtech.edu.cn**

西南交通大学 Southwest Jiaotong University

Southwest Jiaotong University, P.R.China Anticipates Your Working Application

Southwest Jiaotong University (SWJTU), founded in 1896, situates itself in Chengdu, the provincial capital of Sichuan. It is a national key multidisciplinary "211" and "985 Feature" Projects university directly under the jurisdiction of the Ministry of Education, featuring engineering and a comprehensive range of study programs and research disciplines spreading across more than 20 faculties and institutes/centers. Boasting a complete Bachelor-Master-Doctor education system with more than 2,500 members of academic staff, our school also owns 2 first-level national key disciplines, 2 supplementary first-level national key disciplines (in their establishment), 15 first-level doctoral programs, 43 first-level master programs, 75 key undergraduate programs, 10 post-doctoral stations and more than 40 key laboratories at national and provincial levels.

Our university is currently implementing the strategy of "developing and strengthening the university by introducing and cultivating talents". Therefore, we sincerely look forward to your working application.

More information available at http://www.swjtu.edu.cn/

I. Positions and Requirements

A.High-level Leading Talents

It is required that candidates be listed in national top talents programs such as ***Program of Global Experts, Top Talents of National Special Support Program, "Chang Jiang Scholars", China National Funds for Distinguished Young Scientists and National Award for Distinguished Teacher.***

Candidates are supposed to be no more than 50 years old. The limitation could be extended in the most-needed areas of disciplinary development.

Candidates who work in high-level universities/institutes and reach the above requirements are supposed to be no more than 45 years old.

B. Young Leading Scholars

Candidates are supposed to be listed in or qualified to apply for the following programs:

•National Thousand Young Talents Program

•The Top Young Talents of National Special Support Program(Program for Supporting Top Young Talents)

•Science Foundation for the Excellent Youth Scholars

Candidates should have good team spirit and leadership, outstanding academic achievements, broad academic vision and international cooperation experience and have the potential of being a leading academic researcher.

C. Excellent Young Academic Backbones

Candidates under 40 years old are expected to graduate from high-level universities/institutes either in China or other countries. Those who are professors, associate professors and other equal talents from high-level universities/institutes overseas could be employed as professors and associate professors as well.

D. Excellent Doctors and Post Doctoral Fellows

Candidates under 35 years old are supposed to be excellent academic researchers from high-level universities either in China or other countries.

II. Treatments

The candidates will be provided with competitive salaries and welfares that include settling-in allowance, subsidy of rental residence, start-up funds of scientific research, assistance in establishing scientific platform and research group as well as international-level training and promotion . As for outstanding returnees, we can offer further or specific treatments that can be discussed personally.

III . Contact us:

Contacts: Ye ZENG & Yinchuan LI Telephone number: 86-28-66366202 Email: *talent@swjtu.edu.cn*
Address: Human Resources Department of SWJTU, the western park of high-tech zone, Chengdu, Sichuan, P.R.China, 611756

http://www.swjtu.edu.cn/

华北电力大学
NORTH CHINA ELECTRIC POWER UNIVERSITY

Faculty Positions Available in North China Electric Power University, China

Established in 1958, located in Beijing and Baoding (main campus in Beijing), North China Electric Power University (NCEPU) is one of the top research-oriented universities in China, focusing on fundamental cutting edge research and high-level education, covering diverse areas of science, engineering, technology, humanities, economics, management and law. NCEPU, as a key university jointly constructed by the Ministry of Education and the University Council, an organization composed of seven super-large Chinese power enterprises, China Electricity Council and NCEPU, is affiliated with the Ministry of Education, officially listed as one of the "211 Project" and "985 Project" universities as well as a "Predominant Discipline Innovation Platform". It owns 1 national key laboratory, 2 state science and technology innovation platforms and 11 provincial and ministerial key laboratories. At present, the campus covers one million square meters in total, with about 3000 faculty and staff.

North China Electric Power University is on a clear path to grow as a world-class university in engineering and science fields. As part of university's further pursuit for excellence in research and education, we have expanded a global search for the best research talents to join us.

North China Electric Power University invites applications for full-time Professors, Associate Professors and excellent scientists. Preference will be given to candidates whose research emphasis demonstrates the potential to complement and advance our existing research strengths on electric power, clean energy, energy power, mechanical engineering, automation, computer science, chemistry, economics, management, mathematics and physics. Successful candidates will be offered competitive salaries, appropriate positions and start-up funds.

Position Openings

- ●Position offered by the Recruitment Program of Global Experts (1000 Plan Professorship)
- ●Position offered by Chang Jiang Scholars Program
- ●Position offered by the Recruitment Program of Global Young Experts (1000 Plan Professorship for Young Talents)
- ●North China Electric Power University's Professors
- ●North China Electric Power University's Associate Professors
- ●North China Electric Power University's Teachers

Interested individuals should email his/her CV to ncepuscience@163.com, with "Faculty Application from Science" in the title. For more details, please visit our Talent Management Office's website at http://rcb.ncepu.edu.cn, or contact us by email ncepuscience@163.com, or telephone 86-010-61772414.

High-level Talents Online Job Fair 2015

The first action of 2015

will be held on 24th May, from 7AM to 24PM in Beijing.

Recruitment requirements:

Scholars and doctors with working position and graduating doctors

domestic and overseas

Please send your curriculum vitae to:

acabridge@gmail.com chisa.add@gmail.com chisa_yang@163.com

For more information, please check the following web sites

http://www.edu.cn/cv
http://www.chisa.edu.cn/zt/yczt/network_video/index.html



Xinxiang Medical University
Recruitment of Principal Investigators

University Brief

Founded in 1896, Xinxiang Medical University (XXMU) is a historic international research university system located on the north side of the Yellow River. The University comprises 15 colleges/institutes on two main campuses, 5 affiliated hospitals (> 9,000 beds) in Henan, and 1,080 faculty members. The University is renowned by both undergraduate and postgraduate education and emphasizing on interdisciplinary teaching and research worldwide. The research of University ranges from basic biomedical science to public health, pharmaceutical science, nursing, medical administration, psychology, life science, professional education, and clinical sciences. XXMU has established prolific international collaborations with Austria, British, Malaysia, France, Germany, United States, Canada, and Japan. It promotes interdisciplinary studies, dedicated to educating all-rounded students to acquire a strong humanitarian and innovative thinking with a global outlook.

Positions

Positions are open in basic biomedicines, clinical medicines, stomatology, public health, molecular and cellular biology, pharmacology and pharmacy, psychology, biomedical engineering, health administration, and other related professional fields. In particular, the leading disciplines of the University are neuroscience, psychology, cancer research, and immunology. The following applicants are encouraged: assistant professors, associate professors, and full professors oversea; academicians of

the Chinese Academy of Science and the Chinese Academy of Engineering; national candidates of "the Thousands of People Plan", national candidates of "the Special Support Plan"; professors awarded with "The Yangtze Scholar"; awardees of "The National Science Fund for Dis tinguished Young Scholars"; chief principal investigators of "The 863 and 973 Projects"; and awardees of "The Zhong Yuan Scholars". Appointed professors will be qualified to apply for "Henan Talent Professors" and "Tai Hang Scholars".

Salary/Benefits

1.Annual salary for tenure-tracked assistant professor, associate professor, and full professor ranges from $60,000 to $ 350,000.
2.Start-up fund, 3-50million RMB Yuan.
3.Provide one house with living area of 80 – 120 m^2.
4.Independent PI is encouraged to recruit his/her own team members who will be supported by additional funds.
5.The University offers appropriate position for family members.
6.The University provides retirement plan and medical insurance at the national level.
7.Aforementioned salary and benefits are negotiable for the applicants who will work as part-time hires.

Application Procedure

Interested candidates are invited to send:
1) a research plan for the next 5-10 years;
2) full CV with degree certifications and web link;
3) three letters of recommendation ;
4) three to five publications and/or patents with a description of your academic contributions to Mr. Yu or Mr. Gu, 601 Jinsui Avenue, Xinxiang, Henan, 453003.
+(86)373-302-9007 (or -9163),
email:shizike@163.com;
rczp@xxmu.edu.cn

For further information about the University and recruitment, please refer to:

http://www.xxmu.edu.cn/

Wake Forest™ School of Medicine

The Department of Neurobiology and Anatomy at Wake Forest Medical School announces open positions for

Postdoctoral/Predoctoral Training in Multisensory Processes

We seek strong candidates for postdoctoral and predoctoral training funded by an NIH T32 Training Grant. The training program provides a rich collaborative research environment that fosters interdisciplinary approaches to understanding how the brain integrates information from multiple senses to produce perception and adaptive behavior. Candidates with direct experience as well as those in related fields are encouraged to apply. Trainees will have access to any of 10 laboratories using human subjects and/or a variety of animal models (rodents-primates) with approaches spanning molecular/cellular to perceptual/behavioral. Fellowships are awarded on a competitive basis.

Applications including a current curriculum vitae or nominations should be sent to the Training Grant Director: Dr. Barry E. Stein **bestein@wakehealth.edu**, or to its Co-Directors: Dr. Terrence Stanford (**stanford@wakehealth.edu**) and Dr. Dwayne Godwin (**dgodwin@wakehealth.edu**). A description of the faculty and the program can be accessed via the website: **http://graduate.wfu.edu/admissions/t32/training_tpmp.html**

Wake Forest School of Medicine is an Affirmative Action/Equal Opportunity Employer and especially encourages applications from women and minority candidates.

STANFORD SCHOOL OF MEDICINE
Stanford University Medical Center

Stanford University School of Medicine seeks to recruit a new faculty member to join the Institute of Stem Cell Biology and Regenerative Medicine as an Assistant Professor in the University Tenure Line. There will be a co-primary appointment in an appropriate department to be considered in conjunction with the successful applicant. Candidates must have a Ph.D. in computer science, electrical engineering, bioinformatics or a related field. The search committee encourages applications from candidates who have research interests in clinical or translational informatics, bioinformatics, or related subdisciplines, and who have or will develop an independent research program in the computational sciences.

• The predominant criterion for appointment in the University Tenure Line is a major commitment to research and teaching.

The successful candidate will conduct a vigorous, independent research program, teach in the classroom, and advise students in any of a number of graduate programs in computational sciences.
Faculty members appointed as Assistant Professors will have completed one or two years of postdoctoral research experience. Their accomplishments during graduate and postgraduate training should already have stamped them as creative and promising investigators. Preference will be given to candidates who have experience in developing novel analytical tools to analyze the cellular composition of organs and/or tissues and who can complement and enhance existing strengths in stem cell biology, cancer biology, developmental biology, bioinformatics, and bioengineering within the Institute and the University.

Submit CV, a brief statement of research objectives and the names of three references to:

Dr. Michael F. Clarke
Chair, Stem Cell Computation Search Committee
Institute for Stem Cell Biology and Regenerative Medicine
Email: stemcellcomputationsearch@stanford.edu

Stanford University is an Equal Opportunity Employer and is committed to increasing the diversity of its faculty. It welcomes nominations of and applications from women and members of minority groups, protected veterans and individuals with disabilities, as well as others who would bring additional dimensions to the university's research, teaching and clinical missions.

63 north

KNOWLEDGE FOR A BETTER WORLD

THE ONSAGER FELLOWSHIPS

12 tenure-track positions available at NTNU

The Norwegian University of Science and Technology (NTNU) is Norway's primary institution for educating the future's engineers and scientists. The university also has strong programmes in the social sciences, teacher education, the arts and humanities, medicine, architecture and fine art. NTNU's cross-disciplinary research delivers creative innovations that have far-reaching social and economic impact and that help contribute to a better world.

The Onsager Fellowship programme at NTNU is designed to attract the most talented scholars with an established reputation for high quality research and a commitment to learning and teaching at the university level.

APPLY FOR A TENURE-TRACK POSITION AS AN ASSOCIATE PROFESSOR IN:

- Linguistics
- Robotic vision
- Molecular biodiversity
- Medicine – bioinformatics
- Medicine – molecular biology
- Statistical machine learning
- Theoretical condensed matter physics
- Inorganic or hybrid functional materials
- Safety and reliability of complex systems
- Marine structures for the future – marine technology
- Zero emission refurbishment of the built environment
- Economics of natural resources and quantitative peace research

More info at: www.ntnu.edu/onsagerfellowship

Closing date: 25 May.

NTNU – Trondheim
Norwegian University of Science and Technology

TOP RESEARCH DEMANDS BRILLIANT MINDS
– WE'RE ALWAYS LOOKING FOR THE BEST

For recruitment in science, there's only one **Science**

What makes *Science* the best choice?

- Read and respected by 570,400 readers around the globe
- 78% of readers read *Science* more often than any other journal
- Your ad sits on specially labeled pages to draw attention to the ad
- Your ad dollars support AAAS and its programs, which strengthens the global scientific community.

Why choose this biotechnology section for your advertisement?

- Relevant ads lead off the career section with special Biotechnology banner
- Bonus distribution to:

  BIO International Convention
  June 15–18, 2015, Philadelphia, PA

  BIO Career Fair
  June 18, 2015, Philadelphia, PA.

Expand your exposure. Post your print ad online to benefit from:

- Link on the job board homepage directly to biotechnology jobs
- Dedicated landing page for jobs in biotechnology
- Additional marketing driving relevant job seekers to the job board.

* Ads accepted until June 8 on a first-come, first-served basis.

SCIENCECAREERS.ORG

ScienceCareers
FROM THE JOURNAL SCIENCE AAAS

To book your ad: **advertise@sciencecareers.org**

The Americas 202-326-6582
Europe/RoW +44(0)1223-326500
Japan +81-3-3219-5777
China/Korea/Singapore/Taiwan +86-186-0082-9345

FUNDING OPPORTUNITIES — U.S. Department of Defense

Defense Medical Research and Development Program

Peer Reviewed Medical Research Program

The Peer Reviewed Medical Research Program (PRMRP) funds exceptional research with the goal to improve the health and well-being of all military Service Members, Veterans, and their beneficiaries. The PRMRP received ***$247.5 million*** in fiscal year 2015 (FY15) and seeks grant applications in the following ***topic areas:***

Acupuncture
Acute lung injury
Advanced prosthetics
Arthritis
Burn pit exposure
Cardiovascular health
Chronic migraine and post-traumatic headache
Congenital heart disease
Dengue
Diabetes
DNA vaccine technology for post-exposure prophylaxis
Dystonia
Focal segmental glomerulosclerosis
Food allergies
Fragile X syndrome
Healthcare-acquired infection reduction
Hepatitis B
Hereditary angioedema
Hydrocephalus
Inflammatory bowel disease
Integrative medicine
Interstitial cystitis
Lupus
Malaria
Metals toxicology
Mitochondrial disease
Nanomaterials for bone regeneration
Osteoarthritis
Pancreatitis
Pathogen-inactivated dried plasma
Polycystic kidney disease
Post-traumatic osteoarthritis
Psychotropic medications
Pulmonary fibrosis
Respiratory health
Rheumatoid arthritis
Scleroderma
Sleep disorders
Tinnitus
Vascular malformations
Women's heart disease

Descriptions of the FY15 PRMRP Program Announcements and General Application Instructions are anticipated to be posted on Grants.gov by ***mid-April 2015:***

- Clinical Trial Award
- Discovery Award
- Focused Program Award
- Investigator-Initiated Research Award
- Technology/Therapeutic Development Award

All applications must conform to the Program Announcements and General Application Instructions that will be available for electronic downloading from the Grants.gov website (all viewable under CFDA number 12.420). Execution management support will be provided by the Congressionally Directed Medical Research Programs.

http://cdmrp.army.mil
http://cdmrp.army.mil/funding/prmrp.shtml

Director, Materials Research Laboratory & Professor

College of Engineering

University of Illinois at Urbana-Champaign

The College of Engineering at the University of Illinois at Urbana-Champaign invites applications for the position of Director of the Frederick Seitz Materials Research Laboratory (MRL). The MRL is a state-of-the-art research facility that fosters interdisciplinary research at the forefront of materials science. MRL brings together world-class faculty and students in condensed matter physics, materials chemistry, and materials science in a highly collaborative research environment. Participants in the MRL come from many departments across the College of Engineering and the campus. For more information on the MRL, please visit their website at http://mrl.illinois.edu/.

This position provides overall leadership and a long-term vision to leverage the capabilities of the MRL. Candidates must be eligible to hold a tenured full Professor position within the College of Engineering at the University of Illinois. The desired start date for this position is as soon as possible. To ensure full consideration, applications should be received by **September 1, 2015,** but applications will be accepted until the position is filled. **Please visit http://jobs.illinois.edu to view the complete position announcement and application instructions.**

The University is an EEO Employer/Vet/Disabled www.inclusiveillinois.illinois.edu and committed to a family-friendly environment (http://provost.illinois.edu/worklife/index.html).

ILLINOIS
UNIVERSITY OF ILLINOIS AT URBANA-CHAMPAIGN

PARTOUT OÙ IL Y A DE **L'AVENIR**

L'INRA RECRUTE **DES CHERCHEURS**

1er institut européen pour les sciences de l'animal et du végétal

INSCRIPTIONS OUVERTES JUSQU'AU 5 JUIN 2015

JOBS.INRA.FR

INRA SCIENCE & IMPACT

POSITIONS OPEN

FACULTY POSITIONS-MEDICAL SCHOOL

The Saint James School of Medicine, an international medical school (**website: http://www.sjsm.org**), invites applications from candidates with teaching and/or research experience in any of the basic medical sciences for its Caribbean campuses. Faculty positions are currently available in Pathology, Histology, and Anatomy. Applicants must be M.D., D.O., and/or Ph.D. Teaching experience in the U.S. system is desirable but not required. Retired persons are encouraged to apply. Attractive salary and benefits. Submit curriculum vitae electronically to **e-mail: jobs@mail.sjsm.org** or online at **website: http://www.sjsm.org.**

By **Ainissa Ramirez**

The making of a science evangelist

I have wanted to be a scientist ever since I was a little girl. I got the idea from a television program called *3-2-1 Contact*, where I watched a young African-American girl solve problems. I saw my reflection in her and was transfixed. As time passed and my science career progressed, I saw that reflection less often. Now, years later, after a stint in industry and a negative tenure decision, I'm putting myself out there so that others can see their reflection in me. It's a precarious path, exposed and vulnerable, but so far the fruits of my journey have exceeded my fears.

Great teachers nurtured my interest in science. There was Kathleen Donahue in fifth grade, who stoked my passion. There was Jean Howard, the unflappable high school physics teacher who urged me to apply to top colleges.

At Brown University, there were Edelgard Morse, the chemistry professor who rescued me when my grades fell, and also Anne Fausto-Sterling—my learned mentor, professor, and North Star. With a strong sense of purpose, a hungry mind, and a willingness to work hard, I assumed my success was assured. It wasn't; I could easily have been one of the many nameless casualties science routinely sheds. Weary and battle worn, I made it through.

"I saw my reflection in her and was transfixed."

I continued on to Stanford University to seek a Ph.D. As the only black student in the materials science department, I felt lonely and lost. But two good things happened there: I was awarded a AAAS Mass Media Fellowship and spent a summer writing for *Time*. (AAAS is the publisher of *Science*.) And I taught an introductory materials science class at a local community college. I was smitten with science communication. My students were smitten with science. I learned that I loved teaching science and that I have a talent for reaching apprehensive students. There was a third good thing: I finished my degree.

I took a research position at Bell Labs. There, I was in constant contact with other minority scientists. I saw my reflection again. My creativity flourished. I was awarded a spot on *MIT Technology Review*'s Innovators Under 35 list. I wanted to stay forever, but the telecom bubble burst, and my job ended.

So I landed in a tenure-track faculty position at Yale University. I established a well-funded lab, earned top teaching scores, and maintained a respected research program. I hosted a fun lecture series for kids called *Science Saturdays*. Children loved it and I did, too. In fact, I loved it more than I loved my research. Faculty life was not ideal—I could not see my reflection in my colleagues—but it was workable and I hoped to stay. Fate, and the tenure committee, had other plans.

The denial of tenure thrusts you into a caste of the unclean. You're expected to pick up your book bag, your lumbar pillow, and your shredded dignity and sneak meekly out the back door. By the time I left, I was happy to go. My gut told me it could take no more, that academic science wasn't my path. I was ill, fatigued, and uninterested in climbing that ladder again.

I used the tenure decision as an opportunity to explore afresh what I should do with my "one wild and precious life," as Mary Oliver called it in her poem, *The Summer Day*. It was time for me to discover my true vocation, which Aristotle supposedly said could be found at the intersection of the world's needs and my passions.

By now, I knew my passions well enough: science, teaching, sharing my love for science. So I looked at the world's needs and figured out my vocation. In the time I had left at Yale, I produced some science videos and posted them on YouTube. It felt good. Things opened up. TED invited me to give a talk. Dignitaries invited me to meetings. Random House published my book.

I'm now happier and healthier. I'm following a path worn by Isaac Asimov, Carl Sagan, Neil deGrasse Tyson, and Bill Nye: lecturing, writing, and publicizing science. My new vocation offers less security than the old one did, but that seems fitting somehow. It's wilder and more precious. ■

Ainissa Ramirez is the author of two books and co-hosts the science podcast Science Underground. *For more on life and careers, visit ScienceCareers.org. Send your story to SciCareerEditor@aaas.org.*

ILLUSTRATION: ROBERT NEUBECKER

Published by AAAS